ECN
Energy research Centre of the Netherlands

Final report of IEA Task 29, Mexnext (Phase 1):

Analysis of Mexico wind tunnel measurements

J.G. Schepers, K. Boorsma	Energy Research Center of the Netherlands, ECN
T. Cho	Energy Research Center of the Netherlands, ECN and Korea Aerospace Research Institute, KARI
S. Gomez-Iradi	National Renewable Energy Center of Spain, CENER
P. Schaffarczyk, A. Jeromin	University of Applied Sciences Kiel/CEWind EG
W.Z. Shen	The Technical University of Denmark
T. Lutz, K. Meister	University of Stuttgart
B. Stoevesandt	ForWind
S. Schreck	National Renewable Energy Laboratory
D. Micallef, R. Pereira, T. Sant	Delft University of Technology
H.A. Madsen, N. Sørensen	RISØ-DTU

February 2012 ECN-E–12-004

cener centro nacional de energías renovables national renewable energy centre
DTU
ÉTS
ForWind Center for Wind Energy Research
Gotland University Passion & Science
IFE Institute for Energy Technology
INTA
KARI Korea Aerospace Research Institute
Fachhochschule Kiel University of Applied Sciences
KIER Korea Institute of Energy Research
MIE University
NREL National Renewable Energy Laboratory
Risø DTU National Laboratory for Sustainable Energy
Suzlon Blade Technology
Technion Israel Institute of Technology
TU Delft
University of Twente.
IAG Universität Stuttgart
University of Victoria
iea wind

Acknowledgement

The authors would like to thank IEA Wind for facilitating the Mexnext project in their framework.

The contributions of the participants to Mexnext have been funded in various national programmes:

- The contribution from ECN has been funded through the EZS subsidy from the Dutch Ministry of Economic affairs
- The contribution from the University of Victoria has been funded through the Natural Sciences and Engineering Research Council (NSERC)
- NREL participation in IEA Task 29 was funded by the US Department of Energy through the Wind and Water Power Program
- The contribution from RISØ-DTU and DTU MEK has been funded by the Danish Research and Development Program EUDP under contract: 63011-0190 "MexNext Analysis of Wind Tunnel Measurements and Improvement of aerodynamic models"
- The participation of CENER in IEA Task 29 was internally funded and thanks to the MICINN (ICTS-2009-40) program, CPU hours for CFD computations were obtained at CESGA supercomputing centre.
- The researchers from Israel would like to thank the Israel Ministry of National Infrastructures/ Office of the chief Scientist, for the support of the research that was carried out at the Technion - Israel Institute of Technology, Haifa, Israel
- The participation from UAS Kiel was funded by German Federal State of Schleswig-Holstein and the German Federal Ministry for the Environment, Nature Conservation and Nuclear Safety (BMU). Part of the CPU hours for computation was supplied by North-German Supercomputing Alliance (HLRN).

Abstract

This report describes the work performed within the first phase of IEA Task 29 Mexnext.

In this IEA Task 29 a total of 20 organisations from 11 different countries collaborated in analysing the measurements which have been performed in the EU project 'Mexico'. Within this Mexico project 9 European institutes carried out a wind tunnel experiment in the Large Low Speed Facility (LLF) of the German Dutch Wind Facilities DNW on a rotor with a diameter of 4.5 m. Pressure distributions were measured at five locations along the blade along with detailed flow field measurements around the rotor plane using stereo PIV.

The following organisations (and persons) cooperated in the projects:

- Canada: École de technologie supérieur, Montréal, ETS (C. Masson, S. Breton, C. Sibuet), and University of Victoria, UVIC (C. Crawford)
- Denmark: RISØ-DTU (H. Madsen, N. Sørensen, P. Rethouré) and the Technical University of Denmark DTU-MEK (W. Z. Shen)
- Germany: University of Stuttgart, Ustutt (T. Lutz, K. Meister), University of Applied Sciences at Kiel/CEWind EG (P. Schaffarczyk and A. Jeromin), ForWind (B. Stoevesandt and I. Hernandez)
- Israel: Technion, Israel Institute of Technology (A. Rosen, V. Ognev. R. Gordon)
- Japan: Mie University/National Institute of Advanced Industrial Science (T. Maeda, Y. Kamada, J. Murata)
- Korea: Korea Institute of Energy Research KIER, (H. Shin) and Korea Aerospace Research Institute, KARI (C. Kim, T. Cho)
- Netherlands: Energy research Center of the Netherlands, ECN (G. Schepers, K. Boorsma, H. Snel), Delft University of Technology, TUDelft (G. van Bussel, N. Timmer, D. Micallef), Suzlon Blade Technology, SBT (A. Verhoeff), Technical University of Twente, TUTwente (E. van der Weide)
- Norway: Institute for Energy Technology/Norwegian University of Science and Technology, IFE (A. Knauer, J. van Rij)
- Spain: National Renewable Energy Center, CENER (X. Munduate, S. Gomez-Iradi, A. Gonzalez, A. Irisarri) and National Institute for Aerospace Technology, INTA (C. Redondo Calle)
- Sweden: Royal Institute of Technology/University of Gotland, KTH/HGO (S. Ivanell and K. Nilsson)
- USA: National Renewable Energy Laboratory, NREL (S. Schreck)

The Energy research Center of the Netherlands, ECN acted as Operating Agent.

As a result of the international collaboration within this task a very thorough analysis of the data could be carried out and a large number of codes were validated not only in terms of loads but also in terms of underlying flow field.

The detailed pressure measurements along the blade in combination with the detailed flow field measurements gave a unique opportunity to better understand the response of a wind turbine to the incoming flow field. Deficiencies in modelling have been established and directions for model improvement can be given.

Contents

1 Introduction

This report summarizes the results from the first phase of IEA Task 29 Mexnext. Mexnext is a joint project in which 20 parties from 11 different countries cooperate:

- Canada: École de technologie supérieur, Montréal, ETS (C. Masson, S. Breton, C. Sibuet), and University of Victoria, Uvic (C. Crawford)
- Denmark: RISØ-DTU (H. Madsen, N. Sørensen and Pierre-Elouan Rethore) and the Technical University of Denmark DTU-MEK (W. Z. Shen)
- Germany: University of Stuttgart, Ustutt (T. Lutz, K. Meister), University of Applied Sciences at Kiel/CEWind EG (P. Schaffarczyk and A. Jeromin) and ForWind (B. Stoevesandt and I. Hernandez)
- Israel: Technion - Israel Institute of Technology (A. Rosen, V. Ognev. R. Gordon)
- Japan: Mie University/National Institute of Advanced Industrial Science (T. Maeda, Y. Kamada, J. Murata)
- Korea: Korea Institute of Energy Research KIER, (H. Shin) and Korea Aerospace Research Institute, KARI (C. Kim, T. Cho)
- Netherlands: Energy Research Center of the Netherlands, ECN (G. Schepers, K. Boorsma, H. Snel), Delft University of Technology, TUDelft (G. van Bussel, N. Timmer, D. Micallef), Suzlon Blade Technology, SBT (A. Verhoeff) and Technical University of Twente, TUTwente (E. van der Weide)
- Norway: Institute for Energy Technology/Norwegian University of Science and Technology, IFE (A. Knauer, J. van Rij)
- Spain: National Renewable Energy Center, CENER (X. Munduate, S. Gomez) and National Institite for Aerospace Technology, INTA (C. Redondo Calle)
- Sweden: Royal Institute of Technology/University of Gotland, KTH/HGO (S. Ivanell and K. Nilsson)
- USA: National Renewable Energy Laboratory, NREL (S. Schreck)

The focus of Mexnext lies on improving and understanding aerodynamic calculational models by means of dedicated wind tunnel measurements. These measurements have been performed within the EU project Mexico in the year 2006.

Aerodynamic calculational models are extremely important since they form the backbone of every computer program for the design of wind turbine. It is however known from several validation projects, see e.g. [1] and [2], that the uncertainties in the aerodynamic models are very large.

The availability of high quality measurements is considered to be the most important pre-requisite to gain insight into model uncertainties and to validate and improve aerodynamic wind turbine models. However, conventional experimental programs on wind turbines generally do not provide sufficient information for this purpose, since they only measure the integrated, total (blade or rotor) loads. These loads consist of an aerodynamic and a mass induced component and they are integrated over a certain spanwise length. In the late 80's and the 90's it was realized that more direct aerodynamic information was needed in order to improve the aerodynamic modelling. For this reason several institutes initiated experimental programs in which pressure distribution and the resulting normal and tangential forces at different radial positions were measured. Under the auspices of the IEA Wind, many of these measurements were stored into a database in Task 14

and Task 18, see [3]. The results of these measurements turned out to be very useful and important new insights on e.g. 3D stall effects, tip effects and yaw were formed. However, the measurements were taken on turbines in the free atmosphere, where the uncertainty due to the instationary, inhomogeneous and uncontrolled wind conditions formed an important problem (as it is in all field measurements). This problem was overcome in NREL's NASA-Ames wind tunnel experiment which was carried out in 2000 [4]. In this experiment a heavily instrumented rotor with a diameter of 10 meter was placed in the world's largest wind tunnel, i.e. the NASA-Ames (24.4×36.6 m^2) wind tunnel. As such, measurements were performed at stationary and homogeneous conditions. The huge size of the wind tunnel allowed a rotor diameter of 10 m, with little blockage effects. Obviously this rotor diameter is still (much) smaller than the diameter of the nowadays commercial wind turbines, but nevertheless the blade Reynolds number (in the order of 1 Million) is sufficiently high to make the aerodynamic phenomena at least to some extend representative for modern wind turbines. NREL made the measurements from this experiment available to other institutes and they were analysed within IEA Wind Task 20. This Task was finished in December 2007 see [5]. The Mexnext can be considered as the successor of IEA Task 20. It focussed on the wind tunnel measurements which became available in December 2006 within the EU project Mexico [6]. In this project detailed aerodynamic measurements were carried out on a wind turbine model with a diameter of 4.5 m, which was placed in the largest European wind tunnel, the German Dutch Wind Tunnel, DNW with a size of 9.5 x 9.5 m^2. A unique feature of the Mexico measurements lies in the fact that the flow field around the rotor plane was measured simultaneously with the blade properties. At the end of the Mexico project the database with measurements was still in a rather rudimentary form and only limited analysis were carried out.

For this reason the Mexnext project was initiated in which the measurements from the Mexico project are analysed. Thereto it should be realised that the amount of Mexico data is very vast by which the time needed to analyse all data is extremely long for a single country. As such it was considered very beneficial to organise the analysis of the Mexico data under IEA Wind, since this make it possible to share tasks. Added value also lied in the fact that the task served as a forum for discussion and interpretation of the results. It is then possible to generate more value from the data than the summed value from the individual projects.

The Mexnext project started on June 1, 2008. This report describes the first phase which ended on June 1, 2011.

The report is structured as follows: The goal of Mexnext is described in section 2. Since the subject of Mexnext is aerodynamics it is considered important that the reader understands the value of aerodynamic research. This is explained in section 3.

The Mexico experiment is described in section 4. The working procedure and the work plan of Mexnext is described in section 5. It is then explained that the project is carried out in different tasks, the results of these tasks are reported in the sections 6 to 16. Conclusions and recommendations are given in section 17.

2 Goal

The objective of Mexnext was a thorough investigation of the measurements which was carried out in the EU sponsored Mexico project. Special attention was paid to yawed flow, instationary aerodynamics, 3D effects, tip effects, non-uniformity of flow between the blades, near wake aerodynamics, turbulent wake, standstill, tunnel effects etc. These effects were analysed by means of different categories of models (CFD, free wake methods, engineering methods etc.). A comparison of the Mexico findings with the findings from other experiments was also carried out. As such the Task provided insight in the accuracy of different types of models and (descriptions for) improved wind turbine models were made.

3 Value of aerodynamics

As explained in section 2 the main subject of Mexnext lies on the field of wind turbine aerodynamics. To understand the impact of Mexnext (and aerodynamic research in general) for the successful deployment of a wind energy project, the following considerations are given:

- First it should be realized that the main aim of a wind turbine is to extract kinetic energy from the wind into mechanical energy of a wind turbine. This transformation of energy is an aerodynamic process. Therefore it is fair to consider a wind turbine as an aerodynamic machine and to state that the aerodynamic modelling forms the backbone of a wind turbine design code.

- It should also be realised that aerodynamics is a very complicated subject. The complexity of aerodynamics is related to the fact that every aerodynamic process is described by means of the so-called Navier Stokes equations. For practical aerodynamic problems (including wind energy problems) these Navier Stokes equations cannot be solved, nor analytically nor numerically. The extreme difficulty of modelling aerodynamic problems is illustrated by the fact that solving the Navier Stokes equation (as a matter of fact 'only' proving that a smooth solution exists) is one of the seven Millenium Prize Problems see http://www.claymath.org/millennium/

- The complexities inherent to aerodynamics make that fundamental physical phenomena crucial to wind turbine operation are still concealed. It also implies that an aerodynamic problem cannot be solved in an exact way but only in an approximate way by applying many simplifications. These simplification inevitably lead to an uncertainty band in design calculations. This uncertainty band is known to be very large for wind turbine aerodynamic models, see e.g. [1] and [2].

- The large uncertainties in wind turbine models make it very difficult to design cost-effective turbines since an optimisation tool may not produce the 'real' optimum design in terms of energy production and/or loads. If loads are higher than expected this should be covered with (costly) safety factors. Alternatively the loads may be lower than expected which implies an over dimensioned (and costly) design.

  The uncertainty in aerodynamic modelling might also lead to unwanted responses, e.g. power overshoots or instabilities which could cause failure or downtime with consequent high Operation and Maintenance (O&M) costs.

Within the present project aerodynamic phenomena have been isolated and characterised which eventually lead to model improvement (i.e. models with a small uncertainty band). The higher accuracy of the models reduces the cost/kWh due to higher energy production, a more cost effective design and lower O&M costs, where at the same time investment risks are reduced due to the prevention of design errors. These reduced investments risks and the prevention of design errors are extremely important from a business point of view. Thereto it should be realised that some prototypes are known which were less successful due to non-understood aerodynamic problems by which the time to market was delayed with several years. Even more extreme is an example of a wind energy company which went bankrupt. This bankruptcy was at least partly a result of design errors from non-understood aerodynamics.

Equally important are the following considerations:

- Currently there is a trend towards upscaling. However, upscaling is hampered by the so-called 'square cube law' which states that the weight of wind turbines increases more rapidly with the diameter than the power. The Upwind project, see [7] showed that the square cube law can be overcome by means of load control. Load control is generally

based on the use of smart aerodynamic devices. The successful applications of these devices however requires a thorough knowledge of the wind turbine aerodynamics.

- Noise is still one of the major obstacles for the application of wind energy. Numerous examples are known of wind energy projects that were prevented by public concern on noise or by the fact that noise regulations could not be met. In other cases wind turbines have to operate below optimum conditions in order to fulfil the noise regulations. Aerodynamic noise is found to be dominant see [8] and this noise source can only be reduced if the aerodynamics is understood very thoroughly.
- Nowadays wind turbines are placed in clusters where they are subject to power losses and increased loads resulting from exposure to the wakes emanating from one or more upstream turbines. The power losses and load increase are partly determined by the aerodynamics of the rotor and the near wake behind it. Hence a better understanding of the aerodynamics enables a more accurate optimisation (e.g. through farm control) with a higher energy production of a farm and lower loads in a farm.

Quantitative numbers for the benefits of aerodynamic research in terms of costs/kWh are not always easy to give. Thereto it should be realised that not all of the above considerations can be quantified in an economic sense: For example: The impact of noise lies on social acceptance and less on cost reduction. Also the fact that aerodynamics should be understood in order to make upscaling reality cannot be quantified economically.

It can anyhow be stated that the more accurate power production calculation in combination with reduced safety factors will straightforwardly reduce the cost of energy. The possible reduction in costs/kWh from these aspects is estimated to be in the order of 5%.

Also the better wind farm optimisations from more accurate aerodynamic modelling will straightforwardly reduce the cost of energy. This reduction is expected to be in the order of 5% where the following considerations play a role:

- The overall wind farm wake losses are generally in the order of 15% where a better wind farm wake optimisation will at least decrease the wake losses to say 14%.
- A more accurate optimisation yields lower mechanical loads on turbines in the farm. This then leads to less down time and lower O&M costs. Since O&M costs contribute to 30% of the total cost of energy for large off-shore wind farms a 4% reduction in costs of energy from reduced O&M is considered to be a fair number.

Finally it should be emphasized that a wind turbine is an integrated system, for which other disciplines (e.g. structural dynamics, electricity, controls) are also very important.

4 Mexico: Description of experimental set-up

The measurements which are analysed in Mexnext were carried out in the European Union project 'Mexico' (Model Rotor Experiments In Controlled Conditions, see [6]. In that project 10 institutes from 6 countries cooperated in doing experiments on an instrumented, 3 bladed wind turbine of 4.5 m diameter placed in the $9.5 \times 9.5\text{m}^2$ open section of the Large Low-speed Facility (LLF) of DNW in the Netherlands. The measurements were performed in December 2006 and resulted in a database of combined blade pressure distributions, loads and flow field measurements. Although the Mexico project can to some extend be seen as the successor of the NREL Phase VI (NASA-Ames) experiment from [4] it was designed to be complimentary. An obvious difference between the two experiments lies in the larger size of the NASA-Ames experiment but on the other hand the NASA-Ames experiment only contained rotor measurements where the Mexico experiment also included extensive flow field measurements using the stereo PIV technique. Furthermore the Mexico model is three bladed, whereas the NREL model was two bladed. Finally, the majority of the NREL measurements concern stalled flow, while the entire operational envelope is covered in the Mexico measurements.

The LLF facility of DNW is shown in figure 4.1 where the setup of the Mexico experiment is given in figure 4.2. The turbine is placed in an $9.5 \times 9.5\text{m}^2$ open jet configuration with a measurement section of 20 meter length. The rotor plane of the turbine is located 7 meter downstream of the nozzle and 13 meter upstream of the collector.

Figure 4.1 *LLF (Large Scale Low Speed Facility) of DNW (German Dutch Wind Tunnels) (Picture from http://www.twanetwerk.nl)*

Figure 4.2 *Setup of model turbine in the Measurement Section of the DNW LLF*

The external six component balance is the blue structure beneath the model in figure 4.2. This balance recorded the total rotor loads statically. The (twisted, tapered) rotor blades were numerically milled from aluminum, to ensure (within strict tolerances) identical shapes.

Pressure distributions on the blades were obtained from 148 Kulite pressure sensors, distributed over 5 sections at 25, 35, 60, 82 and 92% radial position respectively. It is noted that opposite to the instrumentation of the IEA Task 14/18 facilities and NREL's Phase VI (NASA-Ames) experiment the pressure transducers in the Mexico experiment measured absolute instead of relative pressures. This eliminates the uncertainty from the unknown reference pressure as found at other rotor aerodynamic measurements, see [3]. Furthermore blade loads were monitored at each blade root. Pressures and blade loads were sampled at 5.5 kHz. The measurement period of a datapoint was 5 seconds (i.e. 35 revolutions for a rotor speed of 7 Hz).

Three different aerodynamic profiles (DU91-W2-250, RISØ-A1-21 and NACA 64-418) were used in the blade design. The DU91-W2-250 airfoil was applied from 20 to 45.6% span, the RISØ-A1-21 airfoil from 54.4% to 65.6% span and the NACA 64-418 airfoil outboard of 74.4% span. Hence a constant airfoil is applied over a considerable radial extension around the instrumented sections in order to assure known conditions at each of these sections, where the remaining length is used for the transition from 1 airfoil to another.

The rotational speed at the pressure and load measurements was either 424.5 rpm or 324.5 rpm.

At 424.5 rpm a chord based Reynolds number of approximately 0.8 M was reached without entering into noticeable compressible conditions; the blades were tripped to avoid possible laminar separation phenomena. Pressure and load measurements were done at different tunnel speeds ranging from 10 m/s to 30 m/s, yielding tip speed ratios between 3.3 and 10. Note that the design tip speed ratio is 6.67, which corresponds to V_{tun} = 15 m/s at 424.5 rpm. Different yaw angles and pitch angles were covered, including the design pitch angle of -2.3 degrees.

Extensive flow field mapping of the three velocity components has been done by DNW with stereo PIV measurements. The flow field measurements were combined with measurements of the pressures and the blade root moments. The PIV measurements were performed in the following way:

- Two cameras mounted on a traversing tower focus on a PIV sheet with a size of 337*394 mm^2. The PIV sheet is located horizontally in the symmetry plane of the rotor at the 270 degrees azimuth, i.e. the '9 o' clock' position, see figure 4.3. The PIV tower is moveable in the horizontal streamwise (x) and radial (y) direction;
- The flow field is 'seeded' with small bubbles which are brought into the settling chamber, upstream of the rotor;
- The seeded PIV sheet is illuminated with a laser flash, and two digital photographs are taken with a short delay ($\approx$ 100 microseconds);
- Then the actual seeding of the second photo is compared with the expected seeding for different velocity vector fields using the seeding of the first photo as a basis. The actual velocity vector field is the one resulting in maximum cross correlation between the expected and the real seeding field. Thereto the PIV sheets are subdivided into small interrogation windows (with a size of 4.3x4.3 mm^2).

The PIV samples were taken rotor-phase locked with a frequency of 2.4 Hz. Each PIV data point consists of 30-100 samples. Although all individual samples are stored, it is mainly averaged results which are investigated within Mexnext.

The PIV flow field measurements are done at both non-yawed and yawed flow at different tunnel speeds. The rotational speed at the PIV measurements was always 424.5 rpm. Basically three types of PIV measurements were carried out:

- Radial traverses from 52 to 122% span with PIV sheets just upstream and just downstream of the rotor plane (and a small overlap in the rotor plane), see figure 4.4. The radial traverses were done at 6 positions of blade 1 (denoted with Φ_r or χ) using a 20 degrees interval, see figure 4.5. In this way the non-uniformity of the flow field is measured.
- Axial traverses from x = -4.5 m to x = 5.9 m (i.e. from 1.D upstream of the rotor to 1.31 D downstream of the rotor), see figure 4.6. The azimuthal position of blade 1 was 0 degrees;
- Tip vortex tracking experiments in which the position of the tip vortex is searched by 'trial and error'. The position of blade 3 was 270 degrees.

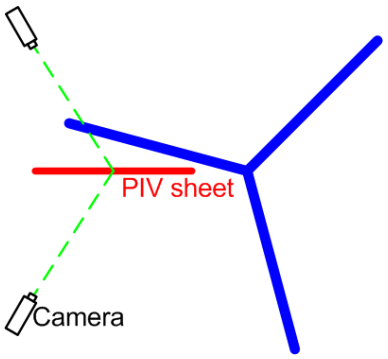

Figure 4.3 *PIV sheet with cameras*

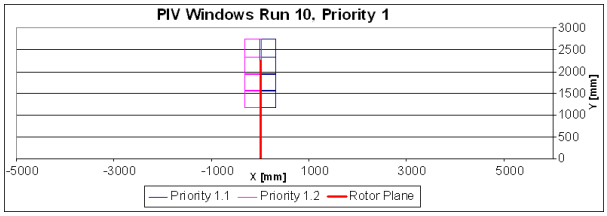

Figure 4.4 *PIV measurement sheets at radial traverses as seen from above*

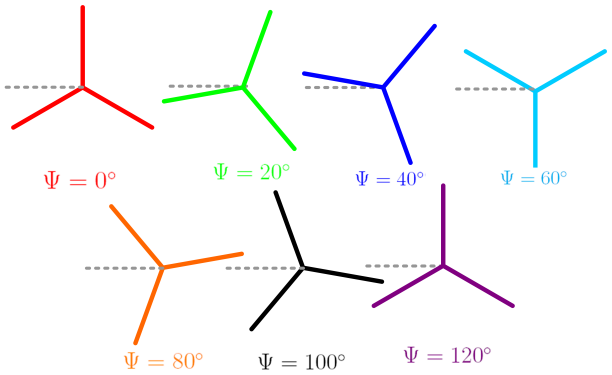

Figure 4.5 *Position of blade 1 at 0, 20, 40, 60, 80, 100, 120 deg*

More detailed information on the measurement procedure can be found in [6]. More information on the setup including test matrix and apparatus can be found in [9] and [10] and [11].

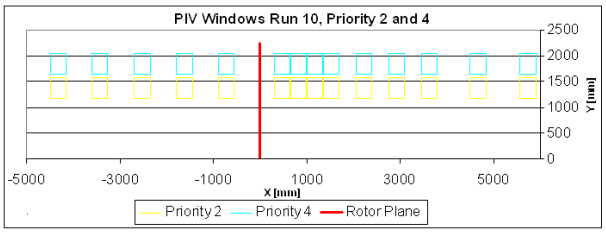

Figure 4.6 *PIV measurement sheets at radial traverses as seen from above*

5 Workplan

The workplan is divided in 5 work packages (WP's):

- WP1: Processing/presentation of data, uncertainties.
  In this Work Package the data are processed, documented and provided to the participants. This Work Package also includes an assessment of the measurement quality.

- WP2: Analysis of tunnel effects.
  As mentioned in section 4 a 4.5 m diameter wind turbine model was placed in the open jet section of the LLF facility with a size of 9.5 x 9.5 m^2. This ratio of turbine diameter over tunnel size may make the wind tunnel situation not fully representative to the free stream situation. Within the Mexico project, tunnel effects were studied with Computational Fluid Dynamics (CFD) and simple engineering models. The complexity of the configuration (open tunnel, slits at the collector) made it necessary to perform more detailed studies within Mexnext.

- WP3: Comparison of calculated results from different types of codes with Mexico measurement data.
  In this WP, the calculated results from several codes were compared to the data from the Mexico experiment. It was meant to be a thorough validation of different codes and it provided insights into the phenomena which need further investigation (see WP4). Most interesting in this comparison is the fact that the comparison is not only made with load measurements but also with the underlying flow field measurements which drive these loads. A comparison between Mexico flow field data and CFD data could be made straightforwardly but this is less true for the comparison with results from the Blade Element Momentum (BEM) theory since the flow model in the momentum theory is of a very simplified nature: BEM only considers the induced velocities in the rotor plane and far downstream where the rotor is represented by a hypothetical actuator disc. Hence the induced velocity in the actuator disc plane is not a real physical quantity which can be compared directly with the measured quantity since it does not include the upwash from the blade and the flow non-uniformity due to the finite number of blades.
  The Work Package has been divided in several tasks:

  - Task 3.1: Preparation:
    In this task an inventory was made of the codes in the Task. Furthermore a selection was made of the measurement campaigns to be simulated. Both yawed and non-yawed cases were simulated. The input and the calculation program has been defined using results from task 3.2 (2D airfoil data), where the blade geometry was provided as IGS files to the CFD participants. Finally the comparison procedure has been defined.

  - Task 3.2: Airfoil data
    In this task the 2D airfoil data were analysed. Three different airfoils were used in the design of the Mexico rotor (The DU91-W2-250, RISOE-A1-21 and NACA 64-418 airfoils). Within the Mexico project, the 2D pressure distributions of the DU91-W2-250 and NACA-64-418 airfoil have been measured at the appropriate Reynolds number and tripped conditions. The measurements have been compared with results from airfoil and CFD codes. The aerodynamic characteristics of the RISOE-A1-21 airfoil were not measured at the appropriate conditions. The analysis resulted in a 'best set' of data which was used in the calculations.

  - Task 3.3: Calculations.

  - Task 3.4: Comparison between calculations and measurements
    The calculational results were supplied to ECN which compared them with the measured results. Thereto a large number of graphs have been generated. These graphs are included in the present report. They are also available in high resolution on the Mexnext intranet site.

  - Task 3.5: Evaluation:
    In this task the comparison between calculations and measurements was evaluated. This included an attempt to explain the differences between calculations and measurements.

- WP4: Deeper investigation into phenomena.
  In this WP a deeper investigation of different phenomena took place. The phenomena were investigated with isolated submodels, simple analytical tools or by physical rules. The work package was subdivided in several tasks:

  - Task 4.1 Parked conditions
  - Task 4.2 Sensitivity of results and rotational speed
  - Task 4.3 Angle of attack
  - Task 4.4 Near wake aerodynamics
  - Task 4.5 Non-uniformity of flow in the rotor plane (i.e. tip corrections)
  - Task 4.6 3D effects
  - Task 4.7 Unsteady effects
  - Task 4.8 Yawed flow
  - Task 4.9 Dynamic Inflow

- WP5: Comparison with results from other (mainly NASA-Ames) measurements.
  Within this Work Package it was investigated whether the findings are consistent with results from other aerodynamic experiments. In particular, a comparison has been made with measurements from IEA Wind Task 20 by NREL (i.e. the NASA-Ames experiment).

6 Task 1: Processing/presentation of data, uncertainties

The Mexico experiment produced 100 Gbyte of data. After the Mexico project ended the data were stored on external hard discs and distributed between the Mexico participants. On the disc, the time series (of pressures and strain gauges) are given in raw form. Furthermore some processed data are stored in ASCII format. The disc also contains a data point overview and the basic software with which the raw time series could be processed. The PIV data were given in processed form (i.e. ASCII data of the velocity vectors at different x-y-z positions). Within this WP the data were made available to all Task participants, including those which were not involved in the Mexico project. Thereto the content of the external hard disc have been stored on a password protected Internet site. In principle the data were organised in a self explanatory way but some further processing, explanations, corrections and descriptions were needed. Thereto the pressure and load data have been reprocessed, taking into account the drift between the zero-calibrations just before and after a run. The reprocessed data were also stored on the Internet site.

Explanatory information to the datafiles were added to [9]. This includes explanatory remarks to the processing software.

Furthermore an uncertainty analysis has been performed in the form of consistency checks and an investigation of the reproducibility of data.

- The repeatability of many data points (for both pressure and balance measurements) has been checked. Generally speaking the reproducibility was found to be very good. An example is shown in figure 6.1.

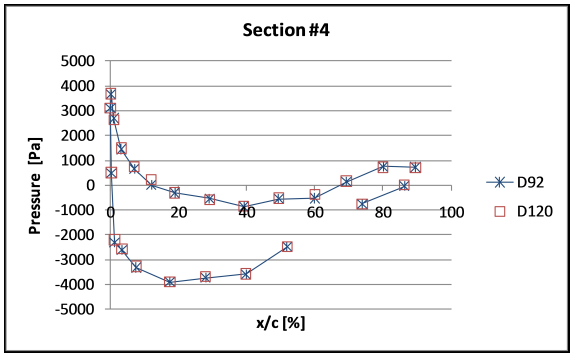

Figure 6.1 *Repeatbility of pressure distribution at 82% span for two different datapoints*

- The inflow conditions are reported in [9]. DNW has released the static and dynamic pressures measured in the nozzle that were used to determine the freestream tunnel velocity. These measures can be used to double check the quoted accuracy of the tunnel speed. A note on the turbulence intensity is made in this document as well. Based on the Kulite measurements at standstill, the turbulence intensity has recently been estimated below 0.4%.

- Something has gone wrong with the calibration of the strain gauges as reported in [9]. Especially the blade 2 strain gauges measurements appear unusable. In addition to that, the drift of the strain gauge signals makes it difficult to obtain accurate absolute values. This restricts the applicability of these measurements to extracting quantitative trends for the blade 1 and 3 signals.

- Observations on and uncertainties of the Kulite pressure sensor measurements is discussed in section 6.1.

- Observations on and uncertainties of the PIV measurements is discussed in section 6.2.

- Observations on and uncertainties of the balance data is discussed in section 6.3. The consistency between pressure and balance data is also subject of investigation in this section.
- A comparison has been made between the manufactured and designed blade contour shape, see also section 6.4.

6.1 Kulites

For the detailed specification of the absolute pressure sensors used in the blades, the reader is referred to [9]. It must be noted that all Kulite pressure sensors were calibrated by NTUA before the Mexico experiment. Special attention was paid to the gain which generally compared well with the gain specified by the manufacturer. However an in-situ calibration (hence using the data acquisition chain that was used during the experiments) has not been performed. Each measurement polar was preceded and followed by a zero measurement (without wind) to exclude the drift from the measurements. These measurements allowed for a comparison between the Kulite sensors and the atmospheric tunnel pressure as measured by the DNW tunnel reference system. It appears that, apart from several outliers, the Kulites measure 2000 to 4000 Pa lower pressure, approximately constant for each sensor over the numerous taken polars. Whether this is due to a zero-offset or a different sensitivity of the sensors is still an open question. Nevertheless the good agreement in pressure readings at different rotational speeds (but equal tip speed ratios, see section 10.2) does not point in this direction.

In the first case, the pre-calibration as described in [9] corrects for this discrepancy. In the case of a different sensitivity of the sensors, the resulting difference in the sectional normal forces could amount to a 4% increase.

The influence of rotation on the sensor readings is considered to be negligible, since the centrifugal force works parallel to the pressure diaphragm of the sensors. It would be worthwhile to verify this assumption, although the good agreement of the pressure measurements for the different rotational speeds does not point in this direction.

Ricardo Pereira [12] and Lucas Pascal [13] have performed consistency checks on the Kulite sensors. Their conclusions are briefly summarized below.

- For the 25% spanwise station, the data often yields an unusual Cp distribution over the upper surface of the airfoil section. As for the pressure distribution obtained in the lower surface of the airfoil, one can see there is a pressure sensor yielding a 'kink' in all considered trials, located approximately at the 35% chord position.
- For the 35% spanwise station the lower surface pressure distribution seems to be according to what was expected. However, at the upper surface, near the trailing edge and for the high rotational speed cases there are very atypical peaks in the Cp distribution. These irregularities seem to indicate there was some sensor malfunctioning at this region of the airfoil. Having this in mind, and since at this radial stations the Cp distributions are often very odd, but not in every trial, it is recommended to check the distribution for any given trial. Only if smooth, 'regular' curves are obtained one should compute the aerodynamic forces.
- For the 60%, 82% and 92% spanwise stations the distributions of the pressure coefficient are coherent and yield smooth curves, and thus, in principle, should be reliable to compute aerodynamic forces from.
- In some trials and for some spanwise sections, in the upper surface, it appears that the transition device may be causing a localized drop in suction.

- Occasionally 'wiggles' in the azimuthal direction were observed when the airfoil is stalled, with decreasing amplitude toward the outboard stations.

Daniel Micallef [14] has compared the cross checking of sensors which were placed at identical radial, chordwise and flapwise location but at different blades. The same was done by ECN, see figure 6.2. The level of disagreement between results of the different blades turns out to be small.

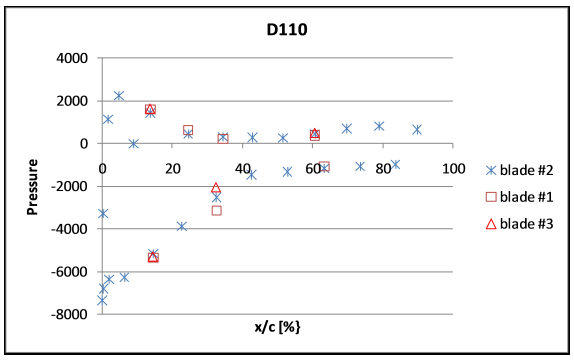

Figure 6.2 *Pressure distribution at 60% span measured on blade 2 and compared with a few pressure measurements taken on blades 1 and 3*

The slight differences could be caused by either a geometrical offset (slightly different position of the sensor) or a signal offset from the sensors. The largest errors occur on the 60% span position (as shown in figure 6.2 at low tip speed ratio cases.

6.2 PIV measurements

The accuracy of the instantaneous velocity fields has been supplied by DNW and depends on the time Δt between frames and the spatial resolution of the camera. The result varies from 0.47 m/s at $U_\infty = 15$ m/s ($\Delta t = 100\mu s$) to 0.75 m/s at $U_\infty = 24$ m/s ($\Delta t = 60\mu s$). Using error analysis for multi-sample experiments as described by [15], the uncertainty in a time-averaged vector is 0.11 m/s at $U_\infty = 24$ m/s. For relatively low velocity variations, the trend within a PIV-sheet does not always correspond with the trend between sheets (e.g. Figure 8.13). This can be due to the fact that the observed variations are within the accuracy range of the measurements.

The upstream edge of the time averaged PIV sheets often displays a distinct velocity discontinuity from the rest of the sheet, as illustrated in Figure 6.3. There is no physical explanation for this effect being a real flow feature. It is expected that the cross correlation procedure for the sheet edges is less accurate. Therefore the edges have been discarded from the comparison in section 8.

The consistency between pressure and PIV measurements has been checked by correlating the strength of the wake vortices as measured with the PIV technique to the bound vortex distribution along the blade as determined from the pressure distributions [16]. Generally speaking a good agreement was found at design conditions.

A good indication for the accuracy of the PIV measurements can be found from the radial traverses. As explained in section 4 these have been done for 7 azimuth positions: viz. 0, 20, 40, 60, 80, 100 and 120 degrees. For the three bladed rotor, the 0 and 120 degree results should be identical. This fact yields a good check on the accuracy of the measurements. Figure 6.4 shows the measured axial velocity at 0.3 m downwind of the rotor, as a function of radial position, comparing the 0 and 120 degree azimuth cases, for the design condition, i.e. at a tunnel speed of 15 m/s. It is clear that the comparison is indeed very good which confirms good acccuracy of the PIV measurements (and also indicating the blades to be similar). The radial extension of the PIV

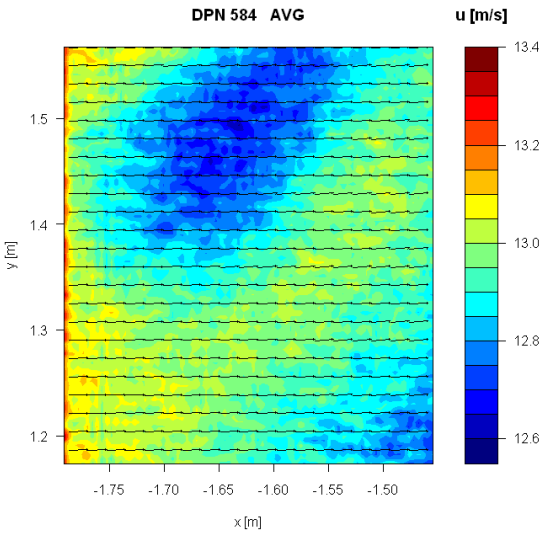

Figure 6.3 *Time averaged contours of axial velocity for datapoint 584.*

sheets is also given in the figure, showing excellent compatibility going from one sheet into the next which again confirms good quality of the PIV measurements.

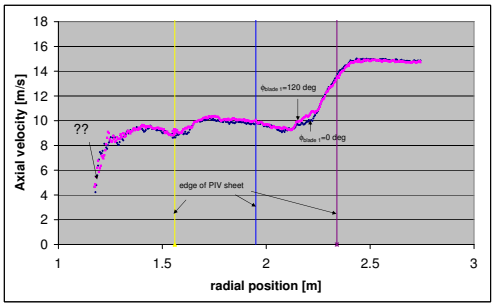

Figure 6.4 *Radial PIV traverse, 0.3 m downstream of the wake at 0 and 120 degrees blade position*

6.3 Balance measurements

The balance measurements show some puzzling results. From the specified ranges in [9] it becomes clear that for most components, only about 10% of the working range is used. However if the accuracy stated by DNW is correct, the results are very usable.

To understand the remainder of this section it must be known that the balance is located at the tower base but the forces and moments have been translated to originate in the rotor center, working in the model coordinate system. Prior to the tunnel test, zero measurements have been performed to correct the balance data for the weight of the model, i.e. only aerodynamic forces and moments are presented. The values are time averaged over a data point hence averaged over approximately 35 revolutions for 424 rpm.

6.3.1 Lateral force and torque

For axial flow conditions it appears that an unexpected significant lateral force (sideways or y-direction) is present in the measurements. The lateral force scales with wind velocity and also shows a trend with pitch angle, indicating this results from an aerodynamic force on the blades.

For parked conditions ($U_\infty = 30$ m/s) the value of the lateral force (around 200 N) is similar to rotating conditions (both 324 and 424 rpm) at this tunnel speed, indicating that the force scales with wind velocity rather than rotational speed. A clear variation of the lateral force with pitch angle is seen, with a maximum around 12 ° pitch and approaching 0 N for vane (pitch=90 °). Combining these two observations gives rise to the hypothesis that the lateral force is caused by the inboard part of the blades. The azimuth angle of the rotor for the parked conditions was 0 ° hence largely preventing interaction with the tower.

A few observations are made and possible explanations are given.

- Wind tunnel setup asymmetry
  The model, nozzle and collector have not been positioned in the middle of the test chamber. This results in asymmetry in the horizontal plane. From CFD analysis [17, 18] it appears that the recirculation zone of the jet impinging on the collector nose is different between both sides. It is possible that this disturbance has made its way upstream affecting the balance readings. However the observed trend with pitch angle for rotor standstill is not expected in this case.

- Wake rotation interaction with nacelle
  The rotor wake could have interacted with the relative large nacelle which extends around 3.3 m downstream from the rotorplane. However the lateral force for 324 and 424 rpm hardly differ and the standstill measurements also show a similar contribution to the lateral force.

- Turbine misalignment/placement
  In case of a turbine misalignment, a trend of the lateral force as a function of axial force is expected. However the axial force varies smoothly with freestream velocity whereas the lateral force shows discontinuities at low ($U_\infty \approx$15 m/s) and high velocities ($U_\infty \approx$24 m/s). For the yawed case however the absolute value of the lateral force differs significantly between +30 ° and -30 ° yaw.

  A placement of the turbine aside from the tunnel centerline can also result in a lateral force. However the resulting lateral force in case of a rotating turbine would greatly have to exceed the value for standstill, which is not the case.

- Pitch angle misalignment
  A pitch angle misalignment could have caused a lateral force. However in the case of the rotating turbine blades with a constant pitch angle deviation, this difference would have averaged out over the 35 rotor revolutions incorporated in the 424 rpm datapoints. Also the good agreement in PIV measurements at Φ_r = 0 degrees and Φ_r = 120 degrees from figure 6.4 makes such misalignment unlikely.

- Lateral contraction of strain gauge load cells
  The balance load cells can contract in lateral direction when a force in axial direction of the load cell is applied, resulting in measurement signal that is interpreted as a lateral force. As pointed out however for the turbine misalignment hypothesis, a clear trend between axial and lateral force is not present.

The collector pressure sensors provide an extra opportunity to check this phenomenon. The measured difference between starboard and port side sensors indicate that a real physical lateral force

is present, working in the same direction as measured by the balance. Although this difference is found to scale with tunnel velocity, it is not found to scale with lateral force in the case of a parked rotor (where the lateral force changes due to pitch angle variation for a constant tunnel speed). The same holds for the yawed rotor cases. The difference between floor and ceiling collector pressures is almost negligible. The collector pressure measurements are however in line with the CFD results [17, 18] that show a difference due to the wind tunnel setup asymmetry.

Since DNW translated the forces from tower foot to rotor center, the lateral force has a huge influence on the measured moment in x-direction or torque. Unfortunately the torque measurements from the balance were shown to be unreliable, see Schepers et al [19] by which a comparison between the pressure torque and the torque from the balance is not considered useful.

6.3.2 Axial force

The axial force obtained with the balance contains next to the contribution of the rotor also tower (and nacelle) drag. These contributions have to be subtracted to determine the axial force on the rotor. Two methods have been identified for this purpose.

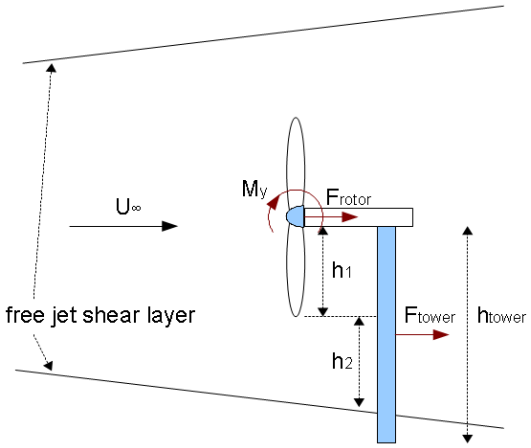

Figure 6.5 *Decomposition of total axial force.*

- First method
  The tower drag can be determined from the total axial force and fore-aft moment (M_y) by assuming a uniform tower drag. In reality however the tower drag is not uniform along the tower since the rotor induction causes the incident tower velocity to decrease on the upper part of the tower. See also Figure 6.5.

- Second method
  The tower drag can be determined from the parked rotor measurements (U_∞=30 m/s, $Re_D = 3.4 \times 10^5$), with the blades pitched into vane. The drag of the blades should be small in attached flow compared to the bluff body drag of the tower and nacelle. For determination of the tower drag in the rotating case, the tower incident velocity is then split into two regimes as illustrated in Figure 6.5 (h1 and h2).

Both methods yield a cross sectional drag coefficient for the tower, which had a spiral flange to provoke transition. It is well known from literature [20], that the cylinder drag coefficient decreases from 1.2 to 0.6 in supercritical conditions ($Re_D >\approx 3 \times 10^5$). The spiral flange

is expected to ensured super-critical flow but also to cause parasitical drag. The first method yields a Cd of approximately 2.0 which seems rather high. The second method yields a Cd of approximately 1.25 which is more in line with the expectations.

In figure 6.6 a comparison is made between 'pressure' and direct loads from the Mexico experiment. Thereto the axial force coefficient is presented as function of tip speed ratio. The results are given for two rotational speeds: 324 rpm and 424 rpm. The directly measured axial force is determined with the balance using the first method for deduction of the tower drag. The pressure value has been determined by integrating the pressure forces along the blade. A linear behaviour of the loads is assumed between the instrumented sections as well as a zero force at the root and tip.

It can be seen that the differences between the 'pressure' and 'balance' axial force are very small giving confidence in both the pressure and balance measurements. Furthermore it can be seen that the dependency of axial force coefficient on the rotational speed is limited. This will be discussed in more detail in section 10.2.

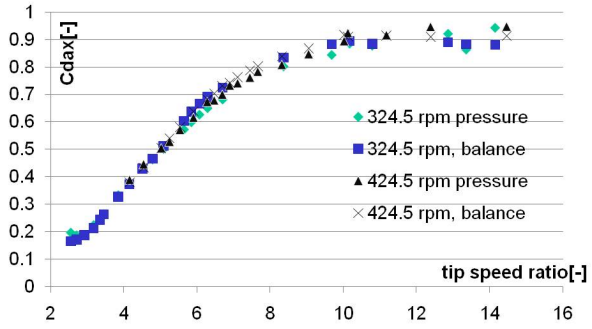

Figure 6.6 *Mexico experiment: Axial force coefficient from pressure distributions and balance (first method) as function of tip speed ratio for two rotational speeds: 324.5 and 424.5 rpm.*

In summary, the generally good agreement between 'direct' and 'pressure' rotor loads gives confidence in the quality of the measurements considered. It also shows that these loads can be predicted accurately (on a time averaged basis) by integrating the correct sectional aerodynamic loads along the blade. Since blade-element momentum methods apply a similar integration procedure, this confirms the necessity of the accurate prediction of the sectional forces. This implies the accurate prediction of induction and resulting angle of attack in combination with accurate airfoil characteristics.

However, a couple of remarks need to be made.

- The axial force coefficient for design conditions ($\lambda = 6.7$, pitch=-2.3 °) only reaches 0.69, whereas momentum theory predicts 0.89 for an axial induction of 1/3. The PIV measurements show a velocity decay in line with the theoretical axial force coefficient.
- As mentioned above, a Cd of around 2.0 for the tower seems rather high. Using the drag coefficient obtained from the parked rotor measurements yields an axial force coefficient around 0.81 for design conditions, which is obviously still much lower than the expected value of 0.89
- The reliability of the kulites has been discussed in (section 6.1). Generally speaking these results are expected to be reliable.
- It is acknowledged that assuming a different spanwise load distribution between the instrumented sections (especially near the tip region) can yield up to 15% difference (increase) in axial force. Nevertheless the assumed linear load distribution seems to agree reasonably

Table 6.1 *Summary of comparison between design and measured blade shape after experiment/instrumentation.*

	Blade 1	Blade 2	Blade 3
Flapwise deviation [mm]	<3.4	<0.3	<2.6
Chordwise deviation [mm]	<0.3	<0.3	<1.7
Twist angle deviation† [°]	less than 0.1		
Airfoil shape deviation	good	bad at LE	worst
Trailing edge point deviation	shorter than design geometry (less than 0.7 mm)		

† Twist angle deviation is determined by visually matching of sectional profiles.

well with the calculated load distributions from section 8.2.2. Also [21] shows an extremely good agreement between the overall axial force and the axial force obtained from (even less) pressure distributions measured in a field experiment. The same was found in [4] on basis of the NASA-Ames torque measurements.

In this respect it is also interesting to note that the computations from section 8 overpredict the forces (on global and sectional level) but also overpredict the velocities, in contradiction with axial momentum theory. However, from section 8.2.2 it appears that the load overprediction not only appears in the global loads but also on a sectional level.

6.4 Blade contour measurements

The WP also included an assessment of the blade manufacturing. Thereto the quality of the airfoil and the blade has been checked by comparing the blade contour measurements of the blade shape with the design specifications. Thereto it mush be known that the actual blade shape was measured by Technion. Generally speaking the agreement turned out to be good, see [9]. It was realised however that the blade shape was measured before the instrumentation. Possible deviations caused by the instrumentation were established within Mexnext. Thereto the shape of the instrumented blades (which were still available) were measured.

In a first step the blade scan results are supplied as 'point files' from which IGS surface files were derived. The quality of the IGS surface files was checked by comparing it with the results from the point files where furthermore a comparison was made between the surface files and the intended design. Generally speaking, after some coordinate transformations, the differences were found to be limited where the largest differences were found for blade 3. The findings are summarised in Table 6.1. The aerodynamic impact of these differences has been assessed. At some locations it was found that the L/D from the actual blade geometry was 15% lower than the L/D of the design geometry.

7 Task 2: Tunnel effects in the Mexico experiment

The Mexico model is placed in the open test section of DNW-LLF with a nozzle and collector where the collector is closed with the nozzle. It is well known that tunnel effects in such open configuration will be less severe than those in a closed tunnel section [22]. As a consequence, the solid blockage by the model can be estimated to be less than a percent [23]. The axial distance between model location and the nozzle amounts to 7 m which is regarded as a safe margin to prevent nozzle blockage (model interference with the static and dynamic pressure sensors located in the nozzle to determine freestream tunnel velocity).

The exact tunnel effects are difficult to quantify due to the free shear layer between the tunnel flow and the outer flow. The presence of the collector which captures the wind turbine wake flow and which is closed with the nozzle adds to the complexity. As such standard tunnel correction methods cannot be applied. It must be noted that the DNW-LLF rarely employs the 9.5×9.5 m^2 nozzle. The collector size approximately has the same cross-sectional area, which does not allow for much expansion of the free jet emerging from the nozzle.

Within the Mexico project the wind tunnel effects were first studied with a qualitative flow model, based on 1D axial momentum theory, see [24]. The model is largely similar to the classical axial momentum theory but in the present situation the flow from the nozzle to the collector has been divided into two stream tubes: An inner stream tube containing the flow passing through the rotor and an outer stream tube which contains the remaining flow, see also figure 7.1.

In a closed system between collector and nozzle, mass is conserved meaning that the lower velocity in the wake should be compensated with a higher velocity in the flow outside the wake. This also accelerates the wake flow. As a result of these phenomena, the collector inlet pressure is smaller than the nozzle outlet pressure. The simple model showed that, compared to the unbounded situation, the wind tunnel situation yields a higher axial force on the turbine at the same velocities in the rotor plane (i.e. at the same axial induced velocity). Vice versa, a similar axial force coefficient gives a higher rotor velocity (i.e. a lower axial induced velocity) in a wind tunnel situation. The severeness of the tunnel effects obviously increases with axial force coefficient.

In a later stage detailed CFD analyses were carried out within the Mexico project, see [25]. They confirmed the results from this simple model, i.e. they showed tunnel effects in the form of a higher velocity in the rotor plane for the same axial force on the rotor (or alternatively: a higher axial force on the rotor at the same induction). Nevertheless in quantitative terms, the disturbance from the tunnel on the flow in the rotor plane was generally speaking limited. This is examplified in figure 7.2 from [26]. The figure shows the axial force coefficient with and without tunnel calculated by DTU-MEK. Maximum differences in axial force coefficient remain limited to approximately 5%. However some tunnel effects appear far downstream in the wake in the form of a flow acceleration.

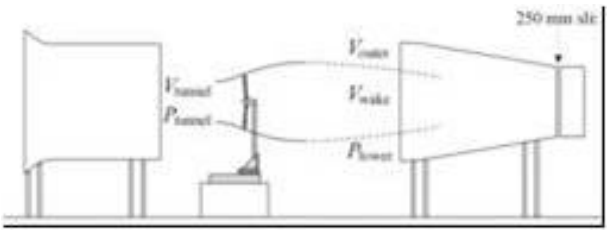

Figure 7.1 *Mexico: Tunnel configuration*

All of these investigations assumed a fully closed system between collector and nozzle. The real wind tunnel has slits with a width of 250 mm at the end of the collector. These slits reduce the tunnel effects since the suction in the collector generates a mass flow from the outer flow field through this opening into the collector. This mass flow was found to be significant in measure-

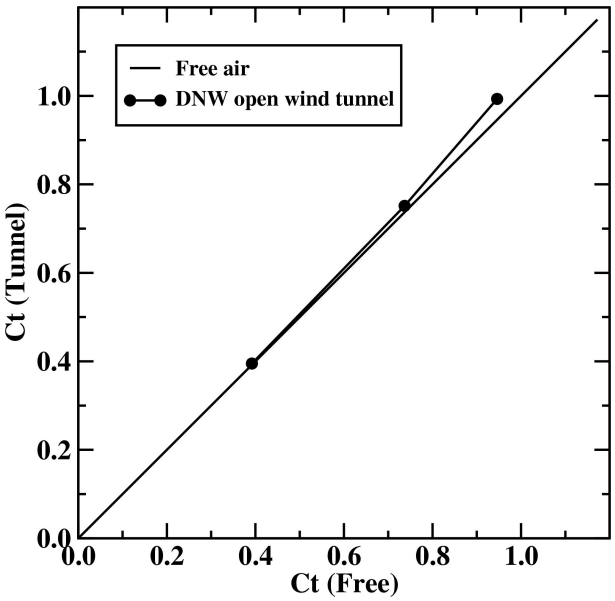

Figure 7.2 *Axial force coefficient calculated by Wen Zhong Shen (DTU-MEK) with and without tunnel*

ments which were carried out in a scaled down version of the LLF tunnel, see [27].

Within the Mexnext project CFD calculations were performed using a tunnel geometry including slits, see [17] and [18]. The investigation showed that the slits lead to further reduction of tunnel effects indeed. Since the tunnel effects without slits were already found to be limited the reduction of tunnel effects from the slits had little practical relevance. Simulations with a DES approach however showed that there could be an oscillation of the wind tunnel jet interface that could potentially create a significant oscillation of the wake. It is unclear if this effect can be observed in the MEXICO measurements and if they had an impact on the quality of the experiment.

It is noted that these studies are still based on an estimate of the tunnel geometry since the exact geometry was supplied at the end of the Mexnext project only.

In summary it can be stated that all studies on tunnel effects which have been performed until now, indicate little disturbance but further CFD calculations are still to be performed. These need to consider more conditions and they need to be based on the exact tunnel geometry.

8 Task 3: Comparison between calculations and measurements

8.1 Introduction

The participants of Mexnext simulated the MEXICO turbine with a variety of aerodynamic codes (both CFD and lifting line codes). The results from these calculations were compared mutually and with the experiment. The comparison has been performed for three axial (section 8.2) and two yawed flow conditions (section 8.3). Except for one yawed flow condition, experimental results are available for both loads (pressures) as well as velocity traverses. The appendices give more detailed information on the compared variables (section A), the experimental data reduction (section B) and the model descriptions corresponding to the displayed calculations (section C).

Figure 8.1 *The MEXICO experiment*

8.2 First round: Axial flow

Three cases are selected which represent design conditions, turbulent wake state and separated flow conditions. A more detailed description of the conditions and the data format can be found in section A.1. The legend of each graph refers to the parties that have performed the calculations. The model description corresponding to the legends can be found in section C.

8.2.1 Pressure distributions

The grey band indicates the band of standard deviation between the processed measured data points for the sensors as explained in section B. The more outboard positions show a smaller band mainly due to the fact that the dynamic pressure is higher and hence the relative accuracy of the pressure sensors increases.

Figure 8.2 and 8.3 show most of the codes to overpredict the suction side pressure level for attached flow conditions. This is mostly pronounced in the front part of the airfoils up to mid chord. The experimental suction side pressures close to the trailing edge at the 25% span station show in both Figure 8.2 and 8.3 an unexplained increase in suction, which is not reproduced by the calculations. The temporal variation of the pressure distributions do not show major unsteadiness accompanied with this phenomenon. It can be questioned whether this is a physical flow feature or a measurement/calibration error.

The separation point location for U_∞=24 m/s (Figure 8.4) is generally predicted closer to the trailing edge than the experimental value. The predicted level of the suction peak in deep stall generally is in good agreement with the experiments. The value of the base pressure (aft of the separation point) is predicted well by most of the codes at all five stations. Apart from some outliers, the flow physics of most computations represent the experiment quite well.

Generally speaking the suction side pressure is overpredicted by most of the codes. A number of hypotheses exist to explain this difference.

- Lower angle of attack as a consequence of differences in pitch and/or local twist. Angle of attack differences are best visible in the suction side of the pressure distribution. However the scanned blade geometry results do not give rise to twist distribution differences.
- The thickness of the tripping tape causes a thicker and hence more decambering boundary layer compared to solely making the boundary layer turbulent as was done in most computations.
- The sensitivity of the absolute pressure sensors was taken from the specifications. The actual sensitivity (including data acquisition chain) during the experiment could have been different. A comparison of the tunnel supplied absolute pressures to the blade sensor pressures during the zero measurements shows constant differences up to 4000 Pa. Supposing this is due to a different sensitivity would cause 3% to 4% higher pressure values. Nevertheless the good agreement in pressure readings at different rotational speeds (but equal tip speed ratios, see section 10.2) does not point in the direction of the gain being incorrect, see also section 6.1.

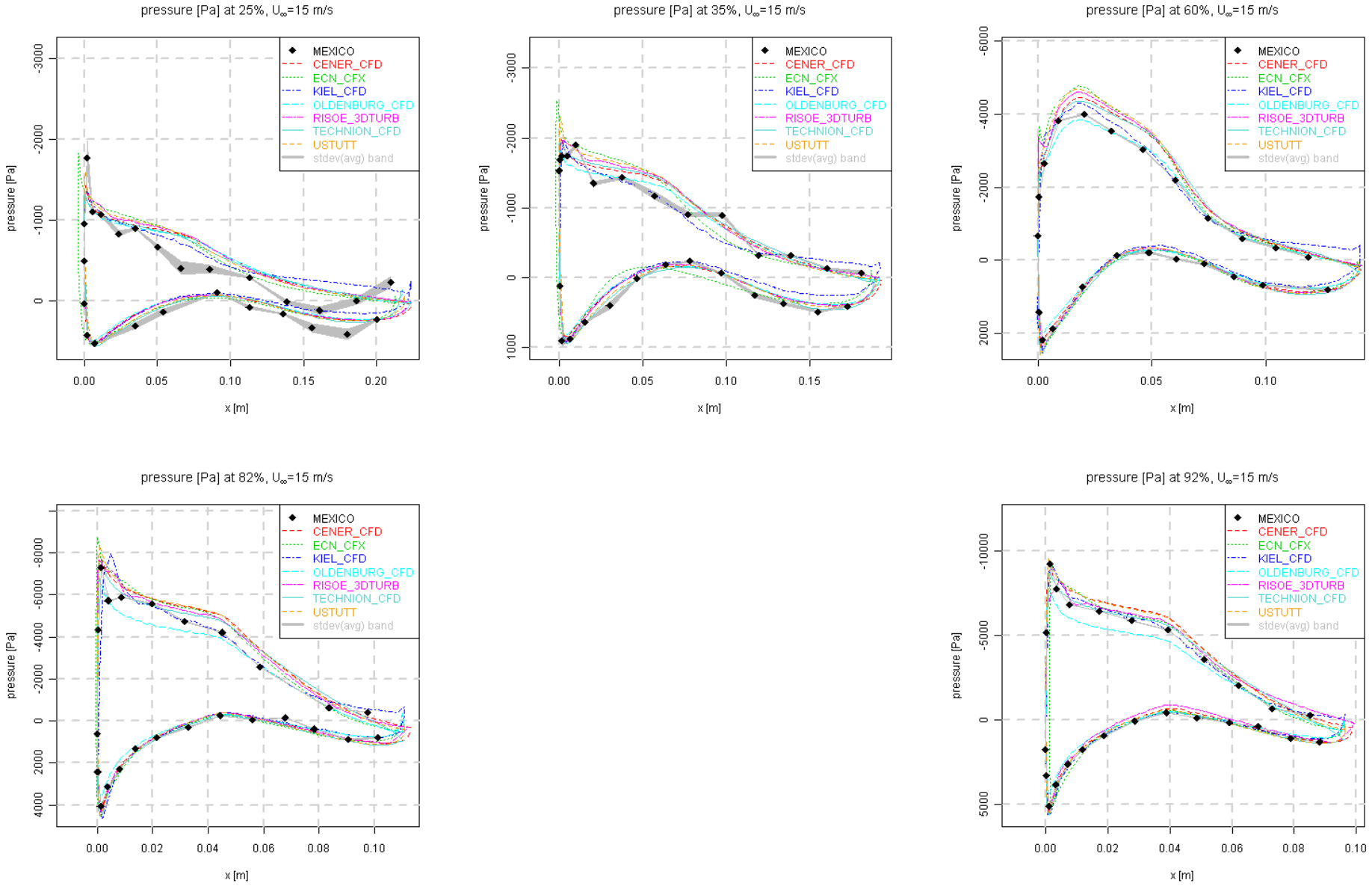

Figure 8.2 *Pressure distributions for $U_\infty = 15$ m/s*

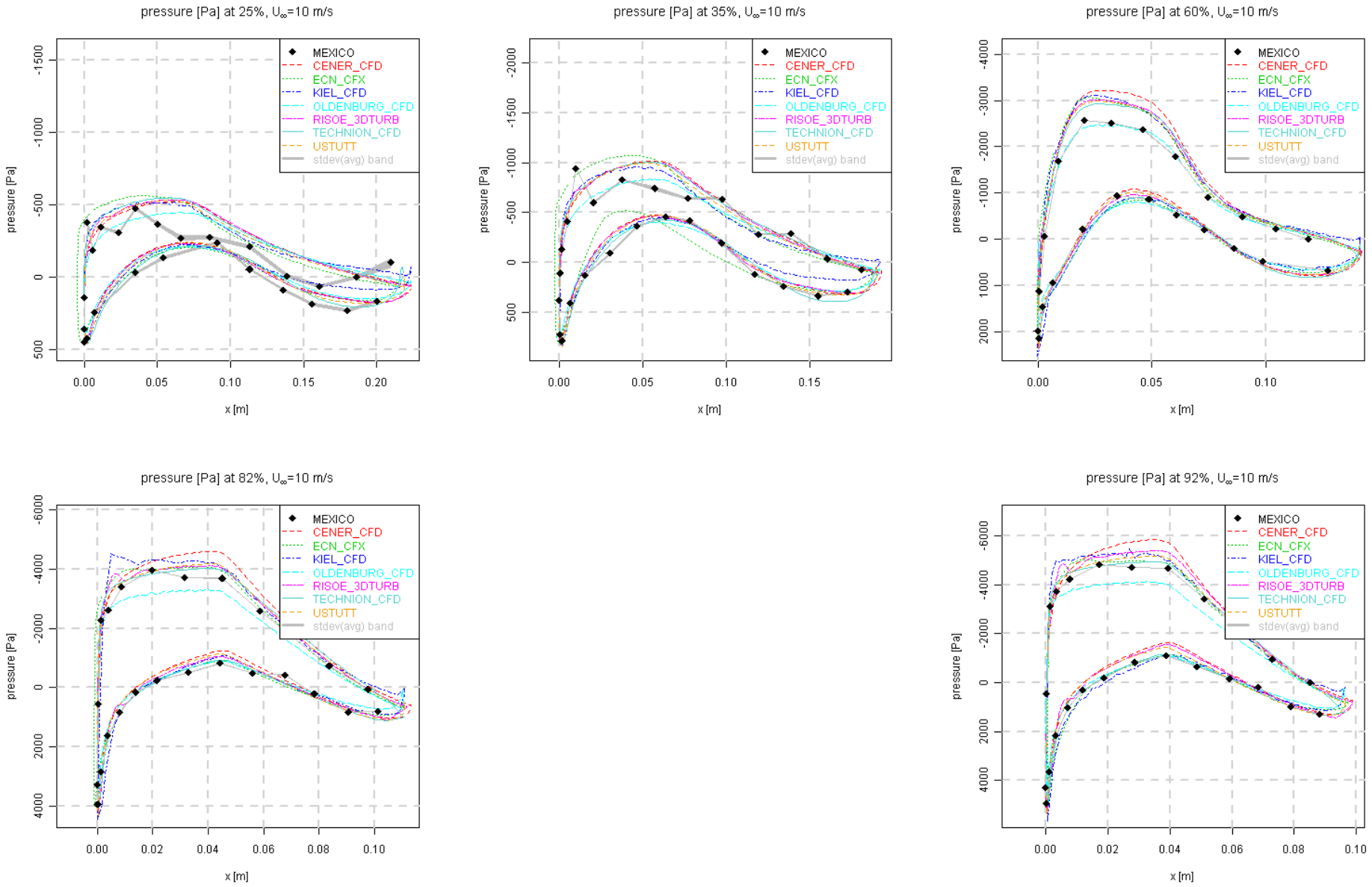

Figure 8.3 *Pressure distributions for* $U_\infty = 10$ *m/s*

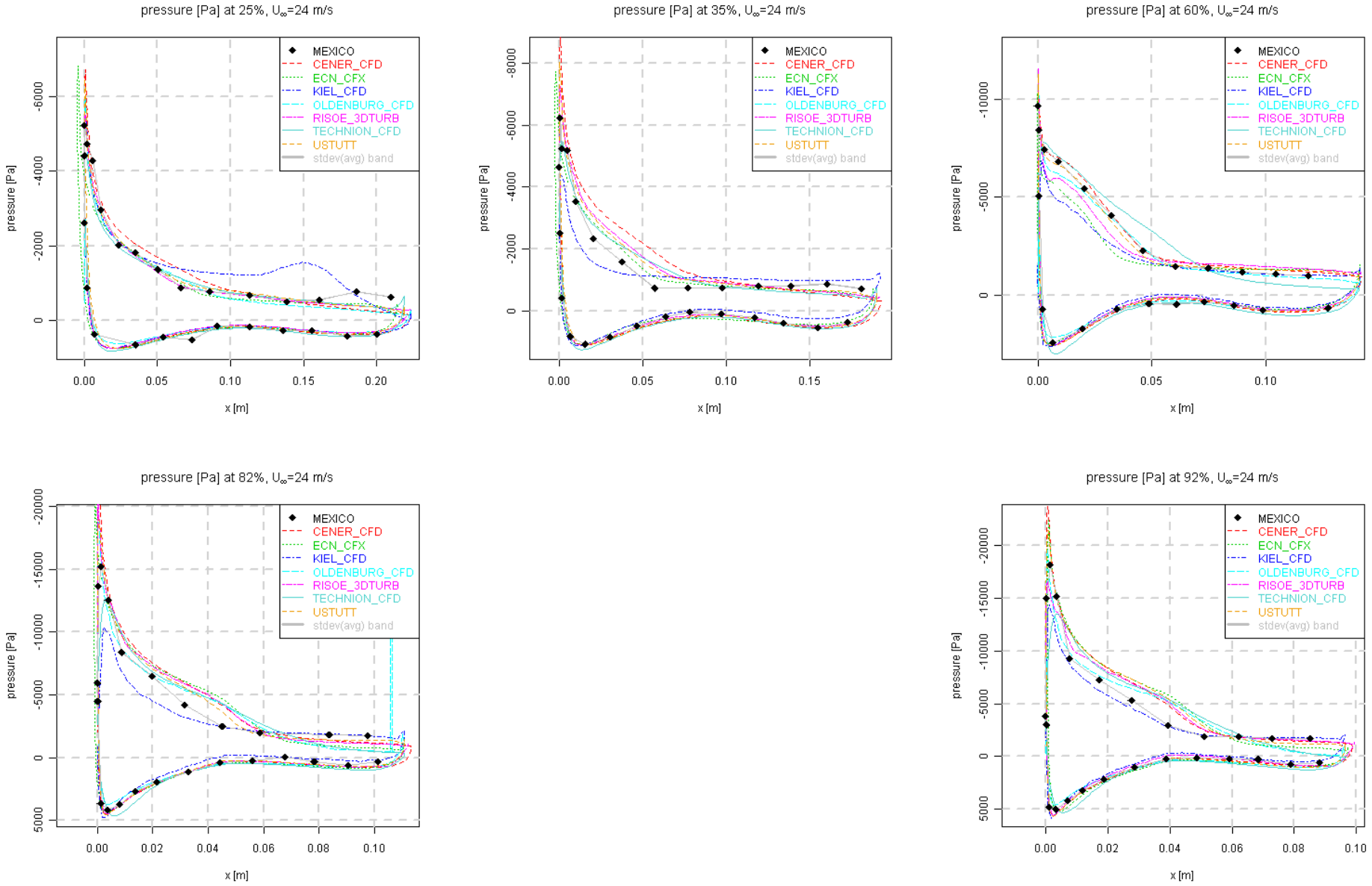

Figure 8.4 *Pressure distributions for $U_\infty = 24$ m/s*

8.2.2 Loads

Different from the pressure distributions, the loads are calculated by both CFD and lifting line codes. Since normal force is mostly dictated by pressure forces, the resulting load prediction for the CFD codes should be congruent to the pressure distributions shown in section 8.2.1. This is however not always the case. From the pressure distributions we concluded that for attached flow the suction on the airfoil upper side generally is overpredicted, whilst for U_∞=24 m/s the separation point is delayed compared to the experiment. Both observations yield a higher normal force which is confirmed by the top graphs (CFD results) in Figure 8.6.

The wide spread of the CFD results for U_∞=24 m/s illustrates the difficulty to simulate separated flows. The lifting codes show less of a spread for this case since they all use the same prescribed airfoil data.

It is however found that the lifting line codes significantly underpredict the normal force at the inner part of the blade at 24 m/s, where the agreement at 10 and 15 m/s is better. This indicates an underprediction of stall delay even though this effect is modelled with a large variety of different 3D corrections. An underprediction from stall delay models was also observed in [21] on basis of field measurements. The corresponding results from the CFD codes are generally in better agreement.

At 60, 82 and 92% span and tunnel speeds of 10 and 15 m/s almost all codes overpredict the normal force. At 92% span an overprediction from the lifting line codes is consistant to the overprediction of tip loads in [21] which was explained by the use of 2D airfoil data near the tip. However this does not explain the overprediction at 60 and 82% span. It also does not explain the overprediction from the CFD codes at 92% span since these codes donot apply airfoil characteristics. However it is interesting to note that generally speaking the overprediction from the CFD codes is less than the overprediction from the lifting line codes.

The lifting line results for U_∞=15 m/s show a shift in normal force roughly between r=1.3 and r=1.7 m. This is attributed to the discontinuity in airfoil distribution, since the RISØ profile has a different zero lift angle of attack compared to the surrounding DU and NACA profiles. In addition to that the validity on the 2D airfoil data of the RISØ profile has been questioned, since this data was obtained in a wind tunnel which features rather high turbulence intensity levels. The fact that this jump is most pronounced for U_∞=15 m/s can be attributed to the difference in lift coefficients being larger for the angle of attack corresponding to this operating condition. The transition part between these profiles in the actual MEXICO blade partly smooths this discontinuity, which makes this jump disappear for the CFD results. Concatenating the PIV sheets in this region (Figure 8.5) shows an unexpected velocity discontinuity in the experiment, which could be well attributed to this phenomenon.

Contrary to the normal force, the contribution of friction to the tangential force is significant in addition to the pressures. This contribution is however not taken into account in the experimental value, which consist solely of the pressure forces. In addition to that, the resulting tangential pressure force is highly dependent on location and number of pressure sensors. These two effects are more dominant for high angles of attack. This should be kept in mind whilst comparing the experiment with calculations.

The tangential force distribution in Figure 8.7 shows much more (relative) scatter between the calculated results than for the normal force. The absolute value of the tangential force is small and hence a small difference is easily visible in the figures. In addition to that it is not entirely clear which participants have removed the frictional contribution from their calculated results, as was instructed in the calculation case description in section A.1.

The overprediction in normal force results in an overprediction in axial force in 8.8. The axial force appears to be well predicted by most of the lifting line codes for U_∞=24 m/s, but a closer look at Figure 8.6 shows that this is a result of outboard overprediction and inboard underpredic-

tion. The same holds for the torque, which is largely dictated by the tangential force distribution.

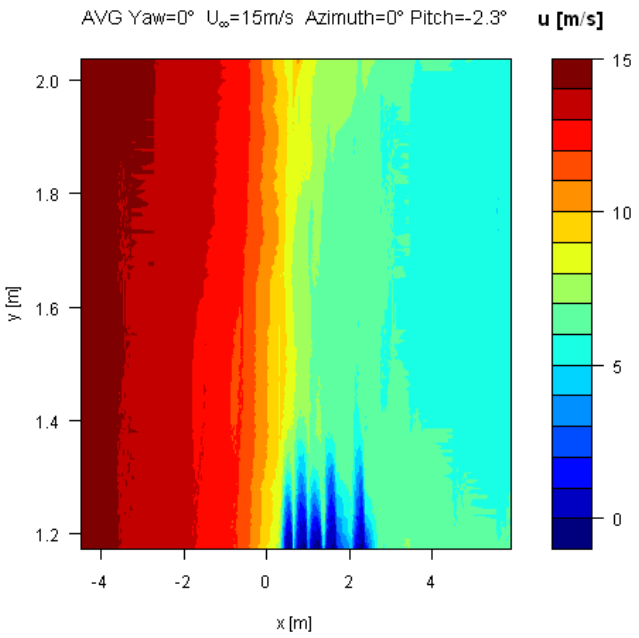

Figure 8.5 *Contours of axial velocity from PIV (x in axial, y in radial direction, origin in rotor center)* ‡

‡ Missing values between PIV sheets have been linearly interpolated

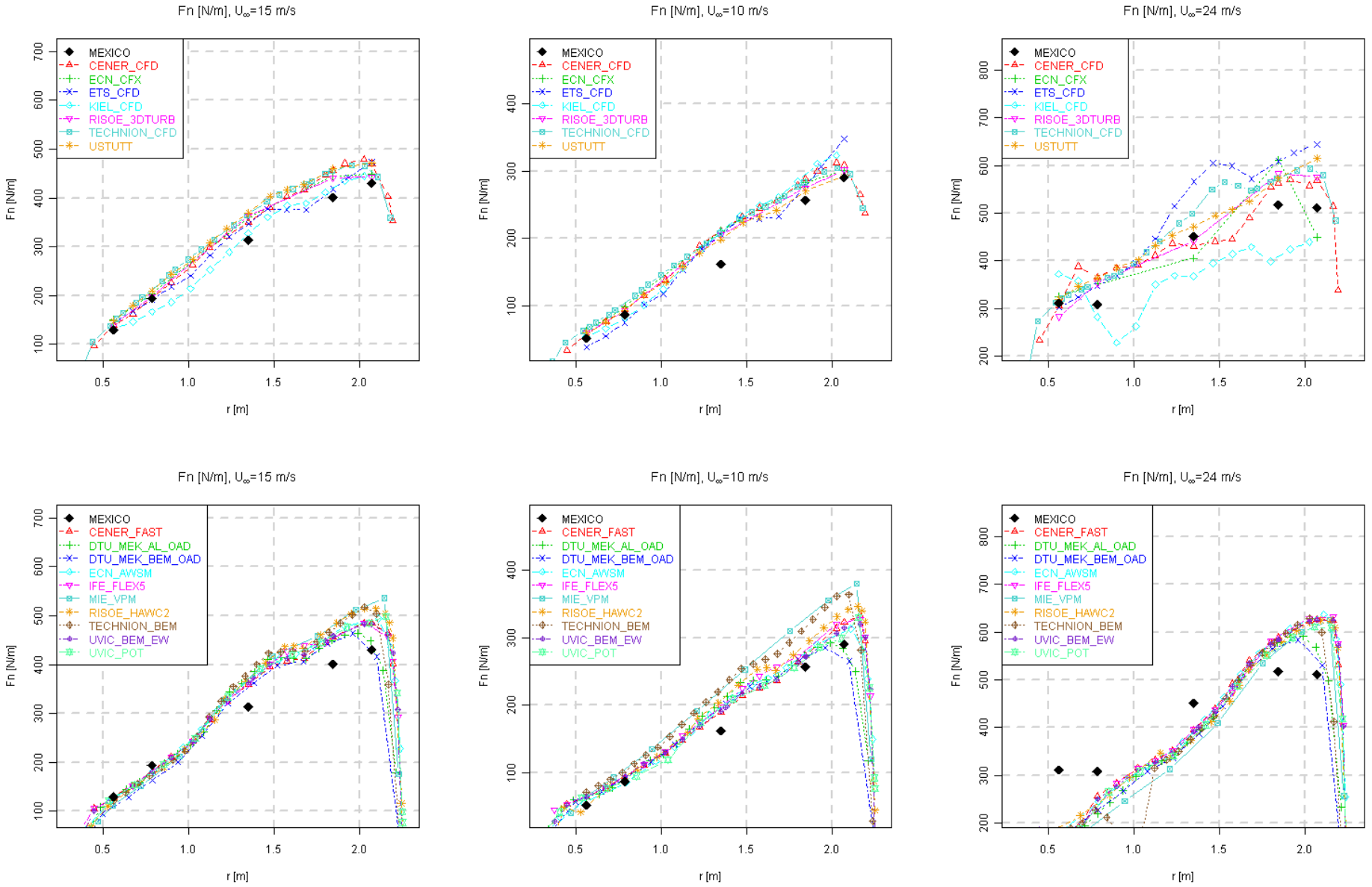

Figure 8.6 *Normal force. Top: CFD, bottom: lifting line codes*

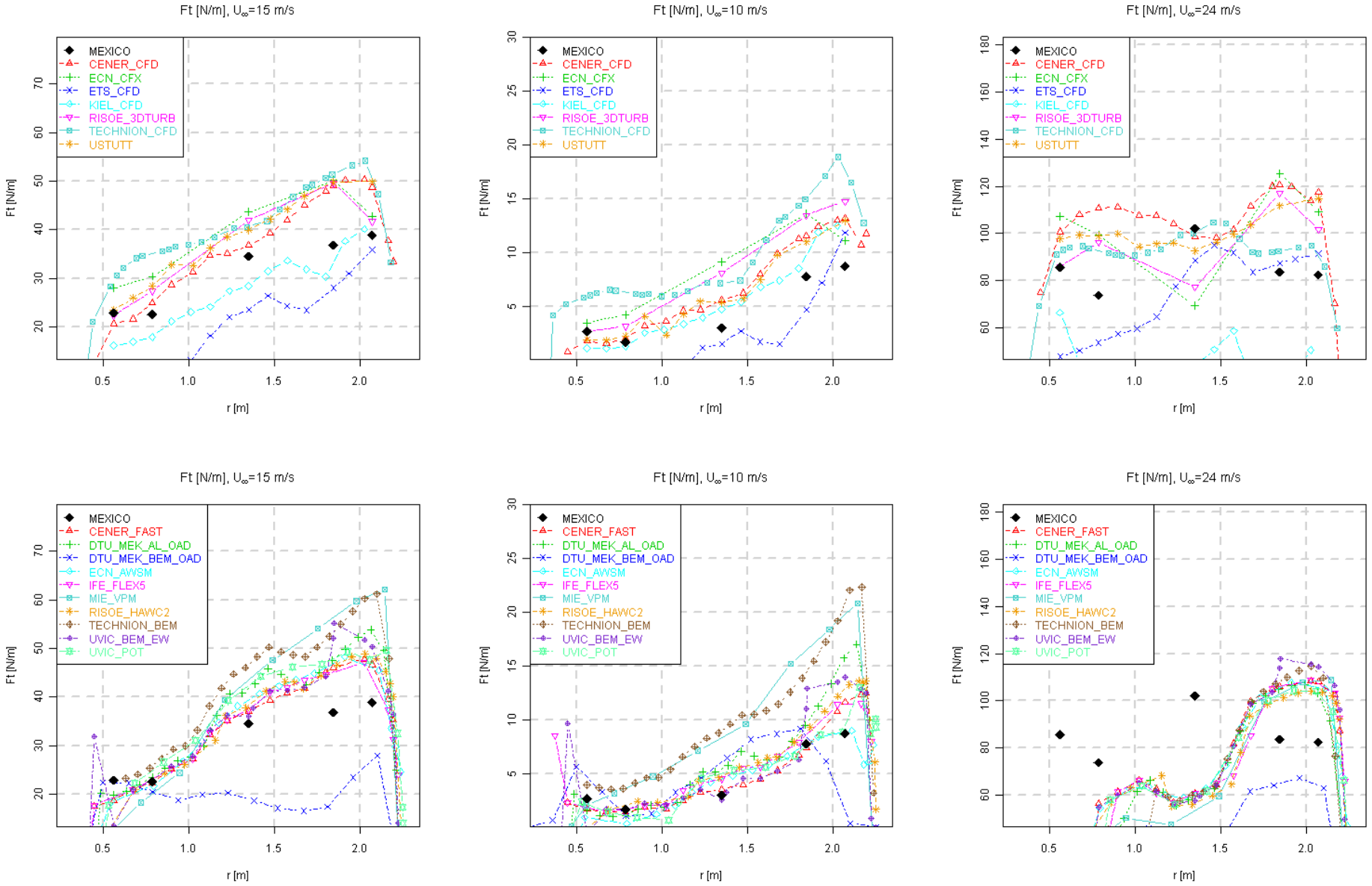

Figure 8.7 *Tangential force. Top: CFD, bottom: lifting line codes*

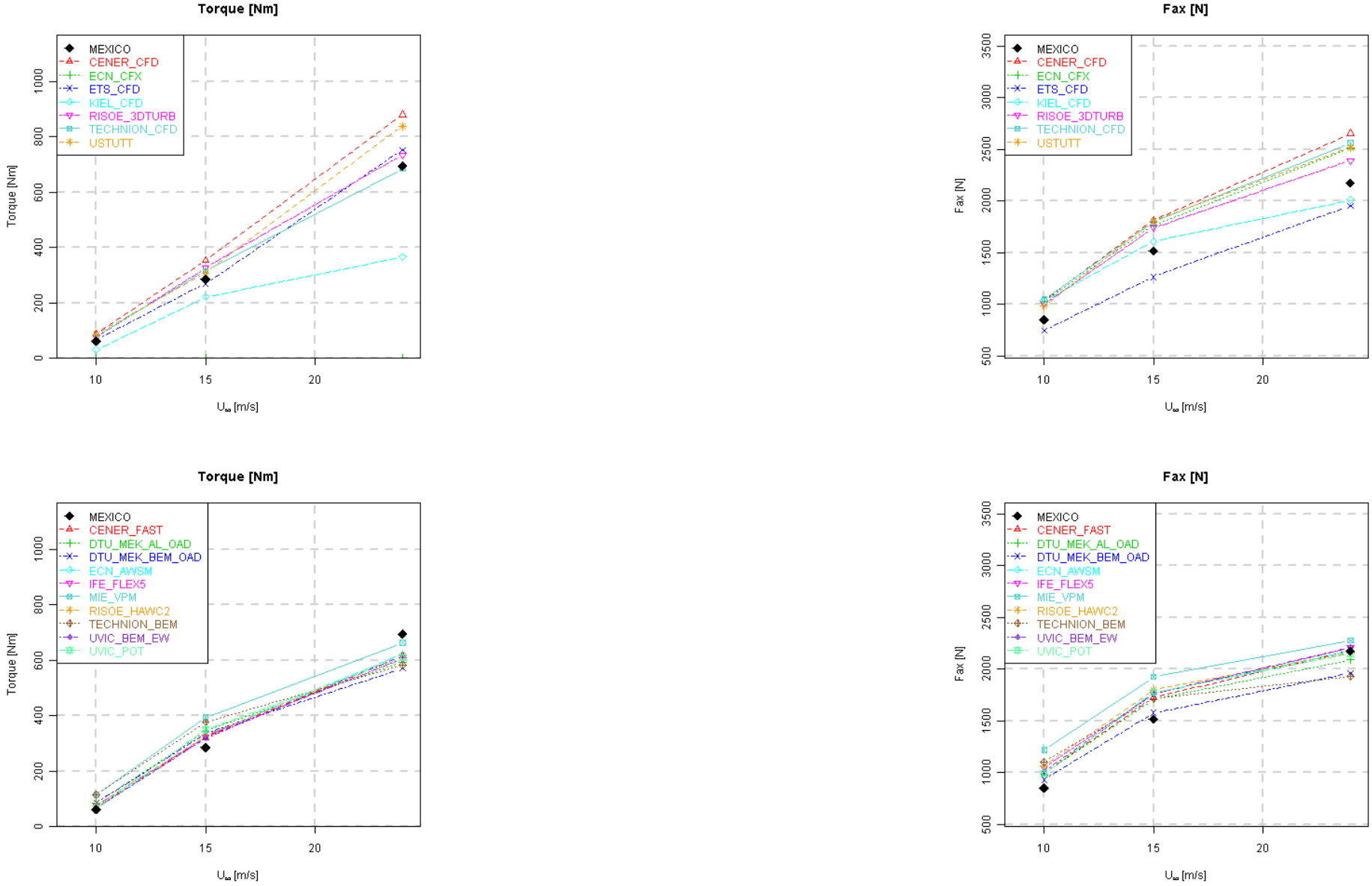

Figure 8.8 *Torque and axial force. Top: CFD, bottom: lifting line codes*

8.2.3 Lifting line variables

The lifting variables consist of angle of attack, effective velocity, normal and tangential force coefficient (c_n and c_t) and axial and tangential induced velocity (u_i and v_i). These variables are not measured experimentally and hence a comparison can only be made between calculated values from the participating lifting line codes.

The angle of attack distribution in Figure 8.9 shows a jump roughly between r=1.3 and r=1.7 m similar to the normal force distribution as described in section 8.2.2. Several codes display an increase of angle of attack in the tip region where a decrease due to the Prandtl tip correction is expected. Possibly the tip correction implementation varies between the codes. The discrepancies at the root can possibly be attributed to the same effect, although results that show an angle of attack decrease at the tip do not always show this at the root as well.

The effective velocity is dominated by the rotational velocity and hence differences due to rotor induction are impossible to distinguish from the effective velocity graphs in Figure 8.9. These figures do however provide a double check on the correct input of operational conditions (rotational and wind velocity).

The normal and tangential force distribution in Figure 8.10 are directly related to the calculated angle of attack. Differences can arise however due to the applied 3D correction models. Dynamic stall effects are not of importance for axial flow conditions although it is interesting to note that even at non-yawed flow the high frequency Mexico measurements showed very strong dynamic stall effects at large angles of attack. Whether this is due to the small and inevitable excitation from e.g. tunnel turbulence or tower shadow or whether this can be considered as self excited dynamic stall is still an open question. These effects are however generally not included.

Hence most of the comments made for the angle of attack e.g. on the midboard discontinuity are valid for the normal and tangential forces too.

Tip and root effects also show different trends in the rotor induced velocities in Figure 8.11. In addition to the different implementation of these effects, it is suspected that several participants have supplied local instead of annulus averaged velocities as described in section C. It is worthwhile to notice that some codes do not take into account the tangential induced velocities.

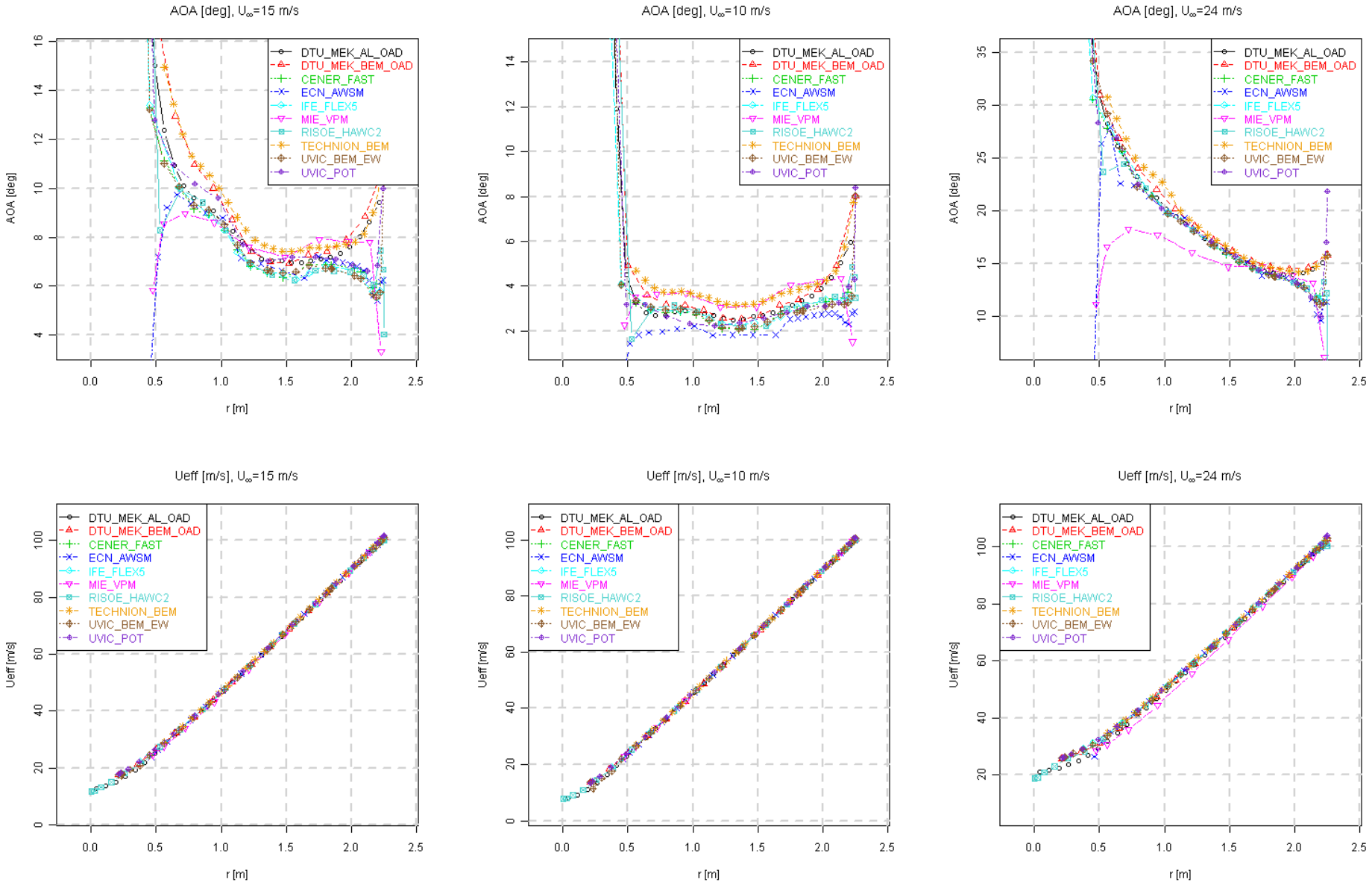

Figure 8.9 *Angle of attack (top) and effective velocity (bottom)*

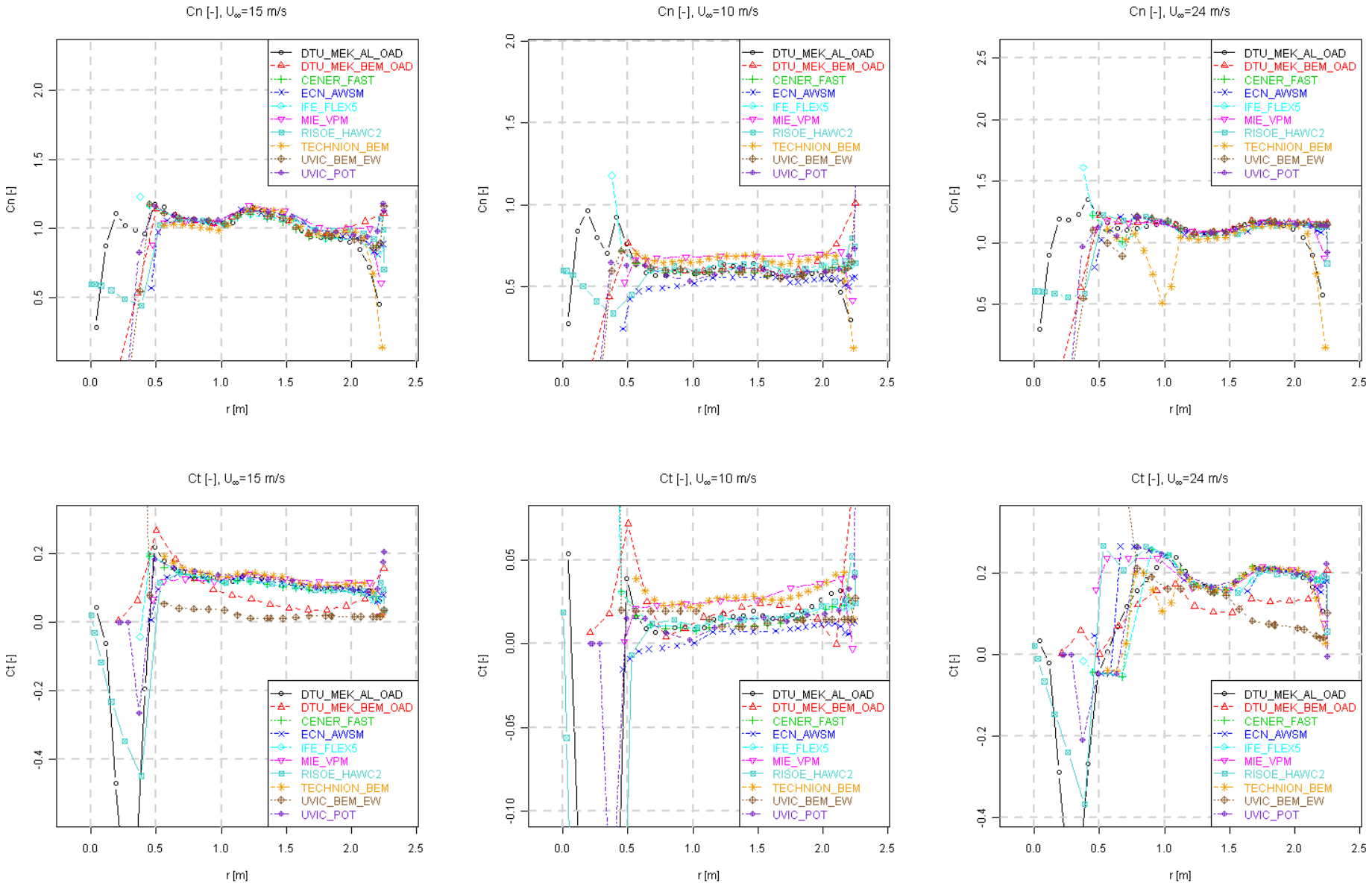

Figure 8.10 *Normal force coefficient Cn (top) and tangential force coefficient Ct (bottom)*

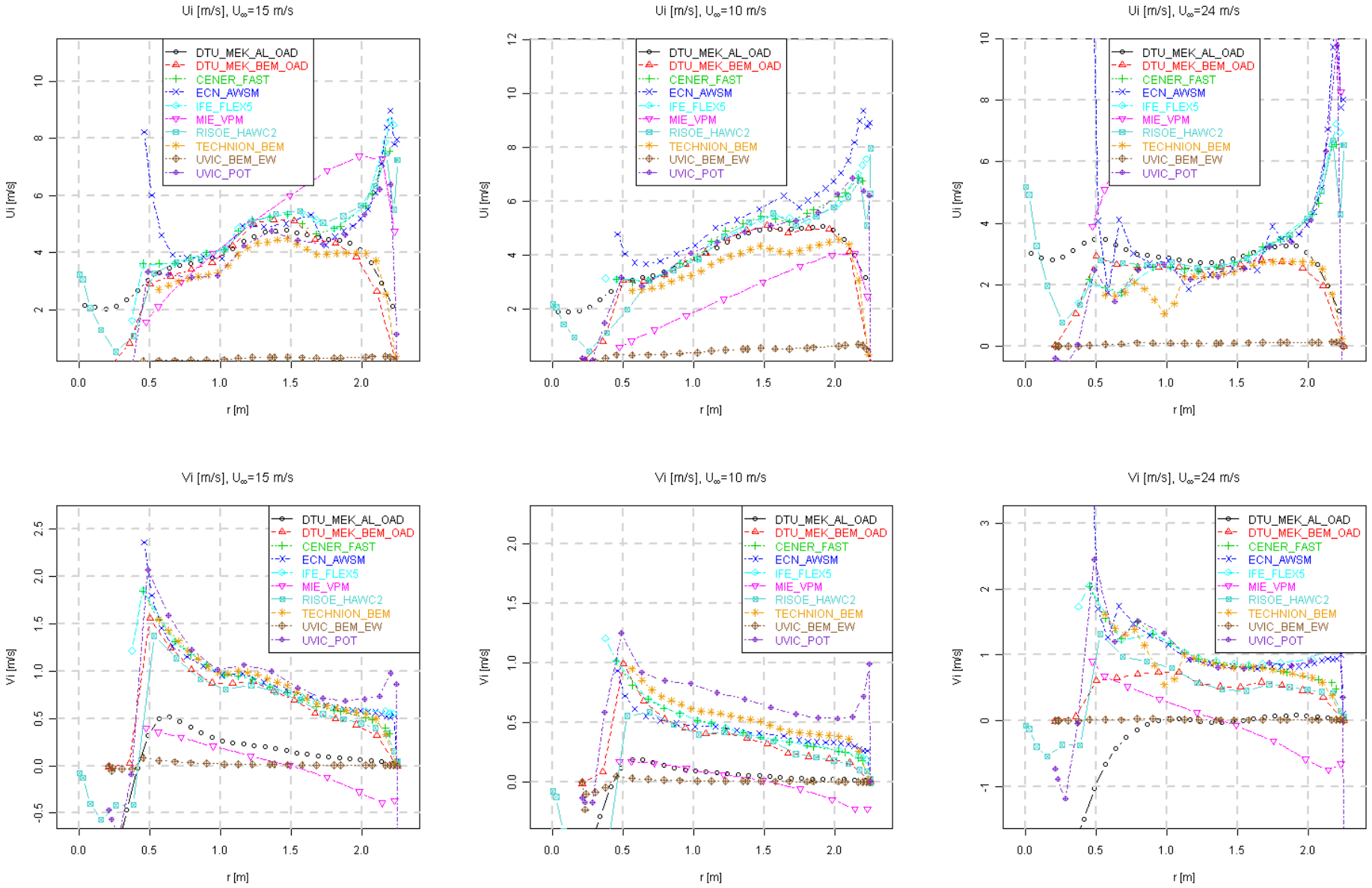

Figure 8.11 *Axial induced velocity Ui (top) and tangential induced velocity Vi (bottom)*

8.2.4 Axial velocity traverse

The axial traverses are performed at a midboard span (r=1.4 m) and an outboard span (r=1.8 m) location as indicated in the title of the graphs in Figure 8.12, 8.13 and 8.14. The rotor azimuth angle for all traverses was fixed at $0\,^{\circ}$. It is interesting to notice that the axial velocity (Figure 8.12) far upstream (x=-4 m) is higher for all CFD codes at U_{∞}=15 and U_{∞}=10 m/s. This is also the case in the rotorplane and in the wake. For U_{∞}=24 m/s, which features less rotor loading due to the lower tip speed ratio, the agreement is better. Some calculated results feature an increasing axial velocity with axial coordinate in the rotor wake. This is attributed to bad convergence, which is most pronounced for the turbulent wake state (U_{∞}=10 m/s). Furthermore it can be observed that the axial induction increases for high rotor loading (U_{∞}=10 m/s) compared to low rotor loading (U_{∞}=24 m/s).

The fluctuations in the near wake at U_{∞}=24 m/s are attributed to vortex shedding in separated flow conditions. They are also predicted by the computations. The measured near wake velocity fluctuations for U_{∞}=15 m/s at r=1.4 m are believed to be caused by the profile transition as depicted in Figure 8.5. None of the computations however reproduce this feature.

Although section 8.2.2 showed the computed loads to overpredict the measurements, the axial velocity in the rotorplane is also higher than measured. A higher rotor loading should however result in more induction and hence a lower axial velocity. Hence these results are in contradiction with momentum theory unless the measured loads/velocities and/or the boundary conditions are incorrect.

The radial velocities in Figure 8.13 show the streamtube expansion towards the rotor plane, which is more pronounced for the outboard location. This trend is well reproduced by the calculations. An interesting observation is the fact that the measured trend within a PIV sheet (a cluster of data points) does not represent the trend between the sheets.

Figure 8.14 shows a drop in the rotorplane due to the tangential induced velocity, both measured and predicted with a reasonable agreement. The fluctuations in the near wake of the rotor are only predicted for separated flow (U_{∞}=24 m/s), which features a thick airfoil wake. The thin viscous wake from the blade sections visible for U_{∞}=15 and U_{∞}=10 m/s are not reproduced by the calculations, probably due to the overly dissipative nature of the used turbulence models. The distance between the peaks represent the different blade wakes from each blade passage, also illustrated in Figure 8.15. For a large freestream velocity the peaks are more distant since the convection speed in the wake is also larger.

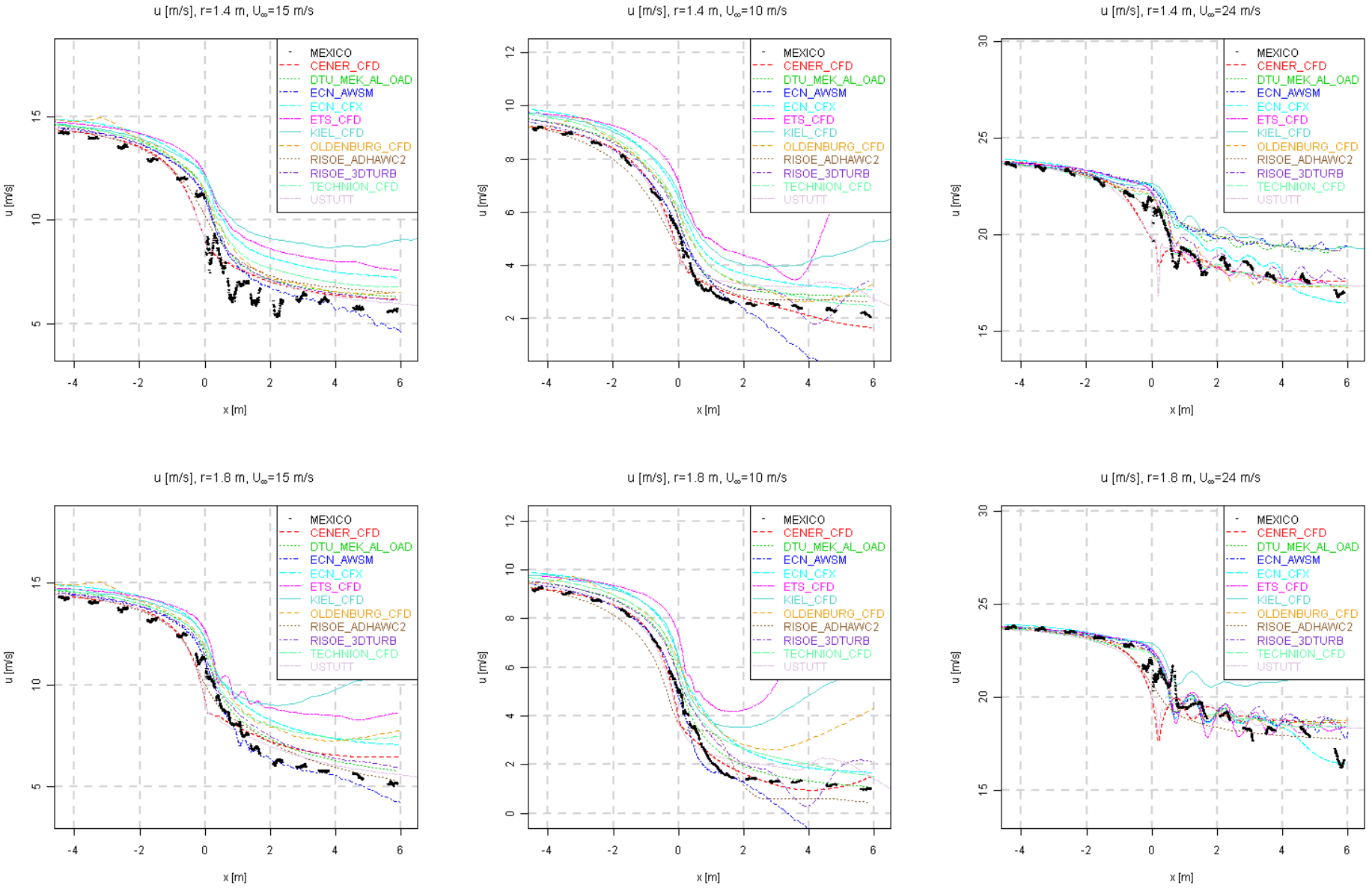

Figure 8.12 *Axial traverse of axial velocity*

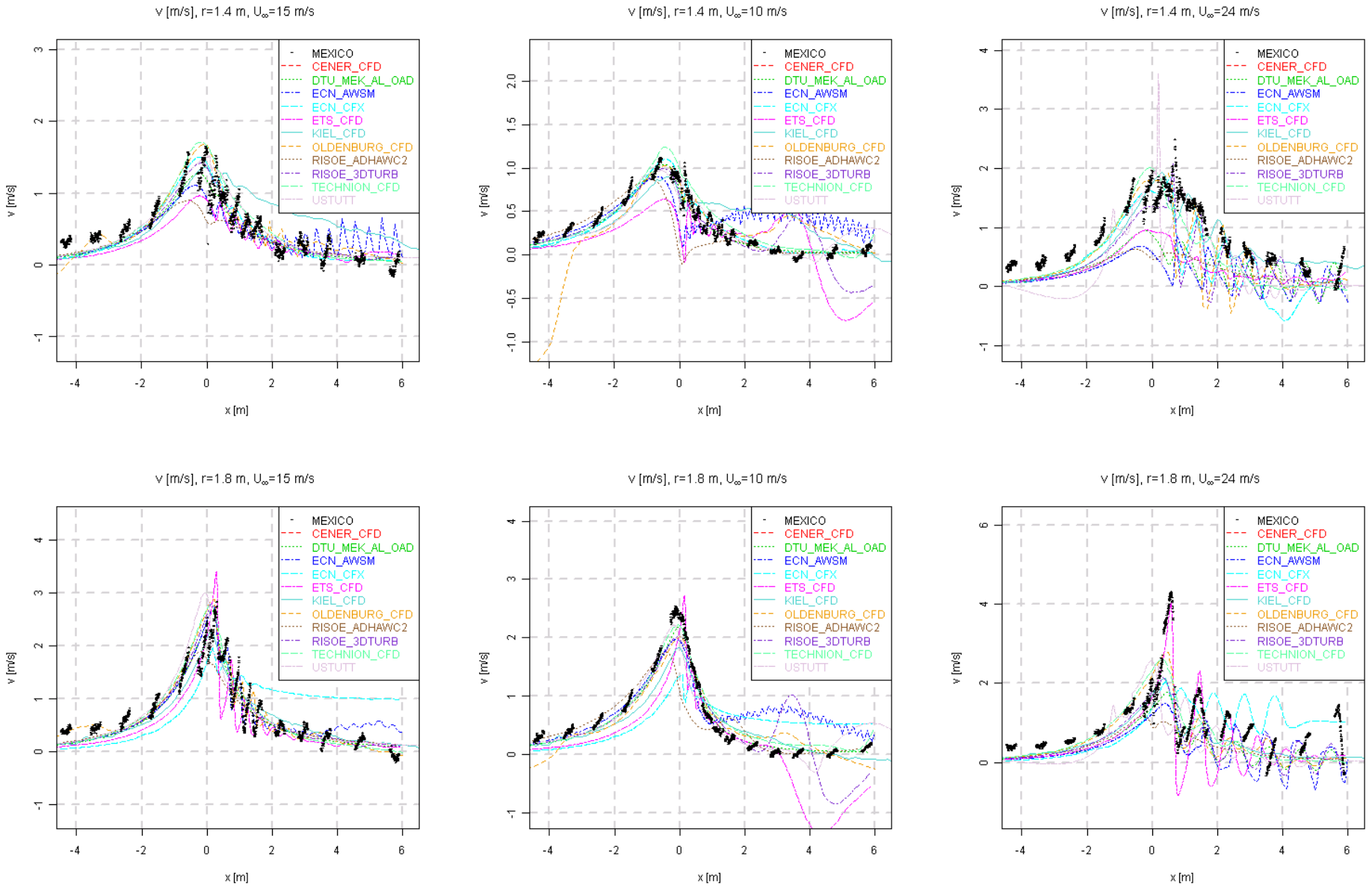

Figure 8.13 *Axial traverse of radial velocity*

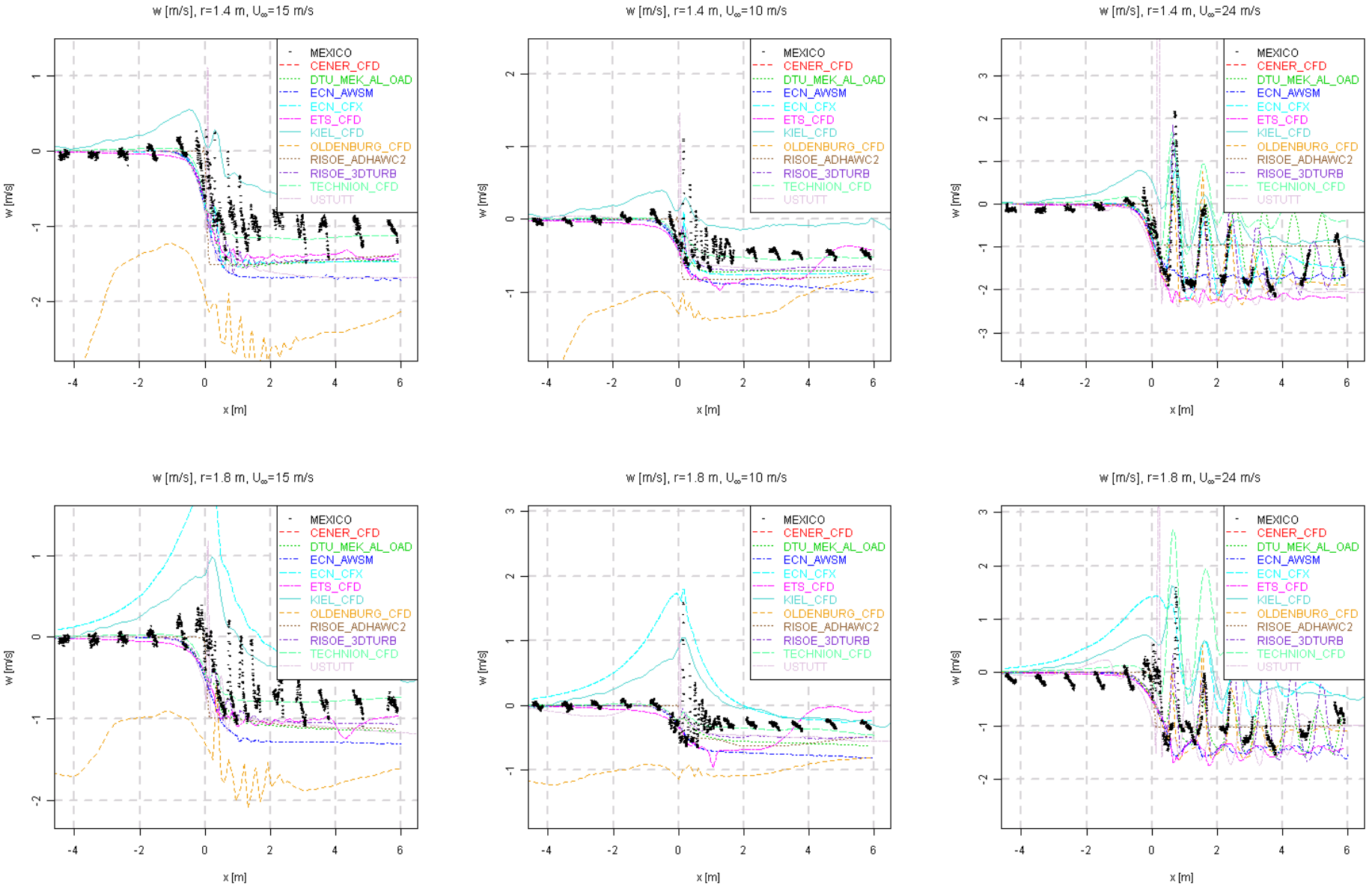

Figure 8.14 *Axial traverse of tangential velocity*

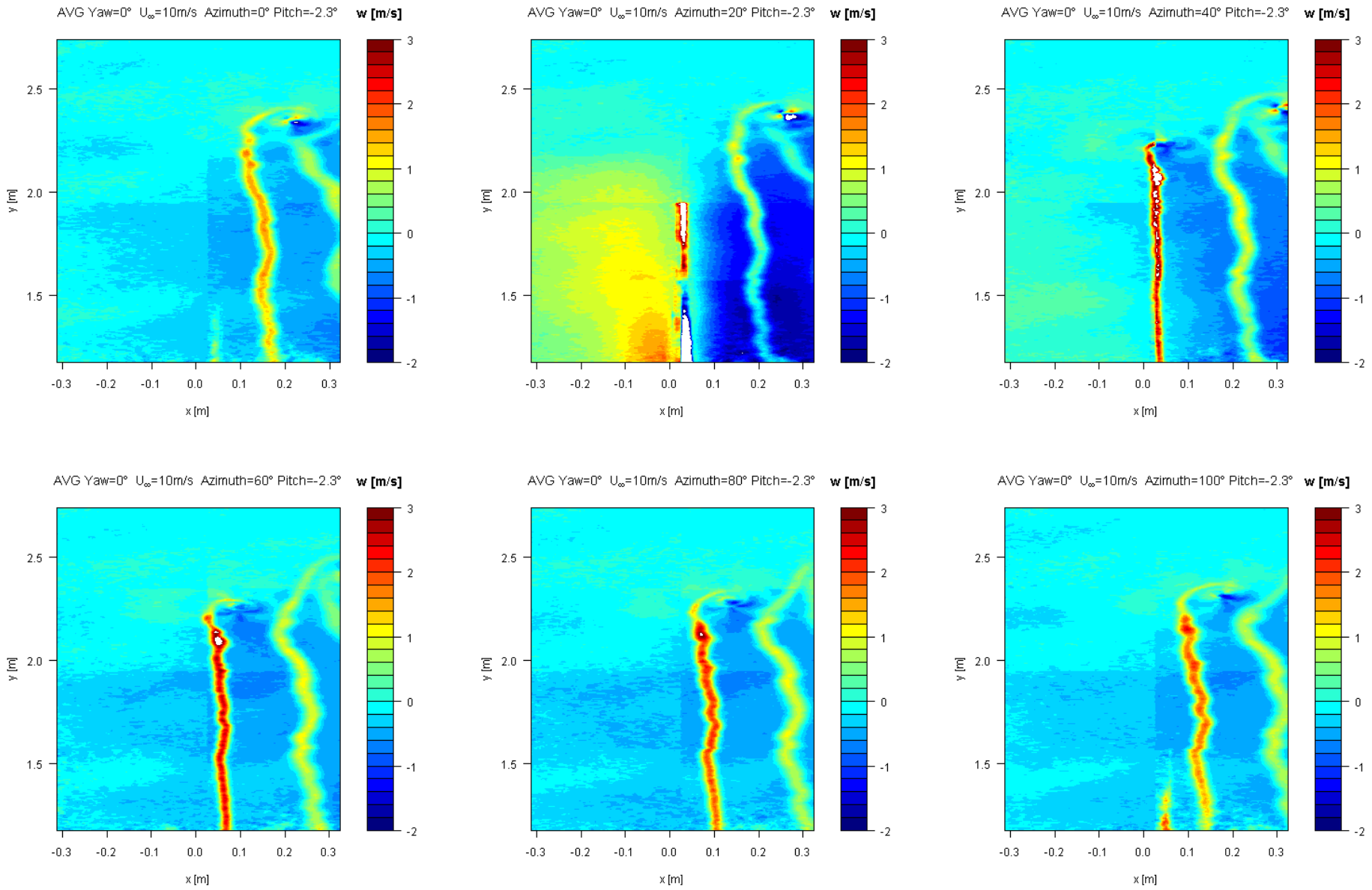

Figure 8.15 *Tangential velocity in the near wake for varying azimuth angle, U_∞=10 m/s*

8.2.5 Radial velocity traverse

The radial traverses have been performed for an upwind (x=-0.3 m) and downwind (x=+0.3 m) location. The rotor azimuth angle varies from 0 ° and 100 ° in steps of 20 ° as indicated in the title of the graphs from Figure 8.16 to 8.33.

Upwind

For the upwind location, the axial induction between r=1 and r=2 m can be noticed to be larger close to the blade passage at 40 ° and 60 ° azimuth. Towards the tip this effect is less due to the finite number of blades. Also in these radial traverses it can be observed that the axial induction increases for high rotor loading (U_∞=10 m/s, Figure 8.17) compared to low rotor loading (U_∞=24 m/s, Figure 8.18). In agreement with the axial traverse, the radial traverse results feature an overprediction of axial velocity.

The measured trend is generally captured well by the computations. The RISØ_ADHAWC result features an actuator disk which does not distinguish between rotor azimuth angle. Hence the velocities of this data set are the same for the azimuth angles in each Figure and do not capture the blade passage.

The radial velocity component shows the wake expansion to increase with rotor loading. The expansion is also more pronounced close to the blade passage, similar to the axial induction. Again the measured trend is well captured by most of the codes. The amount of wake expansion close to the tip for $U_\infty = 10$ m/s is underpredicted by all of the codes, except for the actuator disk results of RISØ.

The measured tangential induced velocity in front of the rotor plane is small as expected. The scatter in the experimental results indicates that the variation lies in the range of the accuracy of the PIV measurements. Apart from some outliers the level and trend (if there is any) is well predicted.

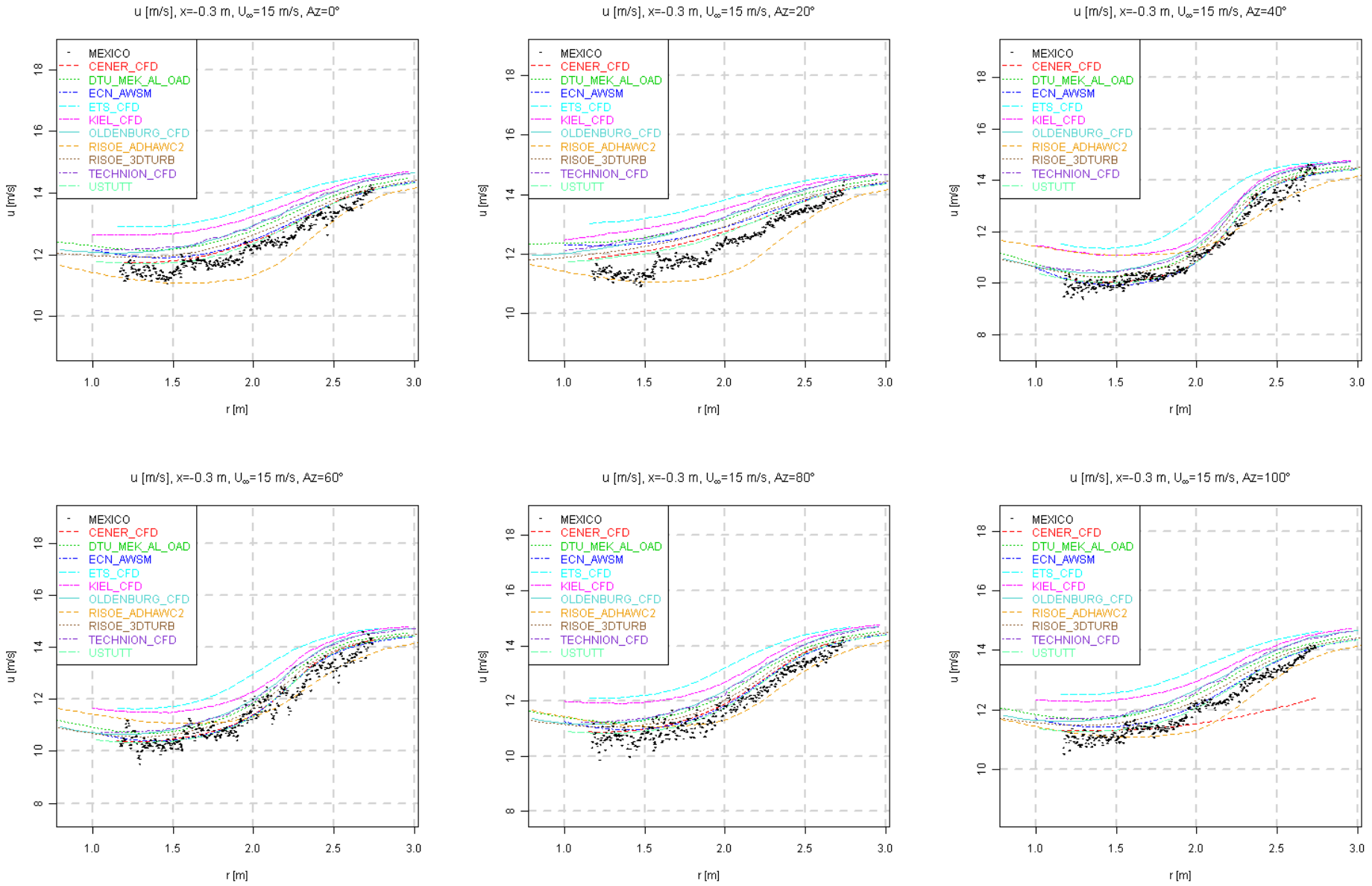

Figure 8.16 *Radial traverse (upwind) of axial velocity, U_∞ =15 m/s*

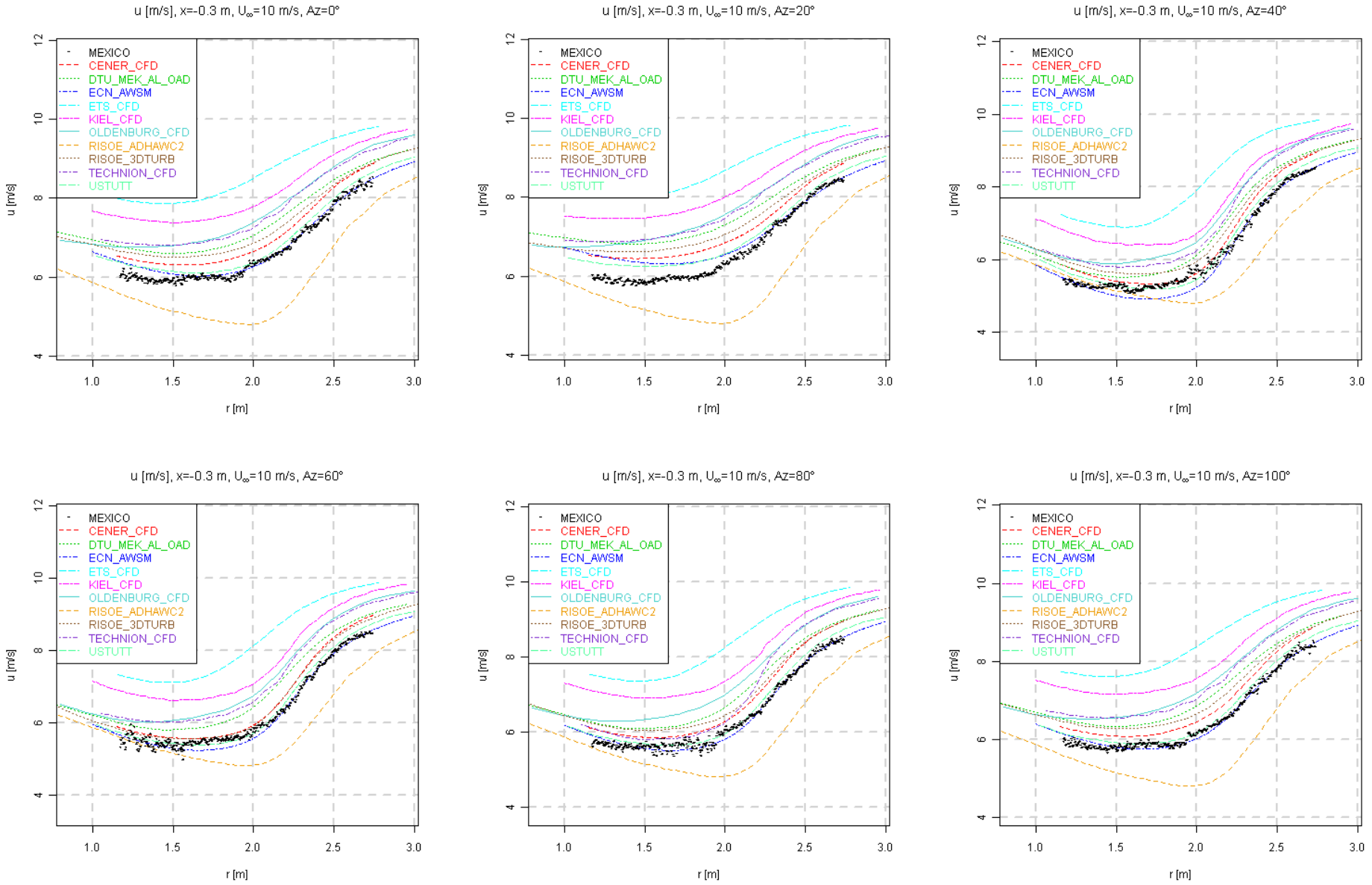

Figure 8.17 *Radial traverse (upwind) of axial velocity, U_∞ =10 m/s*

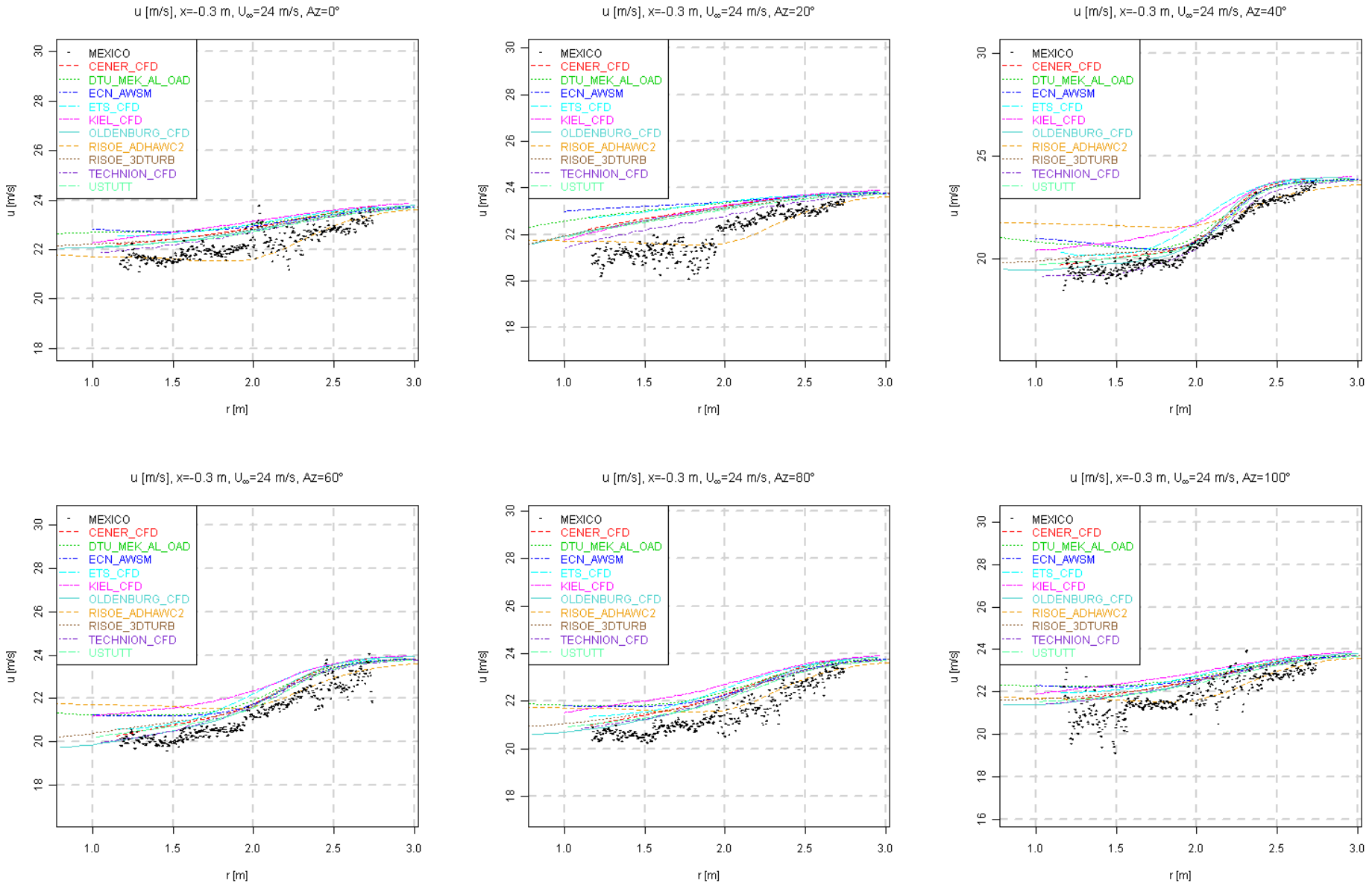

Figure 8.18 *Radial traverse (upwind) of axial velocity, U_∞ =24 m/s*

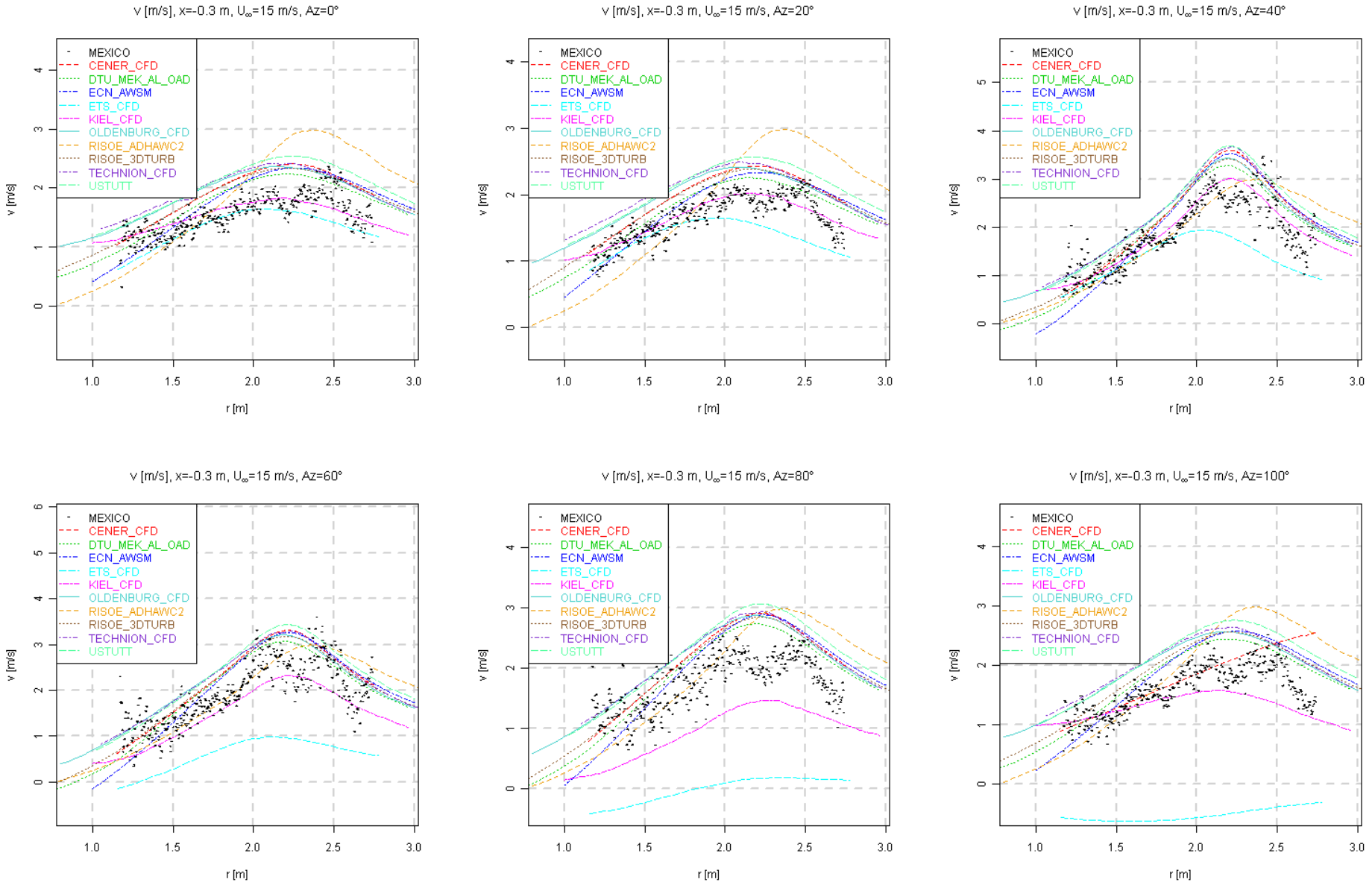

Figure 8.19 *Radial traverse (upwind) of radial velocity, U_∞ =15 m/s*

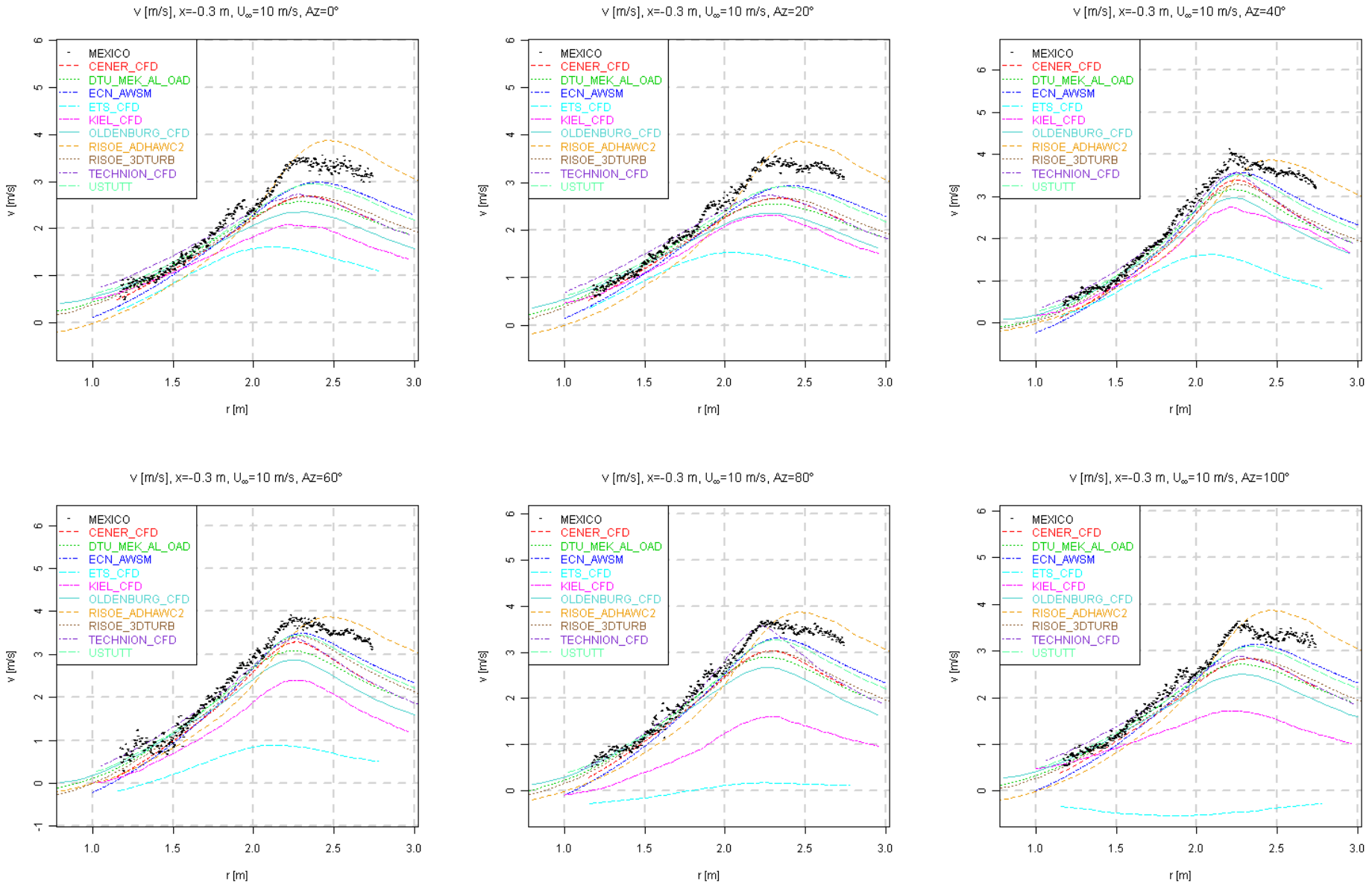

Figure 8.20 *Radial traverse (upwind) of radial velocity, U_∞ =10 m/s*

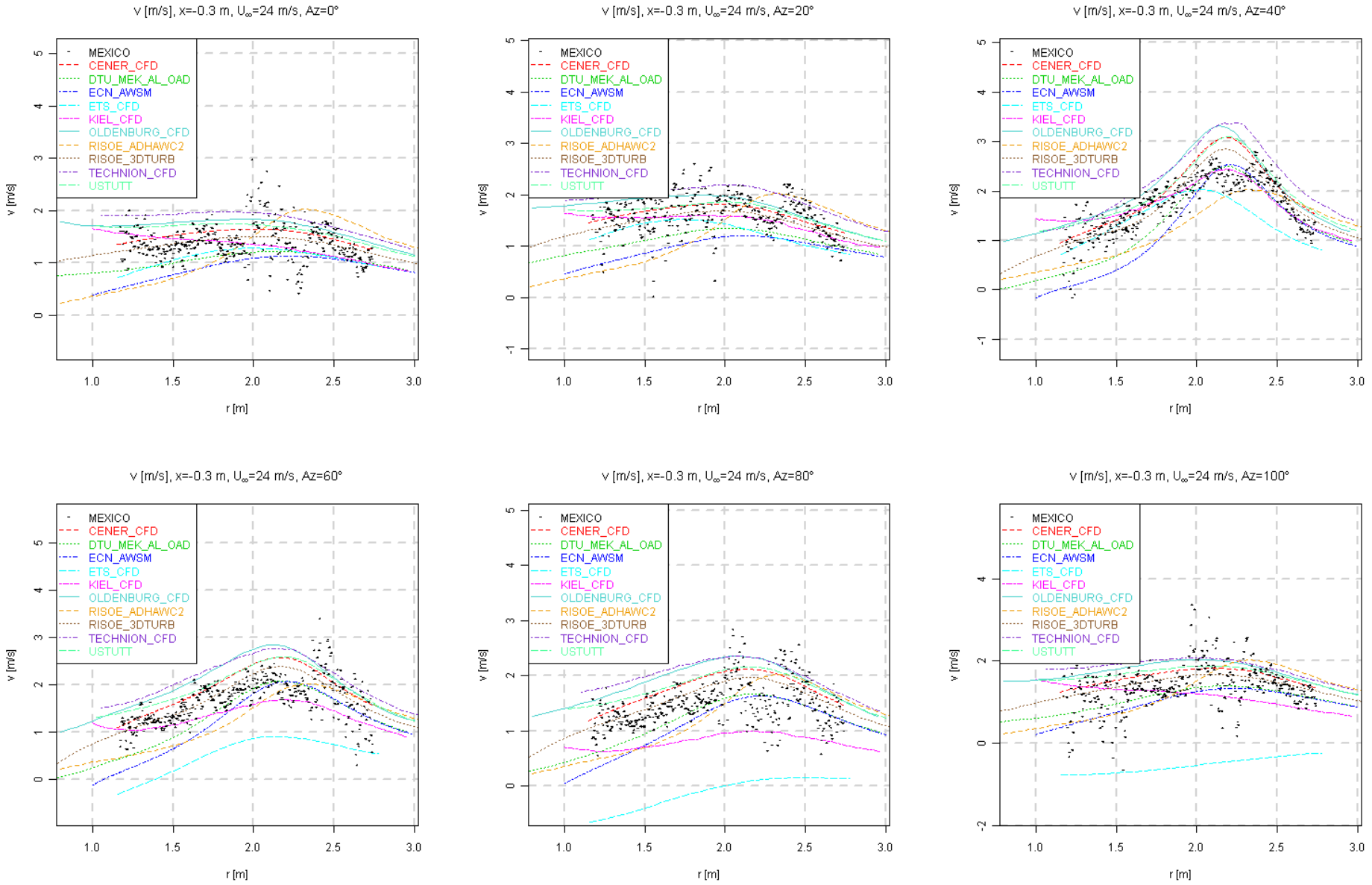

Figure 8.21 *Radial traverse (upwind) of radial velocity, U_∞ =24 m/s*

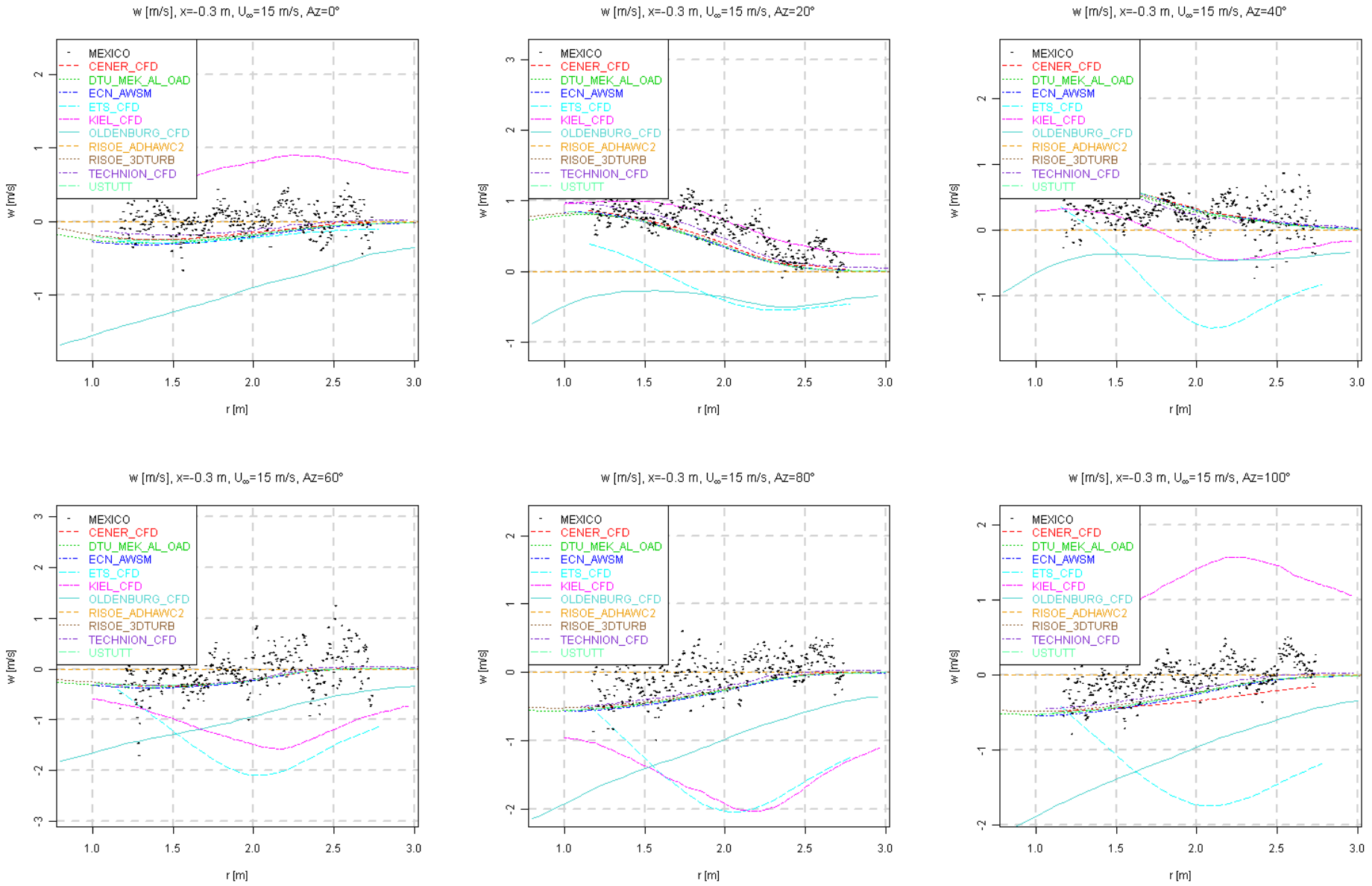

Figure 8.22 *Radial traverse (upwind) of tangential velocity, U_∞ =15 m/s*

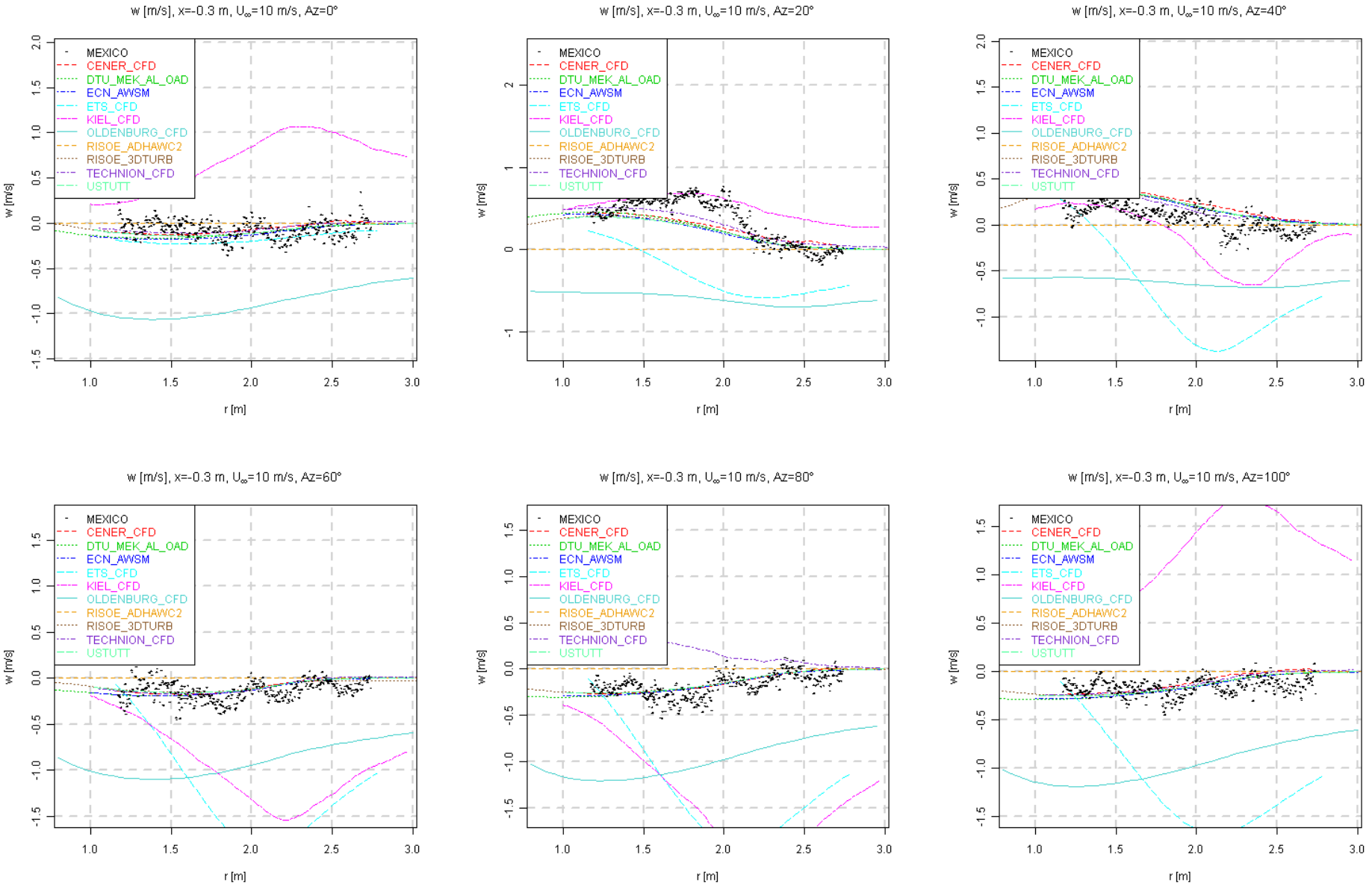

Figure 8.23 *Radial traverse (upwind) of tangential velocity, U_∞ =10 m/s*

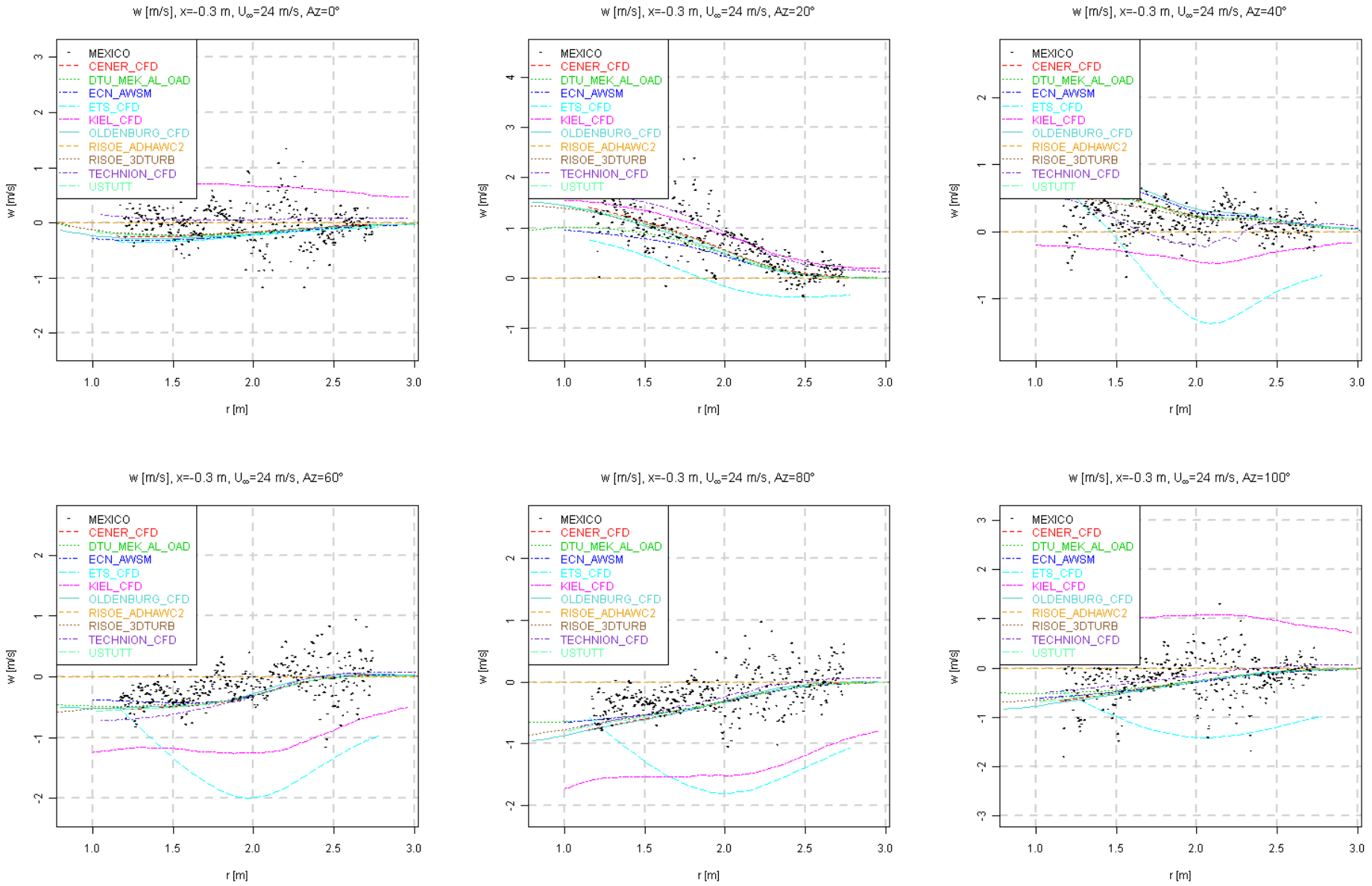

Figure 8.24 *Radial traverse (upwind) of tangential velocity, U_∞ =24 m/s*

Downwind

Downstream of the rotor plane the measured velocities show a large variation with azimuth angle depending on the position of the tip vortex. A small difference in tip vortex location yields a large difference in the obtained velocity field. Figure 8.25 shows a dip in the axial velocity around r=1.2 m. This dip is believed to be related to the transition in airfoil geometry as discussed in section 8.2.2 and illustrated in Figure 8.5. Apart from this dip and the correct location of the tip vortex, the trend of the calculations is in good agreement with the measurements. Several outliers excepted, the same story holds for the radial velocity component v.

The measured tangential velocity shows for several azimuth angles steep gradients with radial location apart from the gradients induced by the tip vortex. These humps are caused by slicing through the viscous blade wake which does not featured a straight line in radial direction due to the varying convection speed along the blade span. Figure 8.15 clearly illustrates the resulting flow field. As we noted in the axial traverse results that the convection of the viscous blade wake is not predicted properly by any of the codes, this effect is also not captured in Figures 8.31 to 8.33.

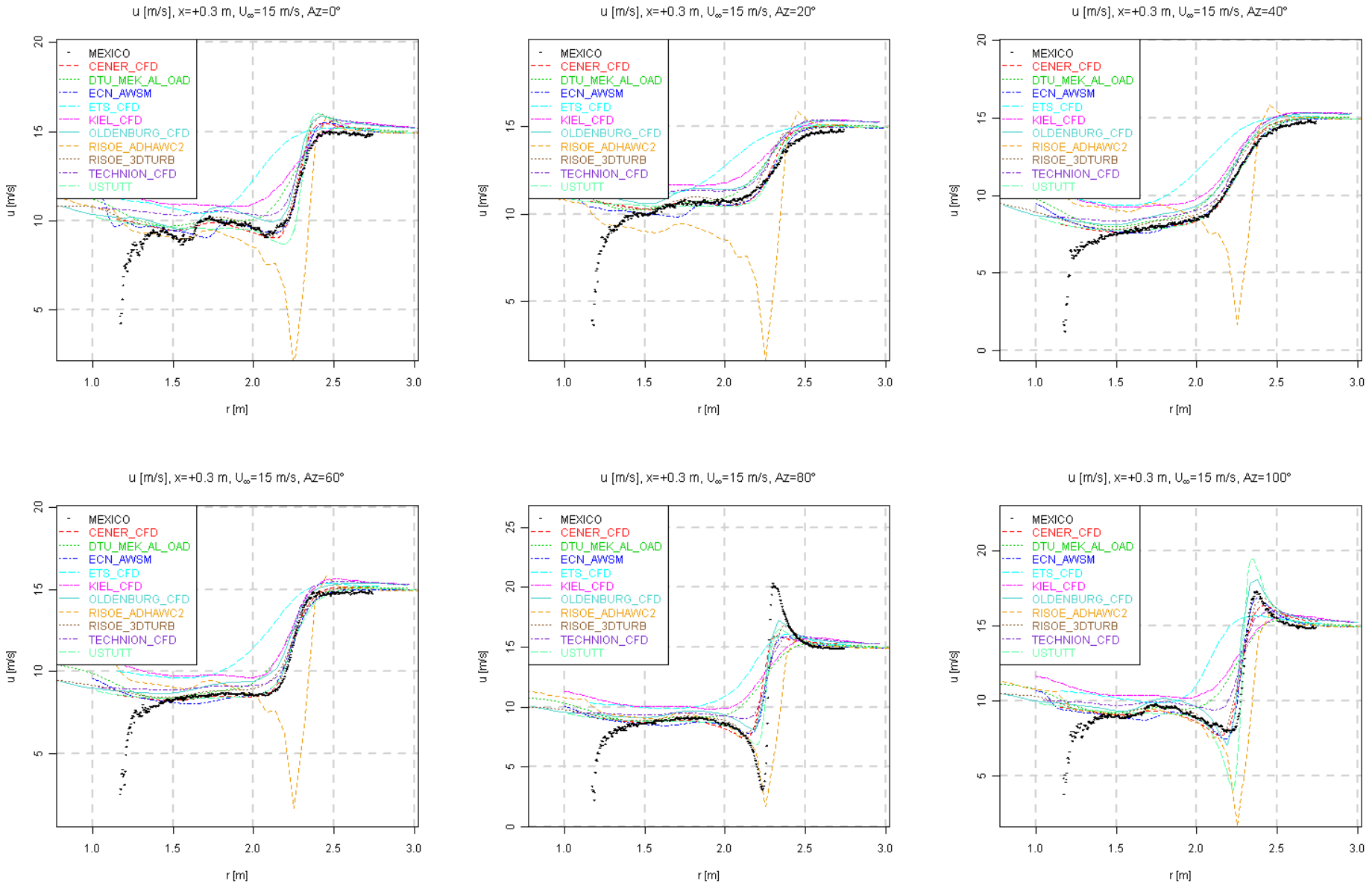

Figure 8.25 *Radial traverse (downwind) of axial velocity, U_∞ =15 m/s*

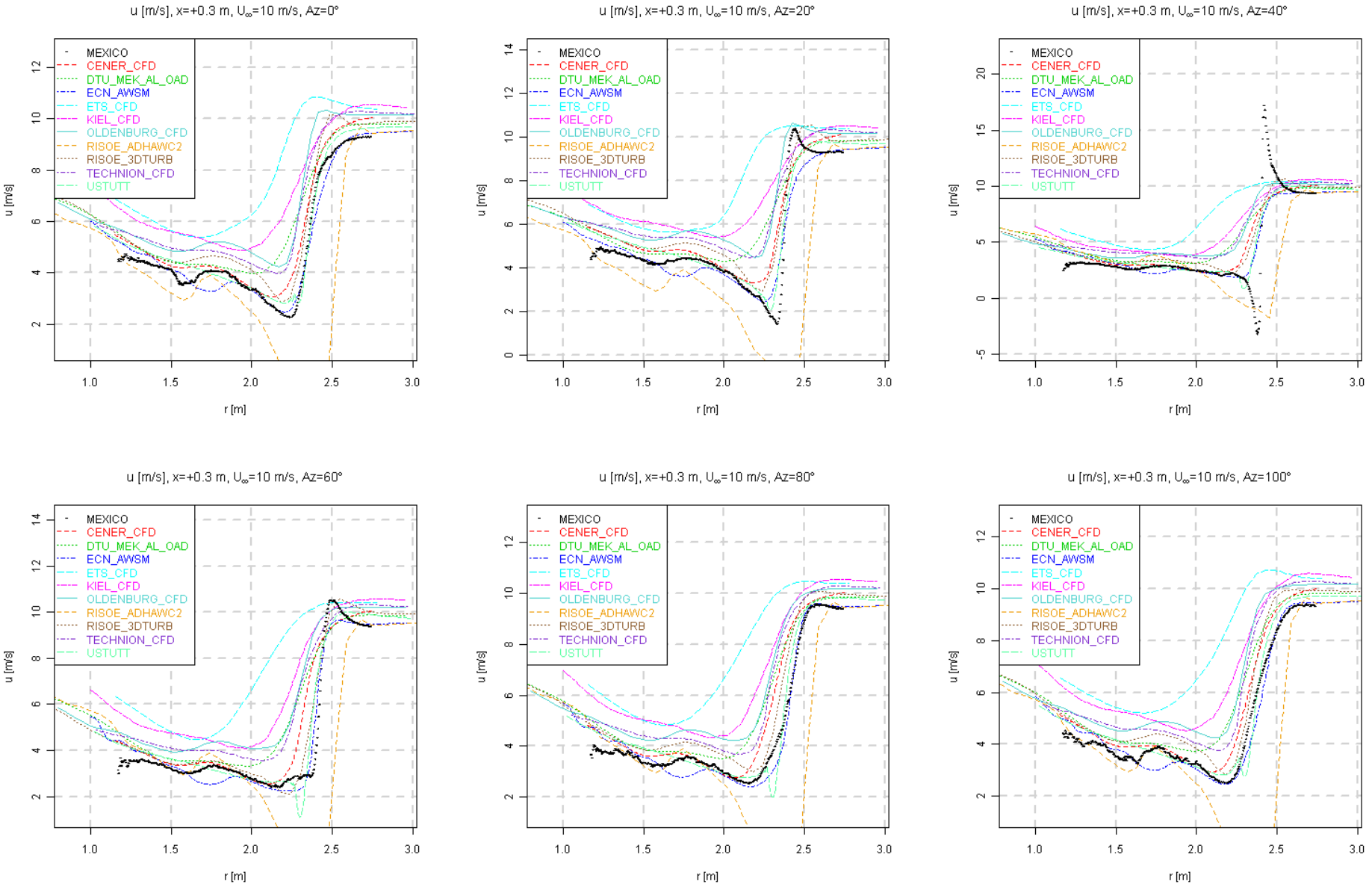

Figure 8.26 *Radial traverse (downwind) of axial velocity, U_∞ =10 m/s*

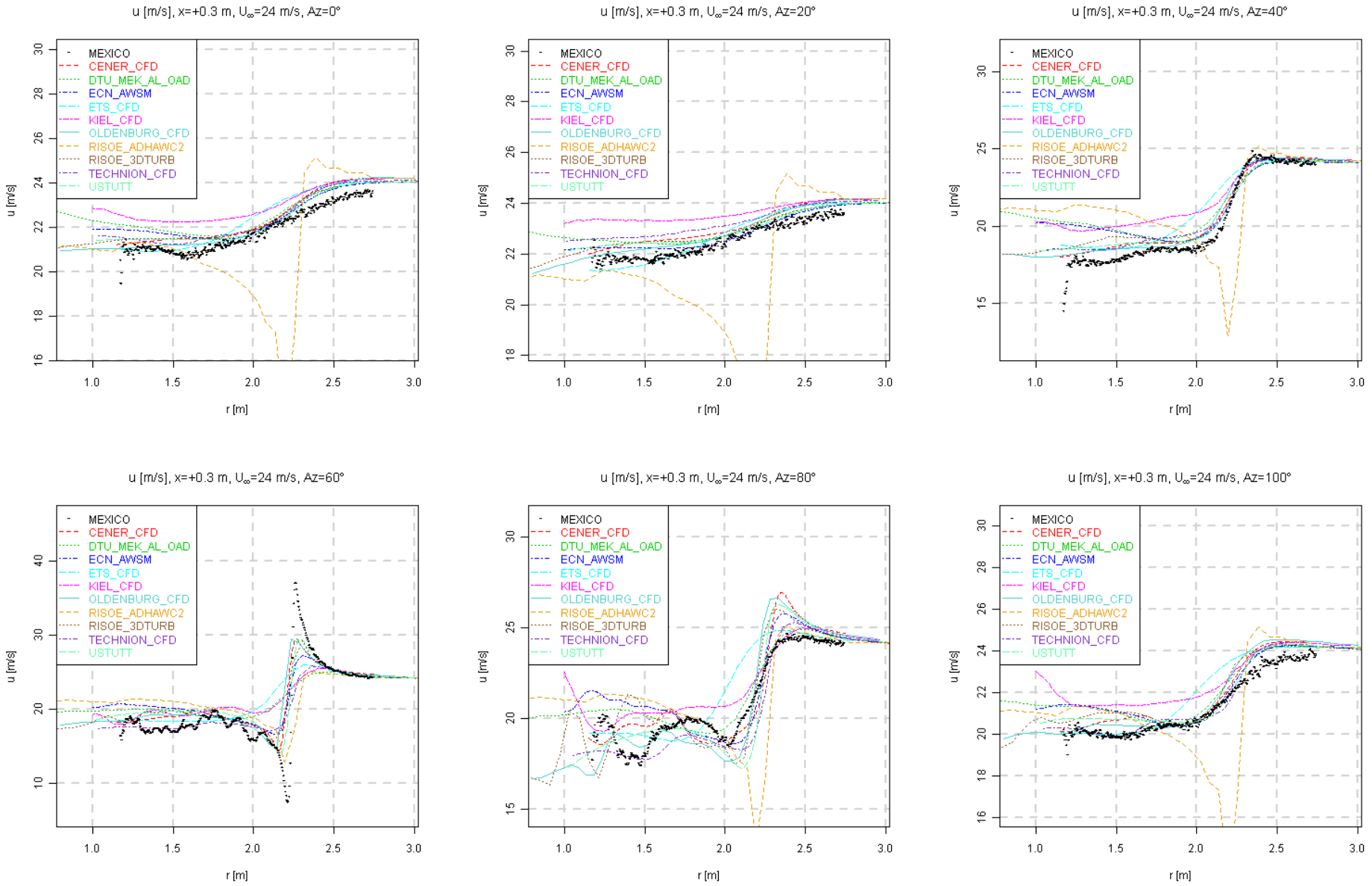

Figure 8.27 *Radial traverse (downwind) of axial velocity, U_∞ =24 m/s*

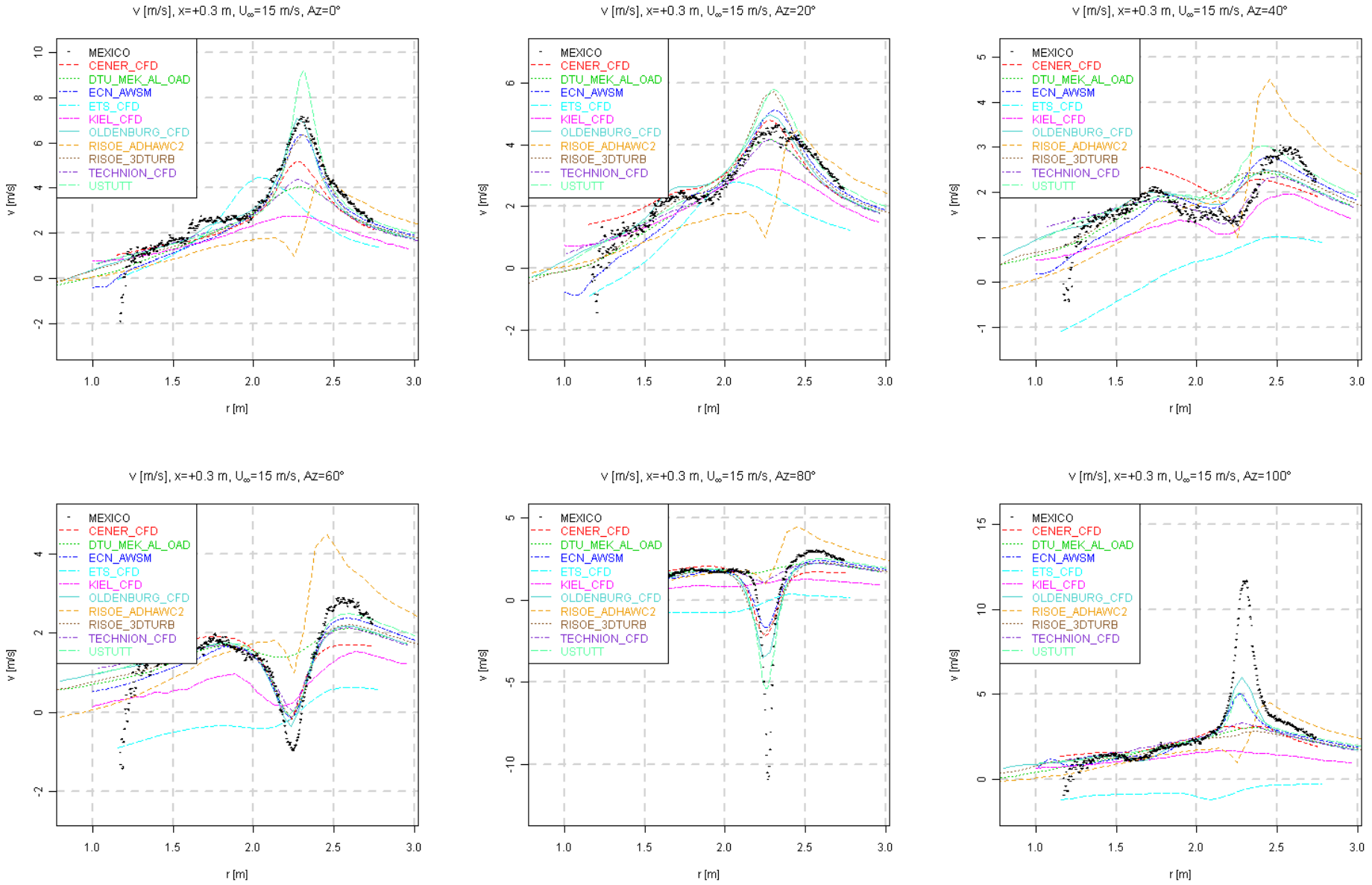

Figure 8.28 *Radial traverse (downwind) of radial velocity, U_∞ =15 m/s*

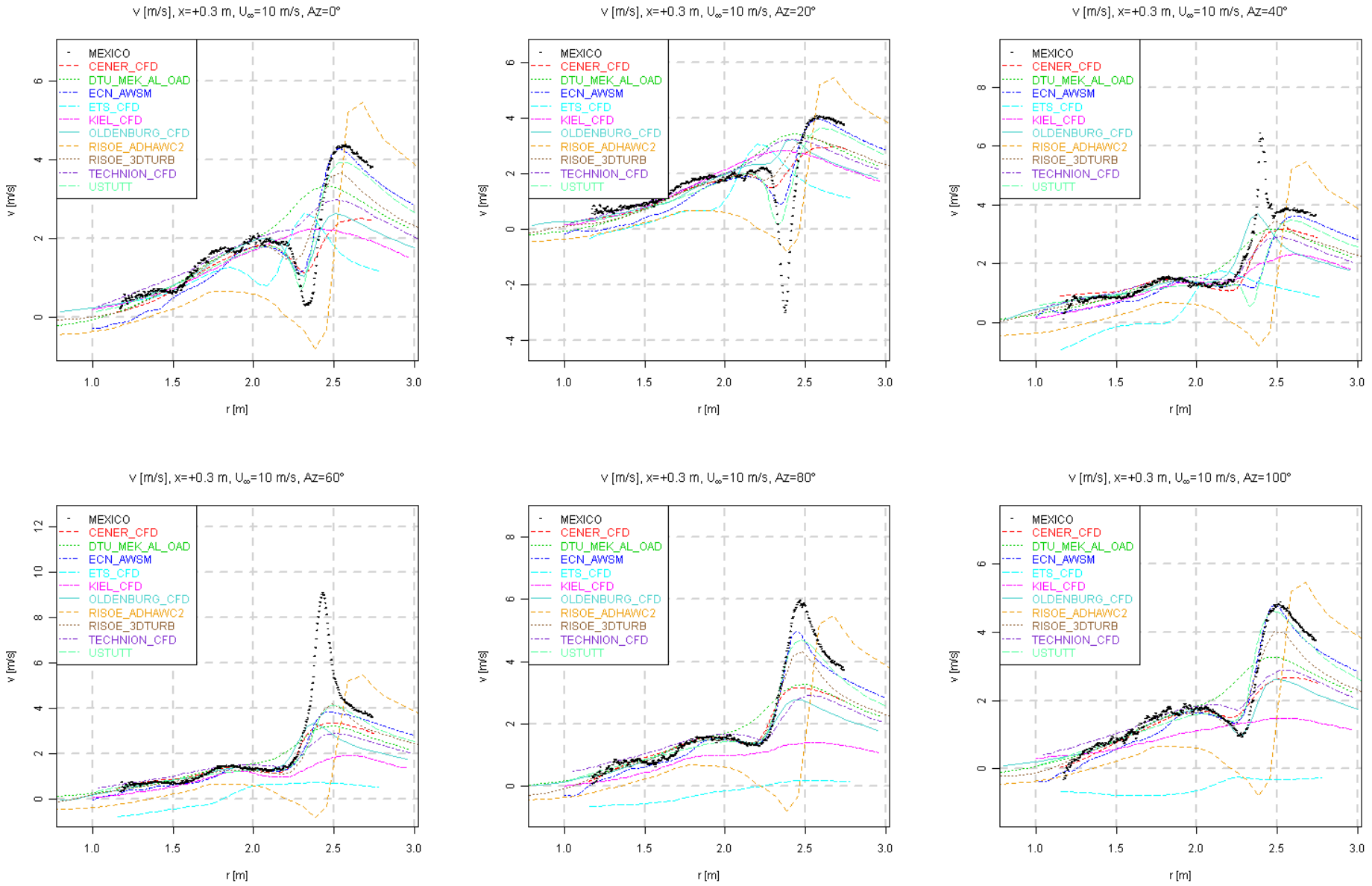

Figure 8.29 *Radial traverse (downwind) of radial velocity, U_∞ =10 m/s*

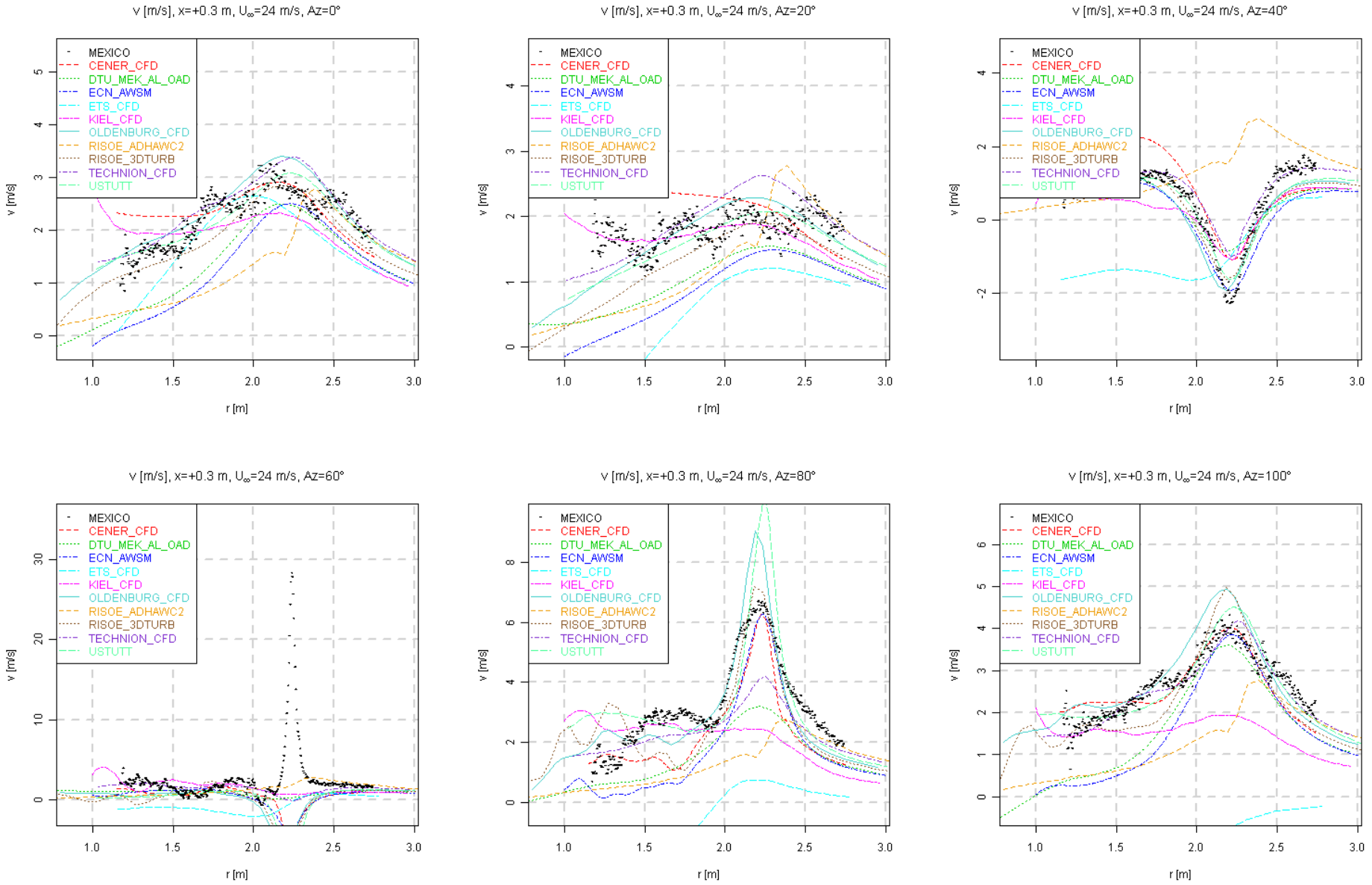

Figure 8.30 *Radial traverse (downwind) of radial velocity, U_∞ =24 m/s*

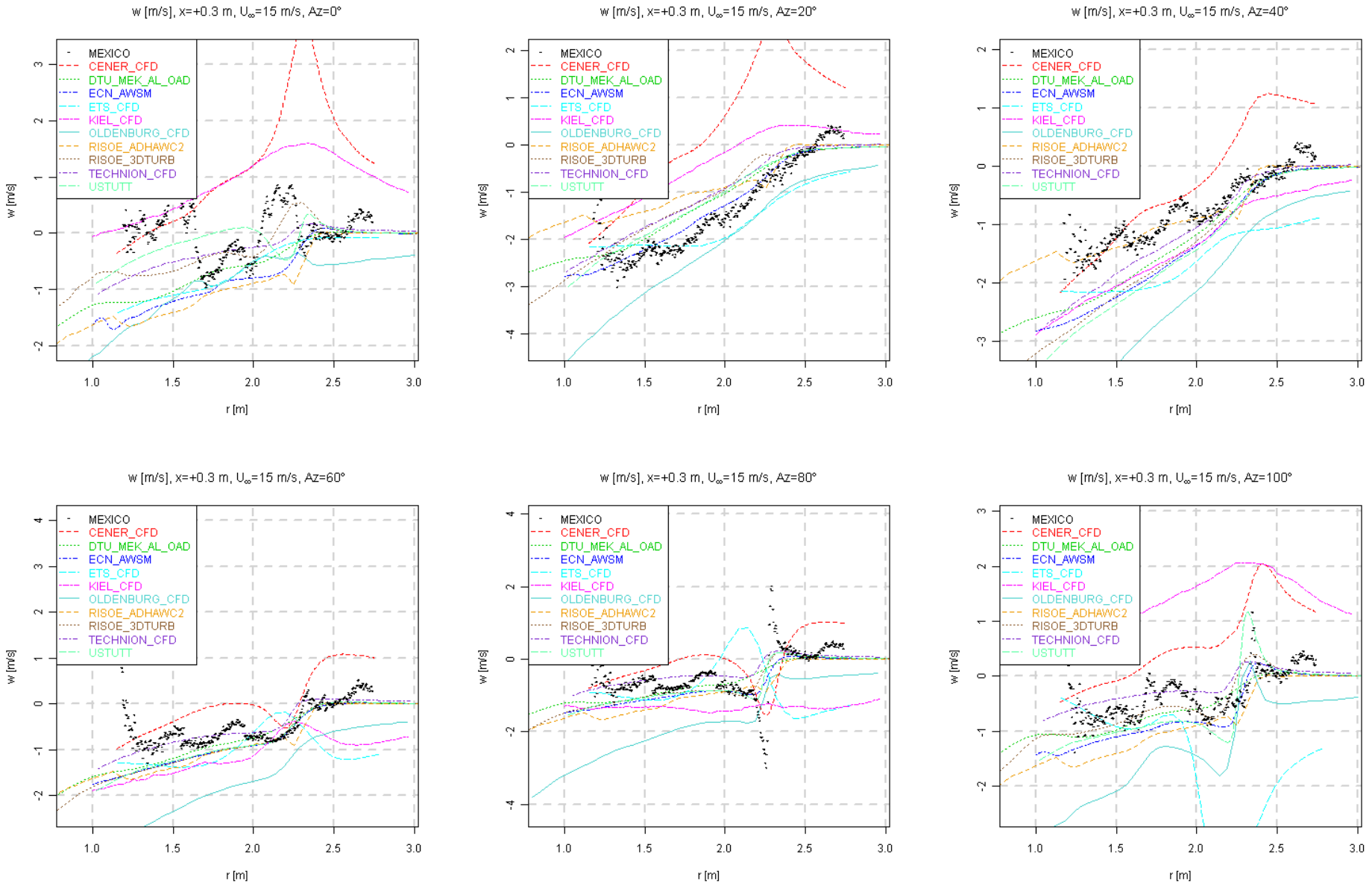

Figure 8.31 *Radial traverse (downwind) of tangential velocity, U_∞ =15 m/s*

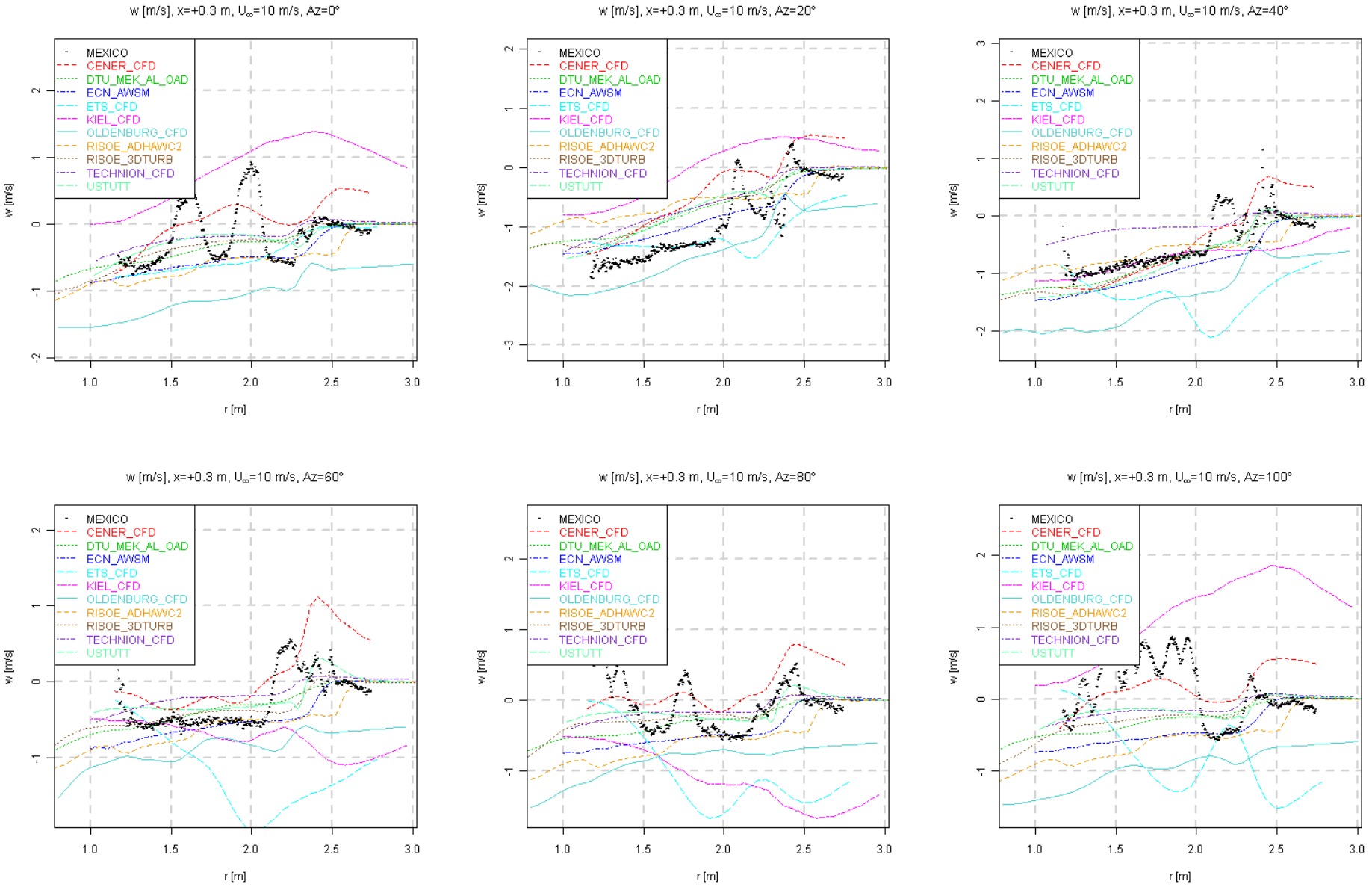

Figure 8.32 *Radial traverse (downwind) of tangential velocity, U_∞ =10 m/s*

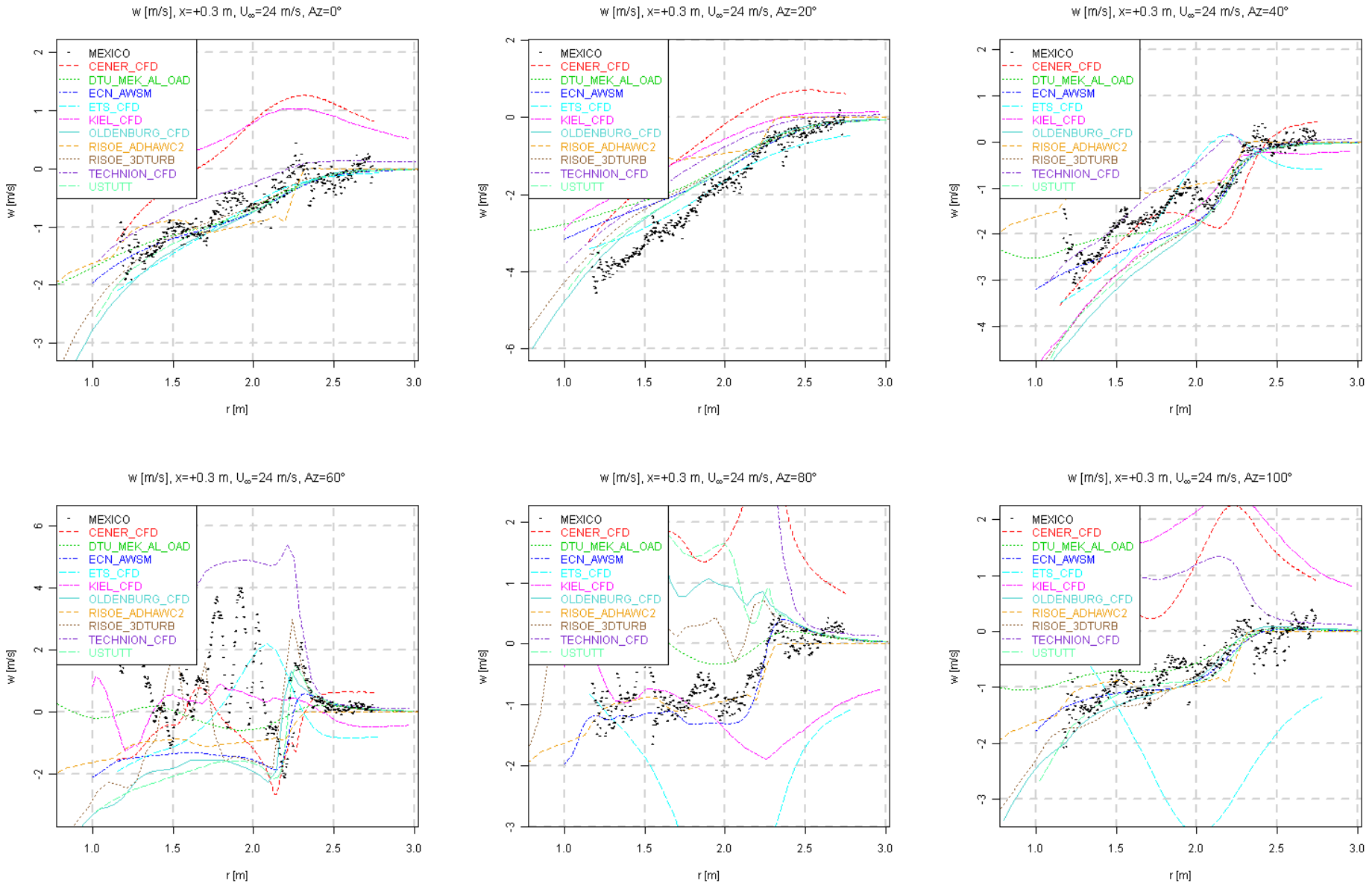

Figure 8.33 *Radial traverse (downwind) of tangential velocity, U_∞ =24 m/s*

8.3 Second round: Yawed flow

Two different cases are selected with a different yaw angle and freestream velocity (U_∞=15 m/s, Yaw=30 $^\circ$ and U_∞=24 m/s, Yaw=15 $^\circ$). A more detailed description of the conditions and the data format can be found in section A.2. It can be seen in Table B.1 that PIV measurements were not taken for case 2.2, which excludes a comparison of velocities with experimental data. The legend of each graph refers to the parties that have performed the calculations. The model description corresponding to the legends can be found in section C.

8.3.1 Loads

For the yawed cases, the loads are presented as a function of azimuth angle. The standard deviation between the processed data points (explained in section B) is displayed using a grey band. The grey band generally is small. At the 35% span station the deviation is often higher due to an intermittently malfunctioning pressure sensor, but the level remains acceptable.

Case 2.1

Both CENER and INTA make use of the FAST code but display different trends, especially for the inboard stations. This could be due to a difference in dynamic stall modelling. For the lifting line codes, the qualitative agreement is generally speaking better for the outboard compared to the inboard sections. This can be explained by the fact that the advancing and retreating blade effect is dominant there and easy to predict. For the inboard sections the aerodynamics becomes more complicated and the combination of a varying induction together with separated flow proves difficult to model. The inboard agreement for the CFD codes is better although it looks like the Delft University panel code result follows an opposite trend with azimuth angle. Similar to the axial flow results, there is an overprediction of sectional forces compared to the experiment, especially outboard.

The sudden dips in the tangential force that some lifting line codes display can be attributed to sudden changes in airfoil data with angle of attack. It is expected that dynamic stall effects prevent these dips to occur in the measurements. This can be one of the reasons why the CFD codes again outperform the lifting line codes.

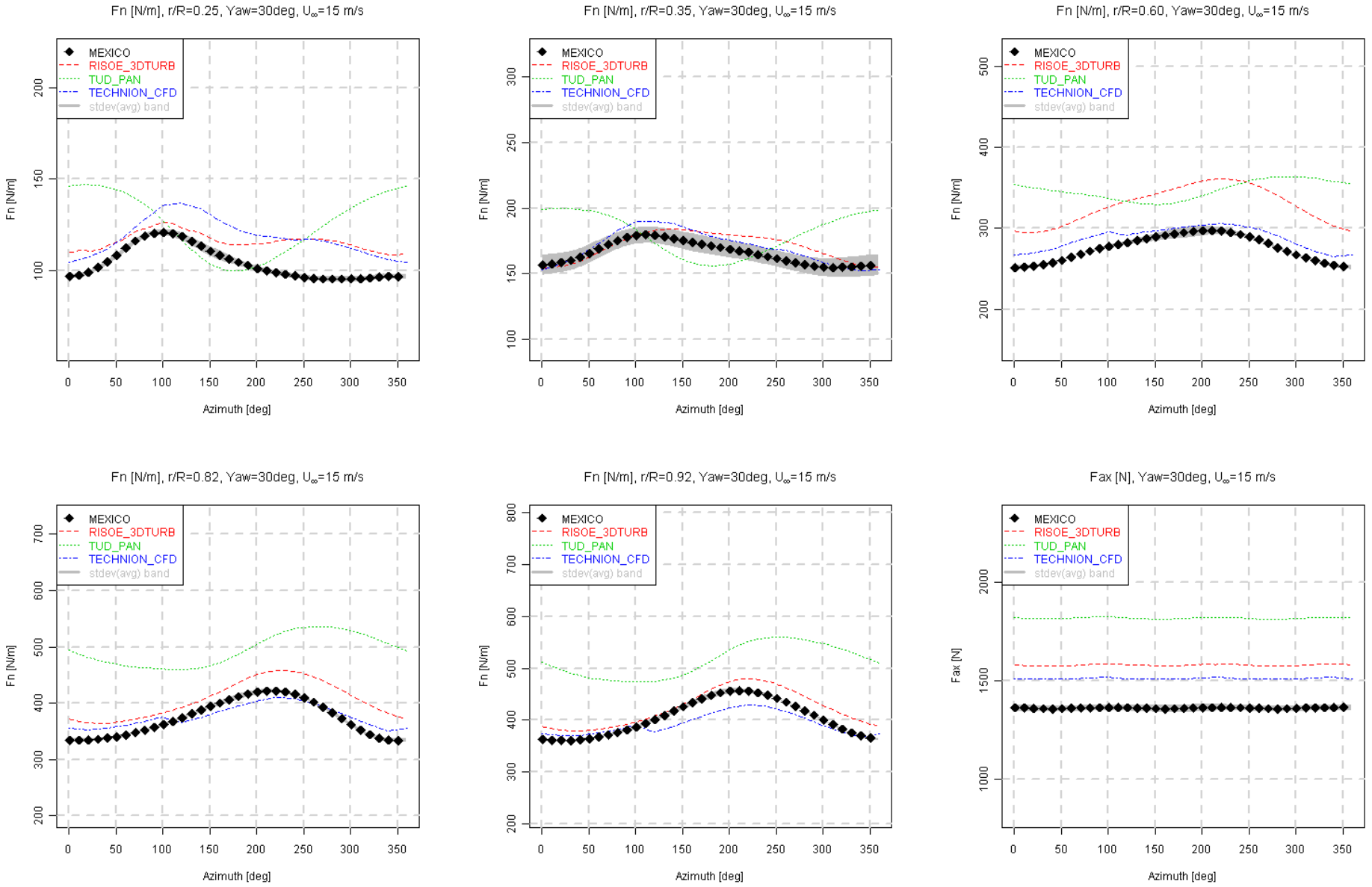

Figure 8.34 *Normal and axial force variation with azimuth angle (CFD), U_∞=15 m/s, Yaw=30°*

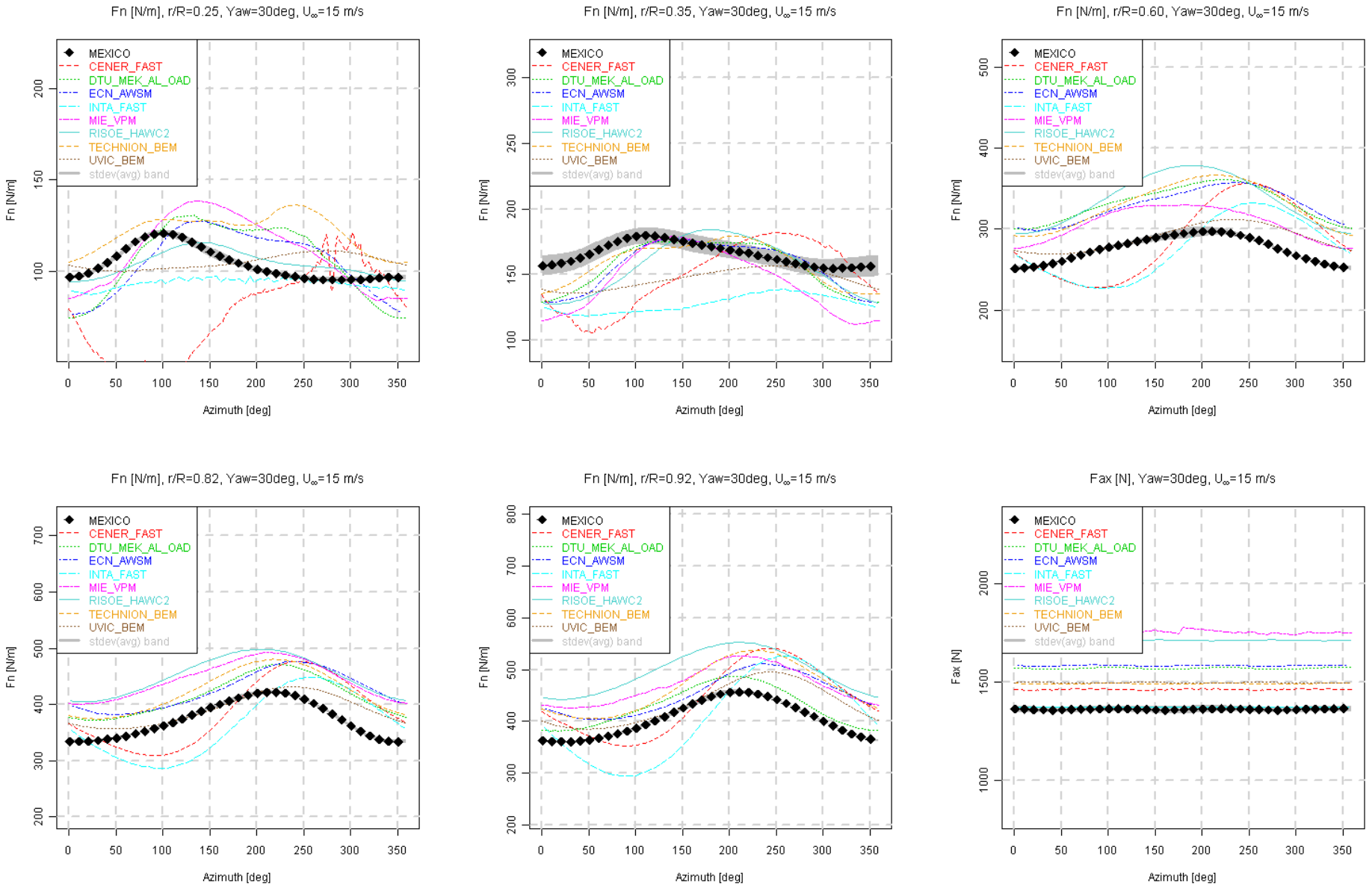

Figure 8.35 *Normal and axial force variation with azimuth angle (lifting line codes), U_∞=15 m/s, Yaw=30°*

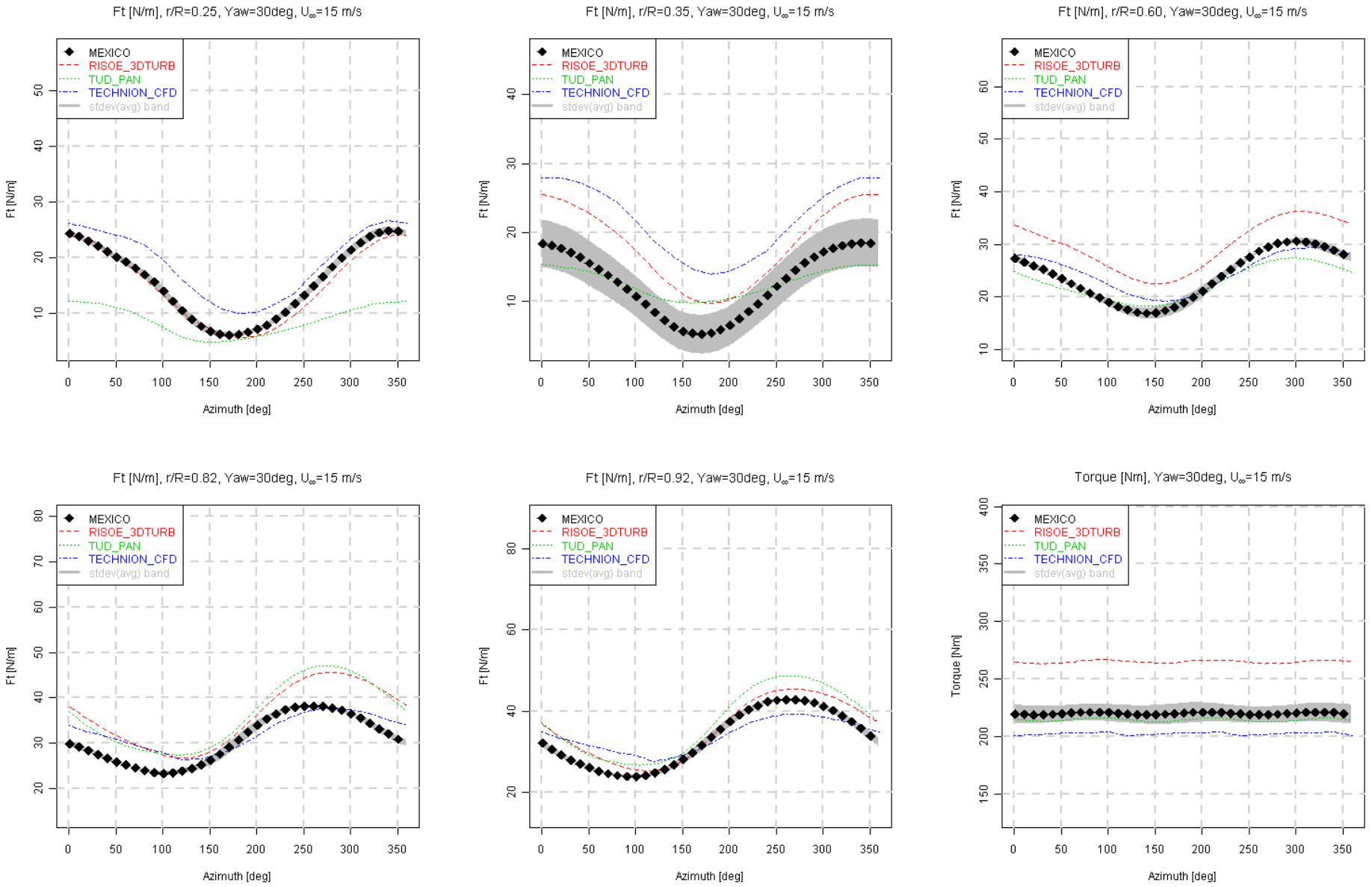

Figure 8.36 *Tangential force and torque variation with azimuth angle (CFD), U_∞=15 m/s, Yaw=30°*

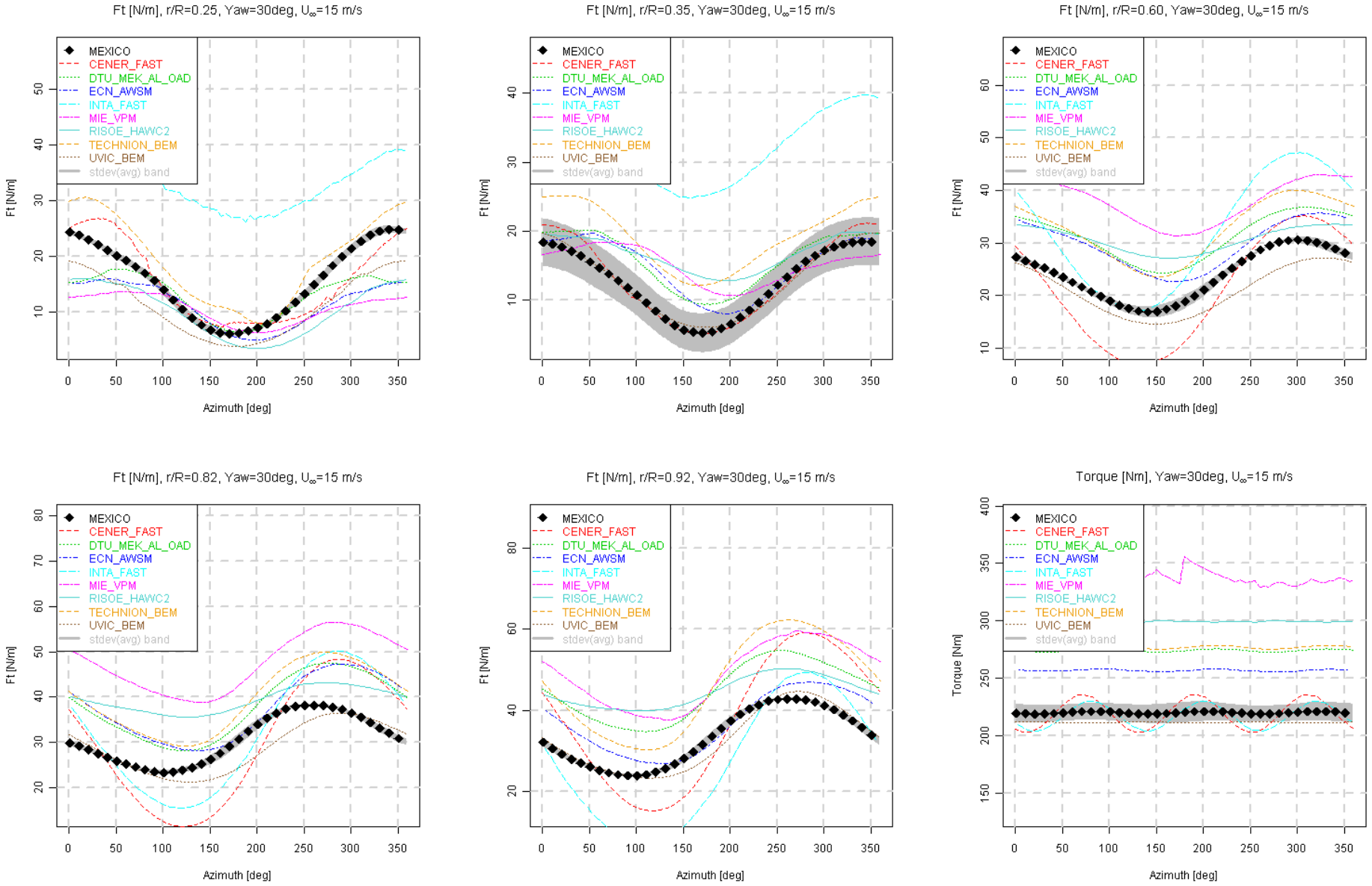

Figure 8.37 *Tangential force and torque variation with azimuth angle (lifting line codes), U_∞=15 m/s, Yaw=30°*

Case 2.2

Since there was only one datapoint featuring the configuration of Case 2.2, a grey standard deviation band is not present in the graphs. Although the yaw angle for this case (15 °) is smaller compared to Case 2.1 (30 °), the measured and calculated variation of normal force with azimuth angle is larger for the outboard sections. This can be explained by the different phase of angle of attack versus effective velocity variation with azimuth (see also the graphs in section 8.3.2) between the two cases. Although the angle of attack lies in the linear part of the Cl-α curve for Case 2.1 (as opposed to Case 2.2), the variation with azimuth angle is out of phase with the effective velocity variation. For Case 2.2 the ΔCl due to the angle of attack variation is less but the effective velocity variation is not out of phase with the angle of attack. Hence the normal force variation (dictated by angle of attack and effective velocity changes) for 15 ° yaw exceeds the value for 30 ° yaw.

As for case 2.1, the qualitative agreement between experiment and lifting line calculations is better for the outboard sections. The good agreement of the axial force for the lifting line codes is a result of the underprediction inboard and overprediction outboard. The Delft University panel code clearly struggles with predicting forces in separated flow conditions. However the agreement of the normal force prediction by the turbulent ELLIPSYS-3D compared to the measurements is satisfactory.

The tangential force variation prediction is worse, especially inboard. This also holds for the lifting line codes. The measured dip between 250 ° and 300 ° azimuth angle at 82% span is not predicted by CFD nor lifting line codes. The relative good agreement of the torque is more a result of coincidence rather than good modelling.

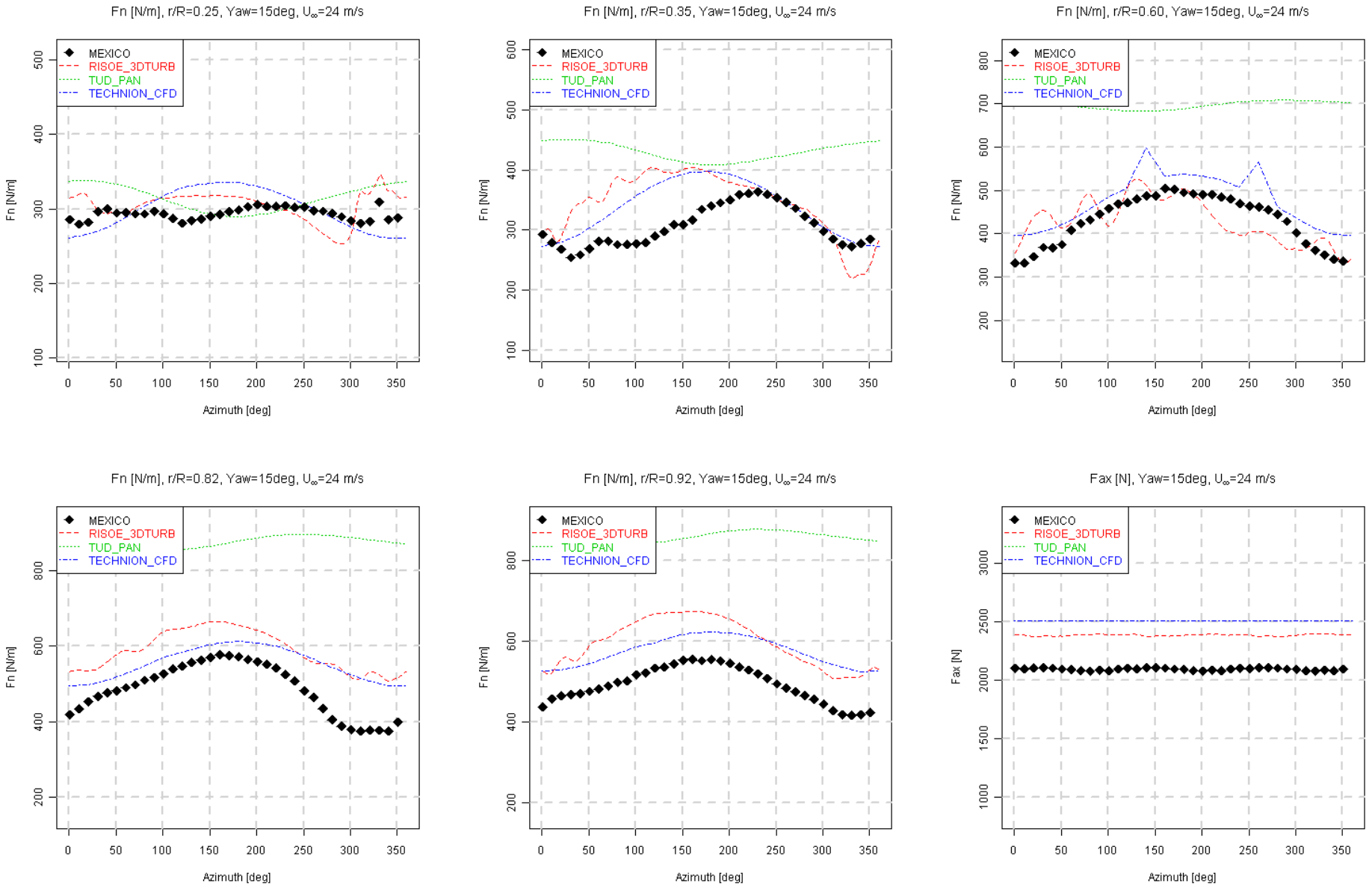

Figure 8.38 *Normal and axial force variation with azimuth angle (CFD), U_∞=24 m/s, Yaw=15°*

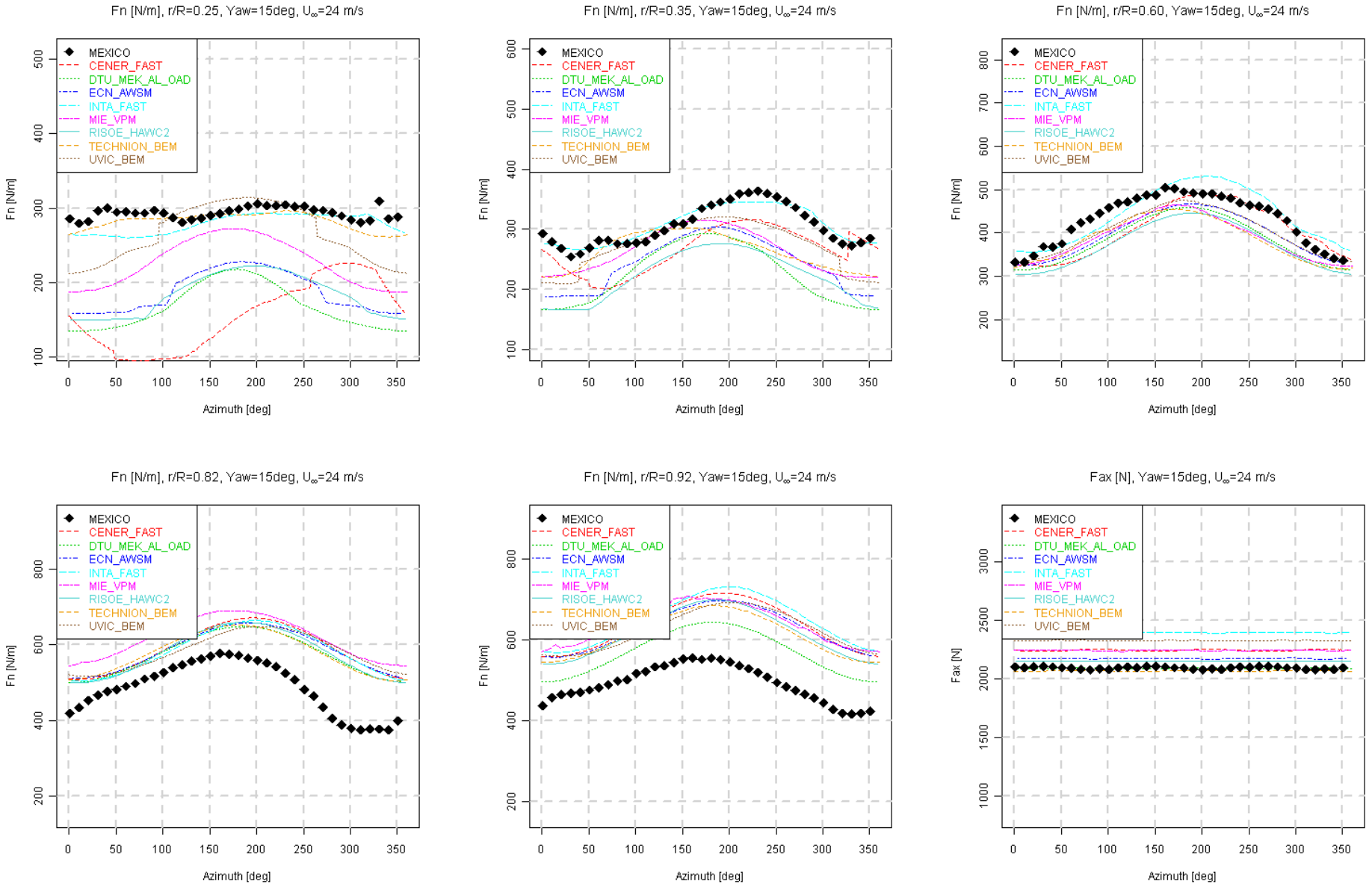

Figure 8.39 *Normal and axial force variation with azimuth angle (lifting line codes), U_∞=24 m/s, Yaw=15°*

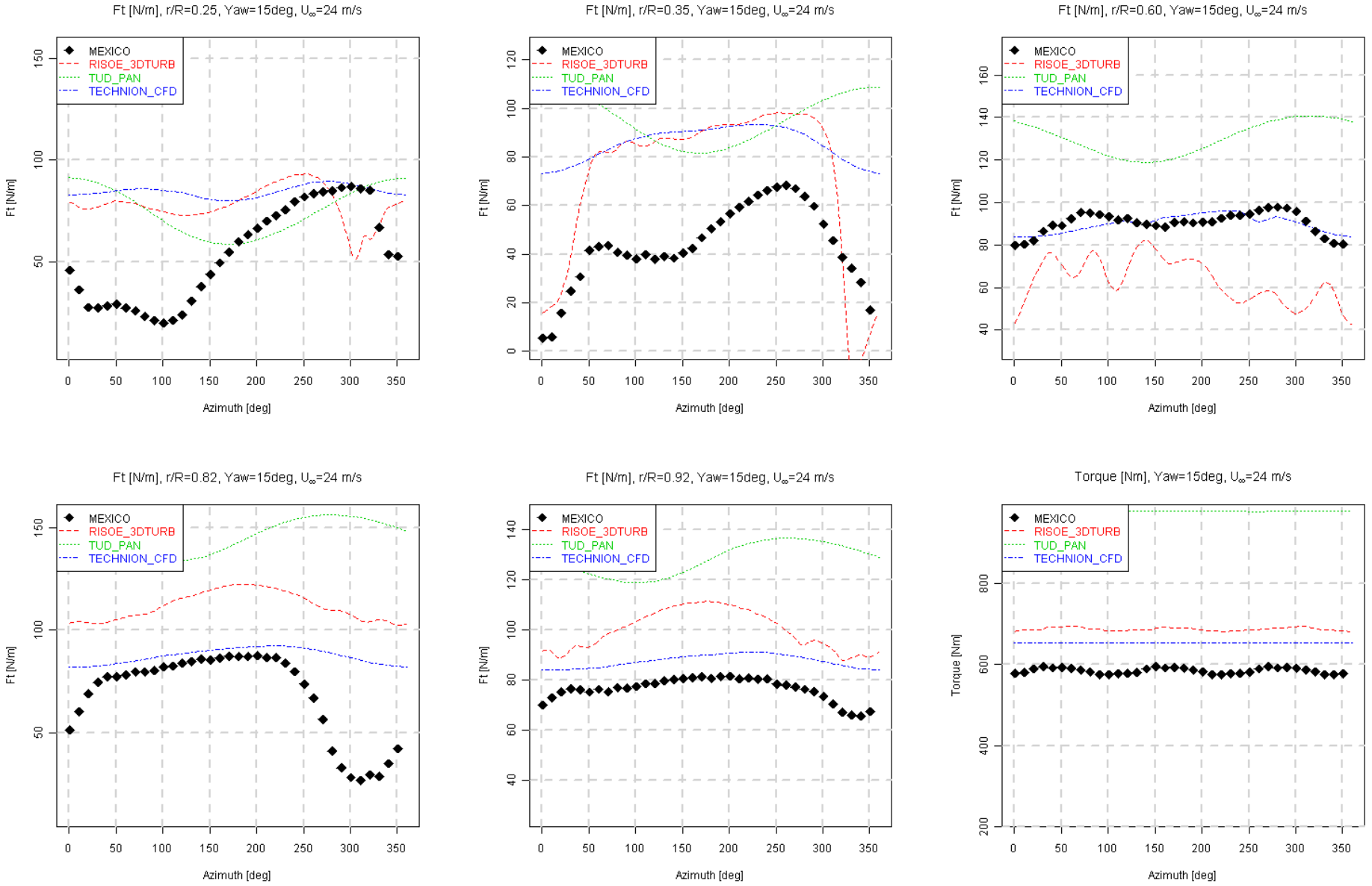

Figure 8.40 *Tangential force and torque variation with azimuth angle (CFD), U_∞=24 m/s, Yaw=15°*

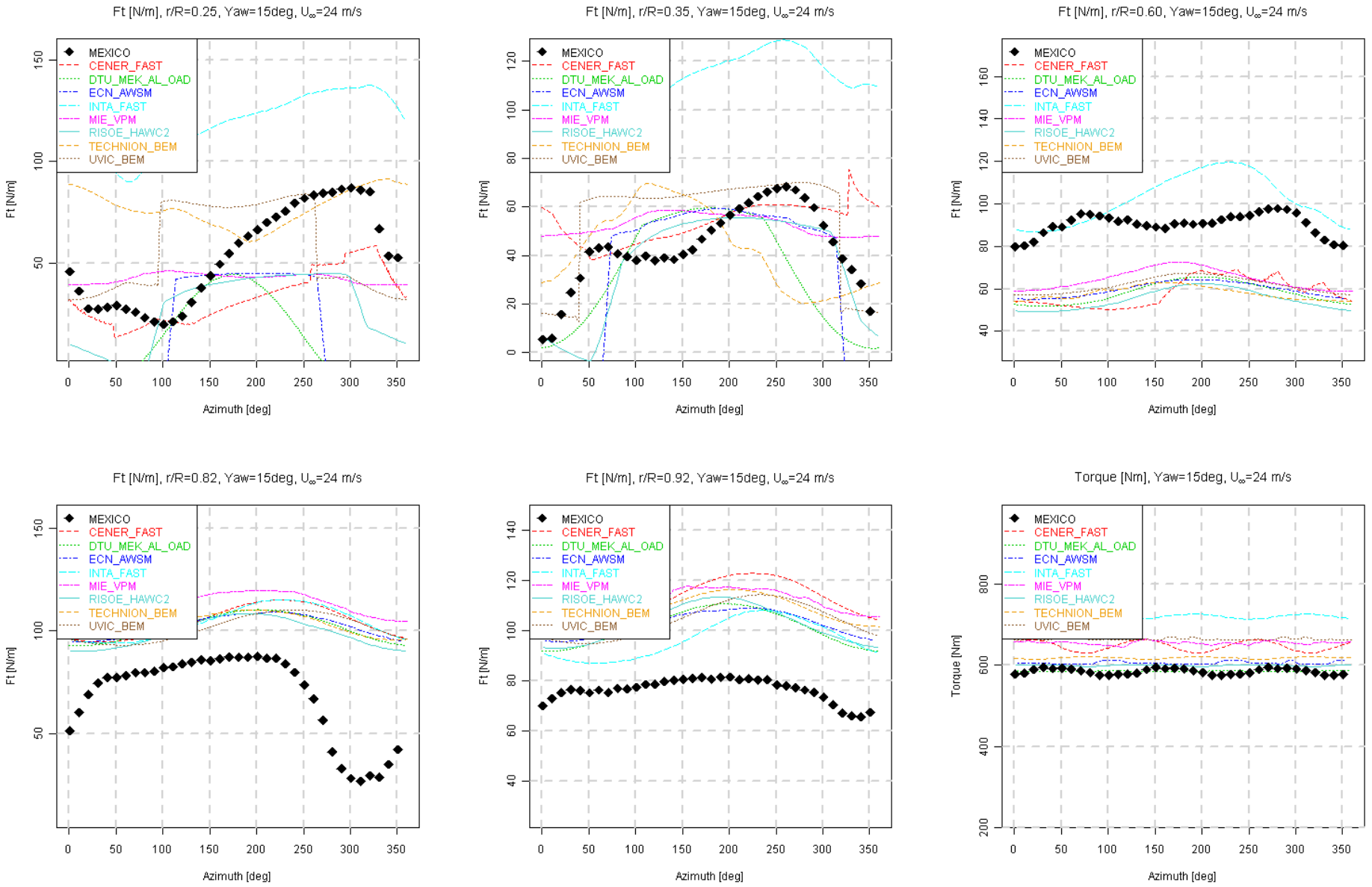

Figure 8.41 *Tangential force and torque variation with azimuth angle (lifting line codes), U_∞=24 m/s, Yaw=15°*

8.3.2 Lifting line variables

The lifting variables consist of angle of attack, effective velocity, normal and tangential force coefficient (Cn and Ct) and axial and tangential induced velocity (Ui and Vi). These variables are not measured experimentally and hence a comparison can only be made between calculated values from the participating lifting line codes.

Case 2.1

The trends on angle of attack variation are generally in agreement. The amplitude of variation with azimuth angle varies between the results, especially outboard. The effective velocity results should be in excellent agreement since they are dictated by the rotational speed, wind speed and yaw angle setting. However both the results from MIE University and University of Victoria show a lower effective velocity from the main trend, indicating either a processing error (wrong radius?) or faulty operational conditions.

Like the angle of attack, the trend of the normal and tangential force coefficients are in reasonable agreement. The TECHNION results show sudden dips at the most inboard station (25% span), probably due to the absence of a dynamic stall model.

The axial induction shows large discrepancy between the codes in Figure 8.46. The predicted trend of the University of Victoria is almost 180° out of phase with the other results. This is in contradiction with the angle of attack variation in Figure 8.42, which is more in phase with the other results. It is suspected that some participants have supplied the local induction whilst others have taken into account tip and root effects in the induction. The tangential induction shows large variations between all results, which is expected to be caused by a mixture of modelling differences and processing errors.

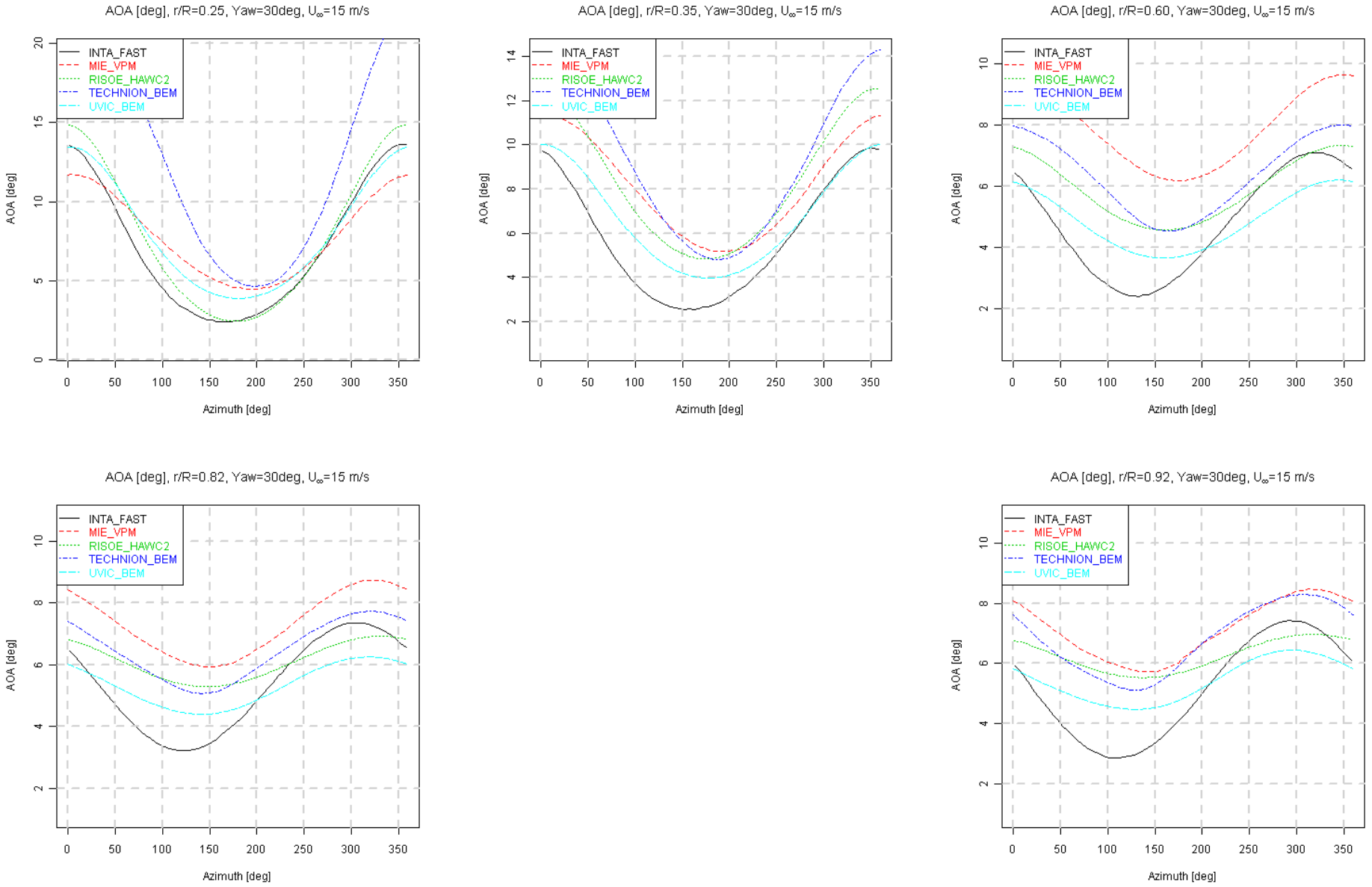

Figure 8.42 *Angle of attack variation with azimuth angle, U_∞=15 m/s, Yaw=30°*

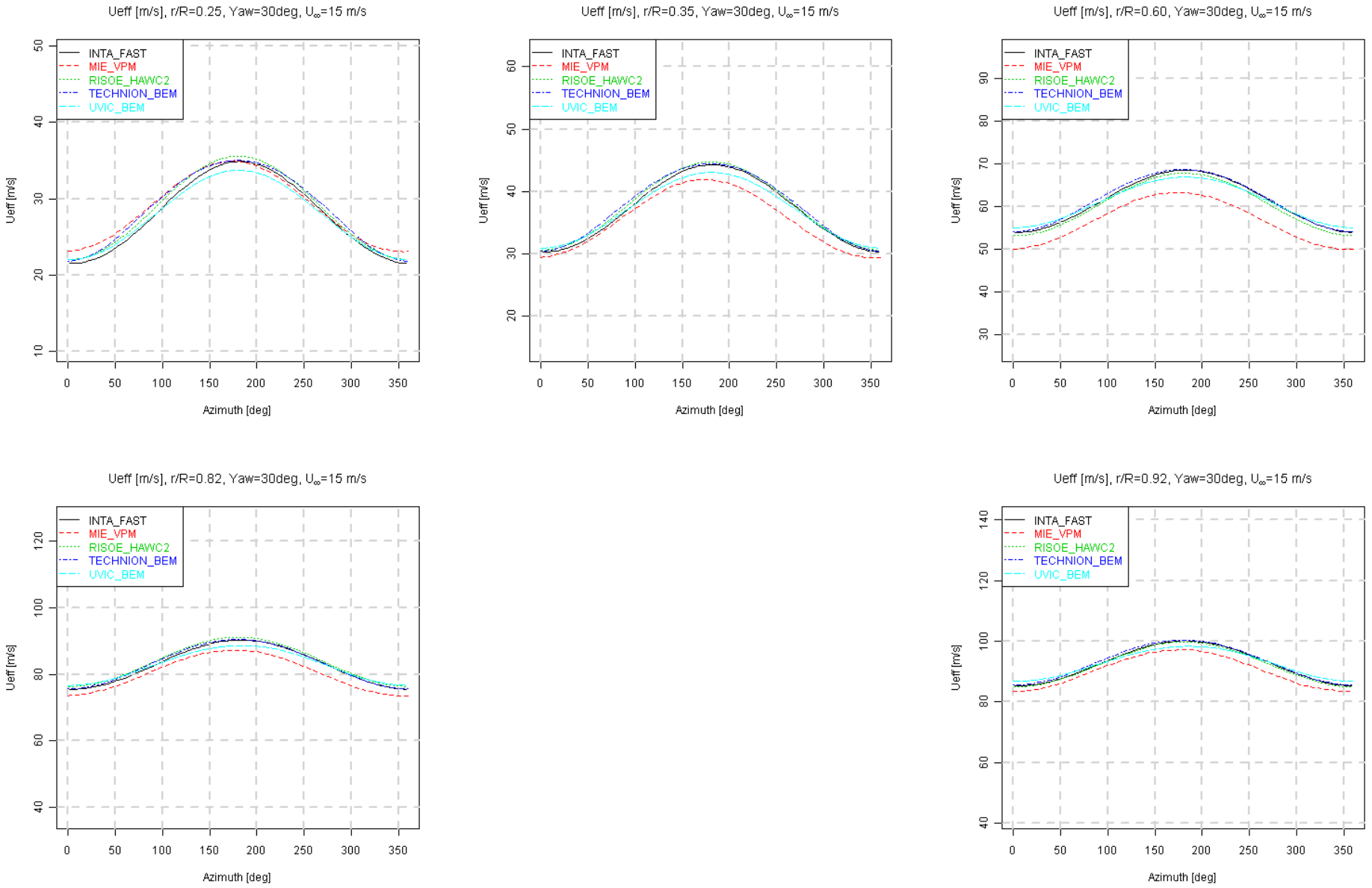

Figure 8.43 *Effective velocity variation with azimuth angle, U_∞=15 m/s, Yaw=30°*

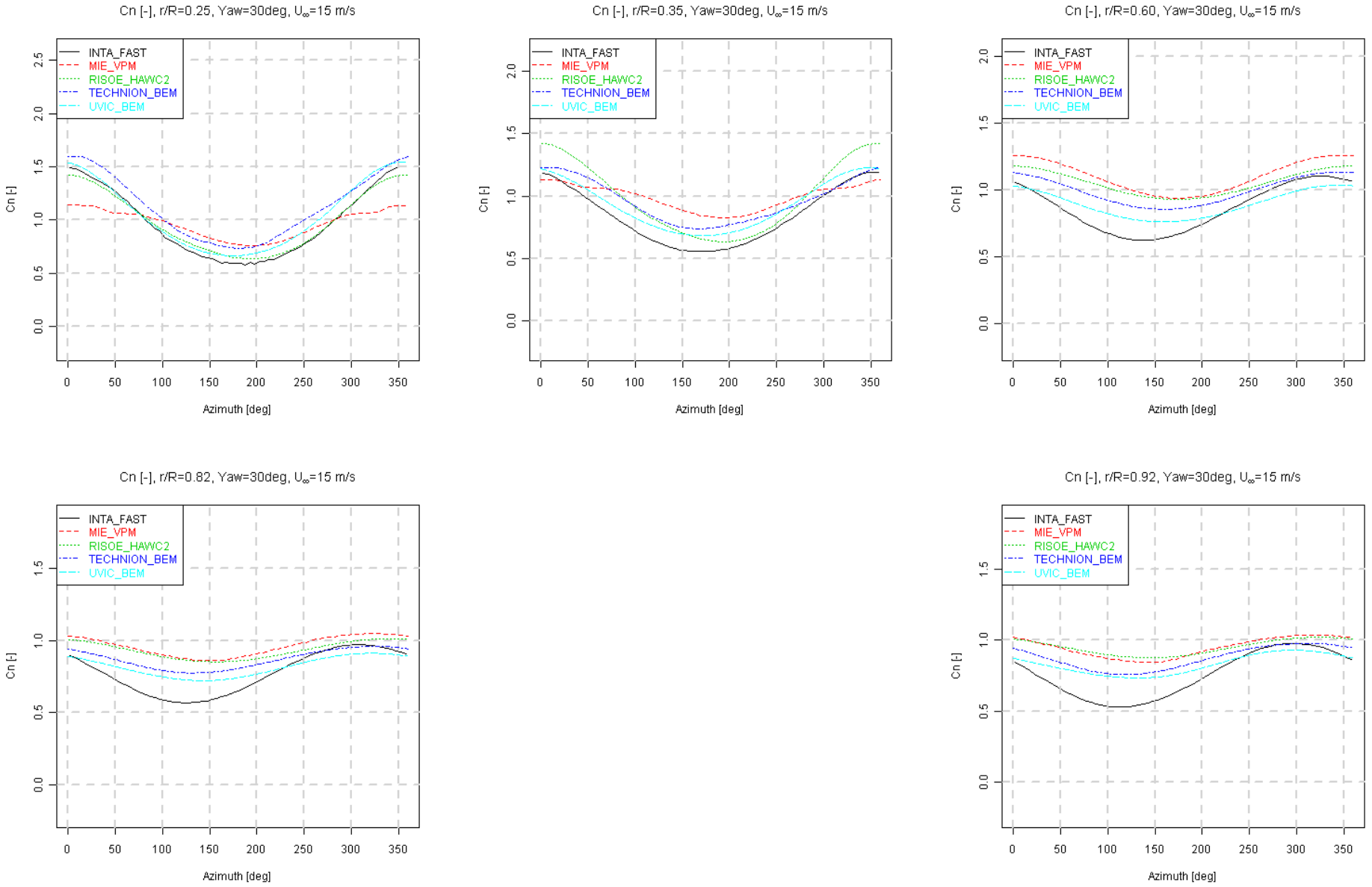

Figure 8.44 *Normal force coefficient variation with azimuth angle, U_∞=15 m/s, Yaw=30°*

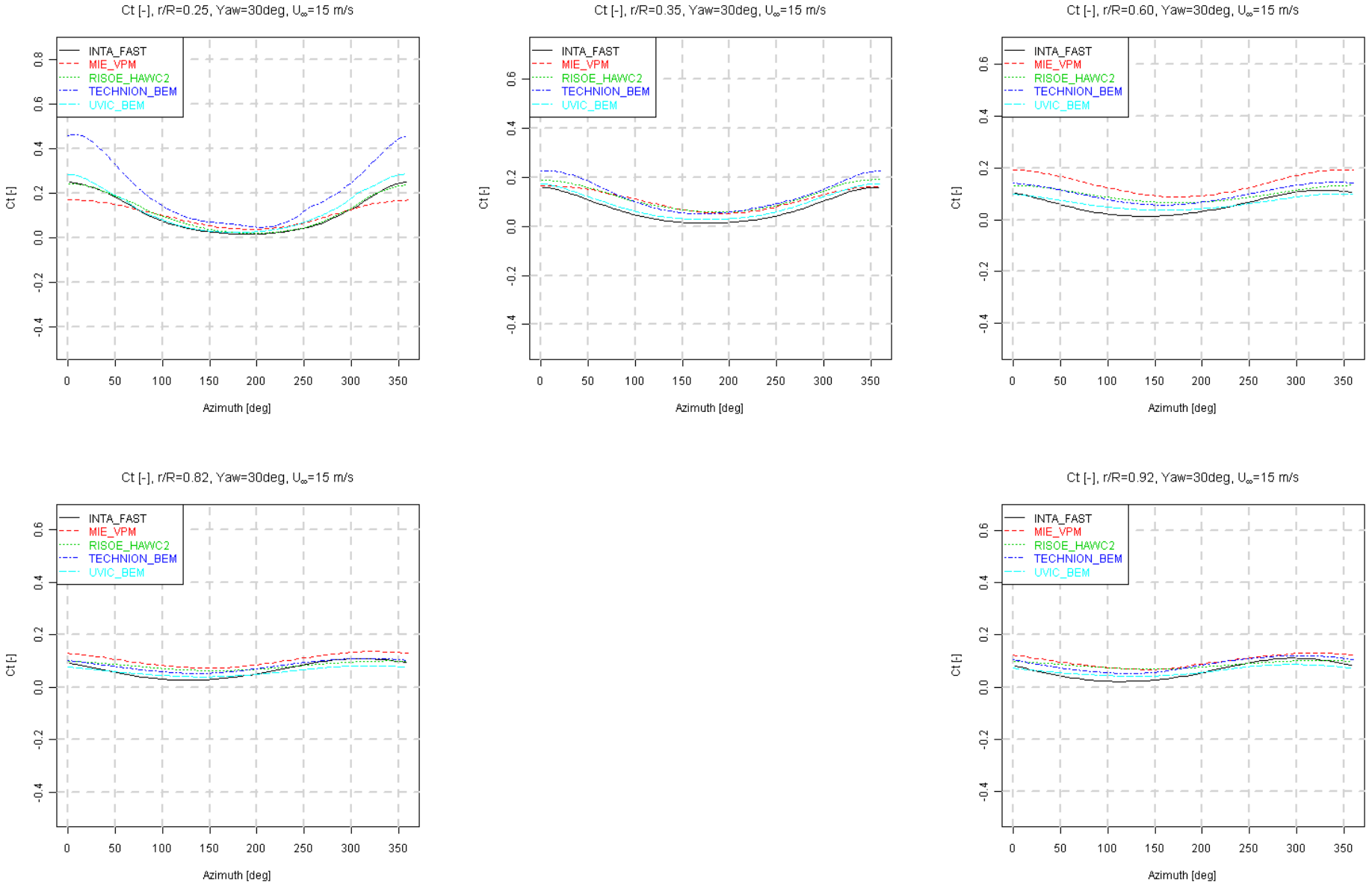

Figure 8.45 *Tangential force coefficient variation with azimuth angle, U_∞=15 m/s, Yaw=30°*

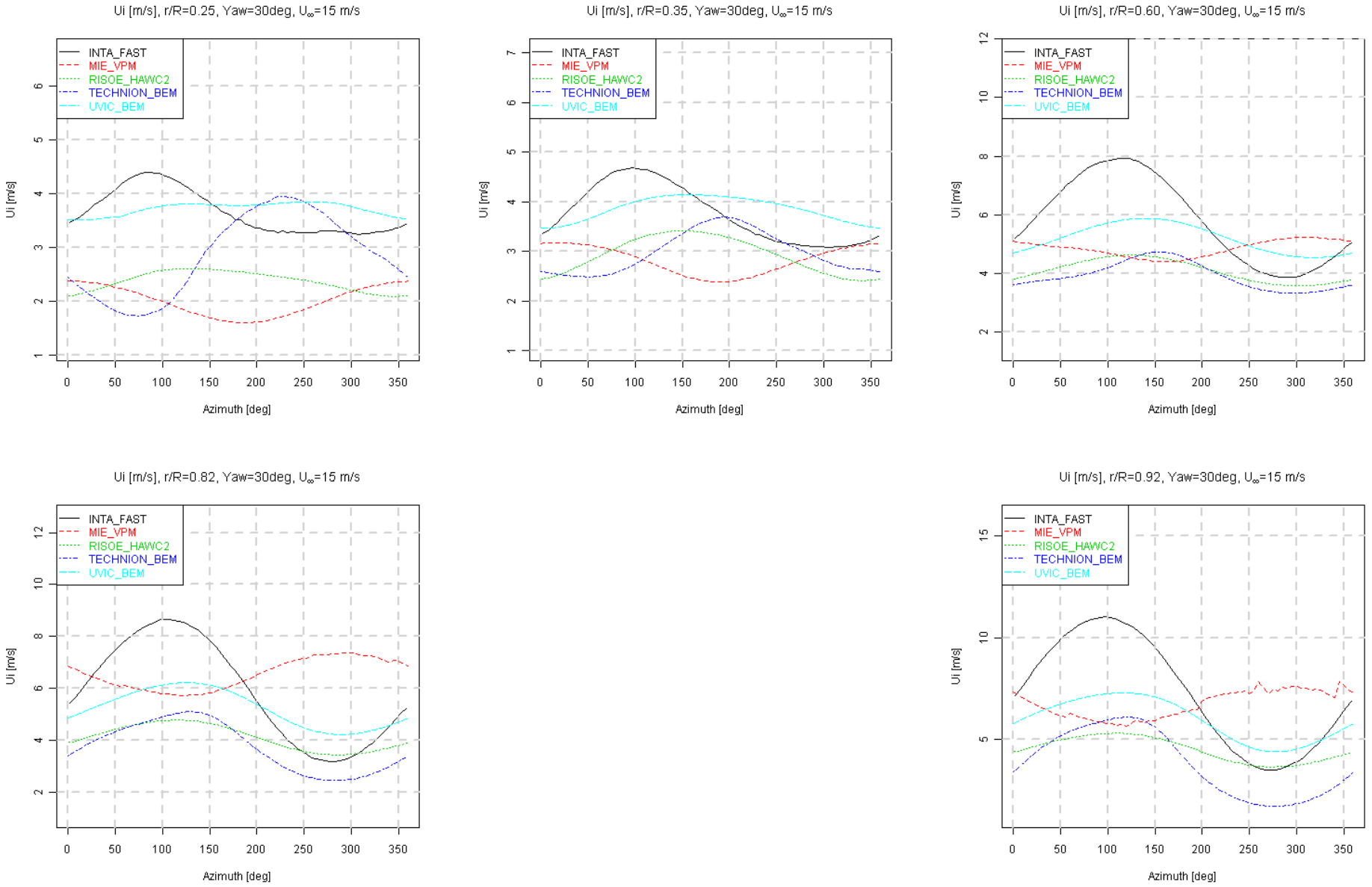

Figure 8.46 *Axial induced velocity variation with azimuth angle, U_∞=15 m/s, Yaw=30°*

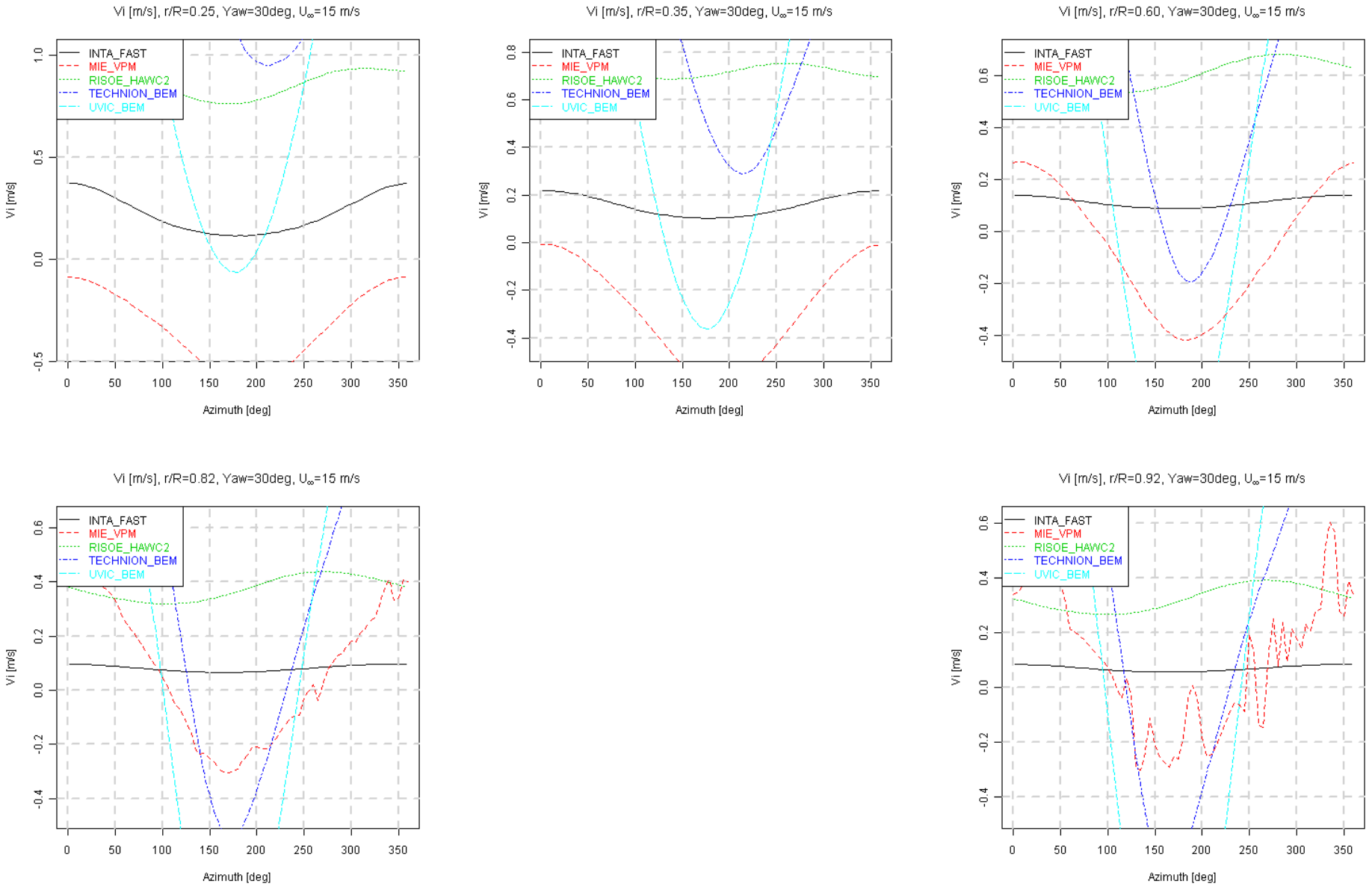

Figure 8.47 *Tangential induced velocity variation with azimuth angle, U_∞=15 m/s, Yaw=30°*

Case 2.2

Similar as for Case 2.1, the trends on angle of attack variation are generally in agreement. Again the MIE University results for the effective velocity are off from the other participants. Multiple codes feature dips in the normal and tangential force coefficient, now not only at the most inboard station, due to the higher angle of attack (U_∞=24 m/s) for this case.

The axial induction prediction of the University of Victoria is again approximately 180 $^\circ$ out of phase with most of the other results, whilst the trend was in good agreement for the angle of attack. The results for the tangential induction are not in agreement with each other (large extreme values and fluctuations), which is expected to be caused by a mixture of modelling differences and processing errors.

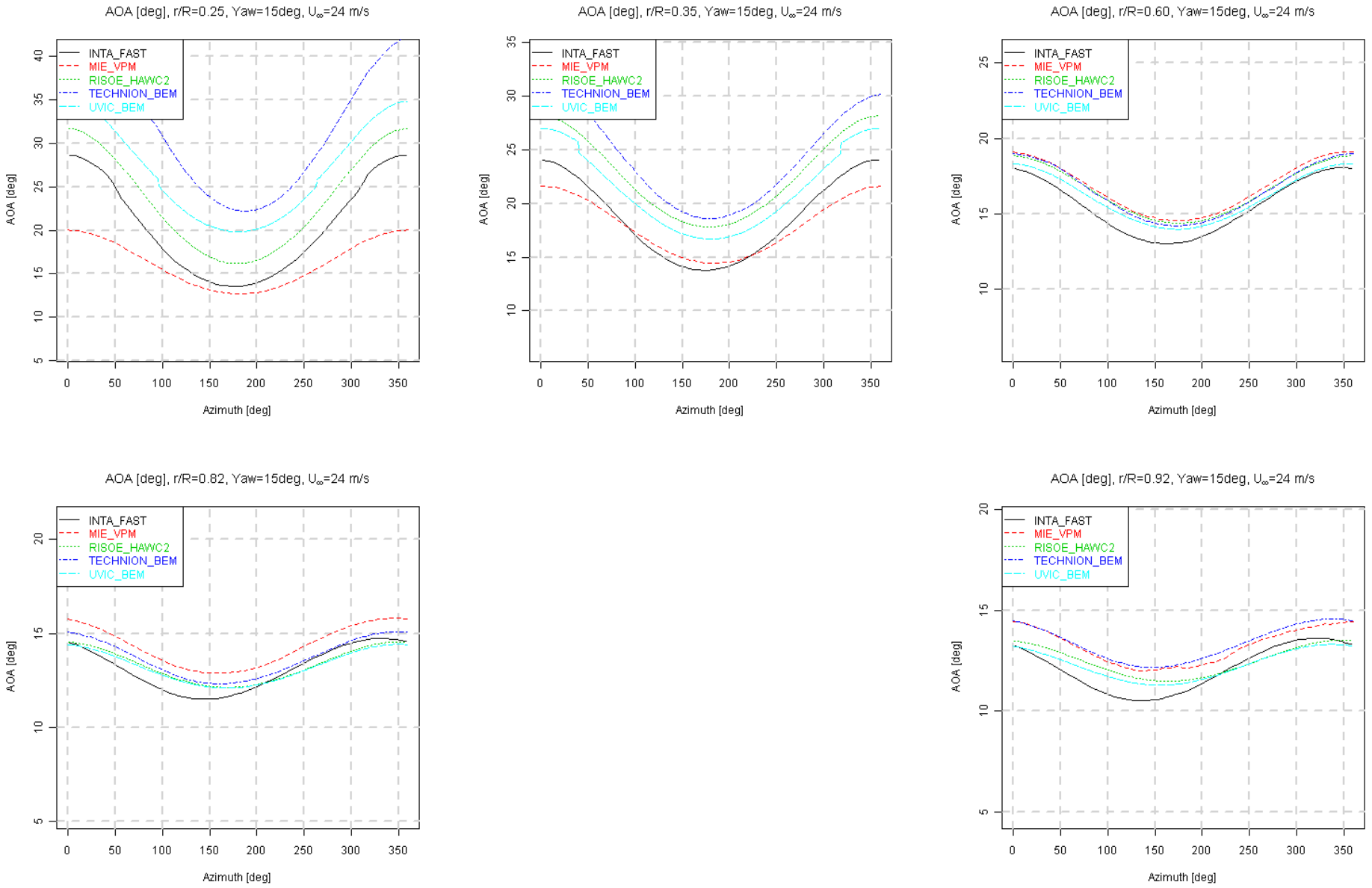

Figure 8.48 *Angle of attack variation with azimuth angle, U_∞=24 m/s, Yaw=15°*

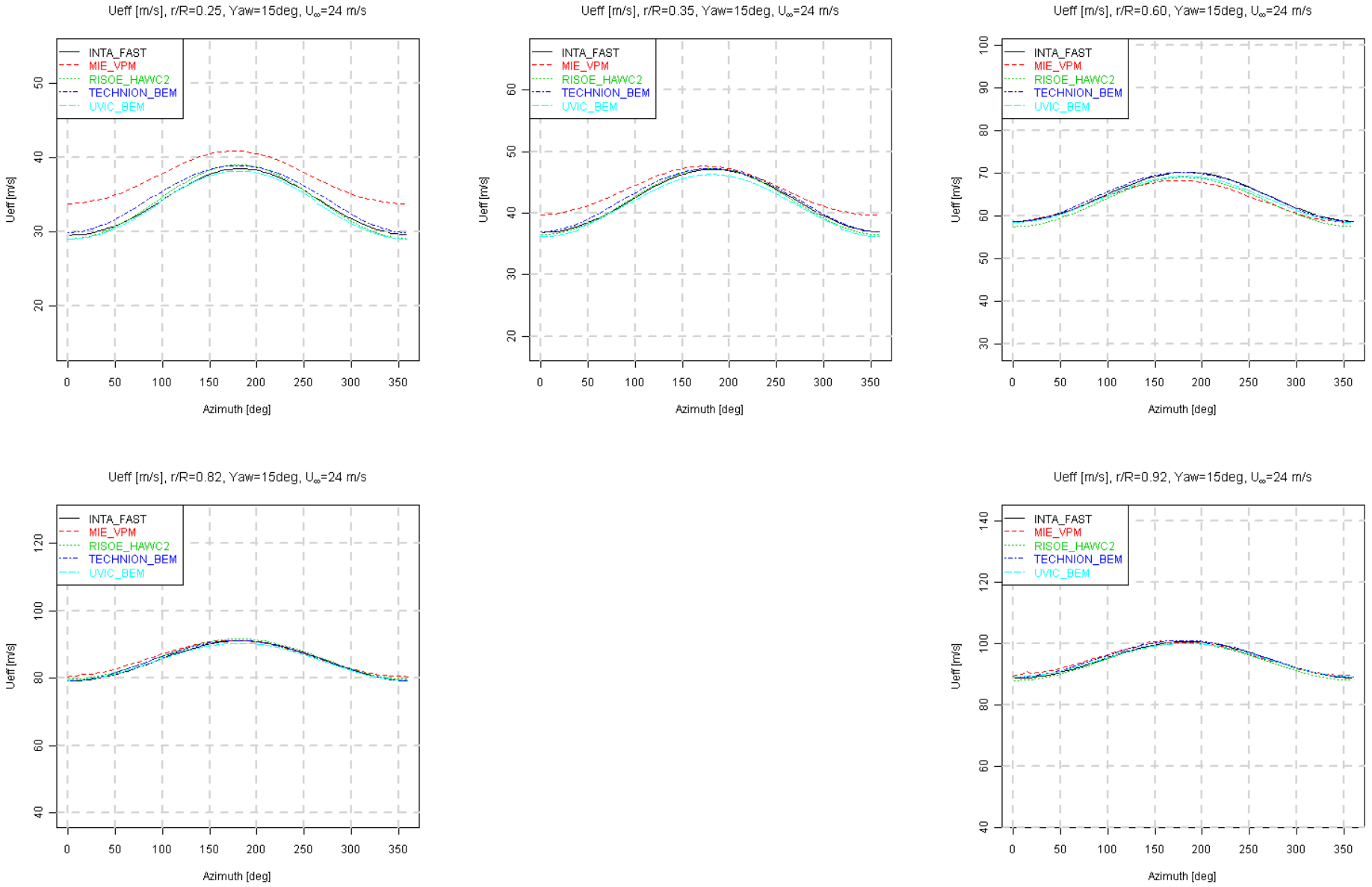

Figure 8.49 *Effective velocity variation with azimuth angle, U_∞=24 m/s, Yaw=15°*

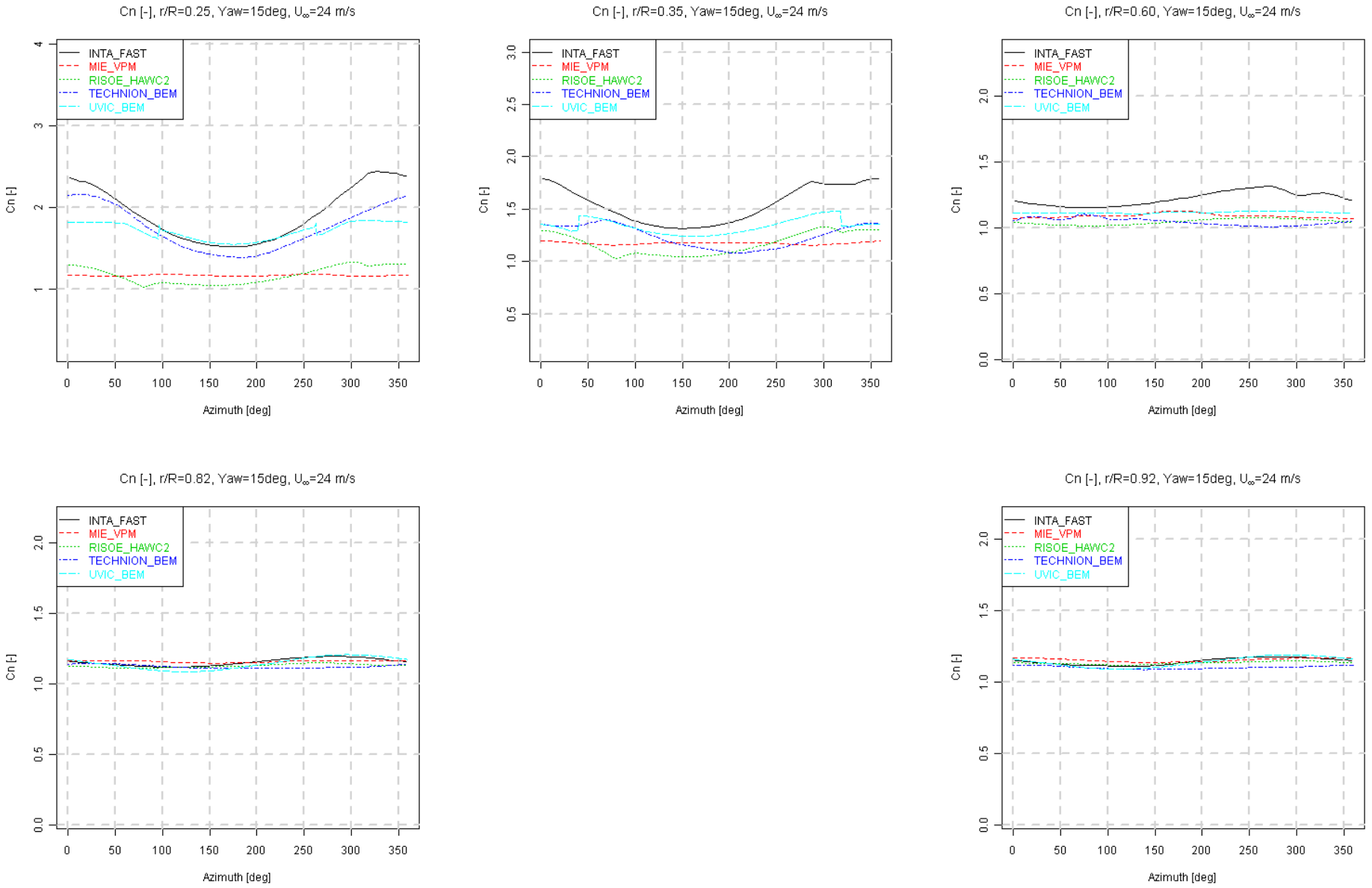

Figure 8.50 *Normal force coefficient variation with azimuth angle, U_∞=24 m/s, Yaw=15°*

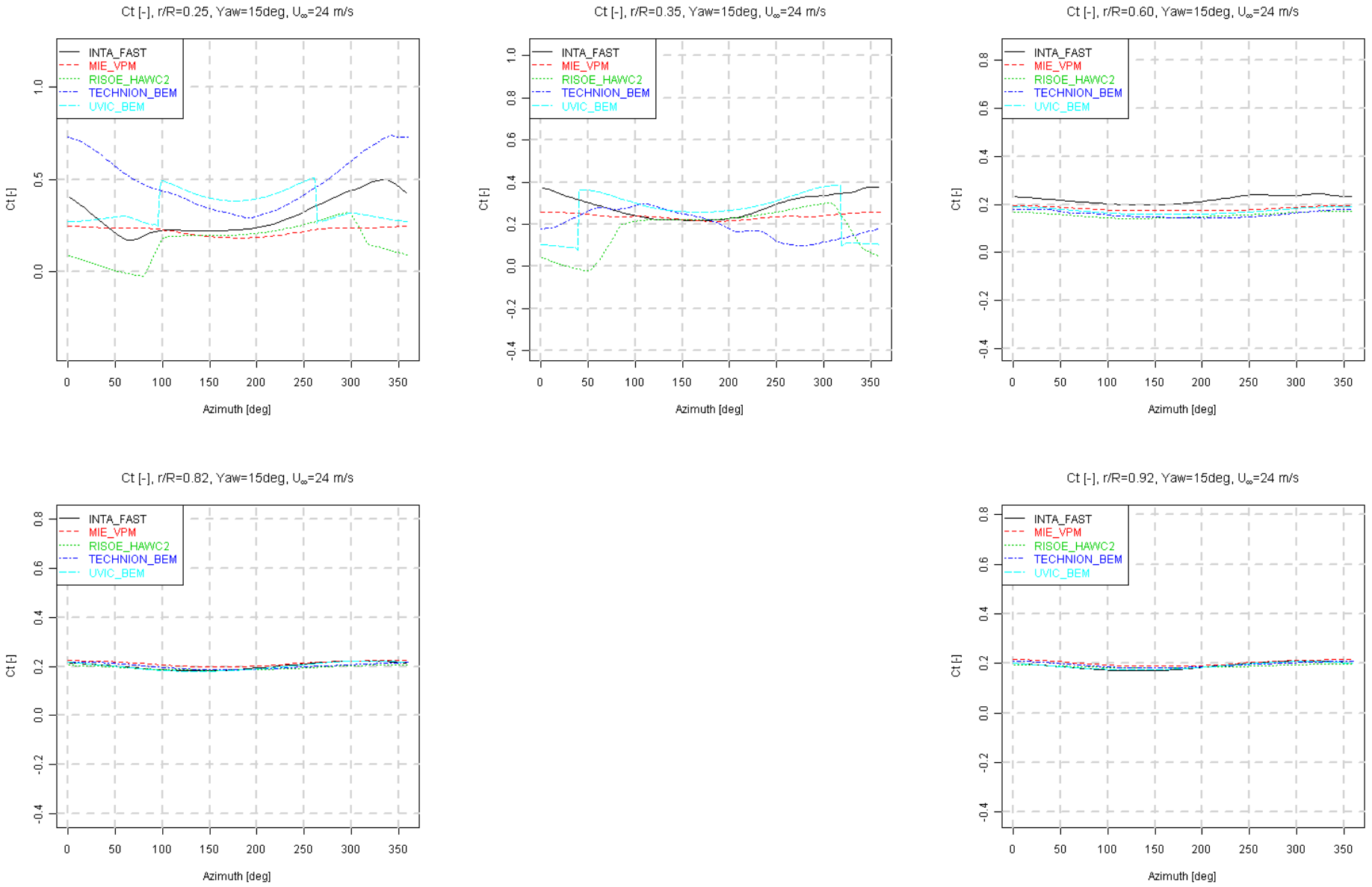

Figure 8.51 *Tangential force coefficient variation with azimuth angle, U_∞=24 m/s, Yaw=15°*

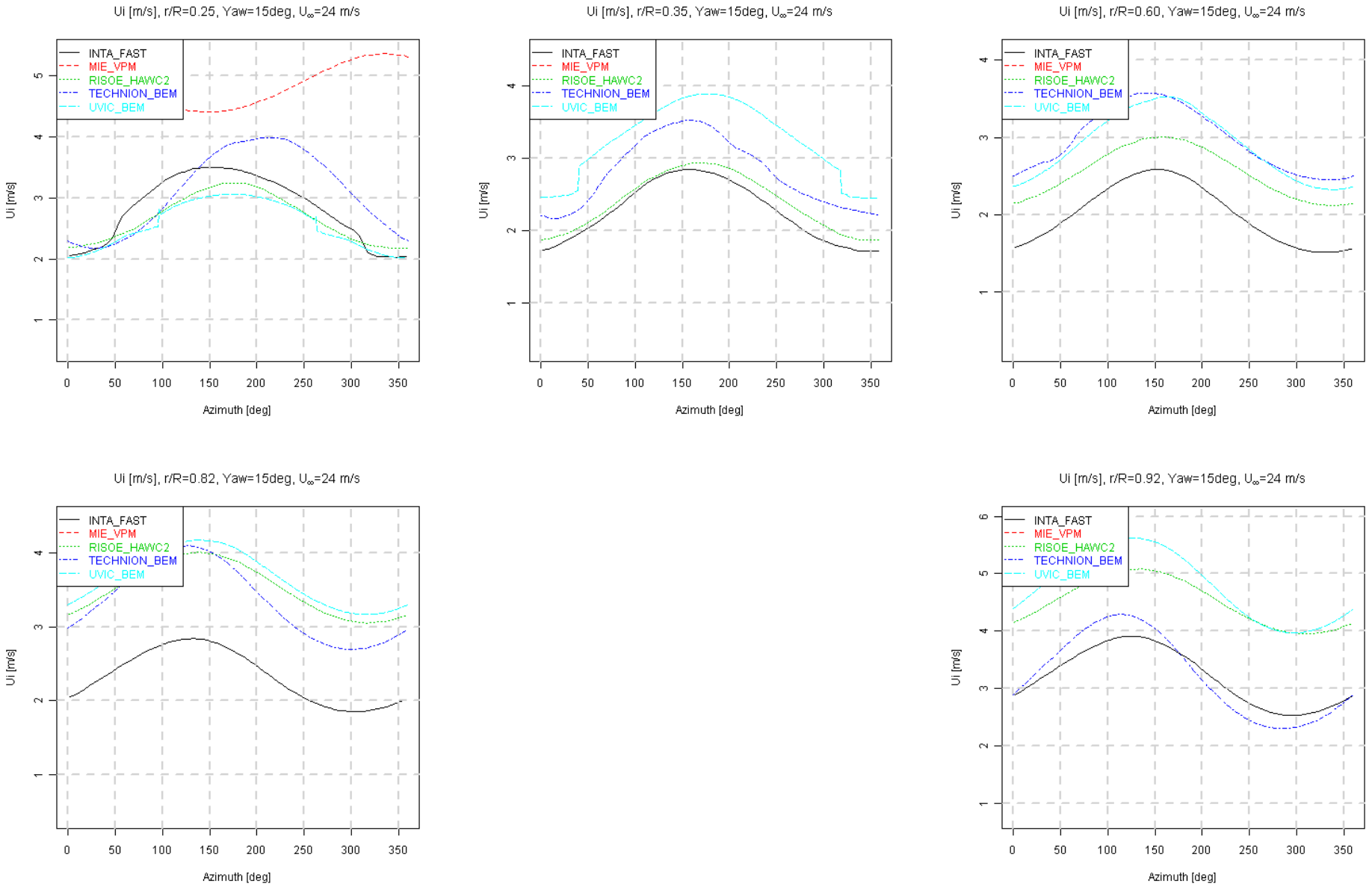

Figure 8.52 *Axial induced velocity variation with azimuth angle, U_∞=24 m/s, Yaw=15°*

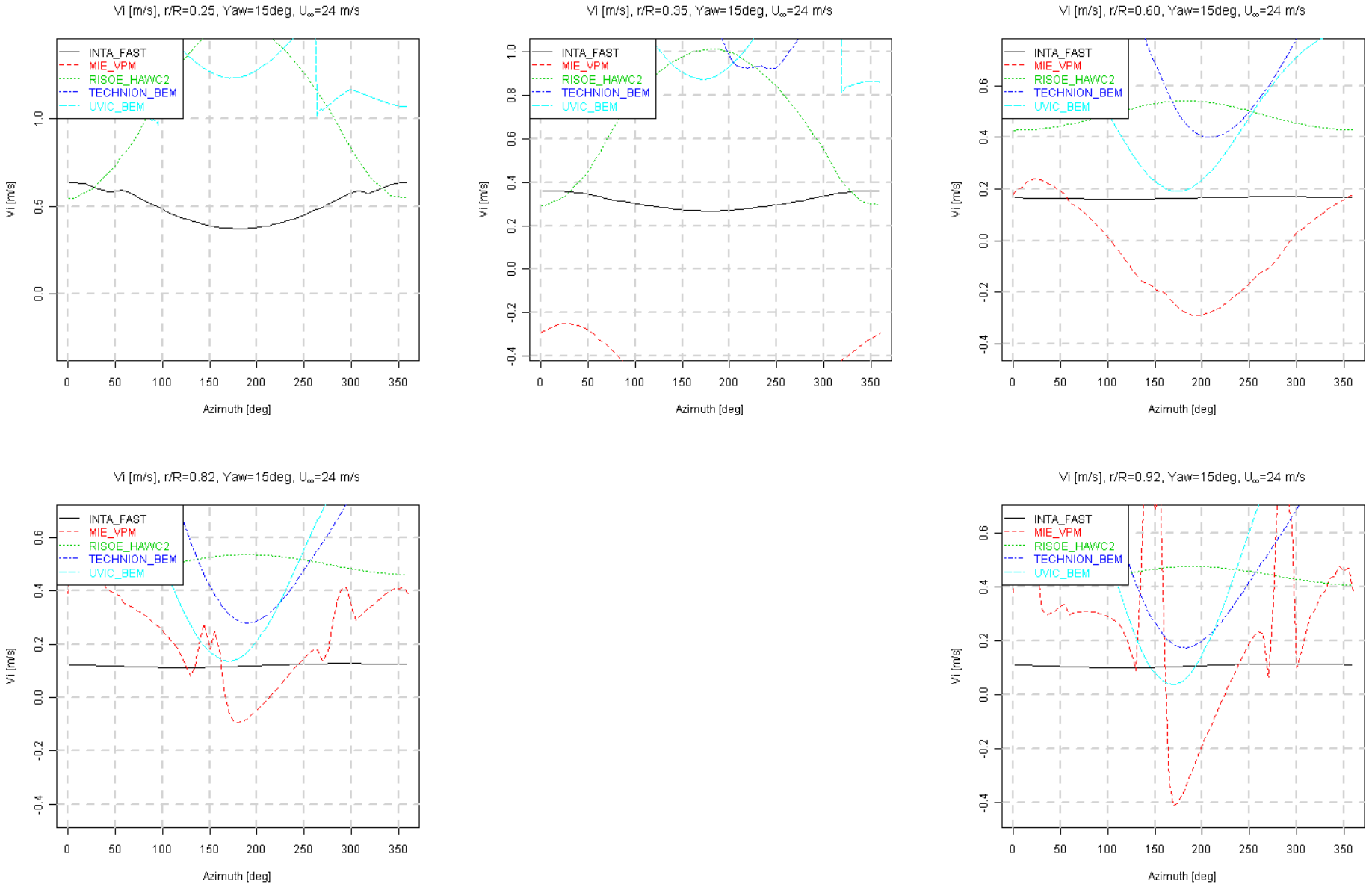

Figure 8.53 *Tangential induced velocity variation with azimuth angle, U_∞=24 m/s, Yaw=15°*

8.3.3 Axial velocity traverse

The axial traverses are performed at a midboard span (y=1.4 m, tunnel coordinate system) and an outboard span (y=1.8 m) location for an azimuth angle of 0 °. Since the measurements have been performed for a yaw angle of +30 ° and -30 °, the results for negative yaw angle are mirrored and interpreted as y=-1.4 m and y=-1.8 m with a corresponding azimuth angle of 60 °. The title of the graphs in Figure 8.54 to 8.59 indicates the operational conditions. Please note that as indicated in section A.2, the velocities are expressed in the tunnel coordinate system.

Case 2.1

At y=-1.4 m, the u-component results of RISØ and DTU are in good agreement with the measurements, except from the near wake (x≈1 m). For axial flow conditions (Figure 8.12 and 8.25) also deviations were measured in this region, which are attributed to the profile transition close to this radial location.

The TECHNION results include the nacelle, which is visible at y=1.4 m between x=2 m and x=4 m for all three velocity components. The stagnation caused by the nacelle forces the flow in y- and z- direction just before the nacelle.

The wake deflection in yawed flow causes the traverse to move outside the wake for x>4 m (y=1.4 m) and x>3 m (y=1.8 m). The sinusoidal fluctuations in the near wake for y=1.8 m are caused by slicing through the tip vortices, which is reproduced in good agreement by both the RISØ and Delft University calculations.

Furthermore it is remarkable that the discrepancy between measured and calculated velocities in x-direction at x=-4 m, which was present for axial flow (Figure 8.12, U_∞=15 m/s), almost disappears.

The wake expansion (Figure 8.55, v-component) for y=-1.4 m and y=-1.8 m is underpredicted by the calculations. The panel code, and to a lesser extent the RISØ code, are the only ones to predict v-component fluctuations in the wake, which is more pronounced in the measurements. The measured w-component displays fluctuations due to traversing the viscous blade wake. Similar to axial flow, this feature is not predicted by any of the codes.

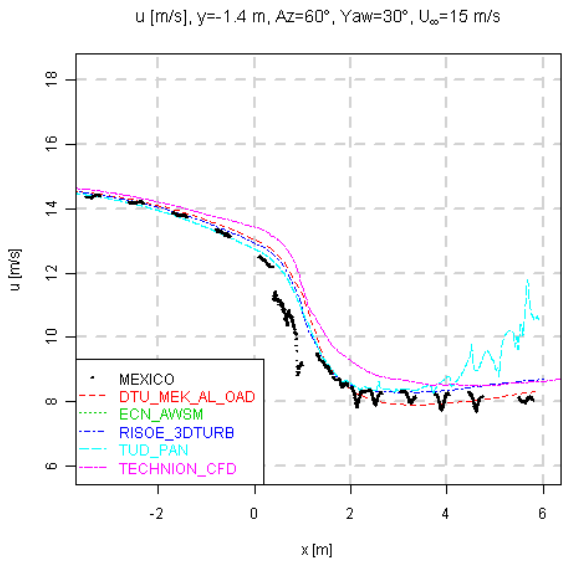

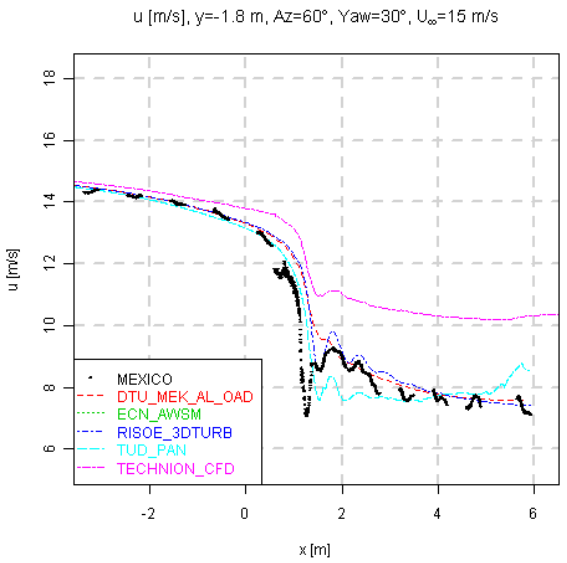

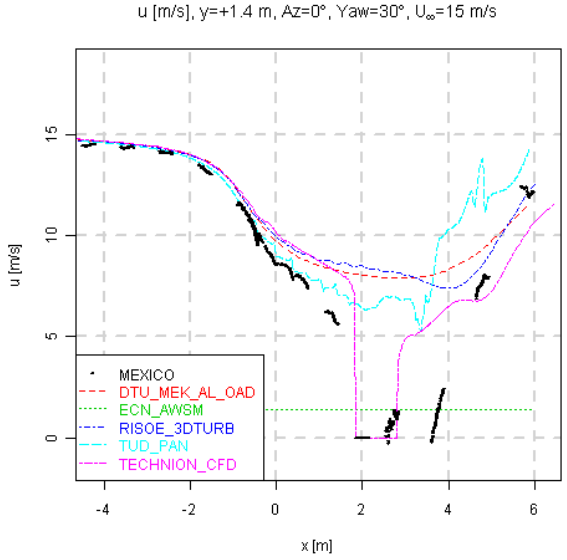

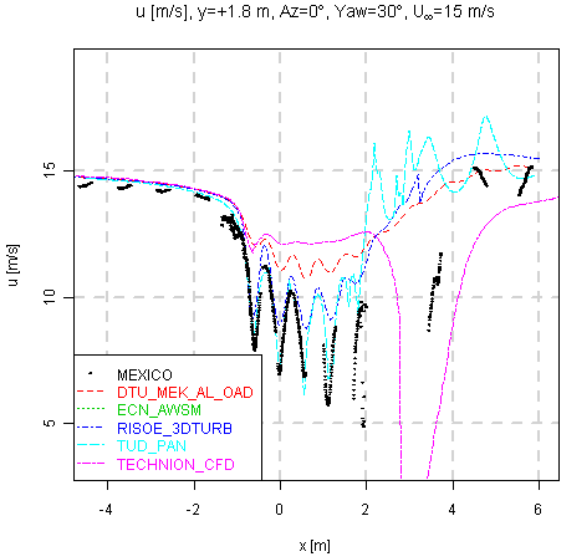

Figure 8.54 *Axial traverse of velocity in x-direction, Yaw=30°, U_∞=15 m/s*

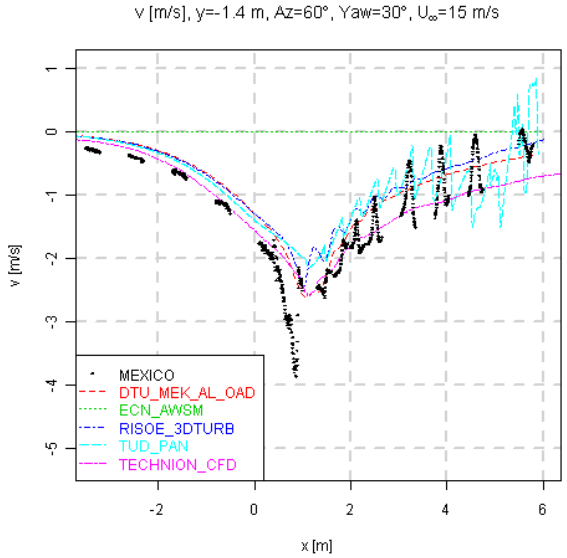

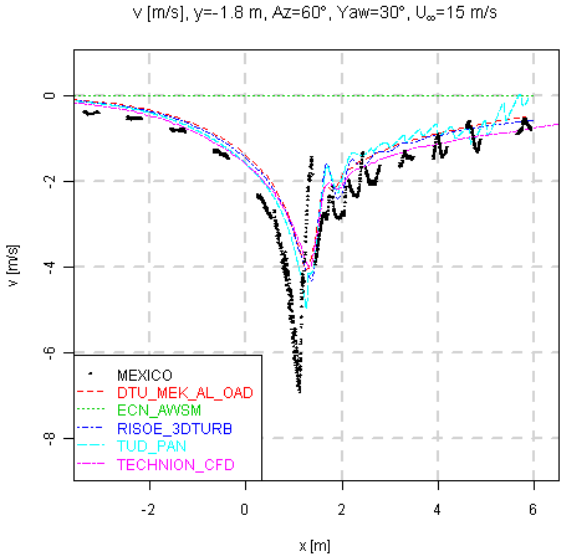

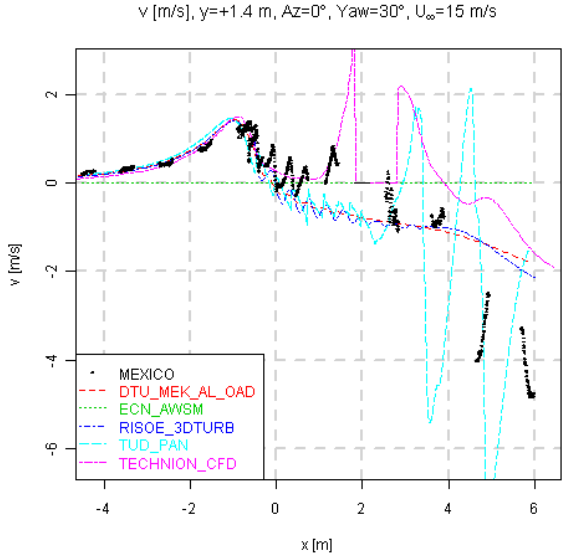

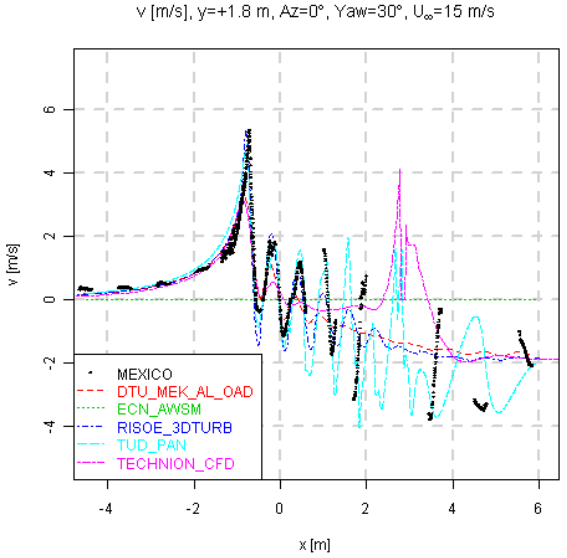

Figure 8.55 *Axial traverse of velocity in y-direction, Yaw=30°, U_∞=15 m/s*

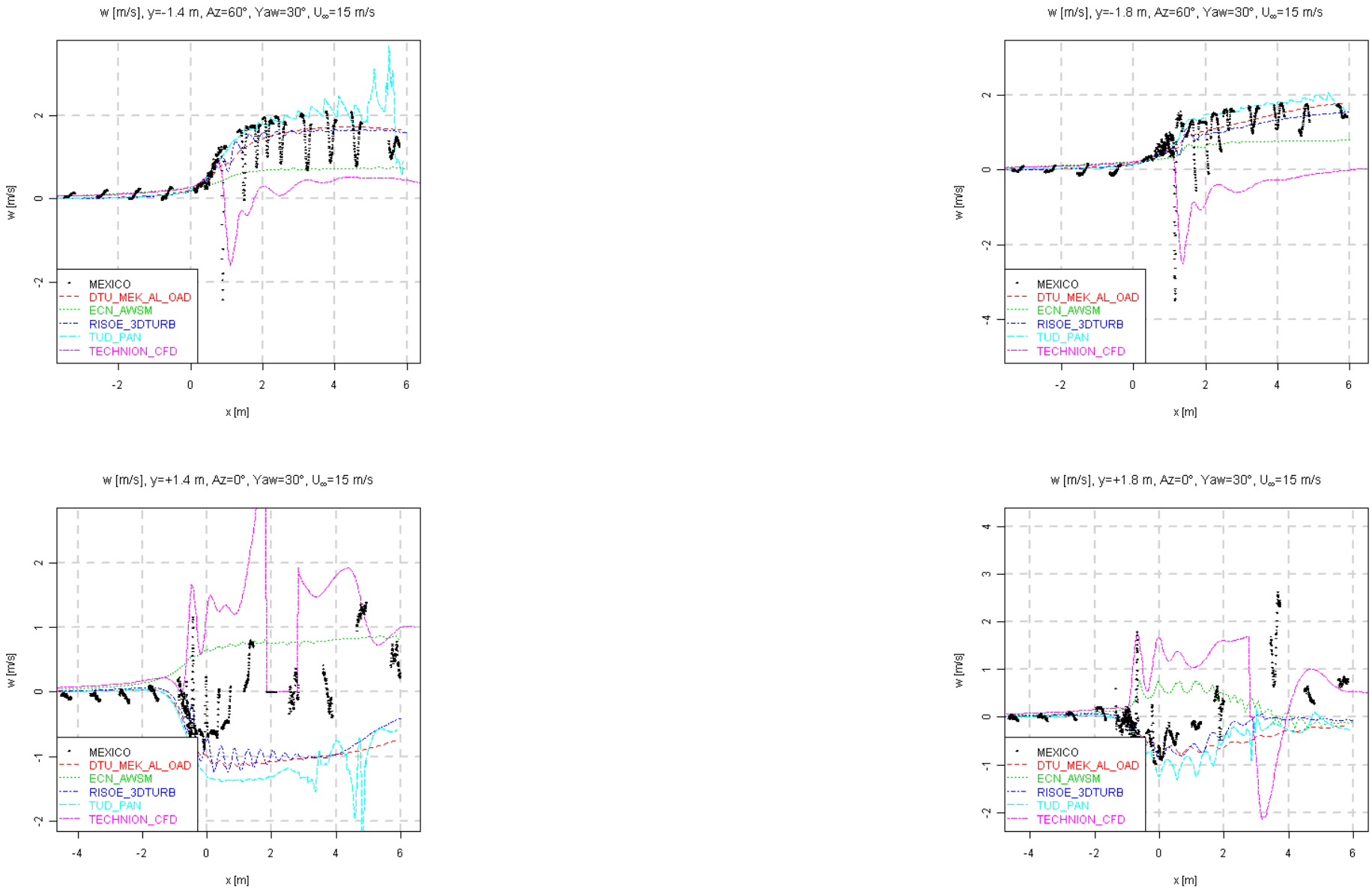

Figure 8.56 *Axial traverse of velocity in z-direction, Yaw=30°, U_∞=15 m/s*

Case 2.2

Since there are no measured velocities available for this case, a description of the results is not given. The following graphs solely display calculated results.

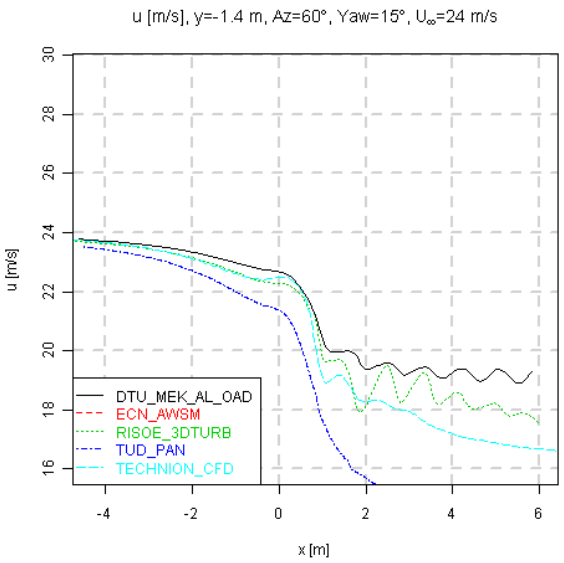

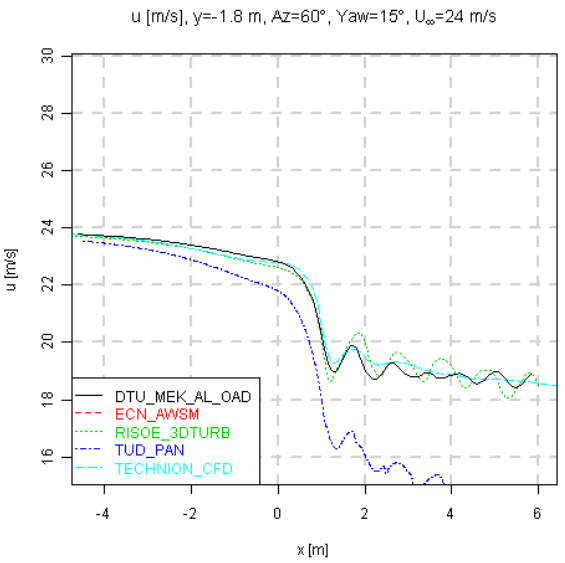

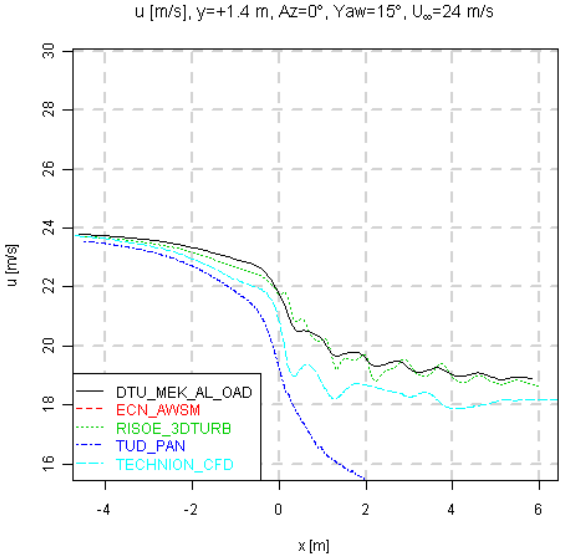

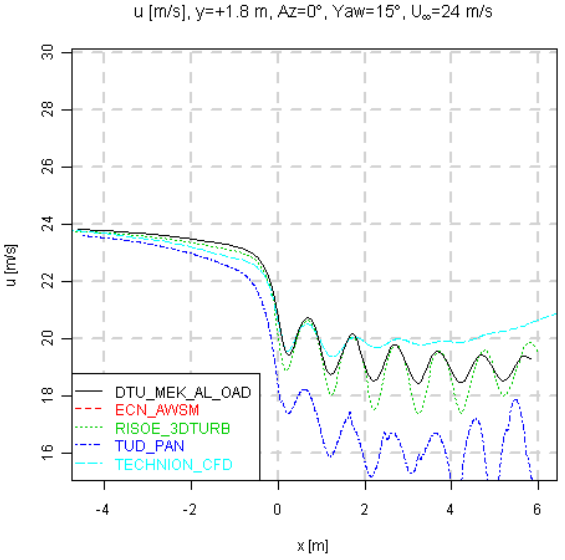

Figure 8.57 *Axial traverse of velocity in x-direction, Yaw=15°, U_∞=24 m/s*

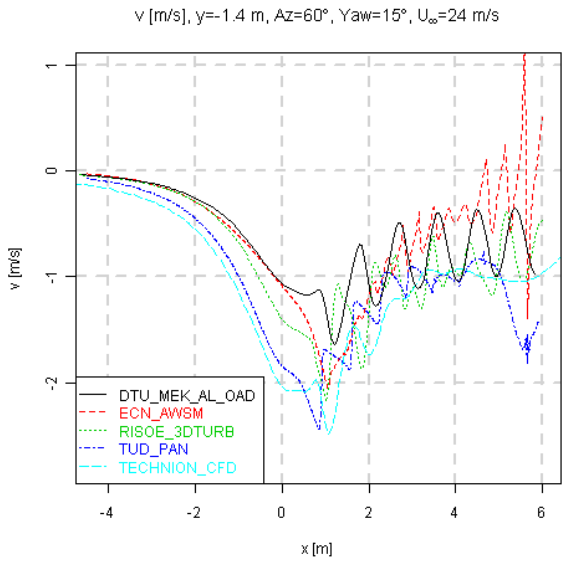

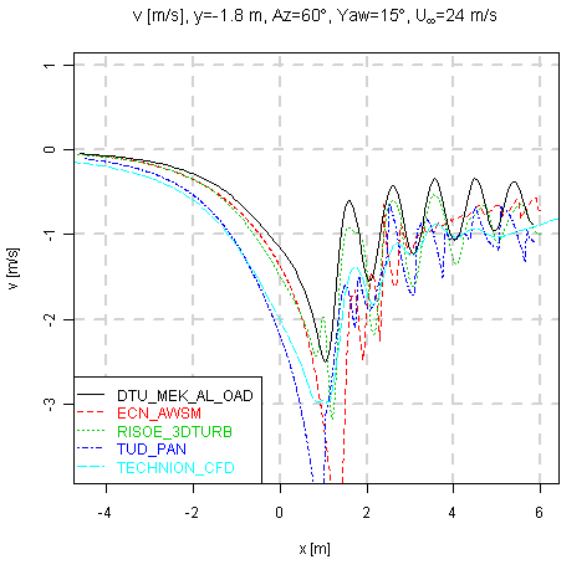

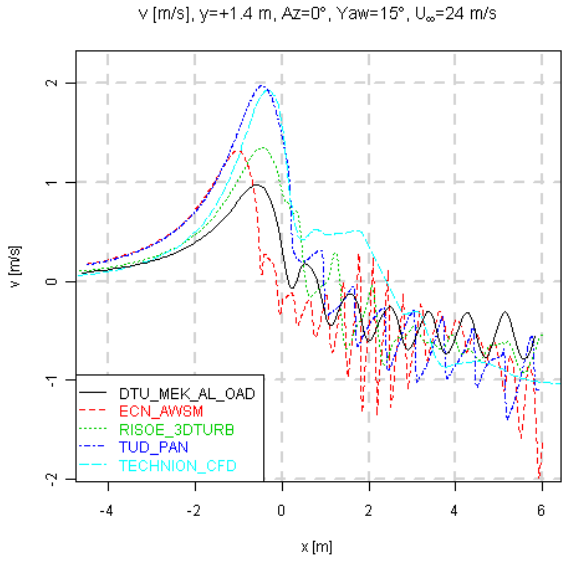

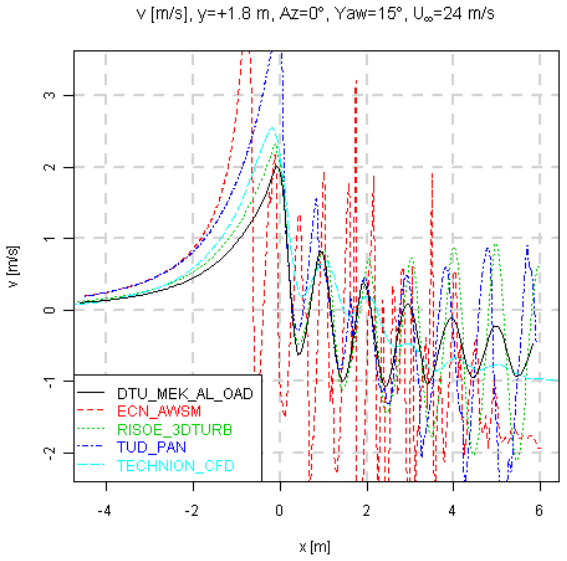

Figure 8.58 *Axial traverse of velocity in y-direction, Yaw=15°, U_∞=24 m/s*

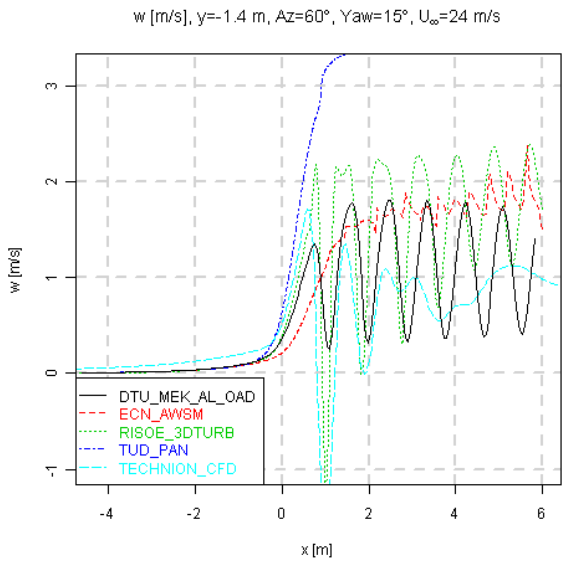

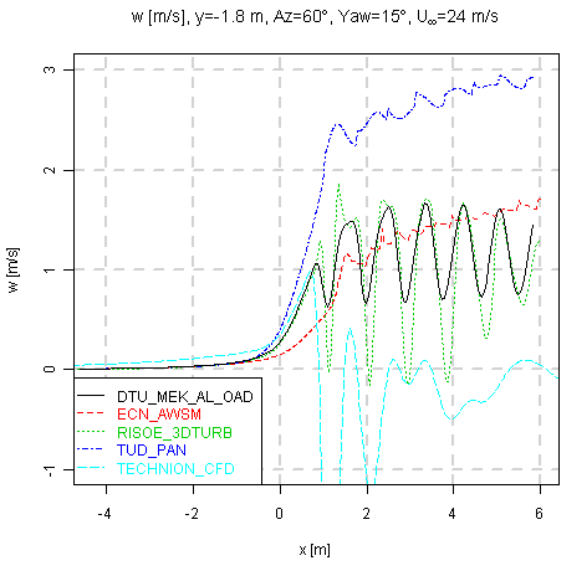

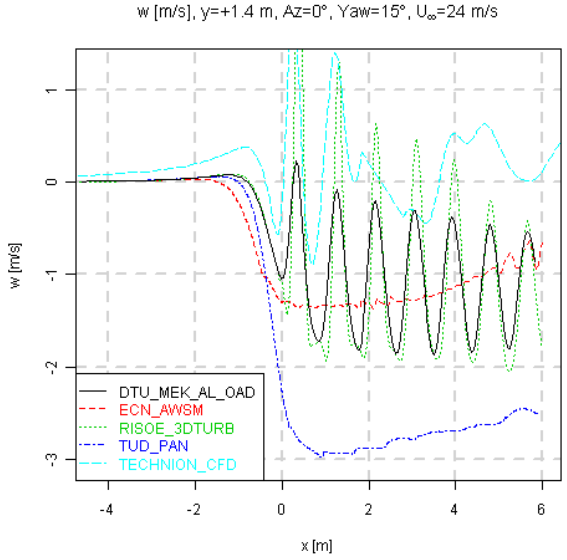

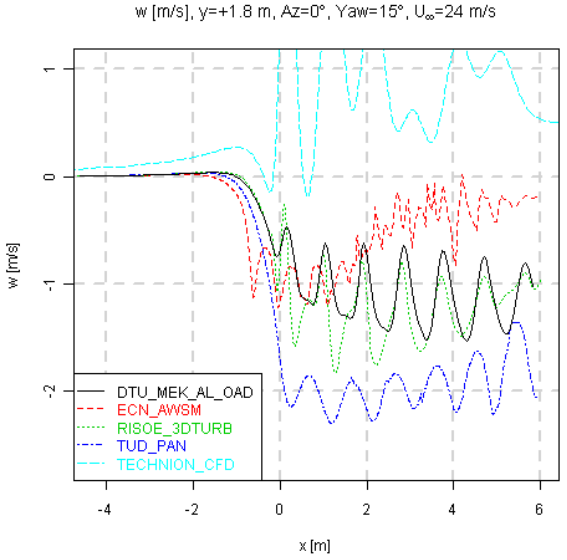

Figure 8.59 *Axial traverse of velocity in z-direction, Yaw=15 °, U_∞=24 m/s*

8.3.4 Radial velocity traverse

The radial traverses have been performed for an upwind (x_m=-0.15 m) and downwind (x_m=+0.15 m) location. The rotor azimuth angle varies from 0° and 100° in steps of 20 $^\circ$ as indicated in the title of the graphs from Figure 8.60 to 8.71. Please note that as indicated in section A.2, the velocities are expressed in the tunnel coordinate system, whilst the locations are expressed in the model coordinate system.

Case 2.1

The agreement between measurements and calculations is surprisingly good also for the downwind traverse. Dependent on the azimuth angle the traverse slices through the tip vortex, of which modes codes are able to predict both position and strength accurately. There are no measurements close to the rotor center but the TECHNION results clearly display the nacelle stagnation. The downwind w-component results (Figure 8.65) show more variation between the results, especially for inboard locations.

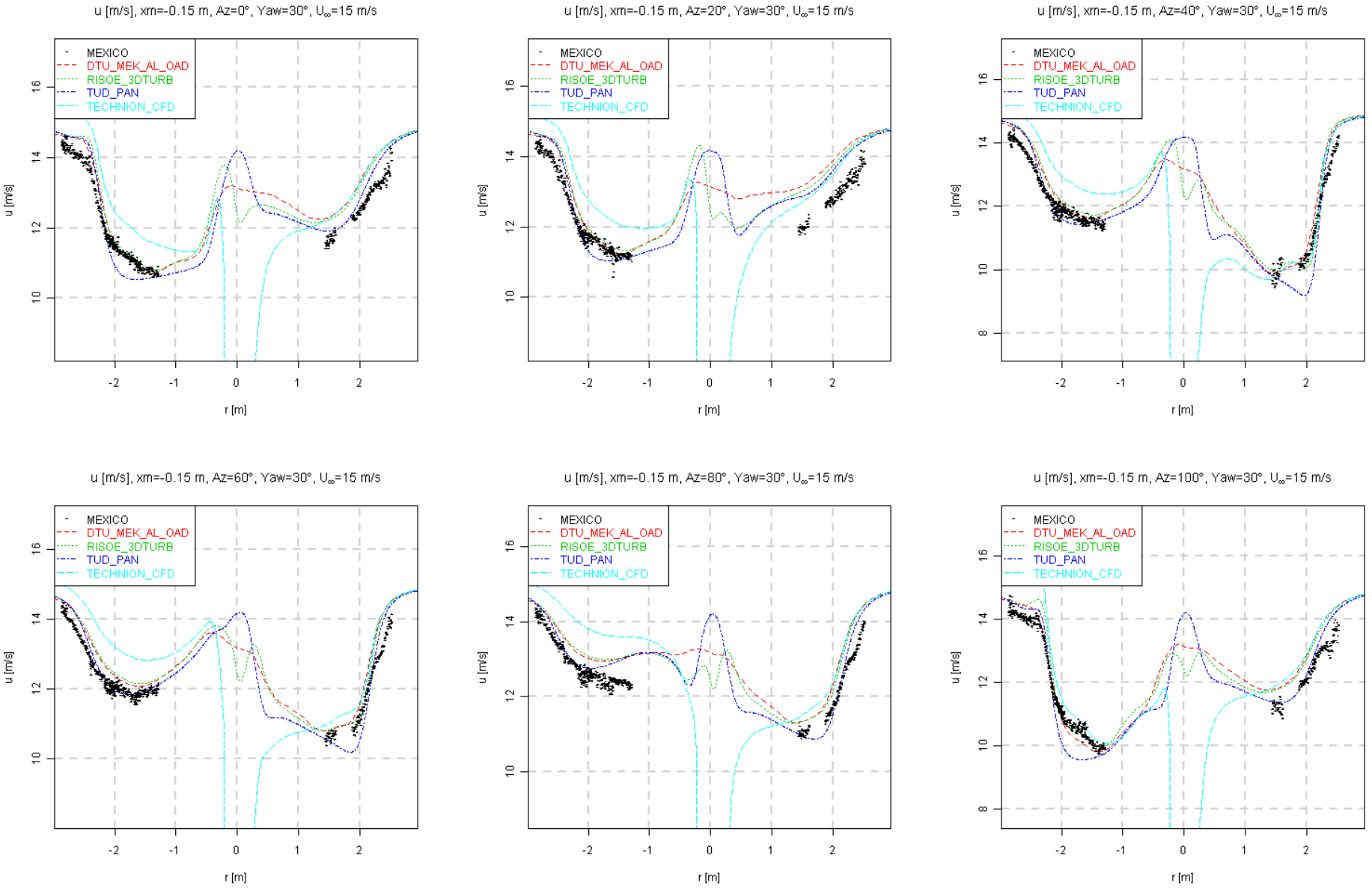

Figure 8.60 *Radial traverse (upwind) of velocity in x-direction, Yaw=30°, U_∞=15 m/s*

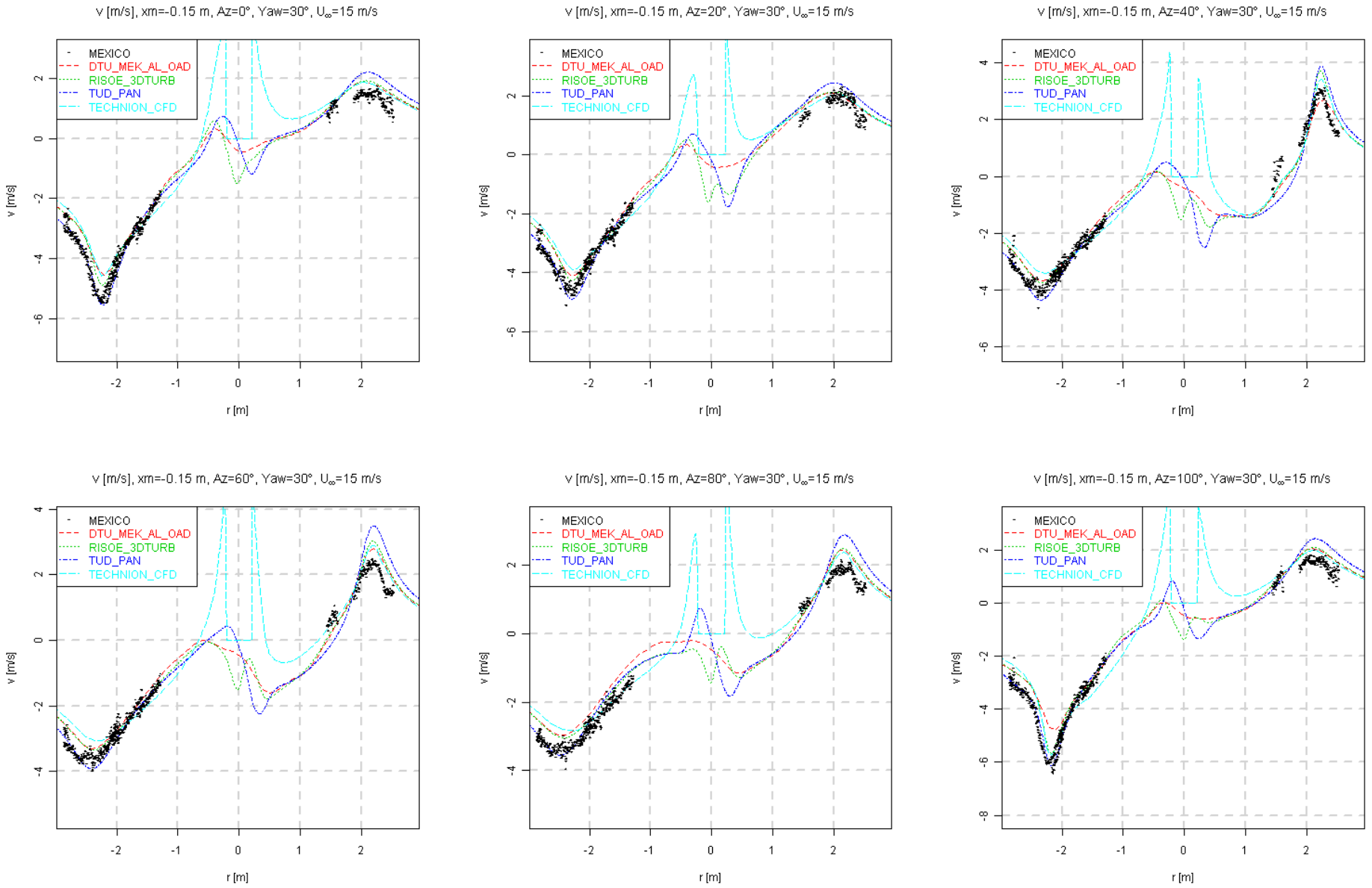

Figure 8.61 *Radial traverse (upwind) of velocity in y-direction, Yaw=30°, U_∞=15 m/s*

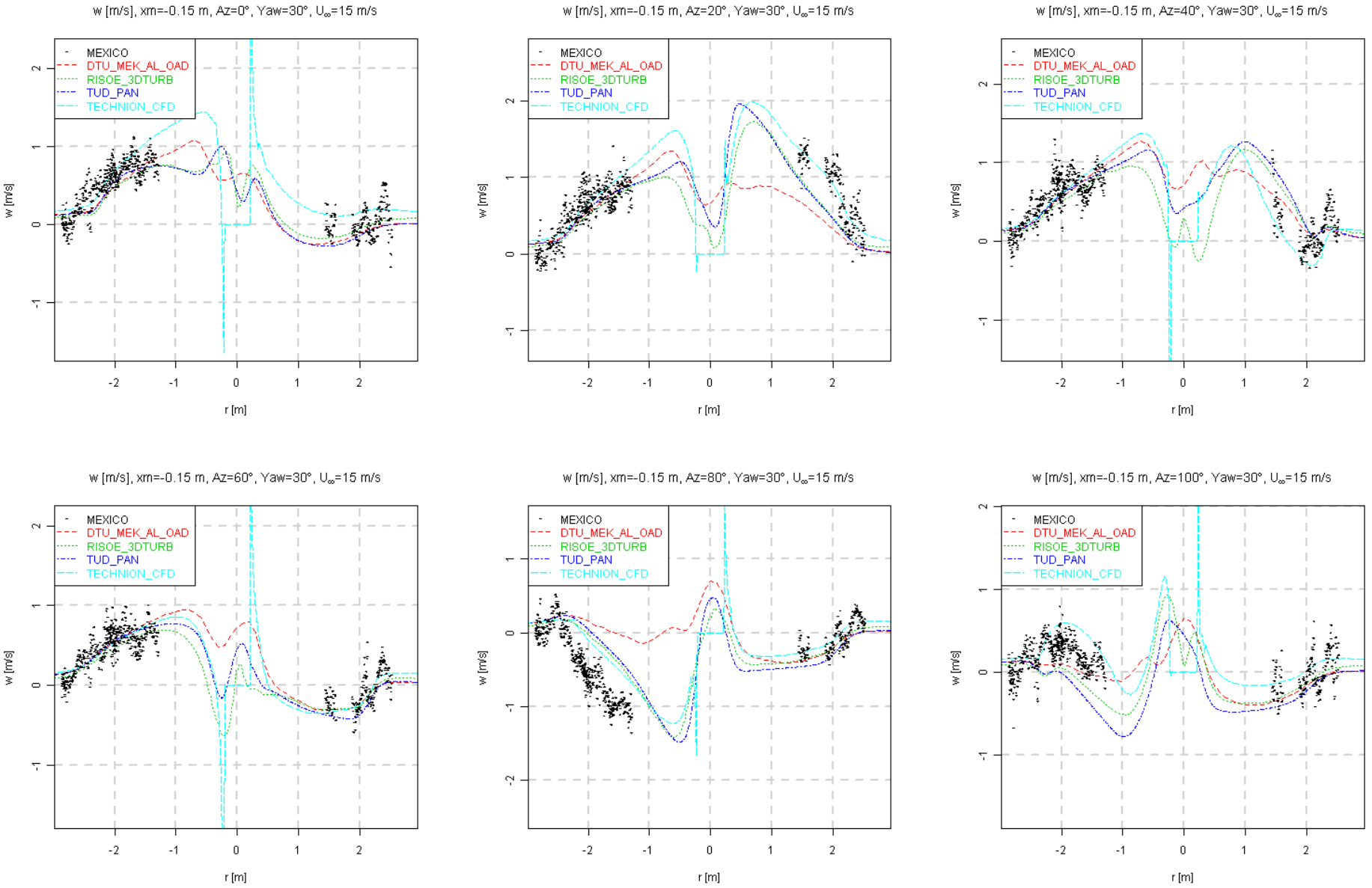

Figure 8.62 *Radial traverse (upwind) of velocity in z-direction, Yaw=30°, U_∞=15 m/s*

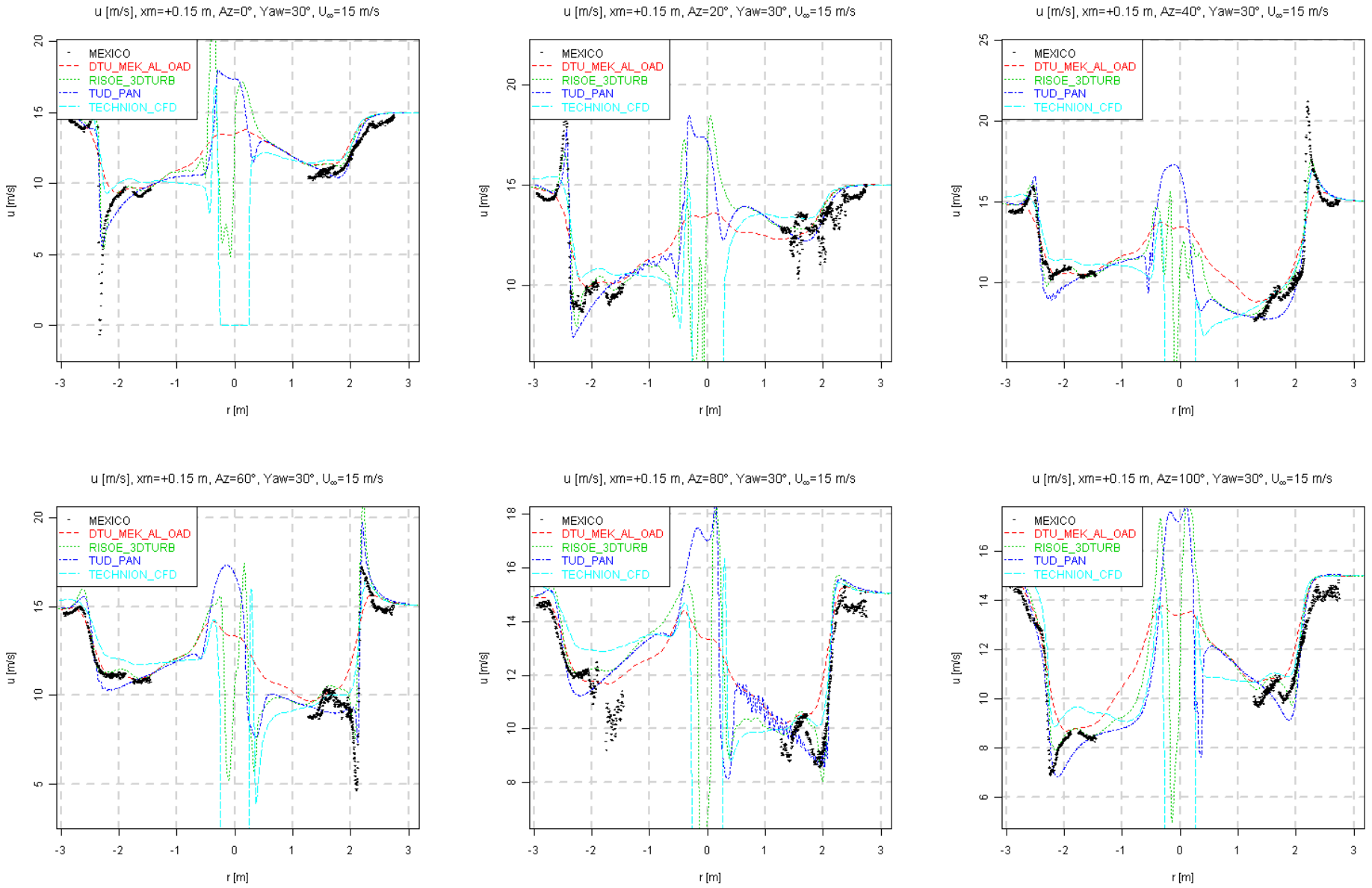

Figure 8.63 *Radial traverse (downwind) of velocity in x-direction, Yaw=30°, U_∞=15 m/s*

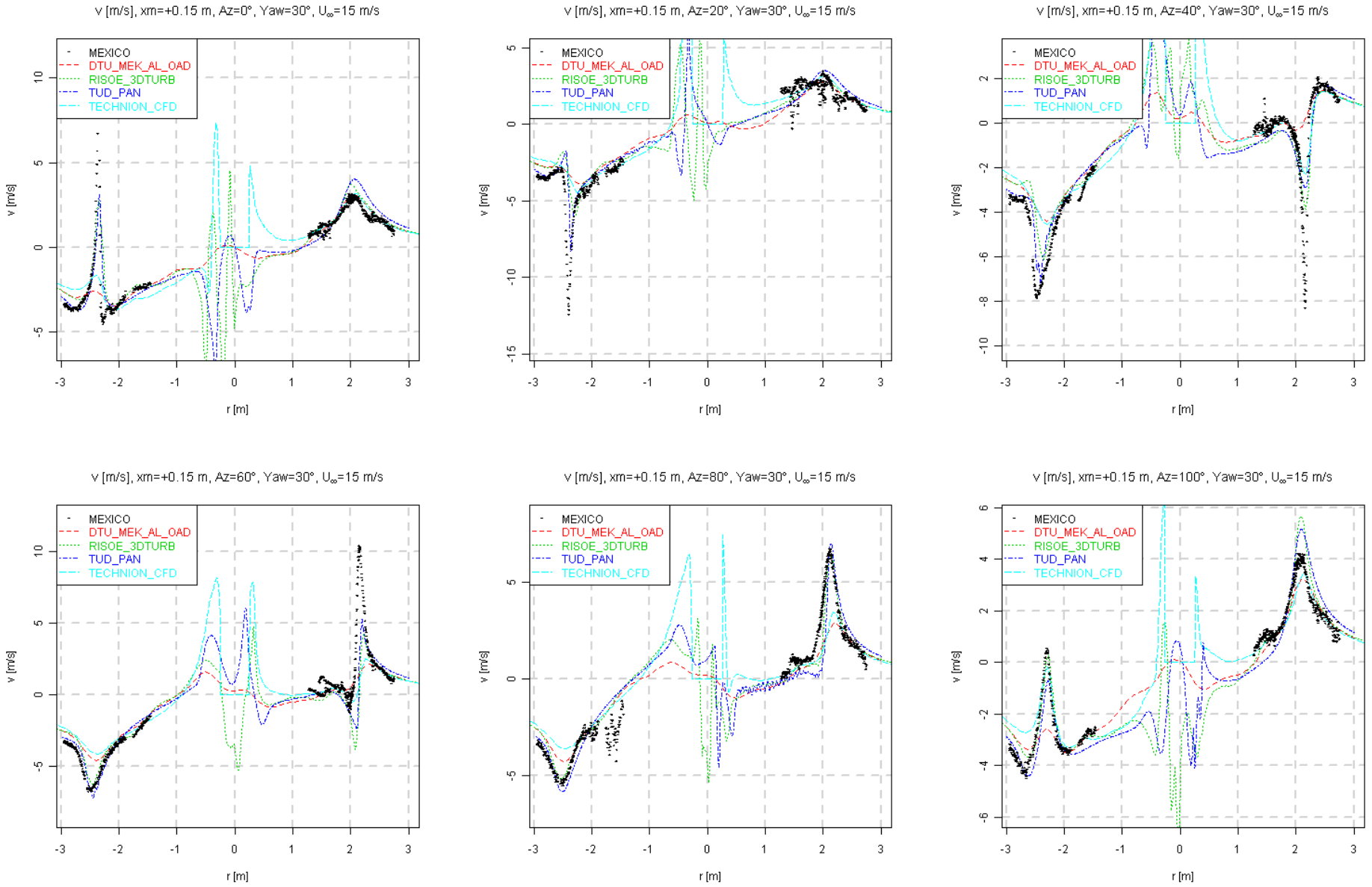

Figure 8.64 *Radial traverse (downwind) of velocity in y-direction, Yaw=30°, U_∞=15 m/s*

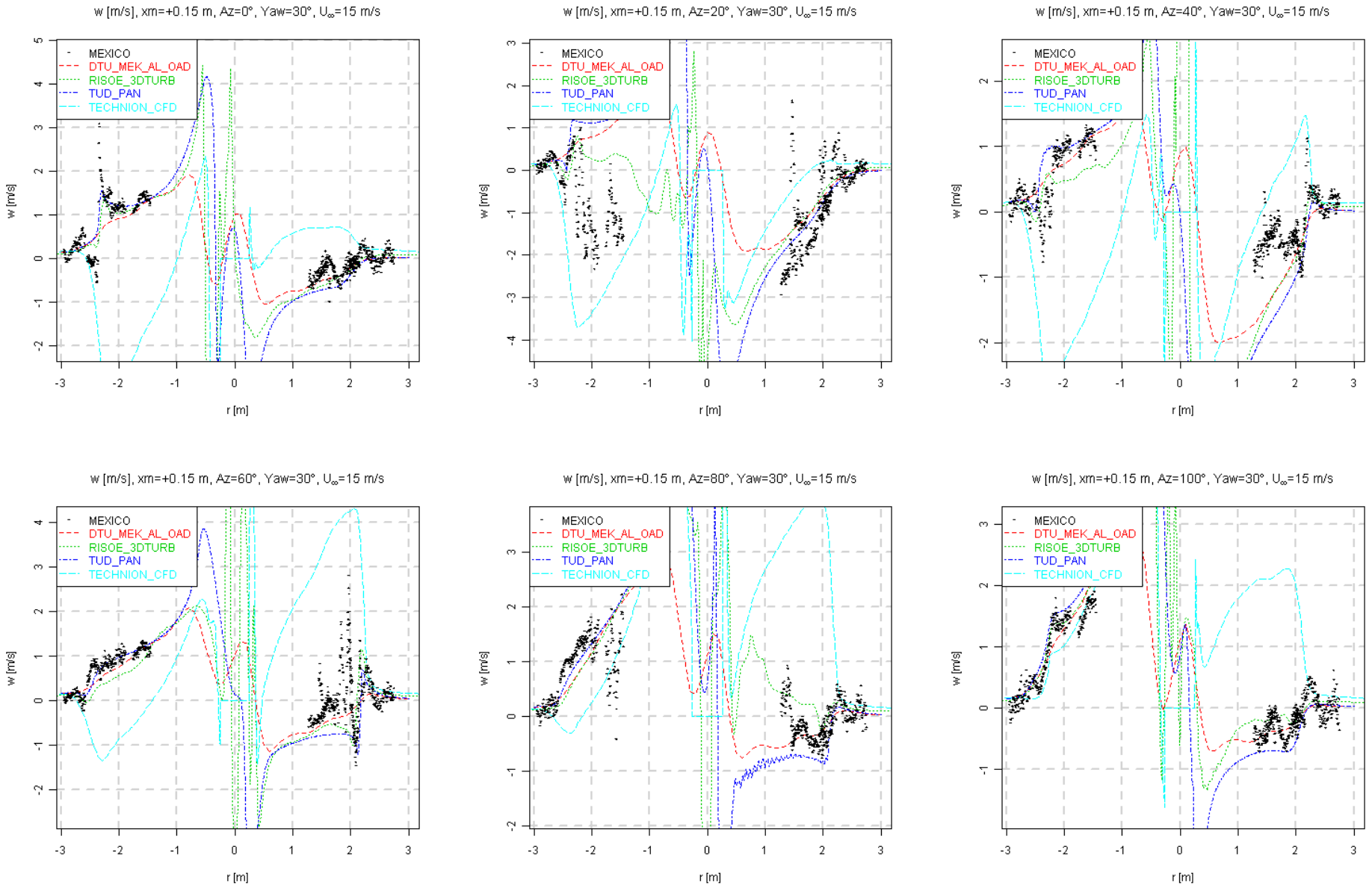

Figure 8.65 *Radial traverse (downwind) of velocity in z-direction, Yaw=30°, U_∞=15 m/s*

Case 2.2

Since there are no measured velocities available for this case, a description of the results is not given. The following graphs solely display calculated results.

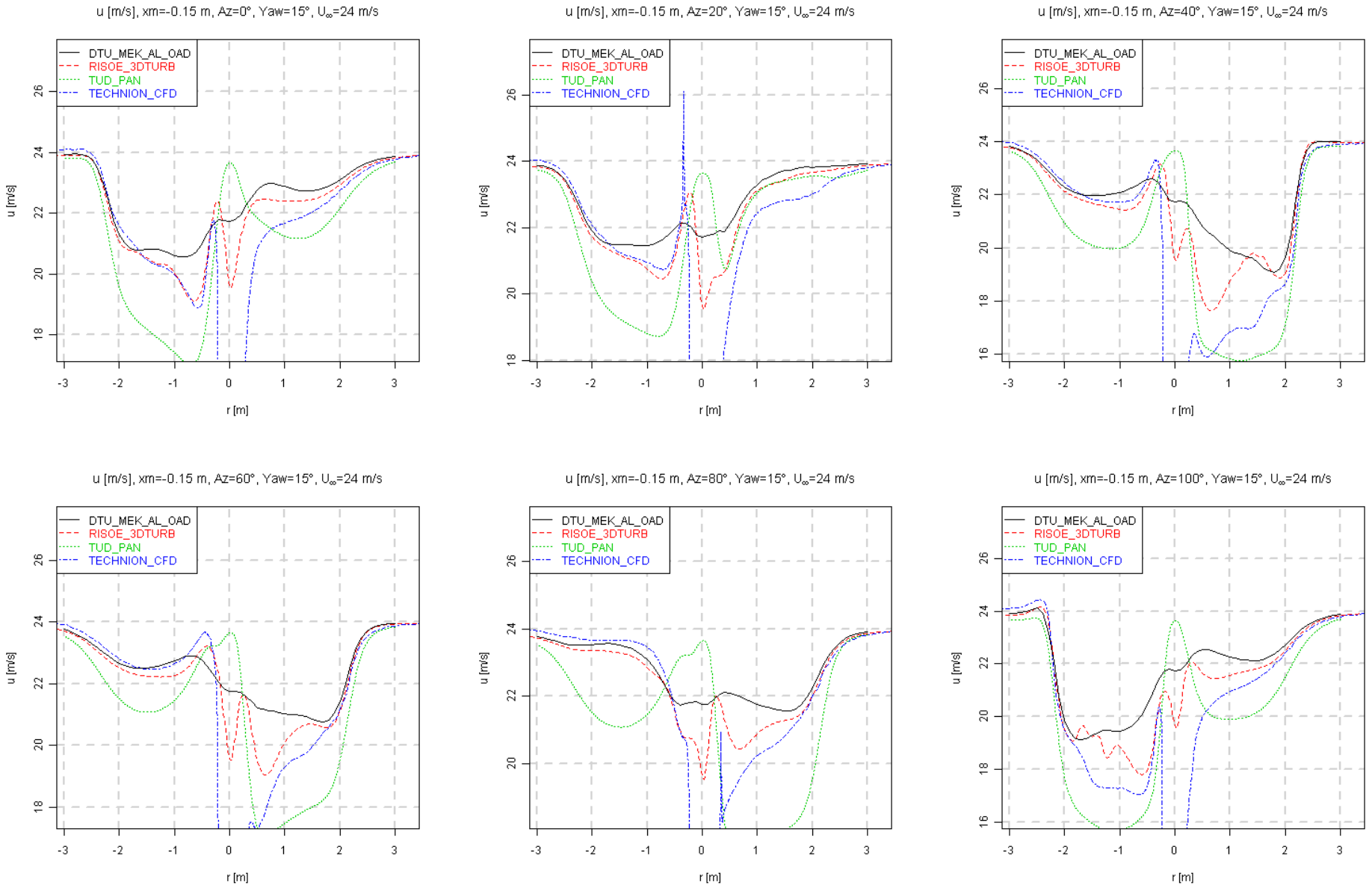

Figure 8.66 *Radial traverse (upwind) of velocity in x-direction, Yaw=15 °, U_∞=24 m/s*

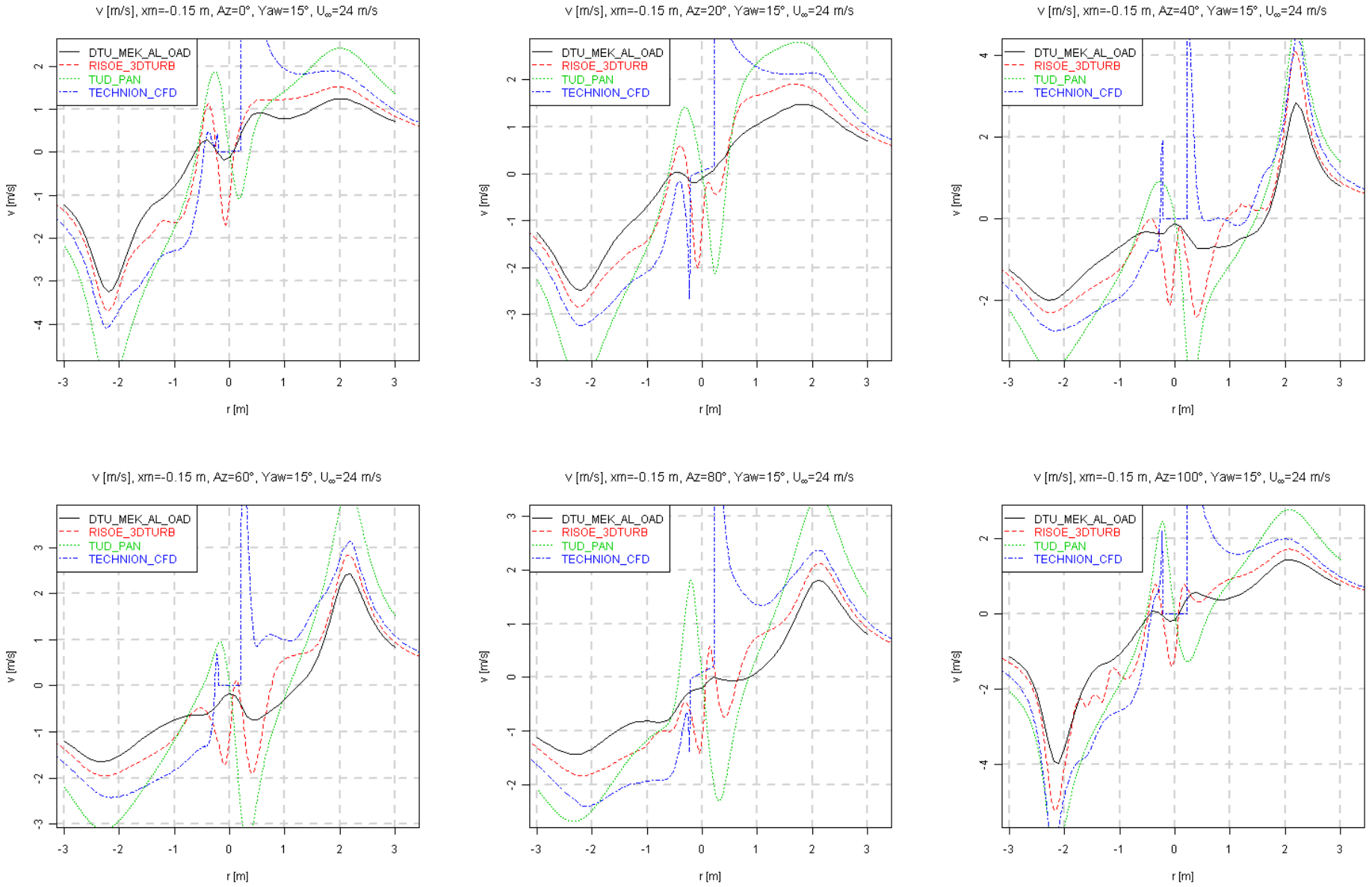

Figure 8.67 *Radial traverse (upwind) of velocity in y-direction, Yaw=15°, U_∞=24 m/s*

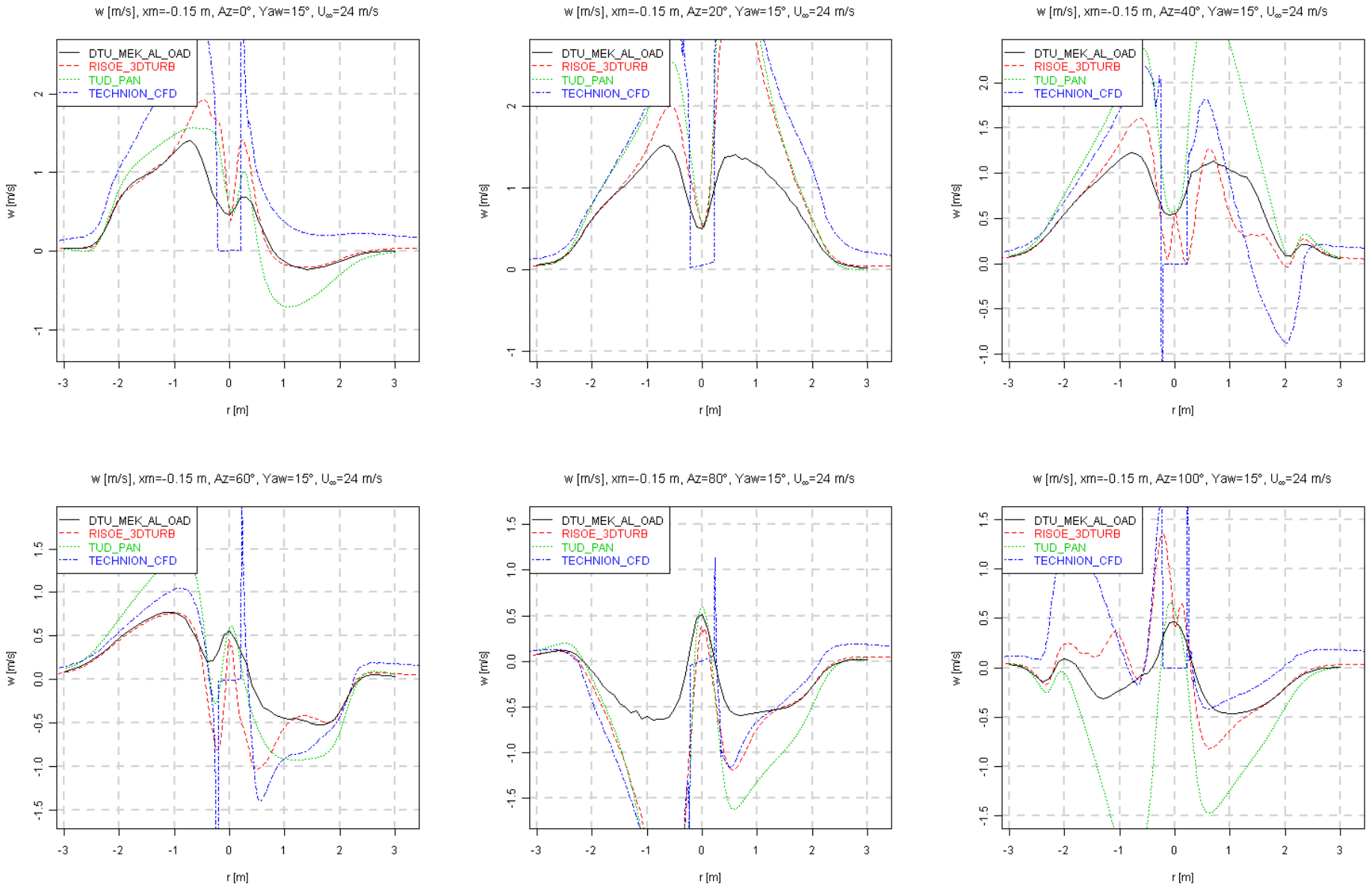

Figure 8.68 *Radial traverse (upwind) of velocity in z-direction, Yaw=15 °, U_∞=24 m/s*

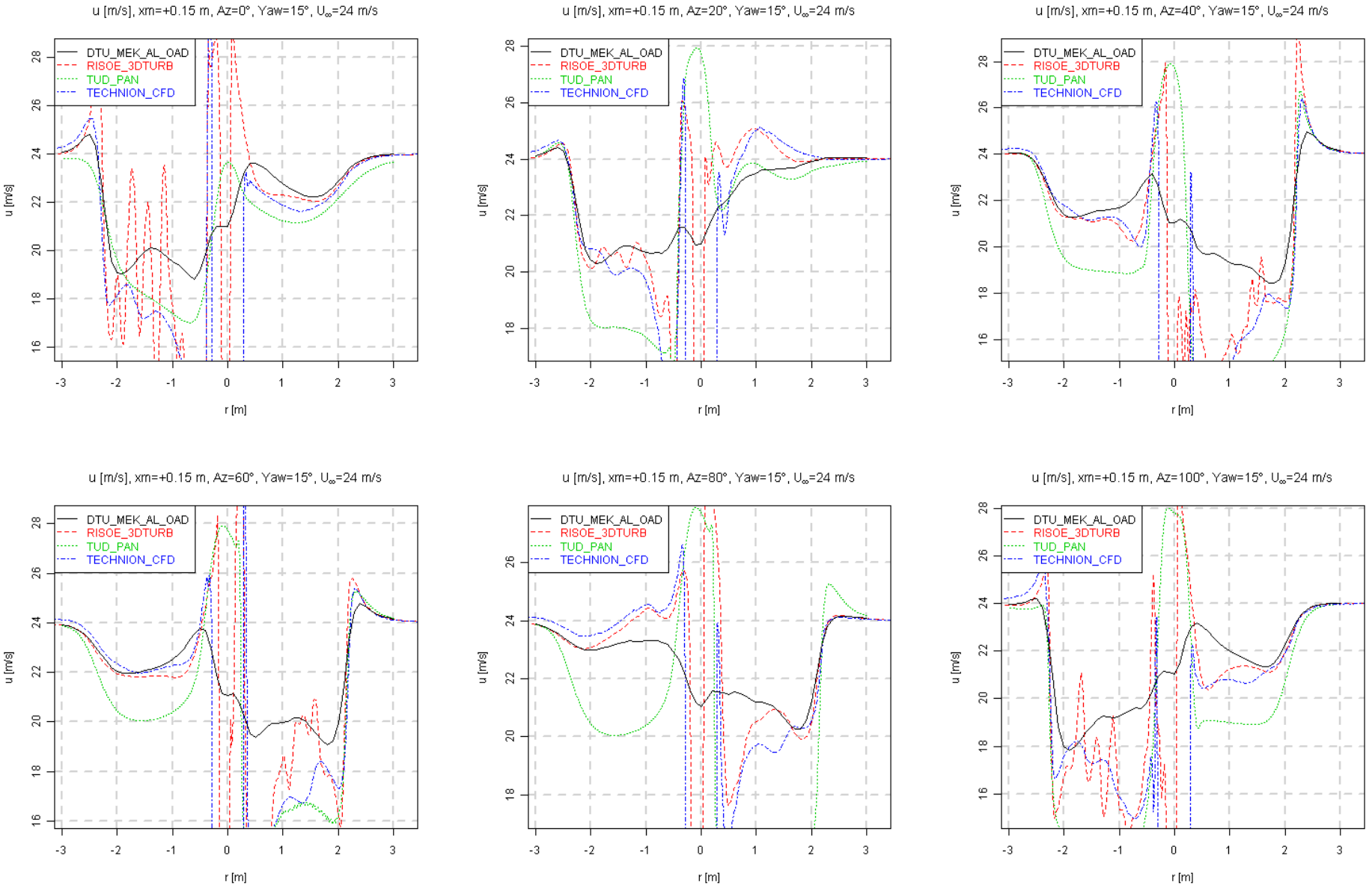

Figure 8.69 *Radial traverse (downwind) of velocity in x-direction, Yaw=15°, U_∞=24 m/s*

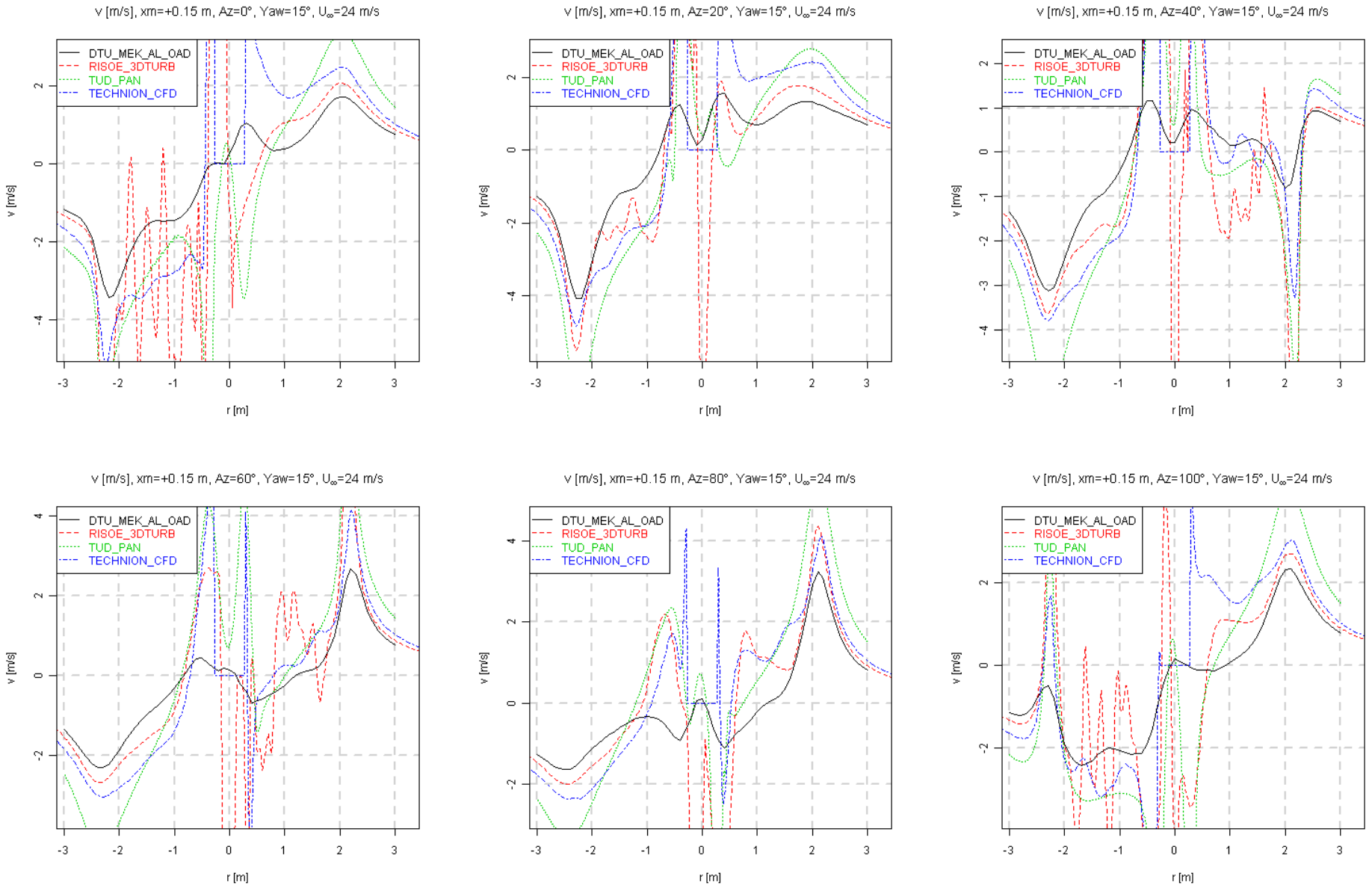

Figure 8.70 *Radial traverse (downwind) of velocity in y-direction, Yaw=15°, U_∞=24 m/s*

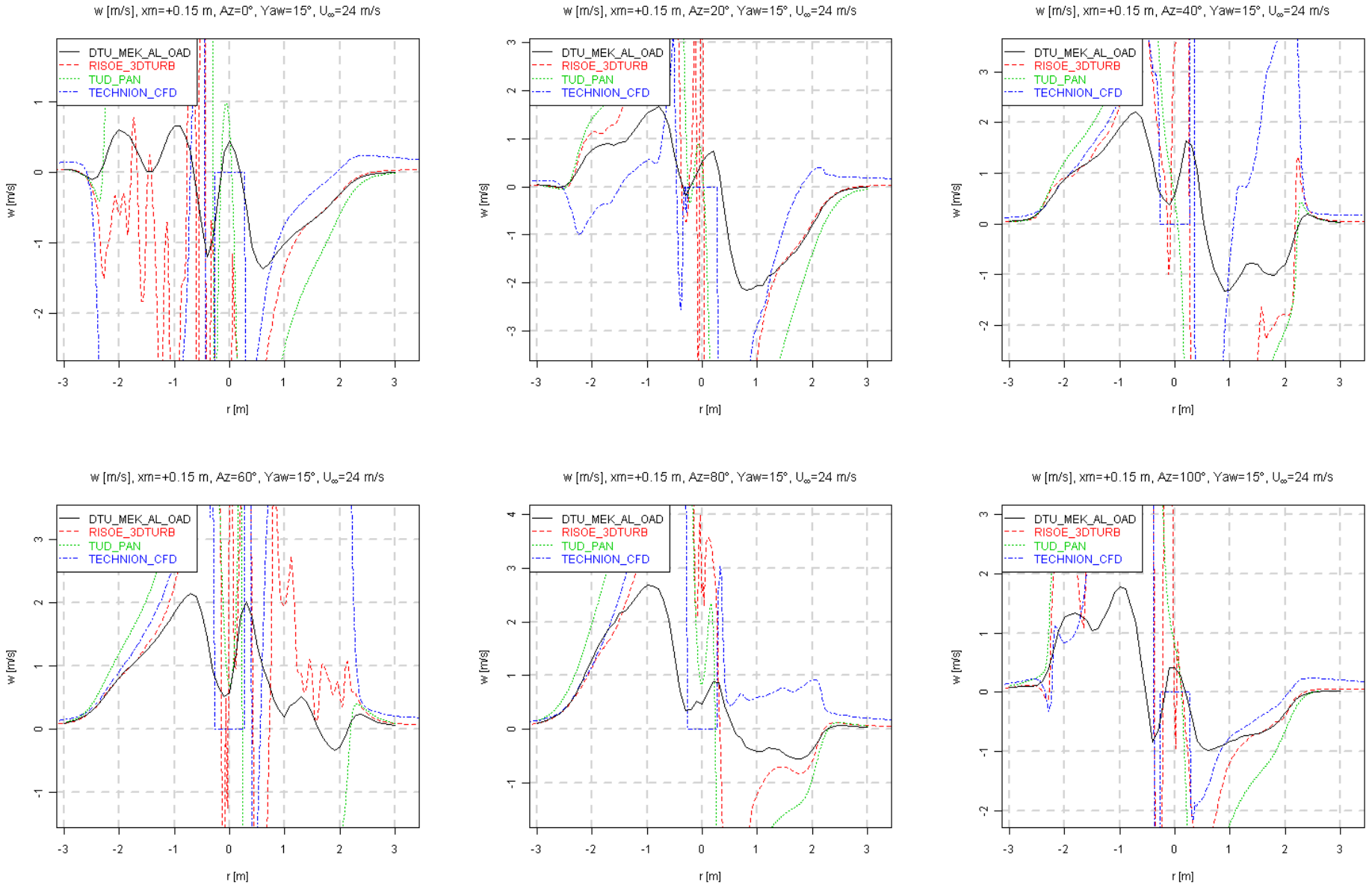

Figure 8.71 *Radial traverse (downwind) of velocity in z-direction, Yaw=15°, U_∞=24 m/s*

9 Task 4.1: Parked conditions

9.1 Introduction on Task 4.1

Parked conditions are amongst the design driving load conditions (storm loads). Within the MEXICO project, pressure distributions have been measured at standstill and a large number of pitch angles. The resulting loads from experiments and computations have been post-processed in order to be useful for future analysis and comparisons with common design standards. It is furthermore expected that these data form a reference for the rotational measurements in order to distinguish rotational effects (see task 4.6). This task has been carried out from June 2008 to June 2011.

It is noted that the measurements are carried out at the highest possible tunnel speed. Nevertheless, the resulting pressures are still in the lower end of the measurement range.

The participants and initial objectives of task 4.1 were:

- AE-Rotortechniek will assess the importance of standstill conditions for design calculations.
- CENER will perform FAST and WMB calculations on the parked rotor. As the task leader will report the work done by the end of the project.
- DUT will carry an investigation of pressure distributions at standstill. A possibility to measure the pressure distribution on a stand-still blade in the DUT-LST wind tunnel will be explored.
- NREL will obtain time averaged aerodynamic force and surface pressure data for parked blade conditions, across the experimental range of inflow angles and blade radial locations.
- RISØ-DTU will made standstill computations using both RANS and DES simulations.

9.2 Standstill Experiments

In this section a description of standstill experiments and the main measured parameters is made. It is followed by an analysis and the conclusions.

9.2.1 Stand still Measurements

In [9] it is explained that the standstill measurements were all done at a wind speed of 30m/s with a locked rotor in order to avoid rotation. Table 9.1 shows the 23 pitch angles that were measured during the Standstill experiments.

From global to local measurements, the three forces and the three moments have been measured at the root of the tower with a 6-components balance. At the root of each blade, the edge-wise and the flat-wise bending moments have also been measured with strain gauges. Moreover pressure distributions measurements have been carried out at standstill at a large number of pitch angles. All datapoints lasted five seconds [28] once the pitch angle was fixed. The pitch angle definition can be seen in Figure 9.1.

It is recalled that the pressure distribution has been measured over 5 sections of the blades with 148 Kulite XCQ-95 series sensors. The pressure taps that had 0.4mm in diameter were flush with blade surface and at each of the transducer the pressure inputs were scanned at 5514Hz. The pressure sensors were distributed along the three blades of the rotor. The blade 1 had the pressure sensors for the 25%R and 35%R stations, the blade 2 for the 60%R and the blade 3 for the 82%R and 92%R stations. For the parked case there were not taken any Particle Image Velocimetry (PIV) measurement.

	V_{avg} = 29.92m/s & σ = $\pm$ 0.02			
Pitch angles	87° to 65°	65° to 20°	12°	-2.3°
Every	2°	5°	-	-

Table 9.1 *The 23 pitch angles where the measurements were taken.*

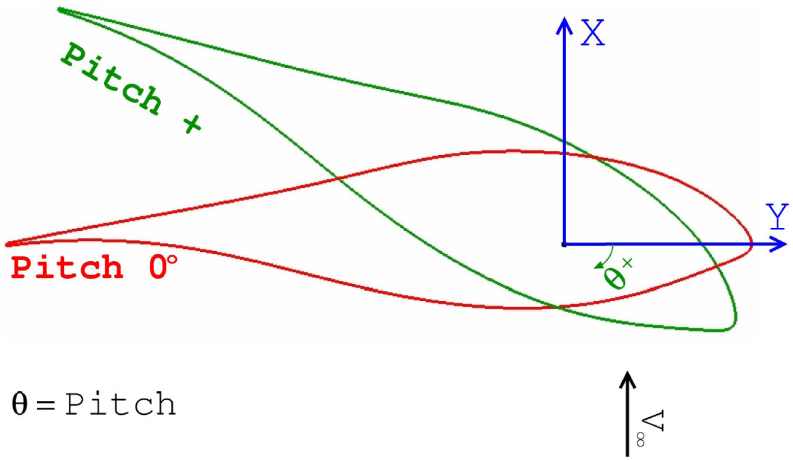

Figure 9.1 *Pitch definition for the parked case (12 o'clock position).*

The relation between pitch angle and local geometrical angle of attack (α_{geom}) can be seen in Table 9.2 for some radial stations, which may be helpful when analysing results from the following sections.

9.2.2 Analysis of Experimental Data

NREL analysed the stand still experimental data and conclusions were obtained about the non usability [29] of the 25%R and 35%R based on Figure 9.2, since the averaged cn values of these two stations were much higher than expected ones. CENER have seen the same and reached to the same conclusion [30]. ECN showed prior to Mexnext project [13] that there are pressure measurements discontinuities. This can be seen in Figure 9.2, where the 82%R and 92%R stations mainly have these discontinuities on the lower surface. It was suggested [13] that the balance data could be used in order to compare integrated values of the blade.

CENER also showed that as can be seen in Figure 9.3, the stagnation point for the 60%R station has not moved from 12 to 50 degrees of geometrical angle of attack, which does not occurred with the computed values. The CFD values are not taken with experimental resolution, but even then there are differences. This does not mean that for geometrical angles of attack larger than 12° the measured results are erroneous, however they need to be used with precaution. As can be seen at Figures 9.4 from NREL, the post-stall region seems the most affected one.

CENER saw that the normalised values for the stagnation point had a post-processing problem. This affirmation is possible to see in Figure 9.3, since normalised stagnation values are larger than

	α_{geom}								
Pitch	20%R	25%R	35%R	50%R	60%R	70%R	82%R	92%R	97%R
90°	-16.40°	-14.25°	-10.20°	-6.10°	-4.80°	-3.70°	-2.38°	-1.24°	-0.56°
85°	-11.40°	-9.25°	-5.20°	-1.10°	0.20°	1.30°	2.62°	3.76°	4.44°
80°	-6.40°	-4.25°	-0.20°	3.90°	5.20°	6.30°	7.62°	8.76°	9.44°
70°	3.60°	5.75°	9.80°	13.90°	15.20°	16.30°	17.62°	18.76°	19.44°
50°	23.60°	25.75°	29.80°	33.90°	35.20°	36.30°	37.62°	38.76°	39.44°
0°	73.60°	75.75°	79.80°	83.90°	85.20°	86.30°	87.62°	88.76°	89.44°

Table 9.2 *Relation between blade pitch angle and local geometrical angle of attack.*

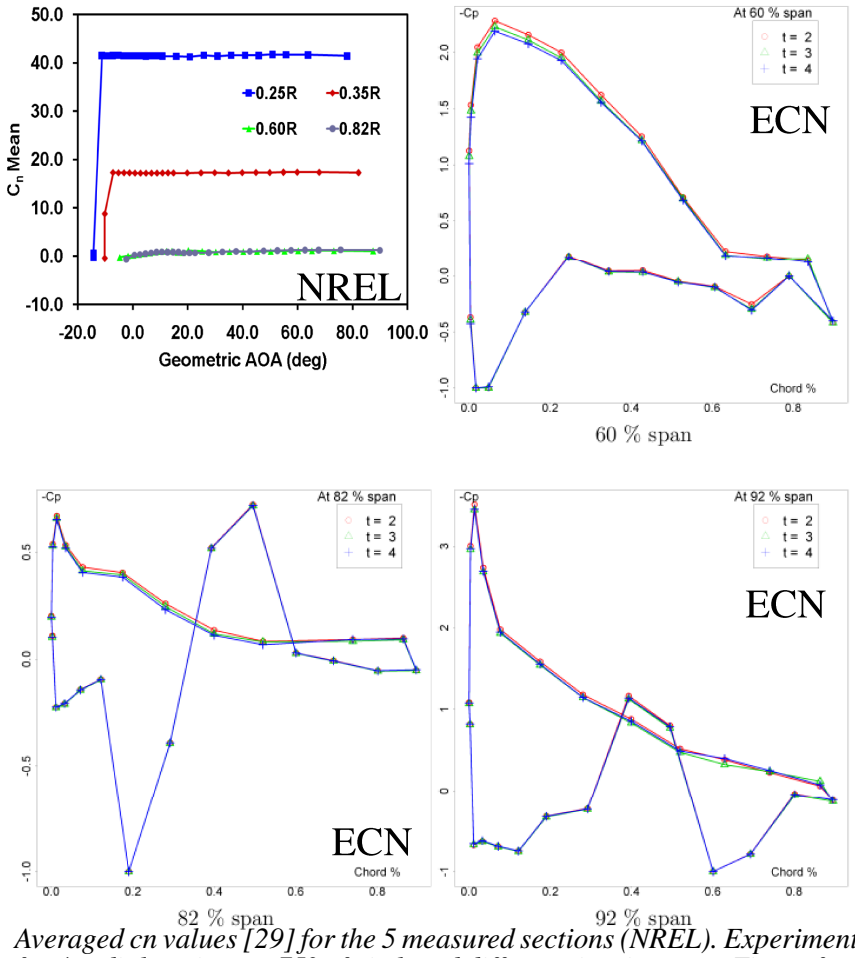

Figure 9.2 *Averaged cn values [29] for the 5 measured sections (NREL). Experimental cp values for 4 radial stations at 75° of pitch and different time instants. Figure from ECN [13].*

one at deep stall for 60%R and 82%R stations, and the same occurs for the 92%R but at earlier geometrical angle of attack.

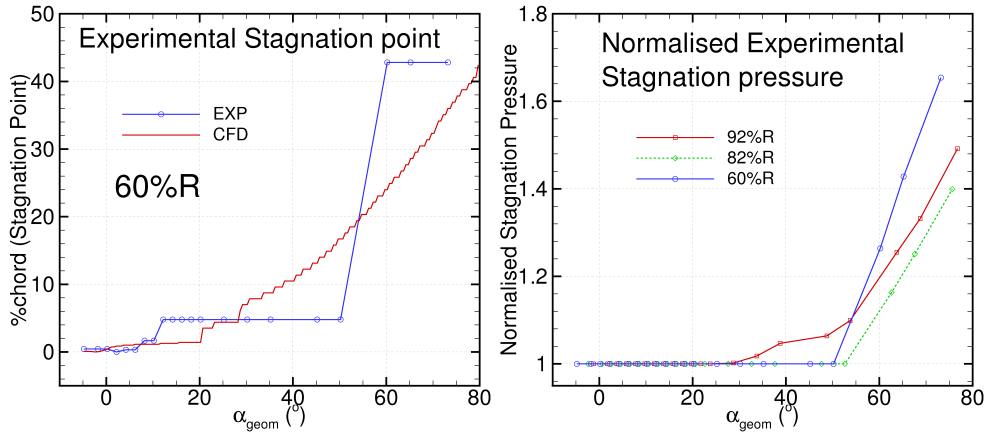

Figure 9.3 *Experimental and CFD calculated stagnation point locations in percentage of chord for the 60%R station and normalised pressure versus the geometrical angle of attack for 3 radial stations.*

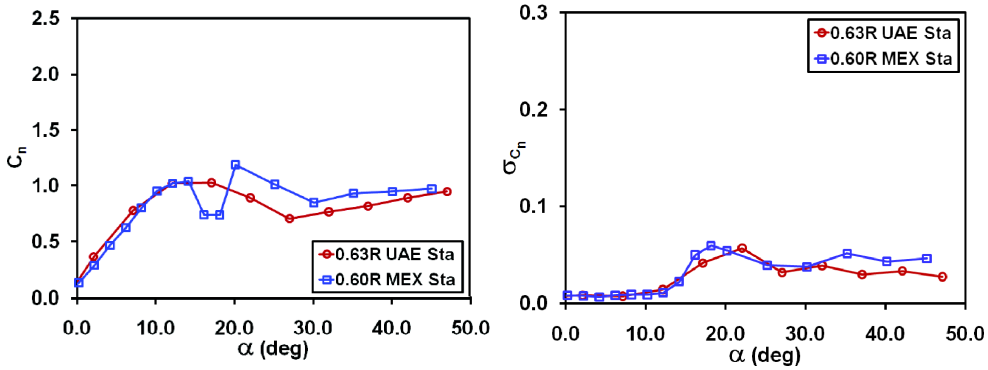

Figure 9.4 *MEXICO and UAE Phase VI cn mean and σ at mid-span radius, for parked blades. Figure from NREL [29].*

NREL, TUDelft & University of Malta post-processed experimental data studying the rotational augmentation versus angle of attack (linking with Task 4.6, rotational augmentation) [28]. For that purpose, they have compared the MEXICO and UAE Phase VI [4] experiments. Comparisons of the two surface pressure data sets included both cn mean and cn standard deviation statistics. Rotational effects on mean cn are active across the entire blade performance envelope. Clearly, the two σ_{cn}-α curves show (see Figure 9.4) striking similarities with respect to maximal magnitudes and slope correlations. Though mid-radius stall kinematics differed as can be seen in Figure 9.4 [28].

As a summary of these analyses, mention that the 25%R and 35%R stations pressure transducer measurements are not useful. At 60%R, above geometrical angles of attack of 12° results need to be taken with precaution due to the non variation of the stagnation point in the following 40°. Also precaution is needed for the deep stall region when the 60%R and 82%R stations are studied, since they were not correctly normalised. Similarly, at 92%R station the normalisation error occurs but at earlier geometrical angle of attack.

9.2.3 Conclusions on the standstill measurements

- NREL, TUDelft, ECN and CENER have seen that the data at 25%R and 35%R are not useful.
- At 60%R, above geometrical angles of attack of 12° results need to be taken with precaution due to the non variation of the stagnation point in the following 40°.
- Also precaution is needed for the deep stall region when the 60%R and 82%R stations are studied, since they were not correctly normalised.
- Similarly, at 92%R station the normalisation error occurs but at earlier geometrical angle of attack than for the 60%R and 82%R stations.
- There is a clear need of a more dedicated post-processing of experimental data in order to clean the cp values from pressure transducers that are erroneous. This will benefit in obtaining more realistic force coefficients based on blade surface pressure.

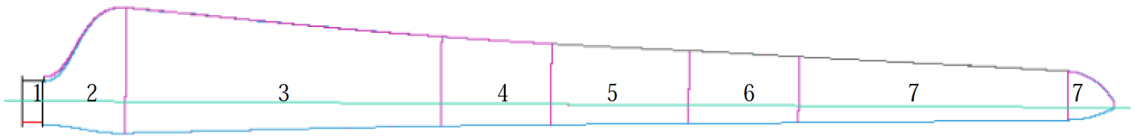

Figure 9.5 *MEXICO blade discretization for FAST computations.*

9.3 BEM Computations

BEM computations were carried out in order to know the potential capacity of the method for parked case investigation.

9.3.1 Code: FAST

The FAST (Fatigue, Aerodynamics, Structures, and Turbulence) code is a comprehensive aeroelastic simulator capable of predicting both the extreme and fatigue loads of horizontal axis wind turbines. The model basically combines the axial and tangential momentum equation with the axial and tangential force from the blade element theory.

9.3.2 Initial conditions

For the specific case of parked simulations, parameters have been defined for a turbine with no control and no rotation, and a brake applied from the beginning of the computation. The wind has been defined as a constant 30m/s wind with no shear.

Blade model:

The blade has been divided in 7 regions (see Figure 9.5) having in total 26 elements covering it. The applied aerofoil data is detached below:

1. Cylinder: Cd = 1.
2. Transition Cylinder-DU.
3. DU91-W2-250, Re=500,000 as provided in the report from ECN [9].
4. Transition DU91-W2-250 - RISØ A1-21.
5. RISØ A1-21:
Cd and Cm: Re=1,600,000 as provided in the report from ECN [9]
Cl:
- [-180,-3.0]: as for Cd and Cm.
- [-3.0,22.2]: CFD data (WMB code), at Re=700,000
- [22.2, 180]: as for Cd and Cm.
6. Transition RISØ A1-21 - NACA64-418.
7. NACA64-418, Re=300,000 as provided in the report from ECN [9], but softened to eliminate discontinuities in the whole range [-180, 180].

Induction calculation:

FAST does not consider the 3D geometry induction when simulating parked cases. That means that the outputs obtained with FAST after a parked computation will exactly match the used 2D input curves. Comparing the FAST calculation with the measured data, it can be seen that the experimental values of Cn and Ct are always below the FAST 2D results as in 9.6.

In order to evaluate the fact of having omitted the effect of the induction, CENER calculates the induction with a Lifting Line Code (LLC) and feeds FAST with the induction results, for comparing this FAST-LLC with the original FAST 2D curves and the experimental data.

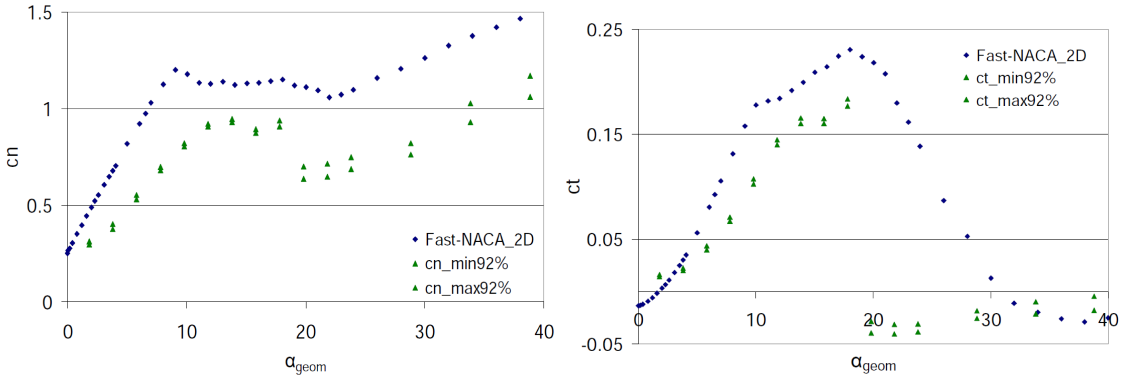

Figure 9.6 *2D aerofoil curves (blue diamonds) and experimental data (green triangles) for 92%R section.*

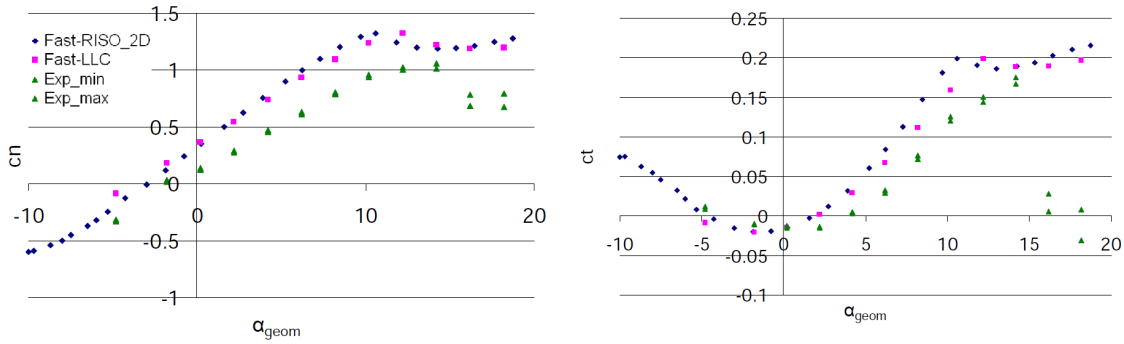

Figure 9.7 *cn-α_{geom} and ct-α_{geom} at 60% radius (RISØA1-21)*

9.3.3 Results

Results for 60%R section (Figure 9.7):

At this intermediate station, FAST 2D curve and FAST-LLC computational results show that the effect of the induction is small, as one would expect from theory. However, the experimental data has a strong discrepancy with the FAST-LLC results. Therefore one could hypothesise that the above discrepancy between FAST-LLC and experiments is not mainly related to the 3D geometric induction. Some hypothesis formulated during the Mexnext project suggest a discrepancy between what is really happening on the real tested blade, and the 2D cl and cd data used as inputs for the BEM calculations at that specific RISØ section.

Results for 92% section (Figure 9.8):

This section is closer to the tip, so the influence of the 3D end geometry induction becomes bigger, influenced by the tip vortex. The computation seems to not represent all the geometric effects on the blade (especially at high angles of attack), but one should keep on mind that LL theory does not cope with viscous and separated flow. Therefore the focus should be on angles of attack lower than around 10 degrees. Thus, the FAST-LLC computation improves the results and compares relatively well with the experiment. The discrepancy between the experimental data and the computational are still present but it seems that the tip vortex is quite well represented with the used method.

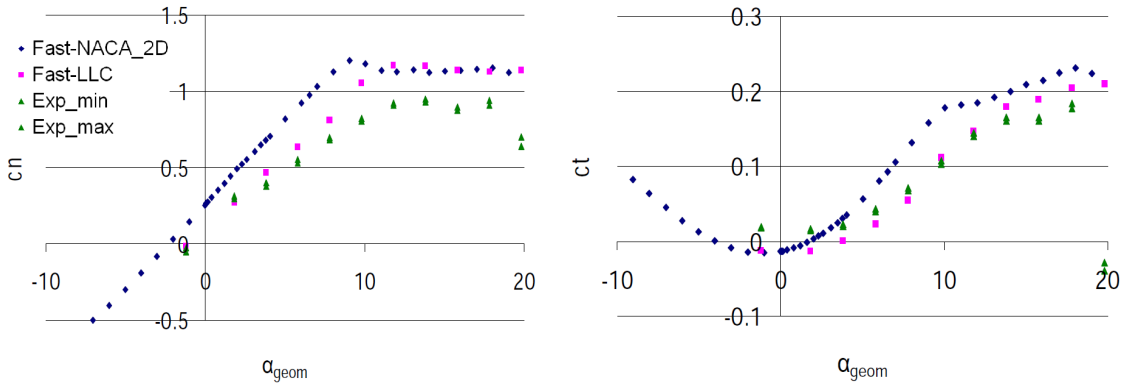

Figure 9.8 *cn-α_{geom} and ct-α_{geom} at 92% radius (NACA 64-418)*

9.3.4 Conclusions of BEM calculations at standstill

- FAST-2D over-estimates loads at parked cases, due to the fact of not considering the induction in such conditions.
- The inclusion of the induction improves the agreement between the computation and the experimental data, mainly towards the tip.
- The lifting line code had limitations because it is devoted to low angles, but anyway the methodology has proven to be a good approximation to obtain the induction influence at the blade span stations.
- It seems necessary to implement a model into the BEM codes to consider the induction due to geometric effects at parked cases.
- There is some non-understood phenomena at the 60%R station where the RISØ section has a low value on the measured forces.

9.4 CFD Computations

CFD computations were carried out to investigate the predictive capacity of the CFD method. In this section the method, as well as the initial conditions are described, and then the obtained results and its comparison with experiments. The section is finalised with conclusions.

9.4.1 Code: WMB

WMB is CENER's CFD method developed together with the University of Liverpool, capable of solving the compressible unsteady Reynolds-averaged Navier-Stokes (URANS) and DES flow equations on multi-block structured grids using a cell-centred finite-volume method for spatial discretization. It is designed to account for the motion of the blades, their structural deformation as well as turbulent flow conditions. An implicit method [31] is employed, and the resulting linear system of equations is solved using a pre-conditioned generalised conjugate gradient (GCG) method. For unsteady simulations, implicit dual-time stepping is used on the basis of Jameson's [32] pseudo-time integration approach. From the beginning, the solver was designed with parallel execution in mind and for this reason, a divide-and-conquer approach was used to allow for multi-block grids to be computed on distributed-memory machines and especially low-cost Beowulf clusters of personal computers. The code has been validated [33, 34] with the NASA-Ames Phase VI [4] experiments.

The computations carried out at this task were done solving the URANS equations. They were computed in parallel at 106 cores (X5650 processors) of the total of 400 real cores that compound CENER's (September 2011) cluster.

9.4.2 Initial Conditions

CFD results were computed in a coarse and fine grids in order to verify the grid convergence. The main grid characteristics are defined in Table 9.3. The structured hexa cell grids were created with ICEMCFD 12.0 (commercial software from Ansys). The surfaces of the employed geometry were given [35] to all Mexnext participants and for the standstill computations just a single blade was modelled.

The computations were done as quasi-steady, which means that the grids were pitched from 90° of pitch to 1° with a pitching speed of 0.02°/second and obtaining solutions at every time step. The idea behind this procedure is to obtain steady results allowing the solver to converge better and faster in each time step.

Mesh name	Total Size (cells)	chord-wise (cells)	span-wise (cells)	Boundaries (Chord units)	Boundaries (R units)
Coarse	5,670,912	230	140	I=56.25, O=56.25	I=6, O=6
Fine	11,435,620	282	191	& FF= 56.25	& FF= 6

Table 9.3 *Employed meshes for CFD computations (I=Inflow, O=Outflow & FF=Far-Field).*

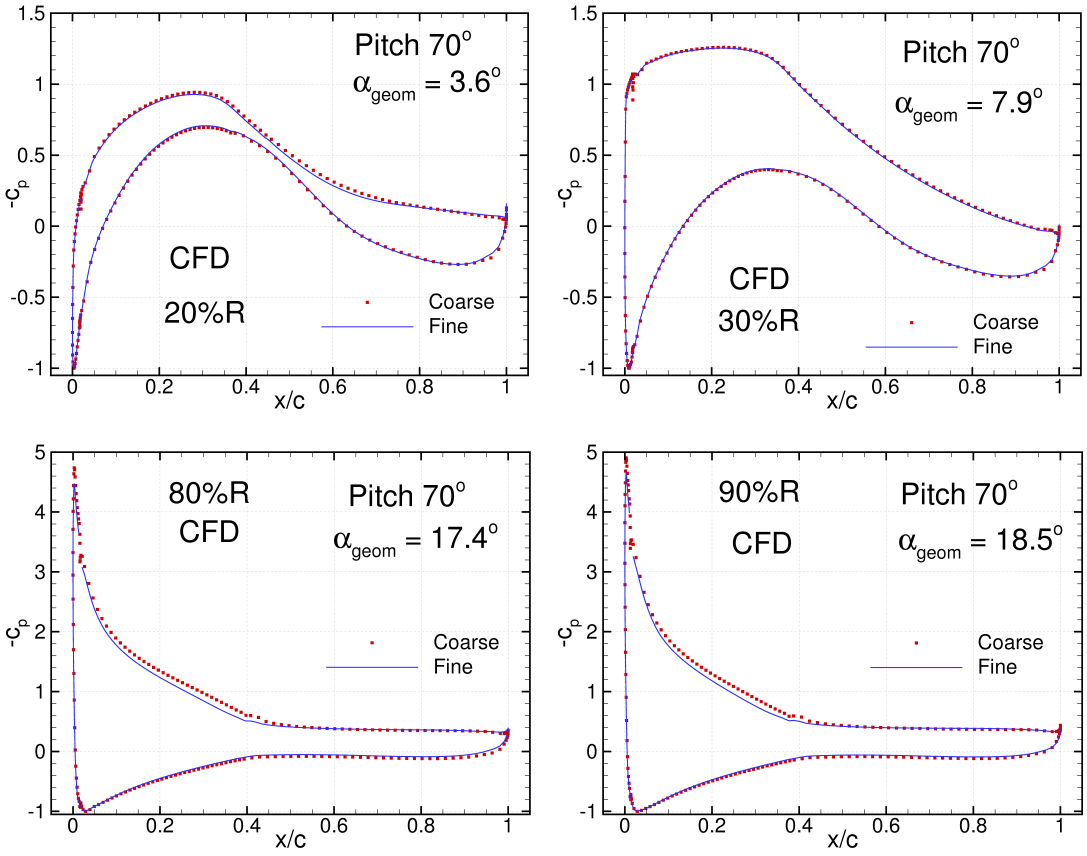

Figure 9.9 *Comparison between WMB computed c_p values at 4 radial positions and pitch angle of 70° for the coarse and fine meshes.*

9.4.3 Results

The convergence of the grid was checked comparing the results obtained with the coarse and fine grids. An example of what is happening when both solutions are compared is shown in Figure 9.9. The discontinuity seen in the blue line is due to a employed H type blocking topology to mesh the blade. Can be said that for 3.6° and 7.9° of geometrical angle of attack the agreement between coarse and fine mesh computations is very good. Some differences appears as the flow stalls, presenting the fine grid solution an earlier stall prediction than the coarser one. The solutions of the fine mesh are presented in the rest of the report since the majority of the pitching angles involved stalled flow and a better prediction is expected from the fine grid.

The results that are shown in the Figures 9.10 to 9.13 follow a similar structure, presenting on the left hand side some interesting pressure coefficient values and on the right hand side the integration of all the cp values as normal and tangential forces, as well as the moment coefficient. As has been mentioned in section 9.2, the experimental values for the 25%R and 35%R were erroneous, so in Figure 9.10 are omitted. Both radial stations shared the DU91-W2-250 profile and the major difference between them is their location (the blade's first aerodynamic section was at 20%R). The three cp graphs shown for these sections are based on the cn and ct curves from Figure 9.10. The α_{geom}≈0° show a very similar behaviour for both stations as occurs for the cn and ct curves, and in a smaller way for the cm. At α_{geom}≈24°, where the flow is on the maximum cn for the 35%R station and the 25%R has still not reached the maximum (α_{geom}≈27°). This difference, together with the smaller cn slope that can be seen indicates that for the same α_{geom} the 25%R station is more influenced by the root geometry discontinuity vortex than the 35%R station. The cp curves for α_{geom}≈60° show a completely separated flow at both sections of the blade with a

different cp values at the suction side. The curve shapes on the pressure side after the stagnation point indicates that the 35%R stations sees a higher angle of attack for the same α_{geom} which is expected since is further from the 20%R section. The integrated forces from Figure 9.10, apart of the mentioned differences, show others like the ones occurred at the post-stall region, where the cn values of the 25%R have a milder stall, as also can be seen in the ct values. Tangential force coefficient values are almost on the top of each other for α_{geom}>48°. The cm values have a similar trend but despite at $\alpha_{geom}\approx$27° crosses having the 25%R station ones higher values.

The results related to the 60%R station of the blade are shown in Figure 9.11. This section had a RisøA1-21 aerofoil and as has been concluded in section 9.2, there are some problems with experimental stagnation values and some upper and lower surface pressure transducer readings. This section is far enough from blade root and tip geometrical discontinuities, so the values shown here should be the cleanest ones, since they are mainly affected by the sectional geometry and almost 2D flow. For α_{geom}=2.2° (see Figure 9.11) the differences are largest on the suction side, over-predicting the cp values by the CFD computation. This over-prediction could be related to the differences in the experimental and computed geometries, since a comparison between CFD computation and XFOIL computation with the same geometry for the 60%R station and α_{geom}=2.2° has shown much smaller differences. Consequently, the computed cn values also over-predict the experimental ones. The computed cn first relative maximum occurred at α_{geom}=12.2°, being still on the liner slope of cn in the experimental case ($\alpha_{geom}(\mathrm{cn}_{max})$=20°). The computation show an stall of about 55% chord of the upper surface. There are large differences between computations and experiments on the upper and lower surfaces. The last α_{geom} selected for the 60%R station was 45.2°, where the flow was fully stalled, as can be seen from CFD and experimental results. At full stall the differences in the sectional geometry between experiments and computations do not play as relevant role as for the previous conditions. At this α_{geom} can be seen that the major difference is provoked by the stagnation point location and the normalisation carried out with that point. If a stagnation point correction based on CFD results is applied, normalising the rest of the pressure transducer values with the one that is at the 14%c of the pressure side, the experimental results and predictions will be much closer on pressure and suctions sides. The integrated forces show cn slope difference between experiments and computations on the first 10 ° of α_{geom}, as well as an a large under-prediction of the computed cn and ct values from α_{geom}=10° to 13°and from 20° to 25°. On the other hand, the computations are not able to predict the reduction in cn and ct experienced by the experiments at α_{geom}=16° to 18°. The post-stall trend is similar for experiments and CFD, despite computations had a general over-prediction respect the experiments. The computed cm trend on the first α_{geom}=20° is different to the experimental one and for higher α_{geom} agrees as occurs for the cn and ct values.

The last two stations that have been evaluated are the 82%R and 92%R stations, which were constructed with the NACA 64-416 aerofoil profile. Figure 9.12 show pressure coefficients and integrated force results for the 82%R station and Figure 9.13 for the 92%R station. The cp graph for α_{geom}=6.4° shows computed and experimental values for a non stalled flow. There are differences between computed and measured values. These differences, again, are not fully understood since they could be associated to the different geometry of the computed and measured blade (specially remarkable these differences for blade 3, which is the one where the measurements at 82%R and 92% were carried out) and also are accompanied by the erroneous readings of some pressure transducer. α_{geom}=12.6° correspond to a relative maximum computed cn value and the maximum experimental value occurred at $\alpha_{geom}\approx$10°. Due to this the computed cp presents smaller stall than the experimental one and an over-prediction on the suction side. At α_{geom} where the flow is fully stalled, 20.6° in this case, the trend between experiments and CFD is similar. However, there are differences in the location of the stagnation point that could be associated to the experimental resolution and in the suction peak, that probably is caused by the employed k-ω SST [36] turbulence model for the computation. As occurs for the previous station, when the

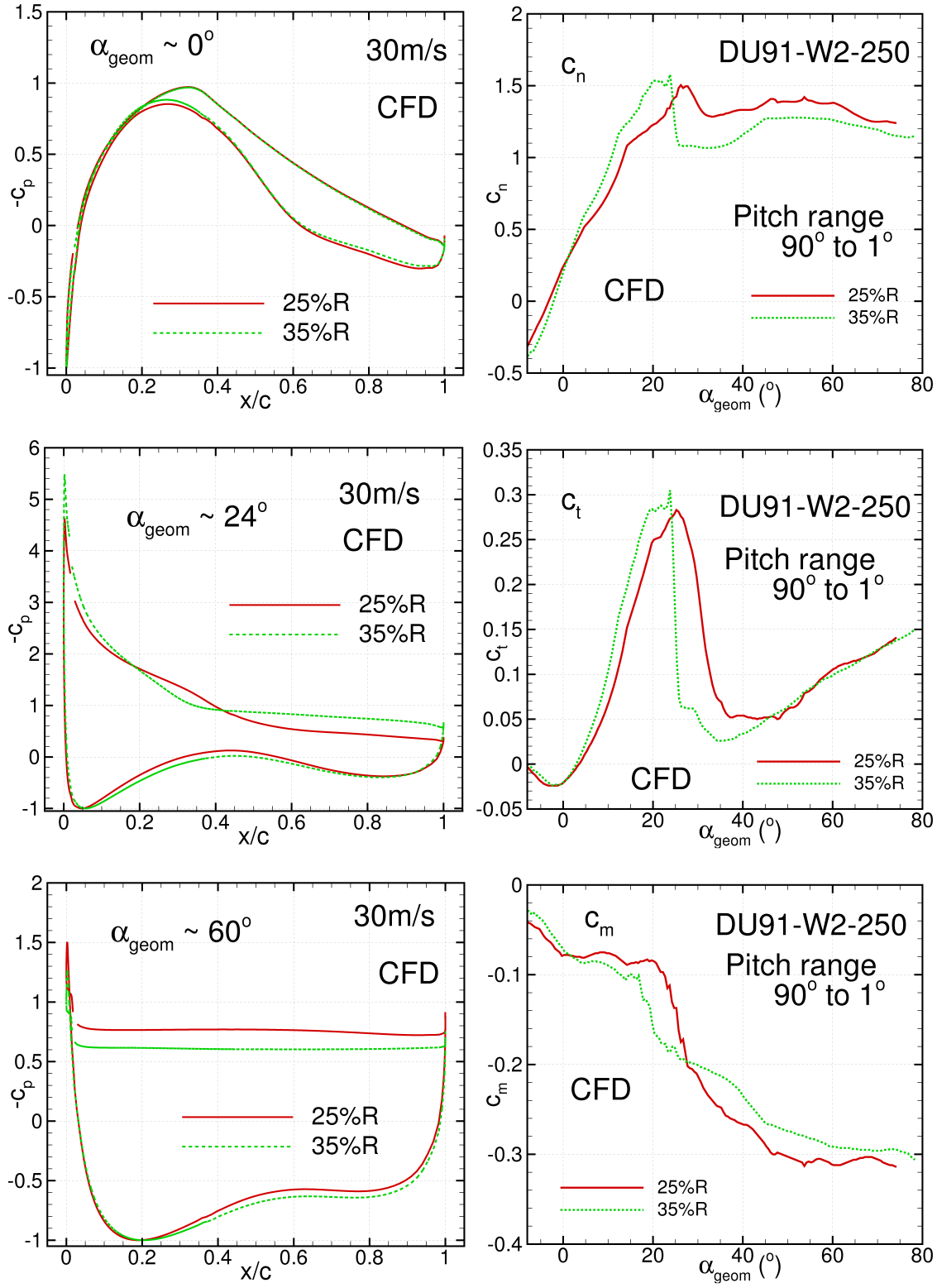

Figure 9.10 *Comparison between WMB computations of the cp and its integrations in chord-wise and normal to chord-wise directions (normal and tangential forces) at 25%R and 35%R stations for parked case.*

blade section geometry is not as critical, there is a closer agreement between CFD and experiments. The normal and tangential forces show a general over-prediction, and on the contrary of what was occurring for the 60%R station, this over-prediction also occurs near the maximum cn and ct values. The general trend is similar if CFD and experiments are compared. This is also true

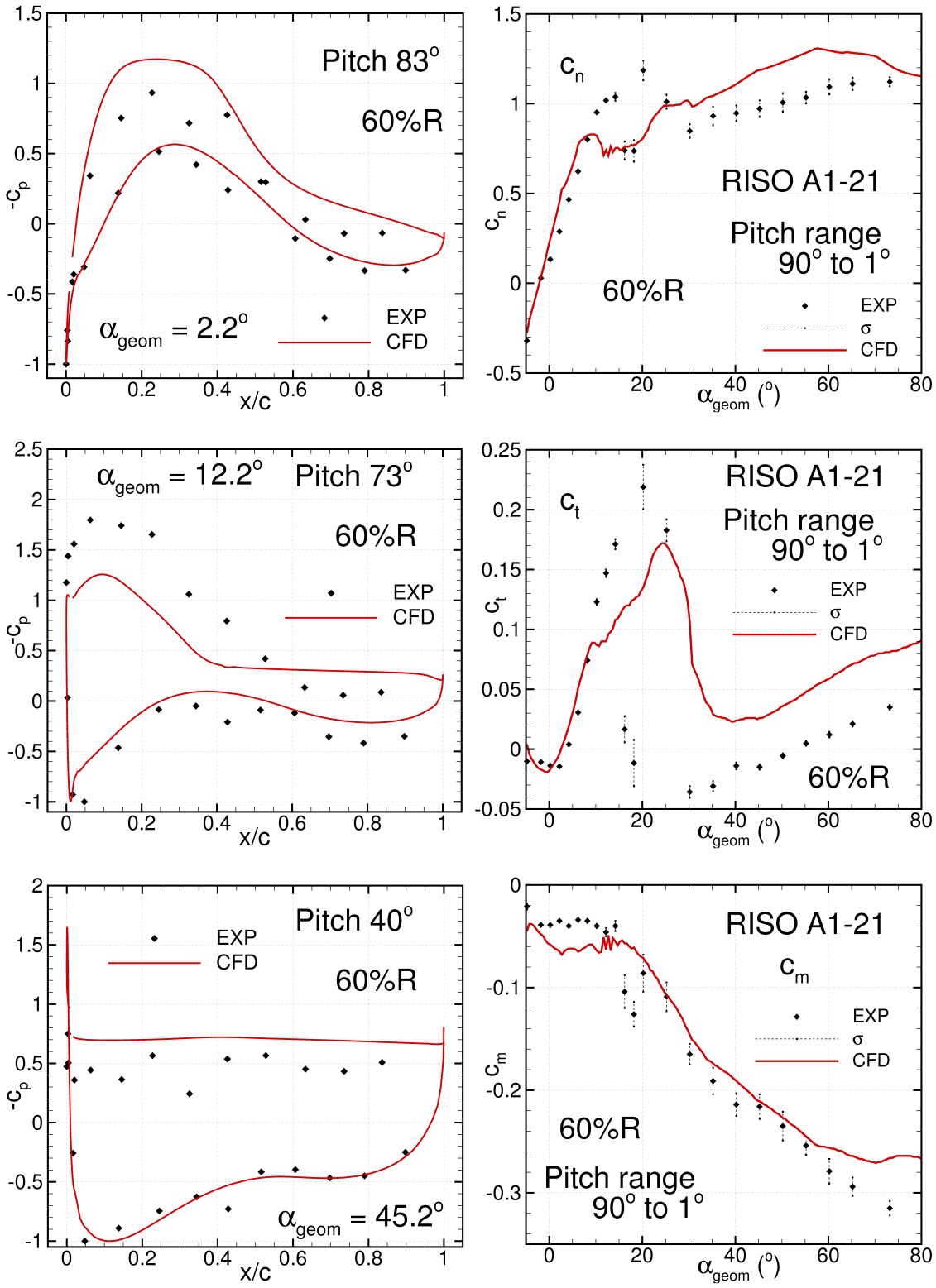

Figure 9.11 *Comparison between WMB computations and experiments of the cp and its integrations in chord-wise and normal to chord-wise directions (normal and tangential forces) at 60%R station for parked case.*

for the moment coefficient which magnitude is under-predicted by the CFD for the first 18° of α_{geom}. For α_{geom}>18° the magnitude is under-predicted to the experimental values.

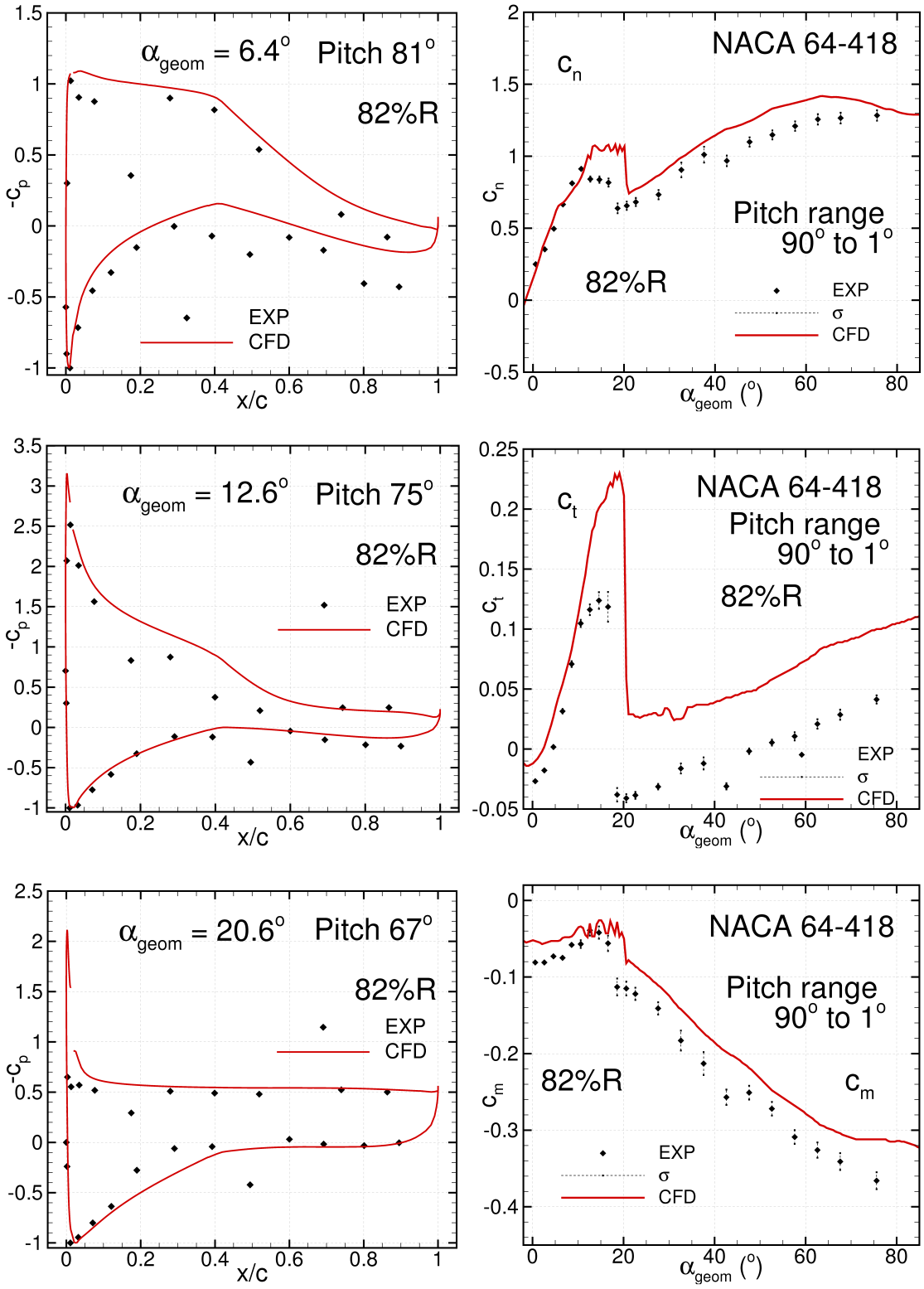

Figure 9.12 *Comparison between WMB computations and experiments of the cp and its integrations in chord-wise and normal to chord-wise directions (normal and tangential forces) at 82%R station for parked case.*

The 92%R station was designed with the same NACA64-416 aerofoil than the 82%R station. The not stalled α_{geom}=7.8° show different cp behaviours in computed and experimental values. The computed values are consistent with the values shown for a α_{geom}=6.4° at 82%R. The experimental values have inconsistencies towards the trailing edge (last 30% of the chord) and on the

7%c and 12%c of the lower surface pressure transducer readings. This non expected values of the measurements appears for all the pitch angles, as can be seen also in the other two cp graphs. At α_{geom}=13.8° there is a relative maximum cn for the experiments but the computations have not predicted the relative maximum until α_{geom} of 22° and neither has predicted the experimental cn plateau that last from α_{geom}=13.8° to ≈16.5°. Looking just the experimental values from 82%R and 92%R stations, can be seen that the 92%R ones has a delay in the maximum cn value of 1.2°. This can be explained with its proximity to the blade tip, and the influence of the tip vortex. CFD computations also follow a similar trend since the cn values before a significant drop has a consistent delay of ≈1.5°. At α_{geom}=23.8°the flow is fully stalled for the experiments and CFD computations. The differences between them are provoked by the stagnation point and the erroneous pressure transducer measurements mentioned before and the non physical suction peak provoked by the employed turbulence model. The integrated forces are closer to the experiments than for the 82%R station and the overall trend is well capture for the cn, ct and cm.

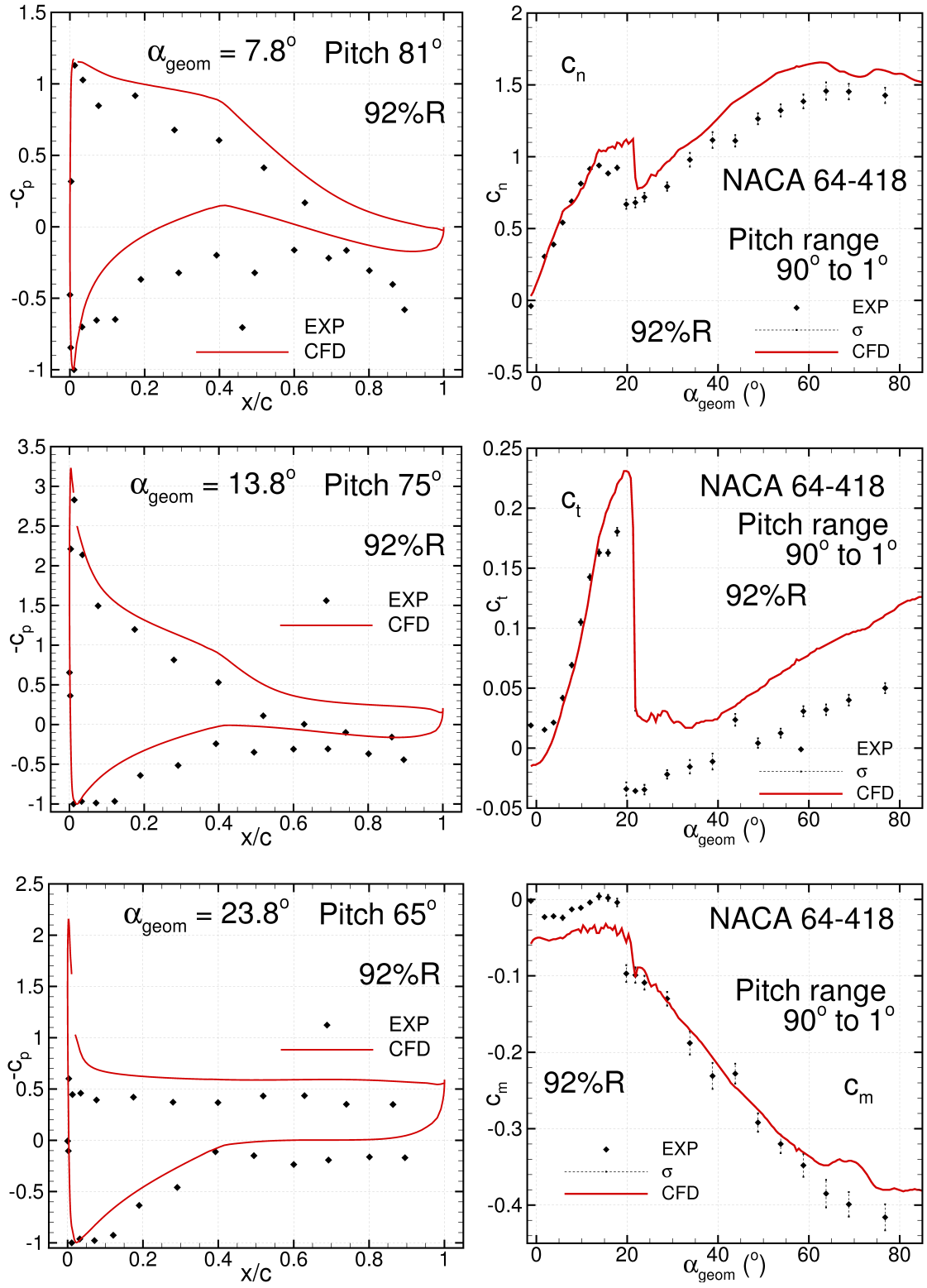

Figure 9.13 *Comparison between WMB computations and experiments of the cp and its integrations in chord-wise and normal to chord-wise directions (normal and tangential forces) at 92%R station for parked case.*

9.4.4 Conclusions of CFD calculations at standstill

- The employed mesh is dense enough for grid independent WMB computations.
- The employed H-type topology for meshing the blade could be improved with a C type topology for avoiding the discontinuities of the cp values.
- CFD generally over-predicts the pressure coefficients and consequently the integrated forces, as occurs with the rotational cases.
- A more detailed computation (DES) or different turbulence model could help in the better predicting the cn_{max} region.
- The inclusion of the recently measured blade geometries will help in a closer prediction of the CFD with the experiments.
- The lack of other CFD computations limit the comparison since they will be useful for better understanding.

9.5 Conclusions & Future Steps from Task 4.1 (Parked conditions)

- Despite a general belief that the non rotational cases are easier to predict, this task has shown that the standstill cases are not fully predictive yet.
- The uncertainties associated to the standstill data made this task more difficult to compare and more laborious.
- It seems necessary to implement a model into the BEM codes to consider the induction due to geometric effects at parked cases.
- CFD was capable to predict well the general trends of the integrated forces but not the pressure coefficients as detailed as it could be done, and consequently neither the quantitative values of the integrated forces.
- More investigation in standstill is needed, and this can be conducted with experimental data, computations or the mix of both of them.
- In order to asses the severity of the geometry deviations,of the measured blades from the theoretical blade, probation with CFD and BEM are recommended to check the effect on the aerodynamic forces when compared with experiments.

10 Task 4.2: Sensitivity of results on Reynolds Number and Rotational speed

10.1 Introduction on Task 4.2

This report deals with the results from subtask 4.2 *Sensitivity of results on Reynolds Number and Rotational Speed.*

Participant were:

ECN and AE Rotortechniek, (now: Suzlon Blade Technology) University of Applied Sciences Kiel, Germany, INTA and CENER, IFE, Norway and KARI.

The chapter is divided into two sections. The fist section deals with the dependence of results on rotational speed and the second sections reports on a full 3D CFD Model spanning a broader range of Reynolds numbers than the MEXICO experiments. The first section is mainly reported by ECN (with help of other participants) where the second section is mainly reported by UAS Kiel. Scaled down measurements from INTA and KIER play an important role in this section.

10.2 Influence of rotational speed on aerodynamic coefficients

One of the main uncertainties in blade aerodynamics lies in the effects from blade rotation on on the airfoil coefficients. These corrections are considered to be driven by the effect from the coriolis force on the chordwise pressure gradient. In [37] an order of magnitude analysis showed the local solidity (c/r) to be the dominant parameter for this effect, i.e. the largest increase in lift is found at the root.

A method to generate rotating $c_l(\alpha)$ curves from the 2D characteristics is introduced in the same reference using a factor f_{cl}. This factor is the ratio of the actual increase in c_l (i.e. $c_{l,3D} - c_{l,2D}$) and the difference dc_l between the non-viscous $c_{l,inviscid}$ (with 'inviscid' slope $dc_l/d\alpha = 2\pi$) and the 2D value of $c_{l,2D}$, Hence

$$c_{l,3D} = c_{l,2D} + f_{cl}(c_{l,inviscid} - c_{l,2D}) \tag{10.1}$$

with f_{cl} dependent on c/r only. As such the rotational speed itself is, somewhat surprisingly not included. A model which does model the rotorspeed dependency is developed by the University of Illinois, [38]. Thereto, f_{cl}, i.e. the factor which accounts for stall delay, see equation 10.1 is assumed to depend on a modified tip speed ratio Λ:

$$\Lambda = \frac{\Omega \cdot R}{\sqrt{(\Omega \cdot R)^2 + U_{hub}^2}}. \tag{10.2}$$

For all measurements which are considered in the sequel of this project, this factor is between 0.97 and 1.0. The sensitivity of the factor f_{cl} to these variations in Λ is, according the model of Illinois, negligible.

In order to assess the correctness of this assumption, the influence of rotational speed on the aerodynamic coefficients of the Mexico rotor has been investigated by considering the axial force coefficients as function of tip speed ratio, see figure 6.6.

By presenting the axial force coefficient as function of tip speed ratio the results become independent of the rotational speed unless the airfoil coefficients depend on the rotational speed. This dependency could be a result of different rotational (3D) effects on the airfoil data and/or different Reynolds influence.

It can be observed that the dependency of axial force coefficient on the rotational speed is limited also at low tip speed ratios, i.e. at large angles of attack where the rotational corrections on the airfoil data becomes much more prominent.

Another indication for the rotor speed sensitivity is found by comparing the power coefficients C_P as function of tip speed ratio. Thereto it should be realized that the axial force coefficients from figure 6.6 are mainly influenced by the lift coefficients, but the power coefficients are also influenced by the drag coefficients which are generally more sensitive to Reynolds number effects. Unfortunately the power has not been measured directly on the Mexico rotor. An attempt was made to derive the rotorshaft torque from the moments and loads at the tower foot balance according to:

$$M_{torq,rotor} = M_{torq,balance} - F_{lat,balance} \cdot towerheight \tag{10.3}$$

The rotorshaft torque obtained in this way was found to be fully rotational speed independent but nevertheless the results were believed to be unrealistic in view of a large lateral balance force even at non-yawed conditions. For this reason the rotor shaft torque has also been derived from the pressure forces even though it is acknowledged that this excludes the effect of viscous drag, which is one of the main drivers for a Reynolds number dependency.

The power coefficients as derived from these rotor shaft torque values at 324 and 424 rpm could be compared with measurements at different rotational speeds which have been taken on a 'daughter' of the Mexico rotor. This daughter has been built by KARI and it is a perfect look alike of the Mexico rotor but scaled down to a rotor diameter of 2 meter. The model is placed in an open measurement section of a KARI wind tunnel with a size of 5 x 3.75 m^2, where the Mexico rotor has a diameter of 4.5 m and was placed in an open measurement section with a size of 9.5x9.5 m^2. The test was conducted at various tip speeds, including the value of 76 m/s, which was used in the Mexico test. The maximum tip speed was 90 m/s (where the maximum tip speed in the Mexico experiment was 100m/s). Transition was fixed at 5% chord line at both the suction and pressure side, to match the Mexico experiment. The torque was directly measured with a torque sensor installed in the rotating axis. In figure 10.2 the power coefficient as function of tip speed ratio is compared for the KARI and Mexico experiment at tip speeds of 76 m/s and 90 m/s (KARI) and 100 m/s (Mexico). The maximum C_P is found near a tip speed ratio of 6.6 (as expected) and the influence of rotational speed is generally small. The $C_{P,max}$ of the KARI wind turbine ≈ 0.33 which is lower than the $C_{P,max} \approx 0.38$ of the Mexico rotor. A lower value for the KARI rotor could be expected, in view of its lower Reynolds number with high drag values: The Reynolds number near the tip of the KARI rotor varies between 1.8 to 3.2 10^5, where the Reynolds number near the tip of the Mexico rotor varies roughly between 6 and 8 10^5. Apart from this the neglect of viscous drag in the Mexico results will lead to a higher power coefficient. At low tip speed ratios (large angles of attack) pressure drag will be dominant above viscous drag but at high tip speed ratios the contribution of viscous drag is larger.

In figure 10.3 the KARI measurements at 5 different rotational speeds are presented in terms of a torque coefficient using the blade tip speed as a reference velocity in order to compare the test results for various rotating speeds:

$$C_{torque} = \frac{Torque}{0.5\rho V_{tip}^2 \pi R^3} = \frac{C_P}{\lambda^3} \tag{10.4}$$

The KARI measurements at low tip speeds (50 to 70 m/s) do indicate a clear rotor speed dependency in particular near stall ($\lambda \approx 4$, i.e $\lambda^{-1} \approx 0.25$ in figure 10.3). The explanation for the relatively strong rotor speed dependency in the KARI experiments at low rotational speeds could be a different stall delay effect. However the factor Λ from equation 10.2 at the stalling point is in the order of 0.97 for all rotational speeds. A more likely explanation might then be a relatively strong Reynolds effect from a different rotational speed, since the Reynolds number sensitivity is known to be strongest at low values of the Reynolds number, i.e. at a small wind turbine.

Figure 10.1 *KARI wind tunnel with scaled down model of Mexico rotor, compare with figure figure 4.2*

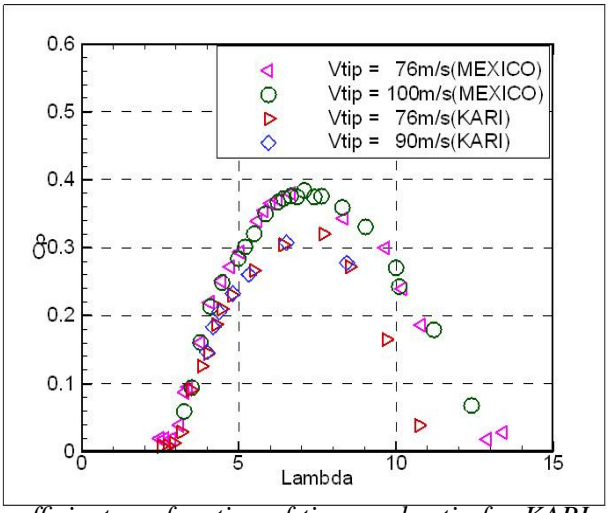

Figure 10.2 *Power coefficients as function of tip speed ratio for KARI and Mexico experiment at different tip speeds*

Finally figure 10.4 shows a very interesting result. It presents the aerodynamic force coefficients according to a procedure from [39]. Thereto the resultant force coefficient is plotted versus the resultant force angle γ for both 324 and 424 rpm. The resultant force coefficient is the resultant aerodynamic force non-dimensionalized with $0.5\rho V_{\mathrm{eff}}^2 c$. Note that V_{eff} has been determined as the sum of the tunnel speed and the rotational speed without induced velocities. The resultant force angle γ is the angle between the resultant force and the chord. Again very little effect of the rotational speed is found. Figure 10.4 shows the result for 82% span but a similar observation can be made for the other instrumented sections. Figure 10.4 also shows the resultant force coefficient from the 2D airfoil measurements. These results compare well with the 3D measurements (although this is less true at more inboard locations where clear 3D effects are apparent).

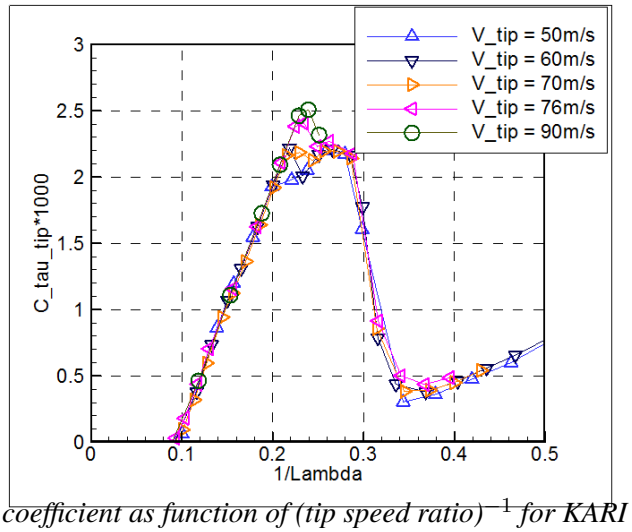

Figure 10.3 *Torque coefficient as function of (tip speed ratio)$^{-1}$ for KARI experiment*

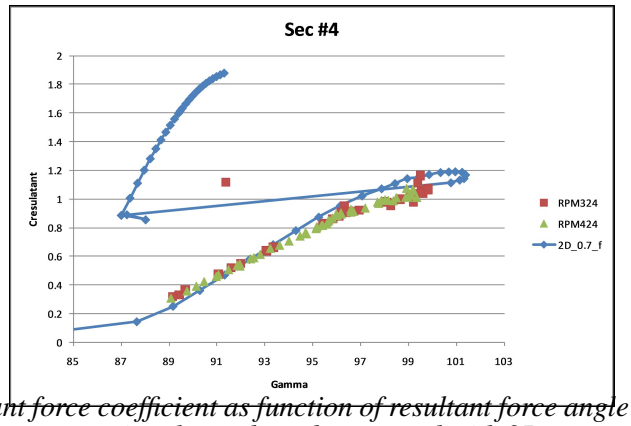

Figure 10.4 *Resultant force coefficient as function of resultant force angle γ for 82% span measured at two rotational speeds and compared with 2D measurements*

10.3 Measurements performed by INTA, Spain

INTA Spain performed wind tunnel tests with an approximately 1:4 scaled-down model [40]. In fig. (10.5) the outline of their experiment is shown. Fig. (10.6) gives c_P vs λ (= Tip-Speed-Ratio). A clear drop in $c_P^{max} \approx 0.1$ compared to the Mexico and KARI measurements can be seen.

Figure 10.5 *Outline of INTA's wind tunnel experiment*

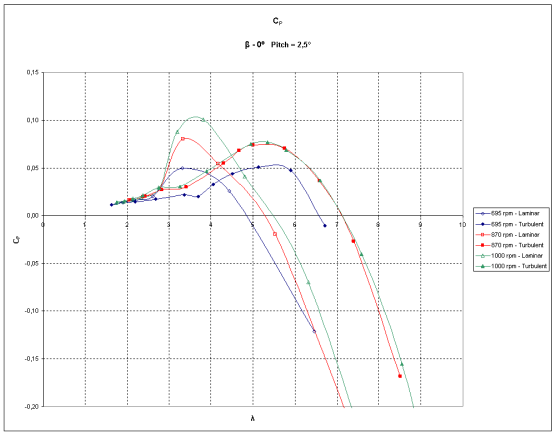

Figure 10.6 *C_P vs tip speed ratio of INTA's 1:4 scaled down model*

10.4 CFD Modeling of Reynolds number sensitivity

Measurements achieved a change of Reynolds number by scaling the MEXICO rotor to smaller diameters. A totally different approach is to keep diameter and tip speed ratio (TSR) constant while wind speed v_∞ and rotational frequency ω are changed. A couple of computations were done for a constant TSR $\lambda = 6.7$ with the TAU code of German Aerospace Center (DLR) which are listed in table 10.1. For the calculations a single blade was put in a $120°$ section with rotational periodicity as described in [41].

Table 10.1 *List of computations for constant TSR* $\lambda = 6.7$

ω [RPM]	62	93	124	224	324	424	524	624
v_∞ [ms^{-1}]	2.2	3.3	4.4	7.9	11.4	14.9	18.4	21.9
Re_c at $0.6R$	25025	38434	52348	99812	149459	200518	252156	304525

The local chord Reynolds number in table 10.1 is defined as

$$Re_c = \frac{c(r) \cdot \sqrt{v_\infty^2 + (\omega r)^2}}{\nu} \quad \text{with} \quad v_\infty = \frac{\omega R}{\lambda} \quad \Rightarrow \quad Re_c = \frac{c}{\nu}\sqrt{\left(\frac{R}{\lambda}\right)^2 + r^2} \cdot \omega \tag{10.5}$$

with $c(r)$ as the local chord length dependent on the local radius r, ν is the viscosity. With λ transposed to wind speed v_∞ we see that $Re_c \propto \omega$ or with λ used again $Re_c \propto v_\infty$.

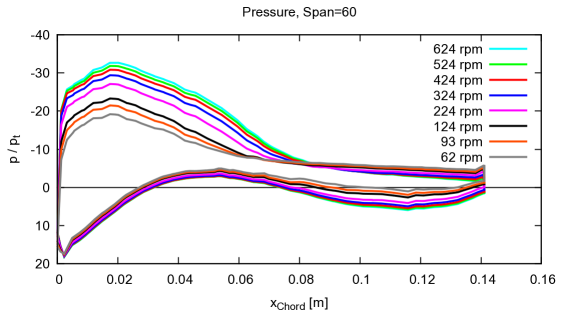

Figure 10.7 *Pressure profiles*

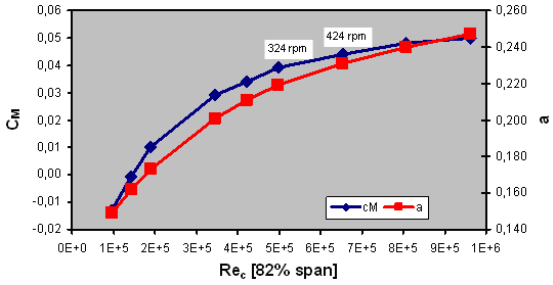

Figure 10.8 *Moment coefficient* c_M *and induction factor* a

Local quantities like the pressure profile at 60 % span (fig. 10.7) were analyzed. The pressure was normalized by the total pressure $p_t = \frac{1}{2}\rho v_\infty^2$. It can be seen that the local pressure stays almost unchanged for $\omega > 224$ RPM. For lower ω the pressure profile changes on the suction side of the blade.

The sensitivity on Re_c can be seen also in the global quantities like moment coefficient c_M or induction factor a in fig. 10.8. It was argued that the decrease of c_M and a with decreasing Re_c is only due to a change in angle of attack α. So α was computed with the method of Shen et al. [42] and the equation

$$\alpha = \Phi - \Theta - \varepsilon \qquad \text{with inflow angle} \quad \Phi = \arctan\left(\frac{(1-a)v_\infty}{(1+a')\omega r}\right) \tag{10.6}$$

where the vertical induction factor is assumed to be $a' \ll 1$, ε is the twist angle.

The findings for both methods are displayed in tab. 10.2 where the angle of attack α is derived by method of Shen et al. [42], $\Delta\alpha$ from both methods and the changes of lift and drag coefficients c_{lift} and c_{drag} for a change of $\alpha = 1°$ in the determined region of α.

The variation of α and the resulting effects on lift and drag are found to be so small that they can

Table 10.2 *Change in angle of attack α between 124 RPM and 424 RPM*

Span (%)	Profile	α by [42] (°)	$\Delta\alpha$ in (°) by ref. [42]	$\Delta\alpha$ in (°) by eq. (10.6)	Δc_{lift} $(1/°)$	Δc_{drag} $(1/°)$
35	DU91-W2-250	8.52	0.83	1.27	0.025	0.004
60	Risø A1-21	5.55	0.69	0.80	0.110	0.001
82	NACA64-418	4.86	0.39	0.59	0.095	0.001

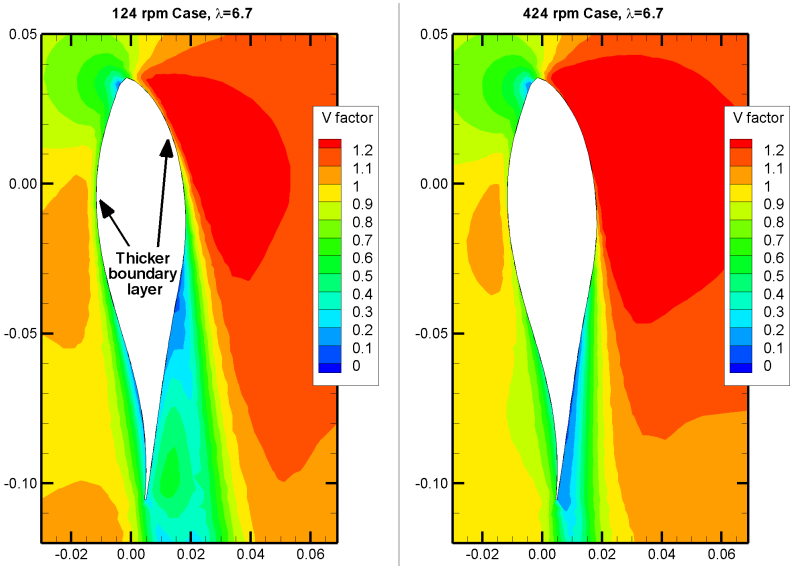

Figure 10.9 *Flow field at 60 % span for 124 RPM and 424 RPM*

not be the only reason for the decrease of c_M in fig. 10.8. An analysis of the aerodynamic flow around the blade has shown that the boundary layer thickness increases with decreasing $\omega \equiv Re_c$ (fig. 10.9). The growth of the boundary layer leads to a decambering of the aerodynamic profile and causes a major drop in lift.

10.5 Summary and Conclusions on task 4.2: Sensitivity of results on Reynolds Number and Rotational speed

Within the subtask *Sensitivity of results on Reynolds Number and Rotational Speed* several approaches were used to investigate the effect of Reynolds number change. In addition to the RPM-variation performed by ECN, KARI and INTA conducted wind-tunnel measurements with scaled-down models of 1:2 and 1:4 resp., in comparison to the original MEXICO rotor.

Therefore experiments spanned a range of Reynolds numbers from 700 10^3 (MEXICO) to 350 10^3 (KARI) and 180 10^3 (INTA).

UAS Kiel performed CFD simulations down to 120 10^3 observing a strong decrease in performance almost down to zero output power. Detailed post-processing showed a small influence of changes of angle of attack, but by far a bigger one in de-cambering due to increased thickness of the boundary-layer. These findings were in general agreement with the measurements mentioned before.

11 Task 4.3: Angle of Attack

11.1 Introduction on task 4.3

In aerodynamic prediction codes using airfoil data, such as Blade Element Momentum (BEM) methods or Actuator Disc/Line/Surface Navier-Stokes techniques, angle of attack is an important quantity which is required to know at each cross-section on rotor blades. When the angle of attack is known, the loading on each cross-section can be calculated by using the blade element theory and tabulated airfoil data obtained from 2D wind tunnel measurements with correction to rotational effects. A wrong estimation of the angle of attack on a rotor blade can influence subsequent predictions of the rotor performance. However the definition, determination and measurement of the angle of attack on a rotating wind turbine blade is far from straightforward. In this task, the goal is to determine the angle of attack on the Mexico rotor using the detailed surface pressure and Particle Image Velocimetry (PIV) flow field data measured in the German-Dutch DNW wind tunnel. When the angle of attack is determined, the lift-drag characteristics can be found subsequently from the surface pressure measurements. The Mexico rotor in both axial flow and yaw conditions will be considered. The task period is from the 1st of September, 2009 to the 30th of September, 2010 and the following partners: CENER, DTU-MEK, DUT, ECN, RISØ-DTU, SBT participated in the task.

It is recalled that the rotor model has three blades with a diameter of 4.5 m. Three different airfoil sections were used in the design: DU91-W2-250 from 20 to 45% span, RISOE-A1-21 from 55 to 65% span and NACA 64-418 from 70 to 100% span. One hundred forty-eight dynamic pressured sensors were installed at five sections of 25, 35, 60, 82 and 92% span to measure the blade surface pressure. Because of geometrical constraints, it was not possible to mount all pressure sensors on one blade. Hence, they were divided over three blades. Blade 1 was instrumented at sections of 25 and 35% span, blade 2 was instrumented at 60% span and blade 3 was instrumented at 82 and 92% span.

Besides the pressure measurements, flow fields were also investigated by stereo PIV and the PIV sheets are divided into two sets: axial and radial transverses. The position of the PIV sheets was always in a horizontal plane and at 270° azimuth when looking at the turbine from upstream. Due to the limited space of the PIV measurements, the velocity in the radial transverse was only measured in the region from 52.3% span to the blade tip.

To determine the angle of attack, three different methods are used to determine the angle of attack on the Mexico blades: Inverse BEM method [43], [44], Inverse free wake method [45], [46] and direct method [47] [48]. The three methods are summarized here:

1 **Inverse BEM method**
To determine the angle of attack on a rotating blade, the most straightforward way is to use the inverse BEM method because the BEM technique uses the concept of angle of attack and airfoil data. The technique employs the measured normal and tangential force on blade sections obtained from pressure measurements and uses the BEM theory iteratively to establish the axial and tangential inductions at the blade which is induced from the turbine wake. When the code converges, the angle of attack can be found from the velocity triangle at the blade. For more details about the technique, the reader is referred to [43], [44], etc..

2 **Inverse free wake method**
The inverse free wake method uses a similar principle as the inverse BEM method. It employs the measured normal and tangential force on blade sections and then establishes the wake in the way as in a free wake model. When the wake is established, the axial and tangential inductions at the blade section can be calculated from the generated wake. Using the obtained inductions, the angle of attack can be determined. For more details about the inverse free wake model, the reader is referred to [45], [49].

3 **Direct method**
The direct method employs both the surface pressure and PIV velocity measurements. First, the blade is divided into a number of cross-sections, where the local blade forces are known. For rotors subject to axial inflow conditions, the angle of attack at a given cross-section does not vary with the azimuth angle. Second, a number of monitor points is chosen where the velocity is known. In the Mexico project, due to the limited space of the PIV measurements, the velocity was measured in the region from 52.3% span to the blade tip. Therefore the airfoil characteristics can be investigated only in this zone, which excludes the DU91-W2-250 profile. Third, the obtained angle of attack may depend slightly on the distance between the monitor point and the airfoil section. The reason is that in the present technique the circulation of bound vortex in a radial cross-section is represented by a point vortex, located at the one quarter point from the leading-edge. Thus, due to the singular nature of a point vortex, the monitor point where the velocity is measured is preferable to be chosen at a distance of more than 1 chord-length away from the leading edge. It should be emphasized that due to the non-uniformity of the velocity field, the pressure and PIV data used to derive the airfoil characteristics, are measured at the same time. For more details about the technique, the reader is referred to [47], [50].

11.2 Results

In this section, results obtained from the three different methods will be summarized and discussed for the Mexico rotor in both axial flow and yaw conditions.

11.2.1 Mexico rotor in axial flow

To determine the angle of attack on the Mexico rotor, the first considered case is the Mexico rotor operated at a rotor speed of 324.5 rpm and a pitch angle of -2.3 degrees. Both the inverse BEM method and the inverse free wake method are used. In figure 11.1 the lift and drag coefficients are plotted in function of angle of attack on the blade at spanwise positions of 25%, 35%, 60%, 82% and 92%. At 25% and 35% span, the lift coefficient at small angles of attack (< 10 degrees) is seen to be smaller than 2D values and after that the 3D Cl increases rapidly and higher than 2D values which is caused by the stall delay phenomenon due to the rotational effects. It is worth noting that the results obtained from the inverse BEM method is higher than those from the inverse free wake model. This is probably due to the contribution of the root vortices. At 60% span, the Cl from both methods is smaller than that of 2D which is because at ($r > 0.5R$) the rotational effects have limited contributions. It should also be remarked that the inverse BEM method predicts higher Cl than the inverse free wake model. At 82% and 92% span, almost the same results are predicted from both methods and they are very close to the 2D values. For the drag coefficient, both methods predict almost the same results at nearly all tested spans.

In figure 11.2, the Cl and Cd at 25% span extracted by the inverse BEM method are plotted in function of angle of attack for the Mexico rotor at a rotor speed of 424 rpm. Similar behaviors can be obsered as it is at 324.5 rpm: the 3D lift coefficient at small angles of attack (< 8 degrees) is smaller than the 2D curve and after that it is higher than the 2D due to the stall delay caused by the rotational effects. In the same figure, different correction models are compared. For the drag coefficient, no big difference can be observed.

The direct method has been applied to determine the angle of attack on the Mexico rotor at a rotor speed of 424 rpm and wind speeds of 10, 15 and 24 m/s. Both pressure and PIV measurements are used simultaneously. Utilizing the technique of determining the AOA [48] and the measured data at the three wind speeds, airfoil characteristics are derived for RISØ and NACA airfoils at various radial stations (see Figure 11.3). Note that only three wind speeds are considered in the present study. The reason is that the PIV system was only used to measure the velocity field at a

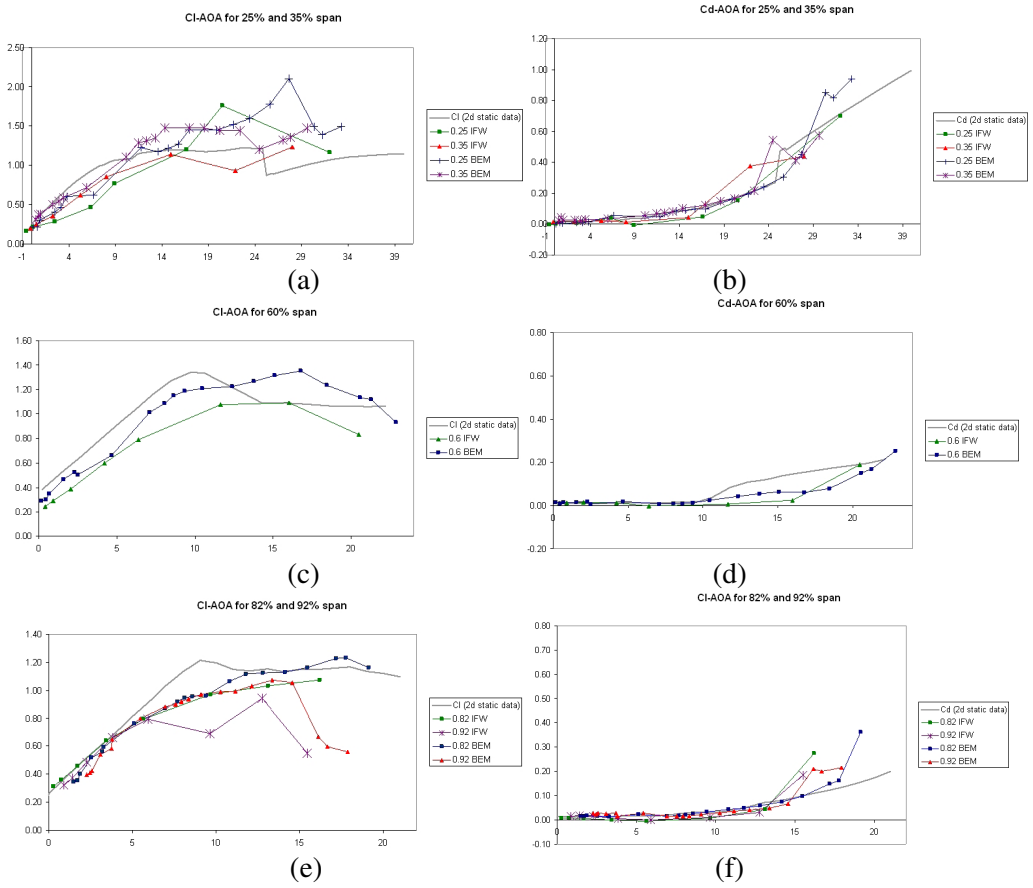

Figure 11.1 *Cl and Cd versus angle of attack for the Mexico rotor at a rotor speed of 324.5 rpm and a pitch angle of -2.3 degrees, (a) Cl-α at 25% and 35% span (b) Cd-α at 25% and 35% span, (c) Cl-α at 60% span,(d) CD-α at 60% span, (e) CL-α at 82% and 92% span, (f) CD-α at 82% and 92% span*

few wind speeds due to the large amount of data required for PIV. Hence, it is difficult to build up a set of airfoil data with a fine resolution. Instead the derived sectional airfoil data are fitted using spline interpolation functions. For comparison, 2D lift and drag coefficients are also plotted in the figure. The lift coefficient of the Risoe airfoil is seen to be smaller than the 2D lift characteristics at low AOA's. At different radial positions, from 0.55R to 0.65R where the RISØ airfoil is used, the derived airfoil data are all different. From an earlier study, the airfoil data for airfoils located in the mid of a blade were found to be almost identical to their corresponding two-dimensional values. Therefore, the difference between the 2D and the 3D airfoil data is most likely due to the change in rotor geometry when going from one airfoil type (DU or RISØ) to another (RISØ or NACA) and possibly with a small positive or negative radial velocity. Hence, the attached flow may be destroyed, which may cause a rise in pressure on the suction side. The slopes of the derived lift curve decreases when the radial position moves towards the tip. At high AOAs, the derived lift coefficient is higher than the 2D value. This is due to the stall delay caused by the Coriolis force which acts as a favorable pressure gradient at positions where a positive radial flow exists.

To check whether the obtained airfoil characteristics can be used to predict the performance of the Mexico rotor at other operating conditions, computations are carried out at different tunnel speeds, pitch angles and rotor speeds. Figures 11.4 and 11.5 show the axial and tangential forces at a rotor speed of 324.5 rpm, different pitch angles and tunnel wind speeds of 11.0 and 16.9 m/s, respectively. From the figures, very good agreement between the BEM code with extracted airfoil data and the experimental data is seen for both axial and tangential forces.

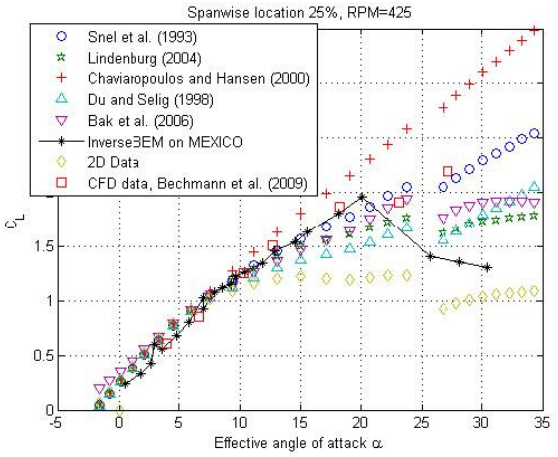

(a)

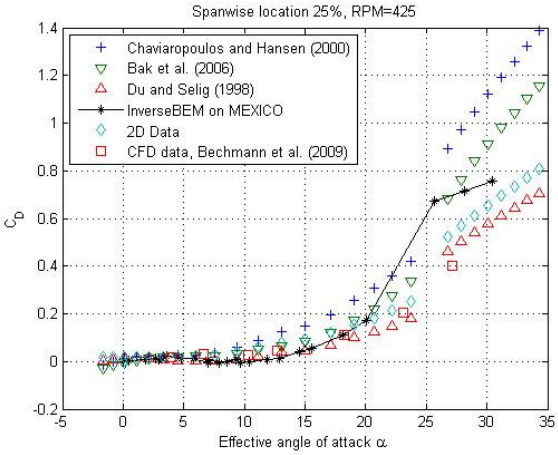

(b)

Figure 11.2 *Cl and Cd versus angle of attack at 25% span of the Mexico rotor at a rotational speed of 424 rpm and a pitch angle of -2.3 degrees*

11.2.2 Mexico rotor in yaw flow

The determination of angle of attack is also performed for flows past the Mexico rotor in yaw. The airfoil characteristics extracted from the flow past the Mexico rotor at a rotor speed of 424 rpm and a wind speed of 15 m/s and a pitch angle of -2.3 degrees is shown in Figure 11.6. The lift coefficient obtained from the inverse free wake method is compared to the 2D static data and the results of BEM and direct free wake models. From the figure, it is seen that the lift of the NACA airfoil from the inverse free wake model has a dynamic lift loop whereas the other two methods aligning with the 2D lift data.

The direct method for determining the angle of attack is also applied to the Mexico rotor in yaw. As the induction is dependent of the azimuth position and the PIV measurements were only performed at 270 degrees, a yaw model is required. From the Actuator Line/Navier-Stokes computations [51], a yaw model was derived

$$a = \overline{a}\{1 + \gamma(\frac{r}{R})^2 \sin[\psi + \frac{\pi}{2}(\frac{r}{R} - 1)]\} \qquad \text{for } r/R > 0.6 \tag{11.1}$$

$$a = \overline{a}(1 - 0.46\gamma \cos\psi) \qquad \text{for } r/R < 0.35 \tag{11.2}$$

where γ is the yaw angle, ψ is the azimuth angle and a is the axial induction factor. Using the yaw model and pressure measurements, the airfoil characteristics is obtained. From Figure 11.7, it is seen that small dynamic loops are observed for both RISØ and NACA airfoils, which are

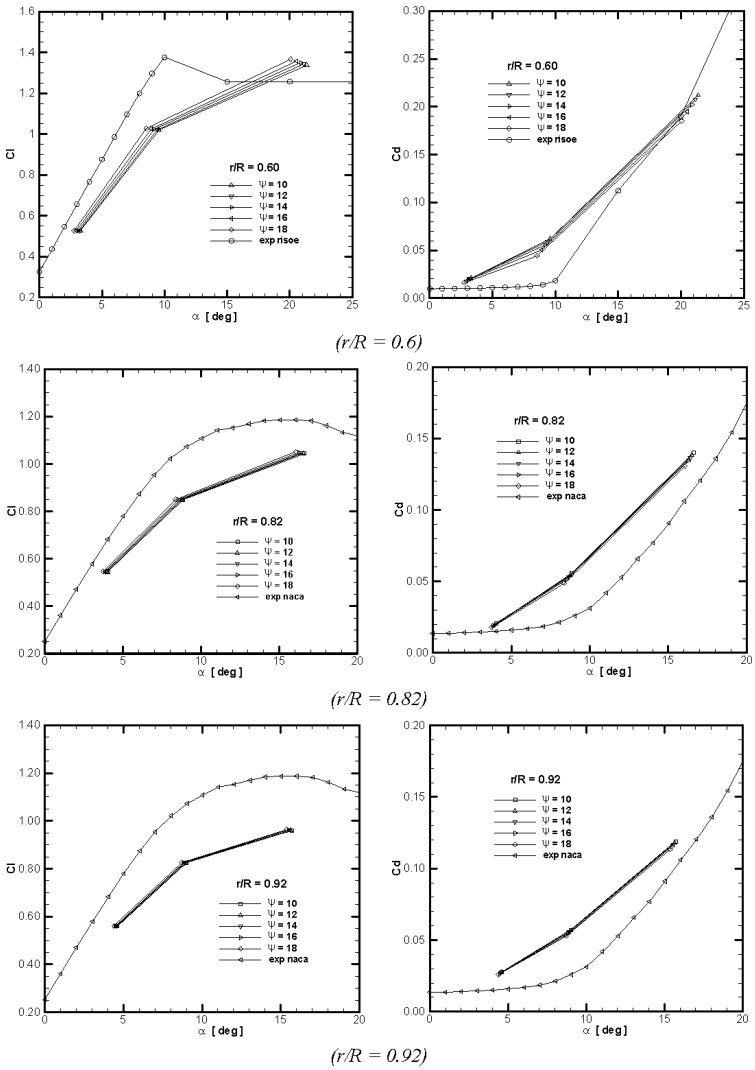

Figure 11.3 *The airfoil characteristics at three radial sections and different azimuth positions*

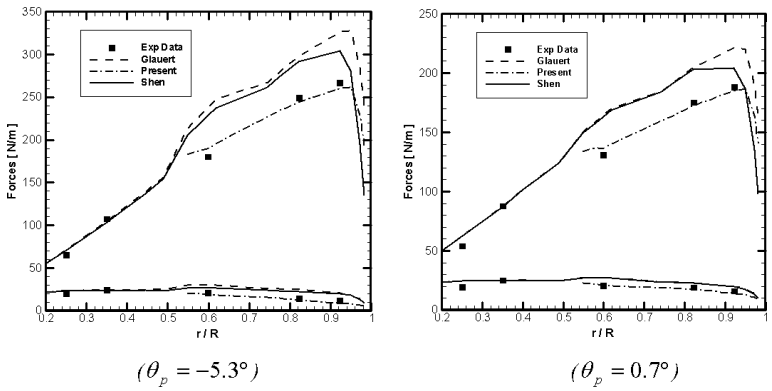

Figure 11.4 *Comparison of axial and tangential force distributions determined from experimental data, BEM using derived airfoil data and BEM using 2D airfoil data for the Mexico rotor at Vo = 11.0 m/s (λ = 6.96) and 324.5 rpm.*

close to the results of the inverse free wake model.

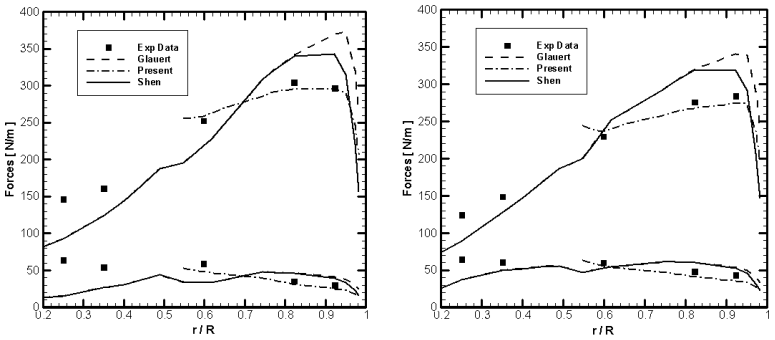

$(\theta_p = -5.3°)$ $(\theta_p = -0.3°)$

Figure 11.5 *Comparison of axial and tangential force distributions determined from experimental data, BEM using derived airfoil data, BEM using 2D airfoil data for the Mexico rotor at Vo = 16.9 m/s (λ = 4.53) and 324.5 rpm*

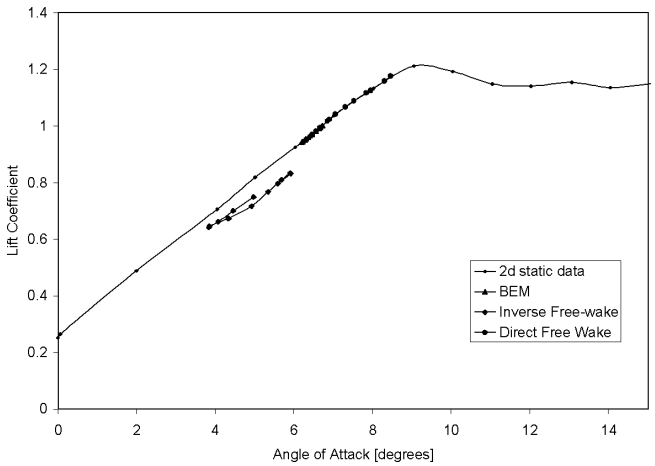

Figure 11.6 *Cl-α data at 92% span obtained with the inverse free wake model for the Mexico rotor at a wind speed of 15 m/s (λ = 6.67), a pitch angle of -2.3 degrees and a rotor speed of 424 rpm*

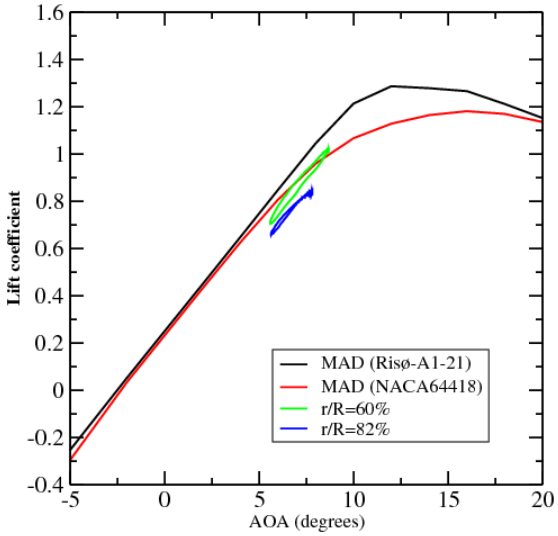

Figure 11.7 *Cl-α data at 82% and 92% span obtained with the direct model for the Mexico rotor at a wind speed of 15 m/s (λ = 6.67), a pitch angle of -2.3 degrees and a rotor speed of 424 rpm*

12 Task 4.4: Near wake aerodynamics, including tip vortex trajectories and the turbulent wake state

12.1 Introduction on task 4.4

The present task is dedicated to wake studies of the MEXICO rotor. This task is structured in the following subtasks:

Task 4.4-A Near wake flow field and wake deficit

Task 4.4-B Vortex trajectory and vortex strength

Task 4.4-C Impact of numerical set-up and discretization

In the present report results of the subsequent institutions will be presented and discussed.

- École de technologie supérieur, Montréal, Canada (ETS)
- University of Victoria, Canada (Uvic)
- University of Stuttgart, Germany (Ustutt)
- Korea Aerospace Research Institute, Korea (KARI)
- University of Gotland, Sweden (HGO)
- Royal Institute of Technology, Sweden (KTH)

Thereby various numerical methods were used. ETS uses a RANS model with an actuator surface model for the blades [52]. UVIC uses a BEM based code and an accelerated potential-flow based code with a lifting line representation of the blades. USTUTT uses unsteady RANS simulations considering the nacelle and the blade geometry with a fully resolved boundary layer [53]. KARI performs fluent calculations. HGO & KTH use the (U)RANS code EllipSys3D in combination with an actuator line model. For additional information about the numerical models see the code description section C.

12.2 Task 4.4-A Near wake flow field and wake deficit

In this section the wake is analyzed by the evaluation of radial traverses behind the rotor. In section 8 the measured axial and radial traverses of the flow field velocities at zero yaw were already compared to numerical results. However these results are also important for the study of the near wake aerodynamics in this task. The investigations from task 3 are completed by the evaluation of additional instantaneous and averaged radial traverses to compare the development of the wake. Therefore several radial traverses were extracted at the following axial locations: $x = +0.306514$; $+1.25$; $+2.25$; $+3.5$; $+4.5$; $+6.75$ and $+9.0$ meter. It shall be mentioned that for $x = +1.25$ / $+2.25$ / $+3.5$ / $+4.5\,\mathrm{m}$ no radial traverses were measured but at least for a noticeable radius regime ($\mathrm{r/R} = 0.51 \approx 0.88$) data could be extracted from the two measured axial traverses. The axial locations of $x = +6.75\,\mathrm{m}$ and $+9.0\,\mathrm{m}$ lie outside of the PIV regime. The investigations in this subtask are intended to study the (numerical) wake dissipation rather than to examine the impact of the wind tunnel environment on the wake aerodynamics which is supposed to influence the flow field at least at $x = 9.0\,\mathrm{m}$ downstream position by the upstream effect of the collector. The radial traverses at the defined positions cover a range from $0\,\mathrm{m} \leq \mathrm{r} \leq 3\,\mathrm{m}$, so that the whole area behind the rotor can be considered. The radial traverses from the numerical

simulations were extracted at a horizontal plane at 9 o'clock position for azimuth angles of 0; 20; 40; 60; 80; 100 degrees for blade one. These positions were also considered in task 3 (section 8). It should be mentioned that an extraction of the radial traverses from the measured axial traverses is only possible for the $0°$ azimuth of blade one. For the other azimuth angles a comparison is only possible between the different numerical simulations. The evaluation of the near wake flow field was performed for the three wind speeds $U_\infty = 10\,\mathrm{m/s};\ 15\,\mathrm{m/s};\ 24\,\mathrm{m/s}$ at zero yaw.

Figures 12.1(a-d) show the axial velocity at four different axial positions behind the rotor for the $U_\infty = 10\,\mathrm{m/s}$ inflow velocity. In general it can be seen that all simulations show a similar trend.

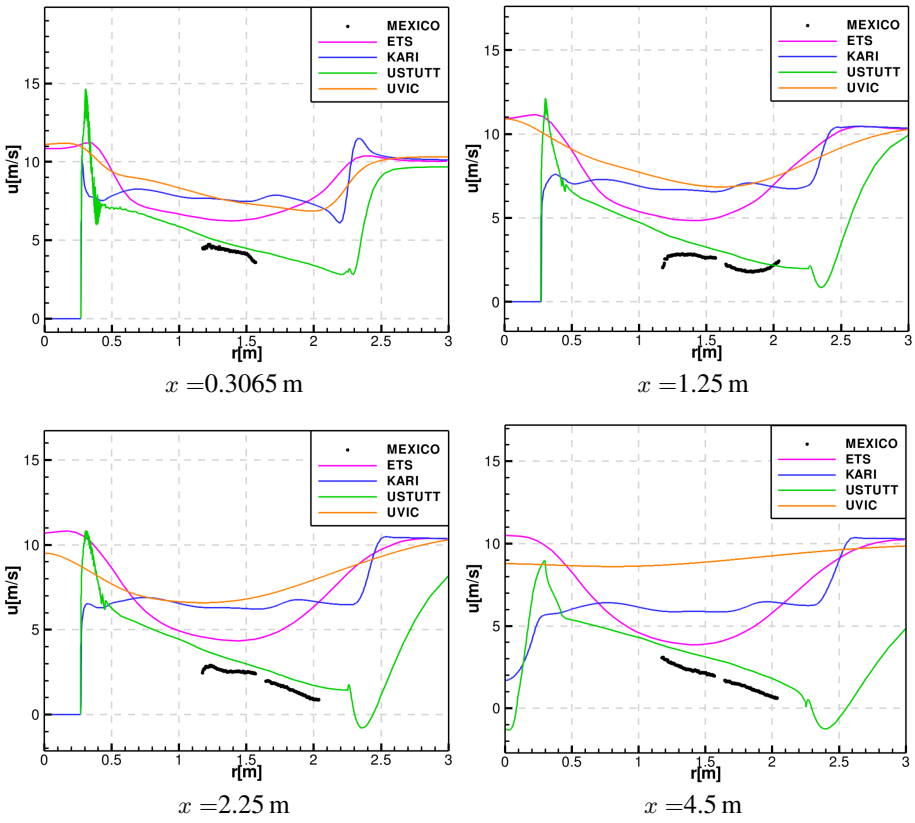

Figure 12.1 *Radial traverse for* $10\,\mathrm{m/s}$ *upstream velocity at* $x = 0.3065\,\mathrm{m}$*;* $1.25\,\mathrm{m}$*;* $2.25\,\mathrm{m}$ *and* $4.5\,\mathrm{m}$ *axial position for* $0°$ *azimuth of blade one*

In the region of the blade between $r = 0.21\,\mathrm{m}$ and $r = 2.25\,\mathrm{m}$ all simulations show a reduction of the axial velocity increasing over the blade radius r. This is also represented by the measurements. Far downstream at $x = 4.5\,\mathrm{m}$ axial position the measurements show a deceleration of the axial velocity up to almost $0\,\mathrm{m/s}$ near the tip region. This strong flow deceleration is predicted by one of the simulations. Significant is that all simulations fit the measurements best in the vicinity of the rotor. Further downstream the results deviate much stronger from the measurements. In contrast to the mid span of the blade, no measurement data is available for the root and the tip region. Comparing the different simulations it can especially be seen in figure 12.1(a) that in the area of $r \approx 0.3\,\mathrm{m}$ two simulations show a significant peak. This peak is caused by the influence of the nacelle geometry which was considered in some simulations. Outside the tip region, which is located at $r = 2.25\,\mathrm{m}$, all simulations show a more or less smooth rising of the axial velocity. The two simulations which model the blade geometry in detail provide the highest velocity gradient in this region. Moreover, it can be seen that the velocity gradients at $2.25\,\mathrm{m}$ radial position decrease downstream.

Figures 12.2 (a-d) show the evaluation for $U_\infty = 15\,\mathrm{m/s}$ inflow velocity. The measurements show a conspicuous decrease of the velocity at $r \approx 1.4\,\mathrm{m}$ (figures 12.2 (a-c)). This decrease is not

represented by any of the simulations. Except for this region the simulations show the same trend as the measurements. In contrast to the behavior for $U_\infty = 10\,\mathrm{m/s}$ the axial wake velocity slightly increases or is more or less constant for $r > 1.6\,\mathrm{m}$. The deceleration of the velocity is smaller than for the results shown in figure 12.1 (a-d). Comparing figure 12.1 (d) with figure 12.2 (d) it can be seen that for the latter the wake expansion is reduced. This could be expected because of the higher upstream velocity which reduces the effect of wake expansion.

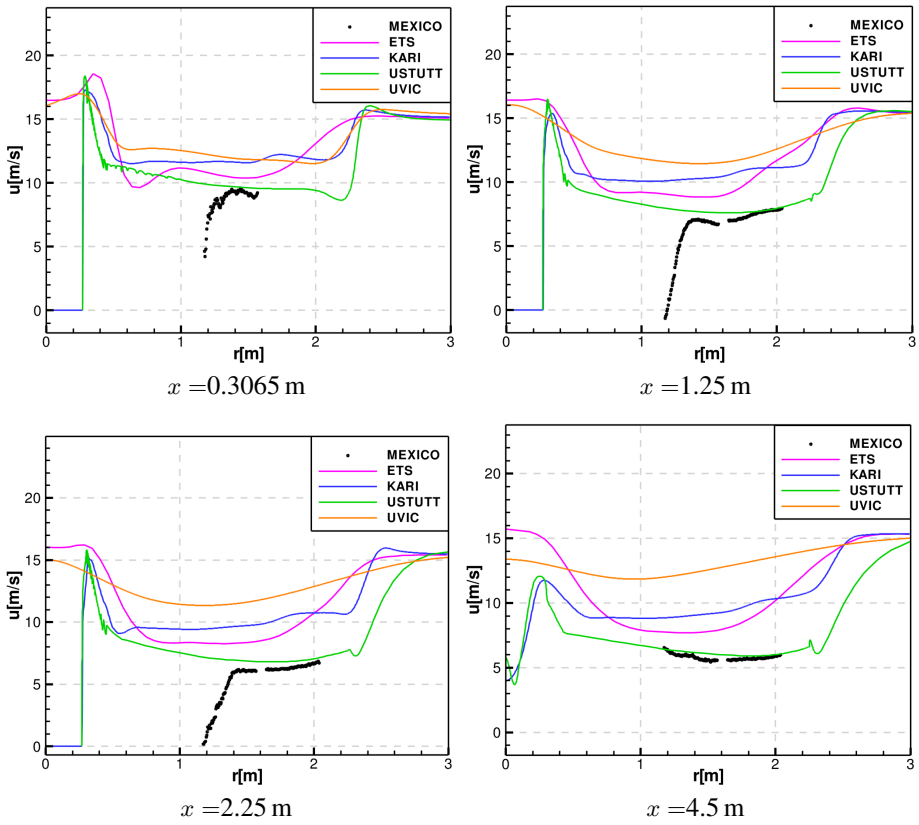

Figure 12.2 *Radial traverse for* $15\,\mathrm{m/s}$ *upstream velocity at* $x = 0.3065\,\mathrm{m}$*;* $1.25\,\mathrm{m}$*;* $2.25\,\mathrm{m}$ *and* $4.5\,\mathrm{m}$ *axial position for* $0°$ *azimuth of blade one*

Finally the results for $U_\infty = 24\,\mathrm{m/s}$ are depicted in figures 12.3 (a-d). It can be seen that the measurements show a similar behavior in the region $1.2\,\mathrm{m} < r < 1.4\,\mathrm{m}$ as for the $15\,\mathrm{m/s}$ case. At the most downstream location ($x = 4.5\,\mathrm{m}$) this behavior cannot be observed. Heading outwards from this region the velocity increases. The simulations predict an increase of the velocity over span except for the root region. The highest deceleration occurs in the inner region. At the tip region the velocity gradient is lower than for the previous inflow velocities. Compared to the previous figures the $U_\infty = 24\,\mathrm{m/s}$ simulations fit best with the measurements. In figure12.3 (a) all results lie close to the measurement results. More downstream three simulations show almost the same behavior.

12.3 Task 4.4-B Vortex trajectory and vortex strength

During the MEXICO project the trajectories of the tip vortices were identified by PIV vortex tracking. In this section the path of the tip vortices is extracted from measurements and simulations and compared to each other. The tip vortices will be analyzed for the three wind speeds $U_\infty = 10\,\mathrm{m/s};\ 15\,\mathrm{m/s};\ 24\,\mathrm{m/s}$ at zero yaw. The tip vortex trajectories were evaluated at the $270°$ position of blade 3 in a plane at 9 o'clock position (x-z plane). To perform the evaluation of the tip vortices a vortex evaluation macro was developed at the University of Stuttgart [53]. This macro is based on the postprocessing software Tecplot. The macro automatically determines vortex pa-

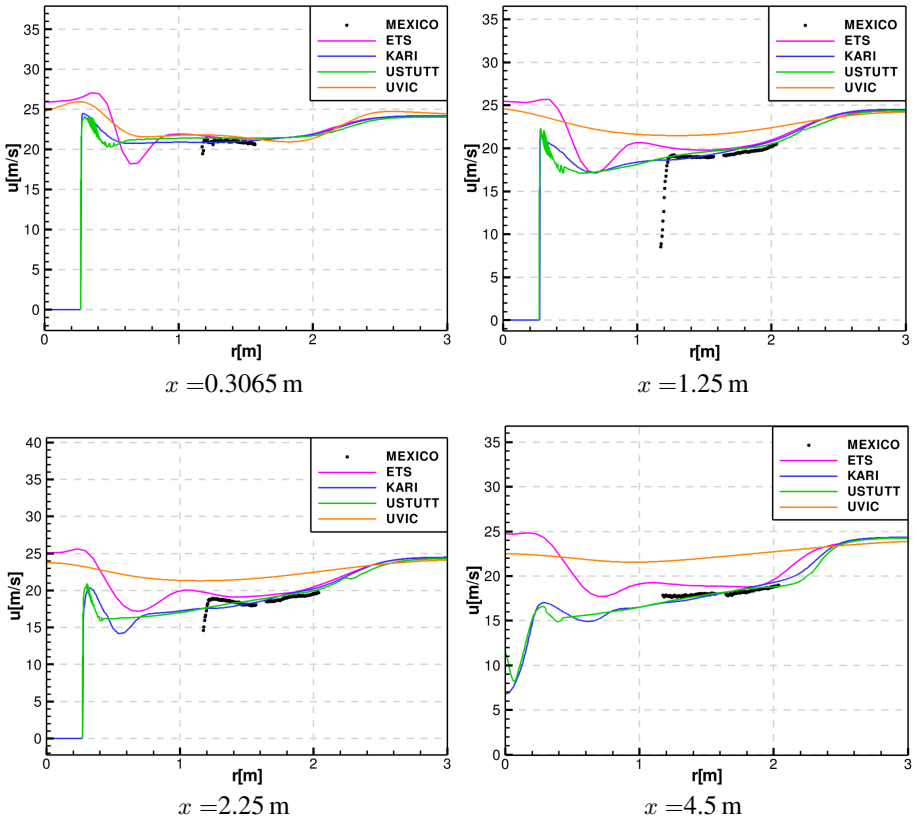

Figure 12.3 *Radial traverse for* $24\,\mathrm{m/s}$ *upstream velocity at* $x = 0.3065\,\mathrm{m}$*;* $1.25\,\mathrm{m}$*;* $2.25\,\mathrm{m}$ *and* $4.5\,\mathrm{m}$ *axial position for* 0° *azimuth of blade one*

rameters on cartesian 2d flow field solutions. The first parameter is the center of the vortex, which is estimated to be the point with the maximum vorticity [54]. The vorticity in the vortex center is the second parameter. Moreover, the vortex core radius is determined which gives an idea of the vortex size. In the present evaluation the vortex core radius is defined by half of the distance between the maximum and minimum induced velocity of the vortex [54]. The last parameter which is determined by the macro is the vortex strength. The strength of a vortex depends on the blade loading and can be predicted well even for coarse meshes. To calculate the vortex strength the macro performs an integration over concentric circles around the vortex center. The upper interpolation boundary is chosen such that the interpolated circulation strength shows a maximum. Increasing the interpolation area further yields to a decay of Γ due to the induction effect of the neighboring tip vortex. The interpolation area is limited to a radius that corresponds to half of the distance to the neighboring tip vortices.

Figures 12.4(a-d) show the vortex parameters for the $10\,\mathrm{m/s}$ inflow velocity. This low wind speed set up is characterized by strong wake expansion (figure 12.4 (a)). The evaluation of the core vorticity and the core radius shows the dissipation of the vortices when being transported downstream. The vortex core strength is reduced while the vortex core radius increases. It can be seen that the integrated vortex strength slightly increases.

Comparing the simulation results to the measurements it can be seen that some of the parameters can be reproduced accurately while for other parameters like vortex core radius or maximum vorticity significant deviations are obvious for all simulations. Most of the deviation from the measurements is caused by low resolution of the tip vortices in the simulations. The resolution of the PIV sheets was $0.0043\,\mathrm{m}$ in each direction. Reproducing this resolution in a CFD simulation is too expensive. Because of the lower resolution the simulations can not predict the vortices correctly. The highest deviation occurs for the core vorticity and the vortex size (figures 12.4(b-c)). Compared to the measurements they show a deviation of up to 1100% for the maximum

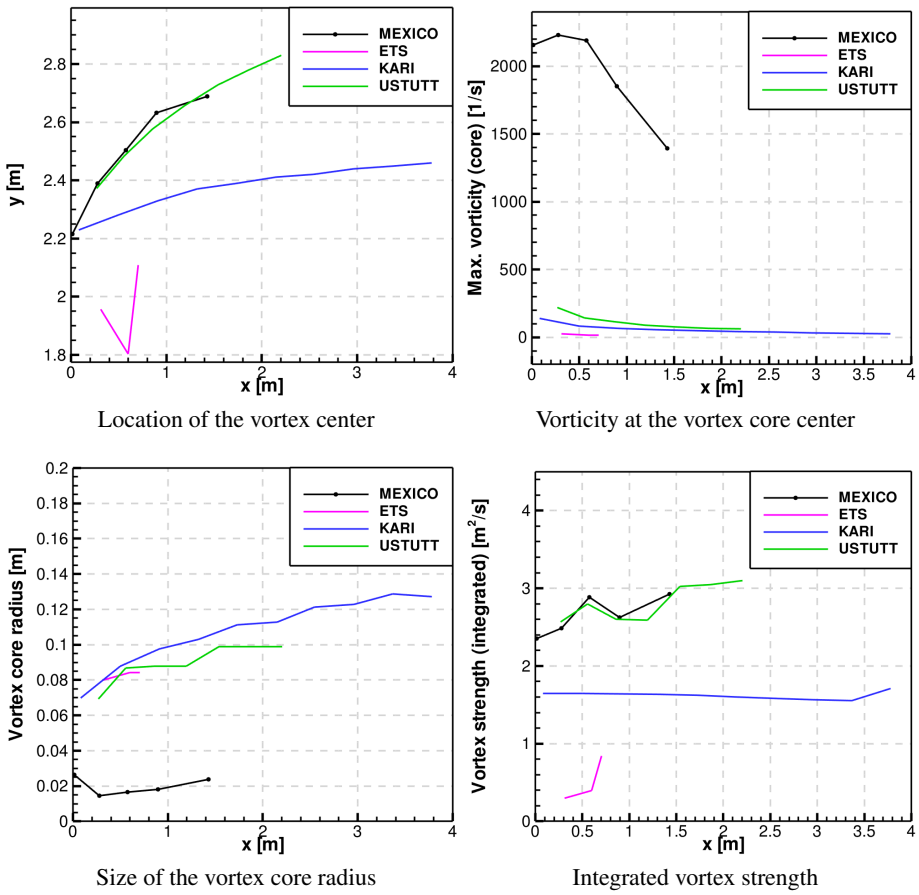

Figure 12.4 *Vortex parameters for* $10\,\mathrm{m/s}$ *inflow velocity for* $270°$ *azimuth of blade three*

vorticity in the core and 300% for the vortex core size. The simulation results show the same trend as the measurements. While the core radius increases the maximum vorticity in the core is reduced. In contrast to this the deviation of the integrated vortex strength is small (up to 200%).

Figure 12.5 shows the evaluation of the tip vortices for the $15\,\mathrm{m/s}$ inflow velocity. Compared to the $10\,\mathrm{m/s}$ inflow velocity the wake expansion is smaller, see figure 12.5 (a). The decrease of the core vorticity and the increase of the vortex core radius are reciprocally proportional like for the lower wind speed. The integrated vortex strength stays more or less constant except for the two rightmost vortices. These vortices were not totally covered by the PIV sheets. Thus the evaluated vortex strength decreases. Nevertheless these vortices are included in the evaluation as their position and core vortex strength can be determined correctly. The simulations predict the expansion of the wake as can be seen in figure 12.5 (a). The core vorticity shown in figure 12.5 (b) and the vortex core radius (figure 12.5 (c)) are not very well predicted like for the $10\,\mathrm{m/s}$ inflow velocity. The integrated vortex strength is not accurately predicted by any of the simulations.

Figure. 12.6 shows the evaluation of the tip vortices for the $24\,\mathrm{m/s}$ inflow velocity. This high wind speed condition is characterized by low wake expansion and flow separation on the blade. The vortex core strength and the core radius show the same trend like for the other wind speeds. The vortices in this scenario are the strongest. Their strength reaches absolute values of greater than $5\,\mathrm{m^2/s}$. Like for the other wind speeds the simulations predict the wake expansion. Moreover, the behavior for the maximum core strength and the core radius is similar. The prediction of the integrated vortex strength is slightly overpredicted by the simulations. Nevertheless it fits better than for the other wind speeds. It should be mentioned that in the simulations of USTUTT a distinct vortex sheds from the upper side of the blade in the tip region. The separation vortex has

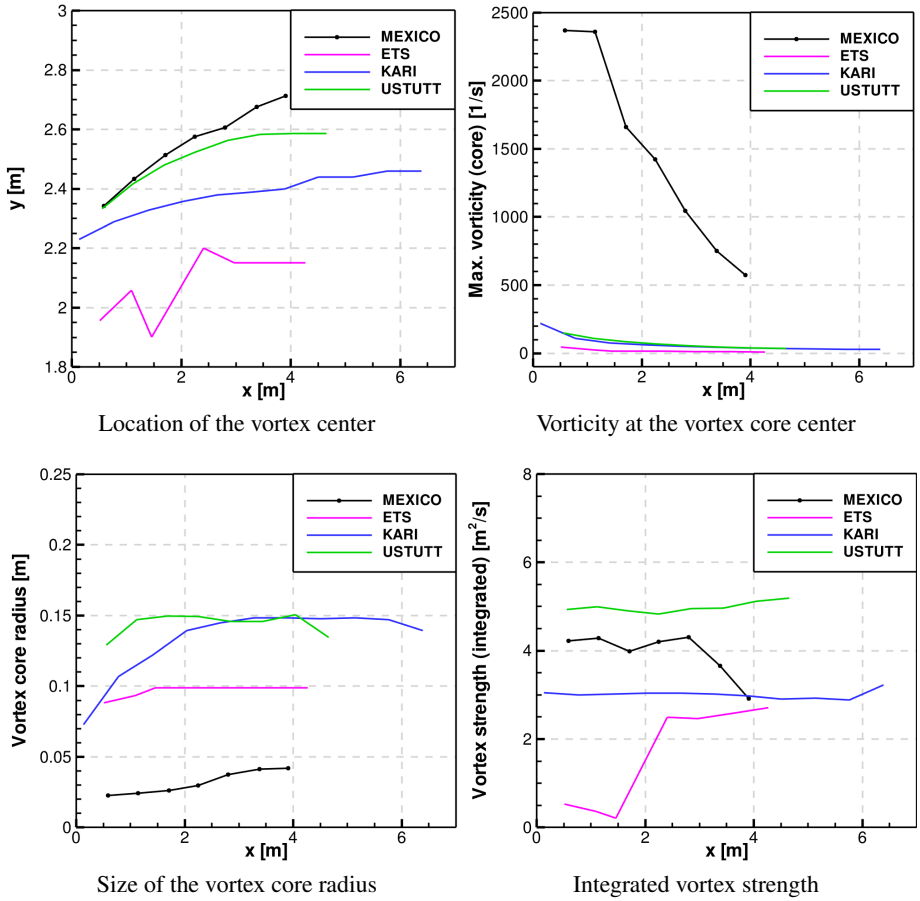

Figure 12.5 *Vortex parameters for* $15\,\mathrm{m/s}$ *inflow velocity for* $270°$ *azimuth of blade three*

opposite direction of rotation compared to the main tip vortex and merges with the latter downstream of the blade. As the vortex is shed from the suction side of the blade and shares the same center with the tip vortex it is considered in the calculation of the integrated vortex strength of USTUTT.
In total it can be said that the simulations predict the trend of the measurements for the vortex evaluation. However all simulations deviate from the measurements. The main reason for this is the numerical dissipation of the simulation codes which is caused by the used numerical scheme and the mesh resolution.

12.4 Task 4.4-C Impact of numerical set-up and discretization

Present low order CFD methods are characterized by strong numerical dissipation which yields a fast decay of the tip vortex strength. This could be already seen in task 4.4 B. The dissipation is dependent on the grid resolution in the vortex regime. In this subtask the impact of grid refinement on vortex preservation is examined. Two different numerical setups are compared to the measurements [53]. The setups are characterized by an additional mesh in the tip region which covers the tip vortices figure 12.7. This mesh is characterized by high resolution in radial and downstream direction with an aspect ratio of approximately one. Moreover the cells have a skewness of approximately zero. Two configurations will be analyzed which differ in the number of cells used for the tip mesh. The coarser mesh has 1.4 million cells the finer one 10 million cells in the tip vortex mesh. This is a difference of approximately two for the number of cells in each direction. The numerical scheme used for the simulations is a second order scheme proposed by Jameson, Smith and Turkel [55]. Figure 12.8 shows the vorticity in the wake of the tip for the

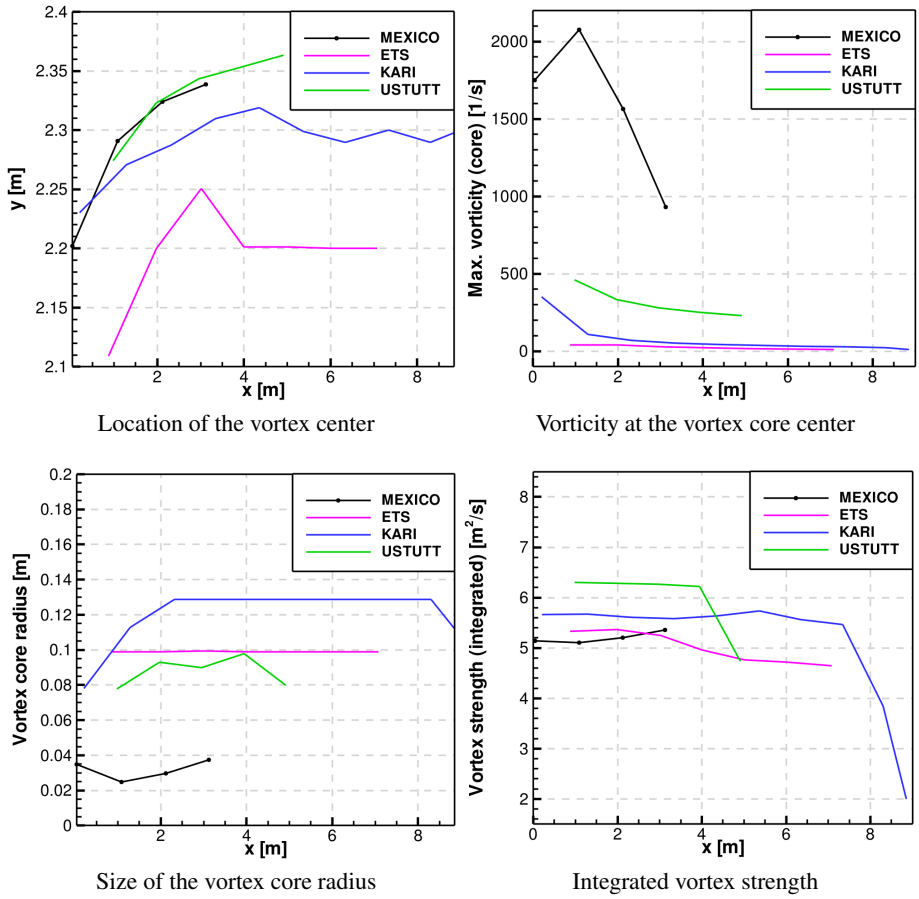

Location of the vortex center | Vorticity at the vortex core center

Size of the vortex core radius | Integrated vortex strength

Figure 12.6 *Vortex parameters for* $24\,\mathrm{m/s}$ *inflow velocity for* $270°$ *azimuth of blade three*

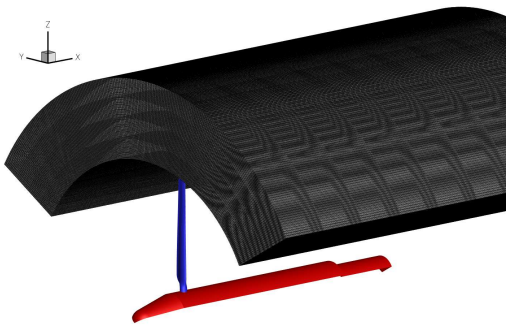

Figure 12.7 *Iso view of a tip vortex mesh covering the region of the tip vortices.*

two setups. This is approximately twice as much cells in each direction of space for the detailed tip mesh. The difference between the two simulations is significant. The low resolved wake simulation predicts bigger vortices, with lower vorticity in the core. Moreover their vortices lose their circular shape when being transported downstream. The higher resolved simulation predicts vortices of almost circular shape. In the region where the low resolved simulation shows only a smeared vorticity band the refined simulation still predicts isolated vortices. At the position of the ninth vortex of the refined simulation the vorticity dissipates abruptly. This point determines the end of the tip vortex mesh. The flow is leaving the high resolved area and enters the coarse background mesh.

Figure 12.9 (a-d) shows the results of the vortex evaluation. It can be seen that the vortex location is affected by the mesh resolution. Moreover, the local induction is stronger for better resolved vortices. This topic has been shown in [53] [56]. For higher x values than $3.5\,\mathrm{m}$, this is where the

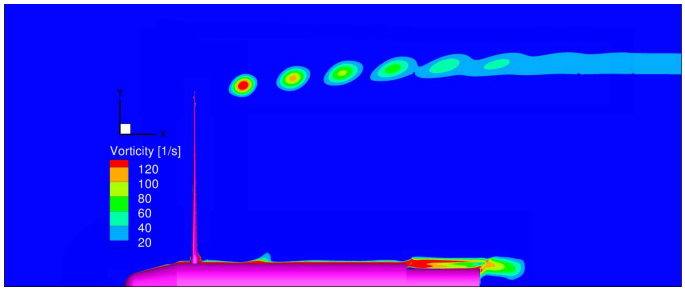

1.4 million tip vortex cells

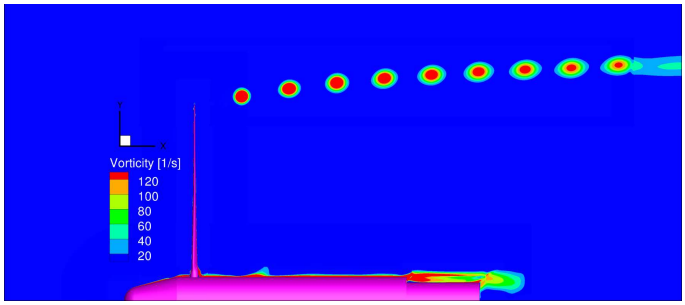

10 million tip vortex cells

Figure 12.8 *Vorticity of the tip vortices for two different tip vortex meshes at* $15\,\mathrm{m/s}$ *upstream velocity and zero yaw.*

nacelle ends, the coarse simulation predicts the end of the wake expansion. In contrast the wake of the refined simulation is still expanding. Anyway, the vortex trajectory of the high resolved simulation differs more compared to the measurements when going downstream. This indicates that there is still a significant dissipation although a large number of cells was introduced.

The increased cell number in the tip region do strongly effect the vorticity in the core (figure 12.9 (b)). The smaller cells result in a better resolution of the velocity gradients which yields to higher maximum vorticity in the core. This effect results in a maximum core vorticity which is 275% higher at $4\,\mathrm{m}$ downstream position for the refined simulation. In spite of this increase the maximum core vorticity of the refined simulation still does not predict the measurements which show a maximum core vorticity of $600\,1/\mathrm{s}$ at this location. This is more than 200% higher as for the detailed wake simulation. The vortex core radius (figure 12.9 (c)) decreases on the detailed mesh. The difference in core radius between the two simulations is approx. $0.06\,\mathrm{m}$. A nyway this is still higher than the core radius from the measurements but fits to what was observed in section 12.3. The smaller the core radius the higher the maximum core vorticity. The integrated vortex strength is illustrated in figure 12.9 (d). The results slightly improve for the detailed simulation, but compared to the other vortex parameters the benefit is small. The decrease of the integrated vortex strength of the measurement downstream of $2.8\,\mathrm{m}$ is caused due to the fact that these vortices are not totally covered by the PIV system. This fact was already mentioned in the previous section.

The previous results in this section showed the influence on several vortex parameters between two different resolutions of the tip vortex region. It was shown that finer meshes in the tip vortex region significantly improve the vortex resolution. Moreover, it could be shown that the resolution of the tip vortices affects the wake expansion. Therefore, it is recommended to resolve the tip vortices in wind turbine wake simulations. The highest influence of the tip vortex refinement could be shown for the core radius and the maximum core strength. The latter be increased by 275% using the refined tip vortex mesh. The influence on the integrated strength was quite small. For sake of completeness it should be mentioned that it is possible to improve vortex resolution on the same mesh by using higher order methods [57].

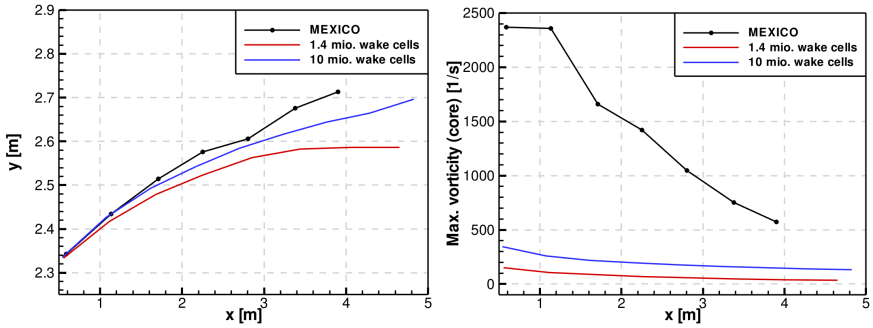

Location of the vortex center | Vorticity in the vortex core

Size of the vortex core radius | Integrated vortex strength

Figure 12.9 *Influence of tip vortex mesh resolution analyzed by evaluation of vortex parameters for* $15\,\mathrm{m/s}$ *upstream velocity for* 270° *azimuth of blade three. Two different tip vortex meshes with 1.4 million and 10 million cells were analyzed.*

13 Task 4.5: Flow non-uniformities in the rotor plane

13.1 Introduction on task 4.5

In this chapter an analysis is given of measurements which are devoted to understanding the flow field in the the radial velocity traverse from the Mexico experiment.

Since the Mexico measurements are performed on a rotor with 3 blades where the momentum theory is applied on an actuator disc, the effects from the finite number of blades (generally described with the Prandtl tip loss factor) should also be taken into account.

It is noted that within the Mexico experiment all three velocity components are measured. However, unless otherwise stated, the present chapter only considers the u-component, i.e. the velocity in streamwise direction

13.2 Radial traverses

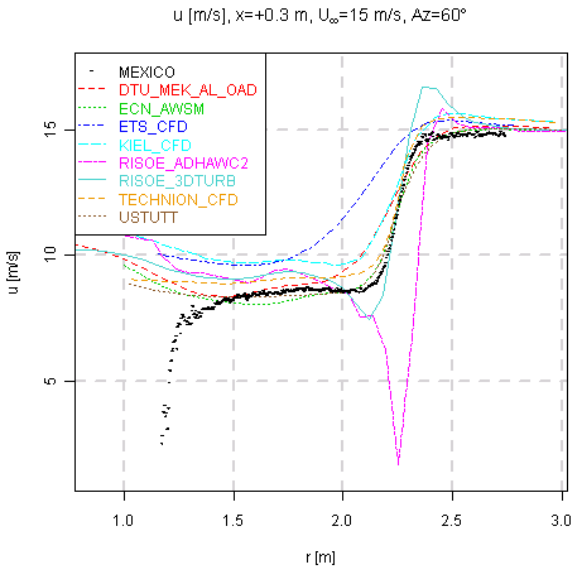

Figure 13.1 *Radial velocity traverse, 30 cm downstream of the rotor, measured and calculated with CFD codes.* V_{tun} *= 15m/s,* Φ_r *= 60 degrees*

In figure 13.1 the results from several CFD calculations are shown for radial velocity traverses at a distance of 30 cm downstream of the rotor plane. The results are compared with measurements. As explained in section 4 radial traverses are measured in a horizontal PIV plane at the 9 o clock position at different blade positions. Figure 13.2 then shows the result for Φ_r = 60 degrees (for the definition of Φ_r see figure 4.5).

In figure 13.2 the corresponding result is shown at a distance of 30 cm upstream of the rotor plane. It can again be seen that all codes overpredict the velocities.

Figure 13.1 shows, in both measurements and calculations a lower velocity in the centre of the wake where the velocity increases at the edge of the wake (i.e. near r $\approx$ 2.25 m). This increase is associated to the presence of the tip vortex. As such it confirms to some extent the stream tube concept from the momentum theory with a constant low velocity in the wake and a sudden abrupt change towards the free stream velocity at the edge of the wake. It can be observed that many CFD codes predict the increase in velocity to be less abrupt than the measured increase. The significant drop in velocity towards the inboard positions is most likely a result of the vorticity

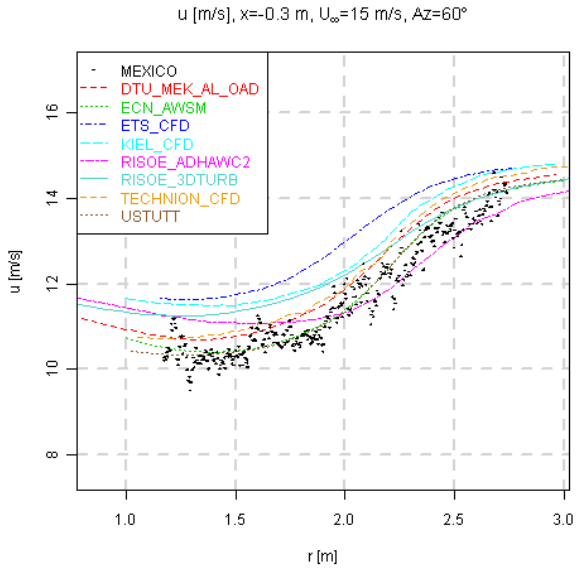

Figure 13.2 *Radial velocity traverse 30 cm upstream of the rotor, measured and calculated with CFD codes.* V_{tun} *= 15m/s,* Φ_r *= 60 degrees*

due to the transition in airfoils which, as stated above, leads to a change in bound vortex strength along the blade.

This vorticity is also present in figure 13.3 in which the PIV sheets in this region are concatenated. The figure shows an unexpected velocity discontinuity which could be well attributed to this phenomenon. It is interesting to note that the CFD calculations, though they do predict a small

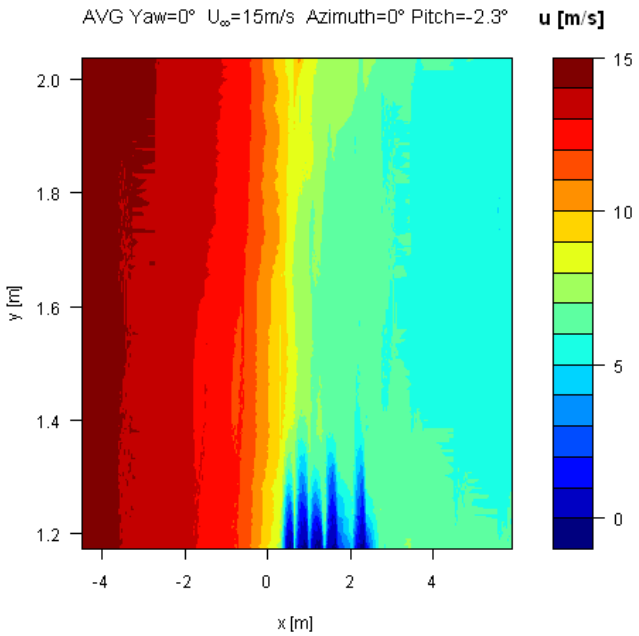

Figure 13.3 *Contours of axial velocity from PIV (x in axial, y in radial direction, origin in rotor center)* ‡

‡ Missing values between PIV sheets have been linearly interpolated

change in bound vortex strength at that location have not been able yet to predict the drop in velocity.

Upstream of the rotor there is good agreement between calculations and measurements. The lowest velocity is found inboard from where it increases towards the free stream velocity, although this value is not reached yet at the edge of the measurement range at 122% span. This is obviously different from the momentum theory concept which assumes a streamtube in which the velocity is constant and lower than the free stream velocity. At the edge of the streamtube the momentum theory assumes a discontinuous jump towards the free stream velocity. The radius of the stream tube upstream of the rotor plane is smaller than the rotor radius and hence definitely smaller than 122% span.

13.3 Flow non-uniformities in the rotor plane

In the figures 13.5 to 13.7 the velocities as measured near the rotor plane are presented. The results are destillated from the radial velocity traverses. They are plotted along the x-range of the two PIV sheets, just upstream and just downstream of the rotor plane at r/R = 80% , 92% and 120%. The two PIV sheets have a small overlap in the rotor plane, see figure 4.4. The tunnel speed is 15 m/s, i.e. λ = 6.67. The different lines represent different blade azimuth positions, the colour legend of which is indicated in figure 13.4.

It is then wortwhile to note the multi-valued curves near x=0, which are a result of the overlapping PIV sheets at this position. The results are usually (but not always) very compatible indicating a good quality of the data. This is also confirmed by the (generally) good compatability of the results at Φ_r = 0 and 120 °. Thereto it should be realised that the flow situation at Φ_r = 0 and 120 ° should be similar for a 3-bladed rotor (at least when the blade geometries (and settings) are similar. The flow similarity between Φ_r = 0 and 120 ° then confirms this to be true).

13.3.1 Outboard sections

At the outboard station (i.e. at 120% span, see figure 13.7) a clear maximum is visible in the velocity traverse u(x), the magnitude and location of which depends on the blade azimuth position. This maximum velocity is induced by the tip vortex at the x-location where it crosses the horizontal plane, i.e. the position where the tip vortex is as close as possible to the PIV sheet, see figure 13.9. This figure shows the tip vortex to induce a positive x-velocity at outboard positions. The x-location where the tip vortex passes the PIV sheet depends on the tip vortex travel speed. In Snel et al [58] the tip vortex tracking measurements have been analysed which resulted in a vortex travel speed in the order of 11.86 m/s, constant throughout the wake. As noted in the same reference this is smaller than the often assumed averaged value of the free stream and wake velocity (which would give 12.5 m/s in the rotor plane based on V_{tun} = 15 m/s and an axial induction factor of 1/3). On basis of the present analysis, an even lower transport velocity of 11.2 m/s is found near the rotor plane (since the tip vortex has travelled from x= 0.0997 m at Φ_r = 40 degrees to x= 0.2774m at Φ_r = 80 degrees). It must be realised however that the maximum in the velocity traverse is very flat which makes it difficult to determine the precise location of the tip vortex and resulting vortex travel speed.

Figure 13.7 shows the maximum velocity at Φ_r = 40 degrees to be smaller than the velocity at Φ_r = 60 degrees, where the velocity at Φ_r = 60 degrees is again smaller than the velocity at Φ_r = 80 degrees. This can be explained by the fact that the relevant tip vortex at Φ_r = 40 degrees is trailed from blade 3 at 280 degrees azimuth (since Φ_r refers to the horizontal plane just downstream of the rotor plane. At this position the wake expansion is still limited by which the tip vortex is relatively far from the 120% span location. Hence the velocity induced by the tip vortex at that position is relatively weak. At Φ_r = 80 degrees the tip vortex is trailed at 320 degrees by which it

crosses the horizontal plane much further downstream. This goes together with a more outboard location, i.e. closer to the 120% span location, where the tip vortex induces a stronger velocity.

13.3.2 Inboard sections

At the inboard stations (80% and 92% span, figures 13.5 and 13.6) a strong non-uniformity in the rotor plane can be observed with a jump in velocity when the blade moves from Φ_r = 20 to Φ_r = 40 degrees. Thereto it should be realised that Φ_r = 20 degrees corresponds to a position of blade 3 at 260 degrees i.e. just below the PIV sheet at 270 degrees azimuth where its bound vortex increases the axial velocity, see figure 13.8. At Φ_r = 40 degrees the blade is just above the PIV sheet and the bound vortex decreases the axial velocity. The jump in velocity at x=0 m is smaller at 92% span due to of a smaller bound vortex strength at this location which can be derived from the pressure measurements, [13].

Also at the other blade positions the non-uniformity in the flow appears to be large: At 80% span and x=0 m, the velocity varies from u = 9.5 m/s at Φ_r = 60 degrees to u = 11.2 m/s at Φ_r = 120 degrees. At 92% span, the velocity varies from u = 11 m/s at Φ_r = 60 degrees to u = 12 m/s at Φ_r = 120 degrees. As a matter of fact, at 92% span, the closer proximity to the discrete tip vortices (the phenomenon modelled with the Prandtl tip correction), was expected to give a stronger flow non-uniformity with a smaller local blade velocity. The present measurements however indicate the flow at 92% span to be slightly more uniform with a higher local blade velocity. This may be a result of the fact that the flow non-uniformity at 92% span is still dominated by the passage of the blade where the bound vortex strength at that position is weaker than at 82% span, as can be derived from the pressure measurements, see [13]. The velocities induced by the tip vortex are visible in the form of a (relatively slight) minimum at those x-locations where the velocity at 120% span appears to be maximum. This is as expected since the positive x-velocity as induced at positions outboard of the tip vortex, turns into a negative velocity at an inboard location.

It is interesting to average the velocities in the rotor plane over all azimuth angles in order to get an indication of the induction in the rotor plane. At 80% span, the averaged velocity is 10.37 m/s (where the results at Φ_r = 20 and 40 degrees are not included in the averaging). At 92% span the averaged velocity is 11.5 m/s At 80% span this yields an axial induction factor of 0.31 close to the expected value of 1/3. At 92% span the averaged induction factor is 0.23

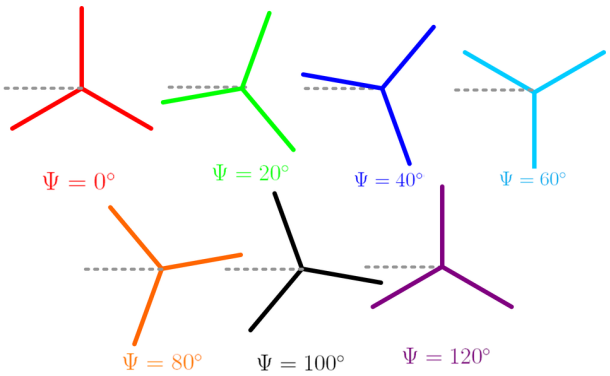

Figure 13.4 *Position of blade 1 at Φ_r = 0, 20, 40, 60, 80, 100, 120 °*

13.3.3 Inflow in case of asymmetric flow conditions

In general it can be observed that the velocities induced by the bound vortex have a large impact on the flow field in the rotor plane. As such the bound vortex of one blade also effects the inflow at the other blades. As noted in [59] BEM methods (generally) do not account for these effects.

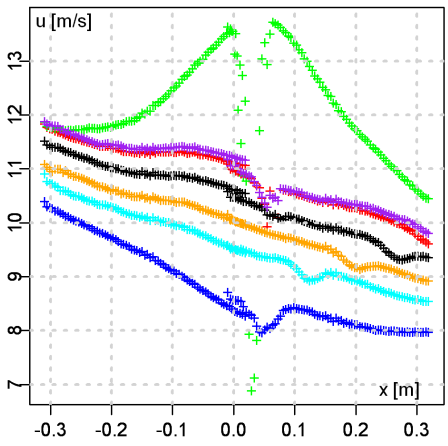

Figure 13.5 *Velocities near the rotor plane as function of axial coordinate at 80% span and* V_{tun}*=15m/s. Different lines represent different blade positions, see figure 13.4*

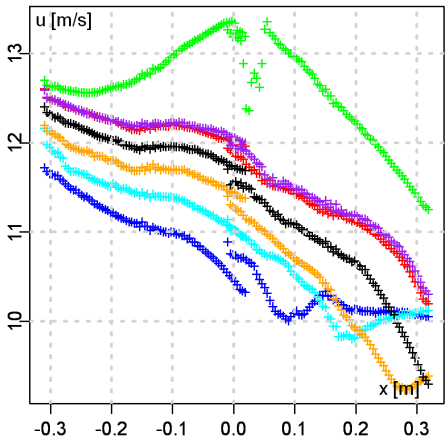

Figure 13.6 *Velocities near the rotor plane as function of axial coordinate at 92% span and* V_{tun} *=15m/s. Different lines represent different blade positions, see figure 13.4*

For axi-symmetric flow, as analysed in the present chapter, the net effect is zero, because the two blades have equal but opposite effects For yawed flow the bound vortex distribution depends on the azimuth angle, hence there is a non-zero effect Estimates based on measured bound vortex

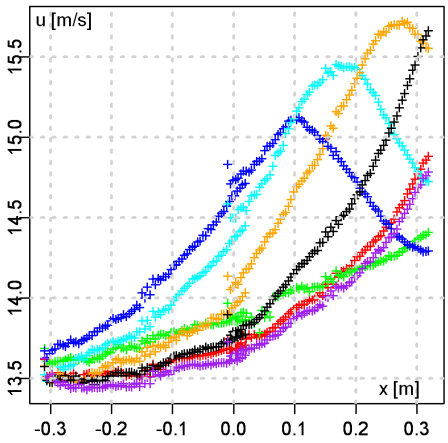

Figure 13.7 *Velocities near the rotor plane as function of axial coordinate at 120% span and* V_{tun} *=15m/s. Different lines represent different blade positions, see figure 13.4*

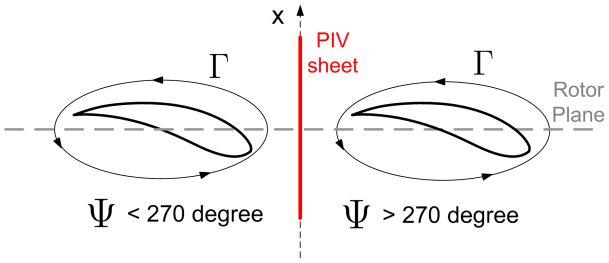

Figure 13.8 *Blade crossing the PIV sheet at 270 degrees azimuth*

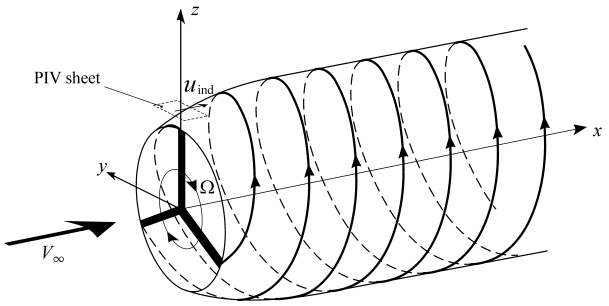

Figure 13.9 *PIV sheet outside helical wake vortex system*

distributions show velocities between 0.9 (root) and 0.3 m/s (tip) for 30 degrees yaw BEM models can be easily adapted for this effect, not only in yawed flow, but also for effects due to shear or other non-uniformities.

13.3.4 Tip effects

It is recalled that the Prandtl tip loss factor has been determined in the pre-computer era (1919) with a very simplified vortex wake model. The presence of nowadays more physical numerical vortex wake methods like AWSM then opens the door to estimate the tip loss factor in a more

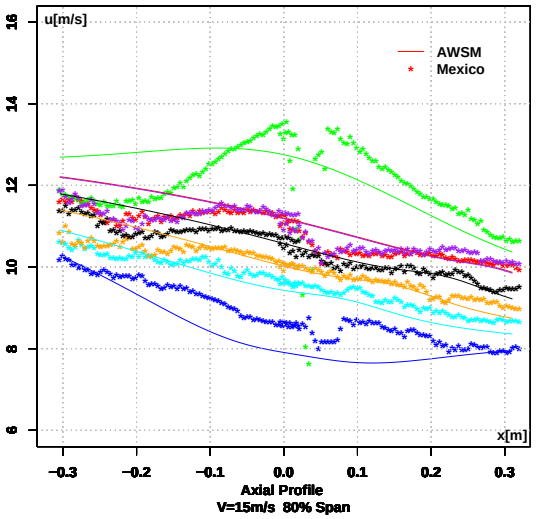

Figure 13.10 *Axial traverse near the rotor at 80% span and V_{tun} = 15 m/s, different blade positions Measured and as calculated with AWSM*

accurate way. For this reason the accuracy of AWSM in predicting the flow field in the rotor plane is assessed by comparing its results with Mexico measurements.

Thereto figure 13.10 shows the measured axial velocities from figure 13.5 compared with calculations from AWSM.

It can be observed that generally speaking the agreement between the measured and AWSM calculated velocities is good, where the agreement is poorest close to the blade positions. This can be explained by the lifting line approximation in AWSM which in the vicinity of the blade leads to a poor representation of the flow around the actual blade geometry.

If the measurements from figures 13.5 to 13.7. are to be used for a direct assessment of the Prandtl tip loss factor it should be realised that this factor relates the local blade velocity to the annulus averaged velocity. The traverses from figures 13.5 to 13.7 have been made at 6 different blade positions but none of them correspond to 270 degrees, i.e. the position where the blade is in the PIV sheet. Such measurements are however available from the so-called tip vortex tracking experiments. This experiment is explained in section 4 where it is described that it measures the flow field near the blade tip at a blade position of 270 degrees.

From these measurements (and calculations), an idea can be formed of the flow non-uniformity between the rotor blades from which the validity of the Prandtl tip correction can be assessed. Thereto the figures 13.11 to 13.13 show velocity measurements near the tip in the rotor plane at V=10, 15 and 24 m/s. The figures show both the azimuthally averaged velocities as well as the local velocities with the blade at a position of 270 degrees.

The measured results are compared with those calculated with AWSM. The azimuthally averaged measured values are averaged over the 6 blade positions from figure 4.5 where the AWSM calculations are averaged over 12 blade positions.

It should be known that the results from the figures 13.11 to 13.13 are derived from data which include the upwash from the bound vortex and which was found to add considerably to the flow non-uniformity as discussed above. The non-uniformity from this upwash is obviously not included in the Prandtl tip correction. At first sight one may think that this makes the results inapplicable for an assessment of the Prandtl tip correction However, the present way of processing filters out the effect from the upwash. This is due to the fact that the data are azimuthally averaged over different blade positions which are all symmetrically positioned around the PIV sheet at 270 degrees. As an example: the upwash at 280 degrees is opposite to the upwash at 260 degrees (at least when the bound vortex is thought to be concentrated in a vortex line). Also the local axial induced velocity, i.e. the axial velocity in the PIV plane with the blade located in this plane, is not disturbed by this upwash since a horizontal bound vortex line in the PIV plane does not induce a velocity in axial direction.

An important observation from the figures 13.11 to 13.13 is the very good agreement between measured and AWSM predicted azimuthally averaged velocities in the rotor plane. This is consistent with the good agreement found at 80% span from figure 13.10.

Another observation is the good qualitative agreement between the calculated and measured local velocities where the drop in velocity followed by an increase in velocity towards the tip, which is a result from the tip vortex (see below), is present in both calculations and measurements. It is noted however that the increase in velocity takes place at a more inboard position than predicted by AWSM. This is a result of the fact that the so-called tip vortex tracking experiments showed that the tip vortex is trailed slightly inboard from the tip where AWSM assumes this vortex to be trailed at the tip. Furthermore it can be seen that the measured velocities are lower at $r < R$ and they do not tend to coincide with the azimuthally averaged velocity at more inboard positions which the AWSM calculations do. This would also be expected from the Prandtl tip loss factor which approaches a value of 1 at inboard positions (A Prandtl tip loss factor of 1 implies the azimuthally averaged velocity to be equal to the local velocity at the blade). It must be noted however that AWSM assumes a lifting line approach where the real blade is obviously having a

finite chord and thickness. Also the blade position might slightly differ from 270 degrees, because the 1P trigger sensor (from which the blade position is derived) was sometimes found to behave unstable during the experiments. Since the velocities local to the blade are very sensitive to the precise value of the blade position the results can be disturbed heavily by a relatively small off-set in position.

Nevertheless the comparison between AWSM results and measurements is considered convincing enough to propose a lifting line free vortex wake method as a basis for a refinement of the tip loss factor.

In the figures 13.14 to 13.16 the tip loss factors from AWSM (i.e. the ratio between the azimuthally averaged induction factor and the local induction factor) are compared with the Prandtl tip loss factors. Most interesting is the behaviour of these factors near the tip (the wiggles at the mid-span positions are most likely a result of intermediate vortex shedding). Generally speaking the AWSM tip loss factor follows the Prandtl tip loss factor very closely but the AWSM tip loss factor is higher at high tip speed ratio (10 m/s) and lower at low tip speed ratio (24 m/s). At the intermediate wind speed of 15 m/s a good agreement is found. This might indicate that the tip speed ratio dependency (i.e. the inflow angle dependency) in the Prandtl tip loss correction factor could be improved. This will be done in future research.

A striking difference between the Prandtl tip loss factor and the ASWM tip loss factor can be seen at the very tip. The Prandtl tip loss factor decreases to 0 but the AWSM factor increases before the tip. This is consistent with the results from the figures 13.11 to 13.13 which show that the local blade velocity exceeds the azimuthally averaged velocities already inboard from the tip. In order to understand this, it needs to be realised that the AWSM tip vortex is a singularity which in principle yields an infinite induced velocity and hence an infinite decrease of total velocity towards the tip. This however assumes the flow to be inviscid where viscosity will prevent such a singularity to exist in the real flow. Consequently AWSM applies a so-called cut-off radius, the default value of which is 5%. This means that if the distance between a point and a segment of the wake is less than 5% of the segment length, the velocity induced by the segment is neglected. As a result of this cut-off radius, the velocity local to the blade increases towards the tip.

A sensitivity study showed only a significant effect of the cut-off radius at the very tip, i.e. at the outer 2% of the radius. Together with the fact that the qualitative agreement between the AWSM results with 5% cut-off radius and measured results is good, it is believed that AWSM with this default cut-off radius can be used with sufficient confidence for a better assessment of the tip loss effects.

Another interesting observation is the behaviour of the loss factor near the root. In the figures 13.14 to 13.16 the Prandtl tip loss factor has, despite the name **tip** loss factor, also been applied at the root. Thereto the tip radius in the original tip loss factor has been replaced by a root radius which is obviously less well defined than the tip radius. In the figures 13.14 to 13.16 the root radius has been set as the location of the maximum chord which seems to be a reasonable choice.

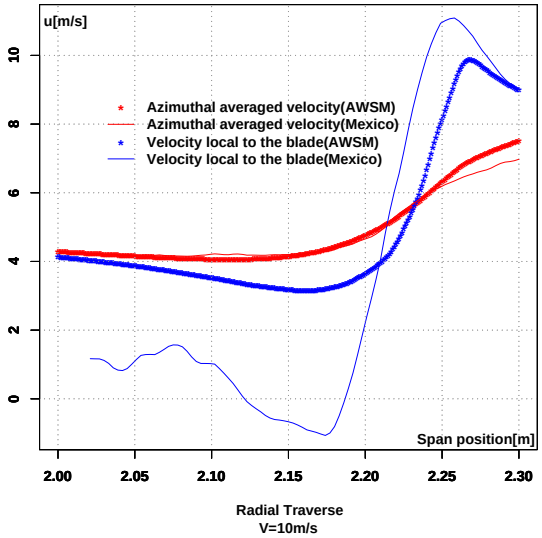

Figure 13.11 *Local and azimuthally averaged velocities in the rotor plane, measured and AWSM calculated, V = 10 m/s*

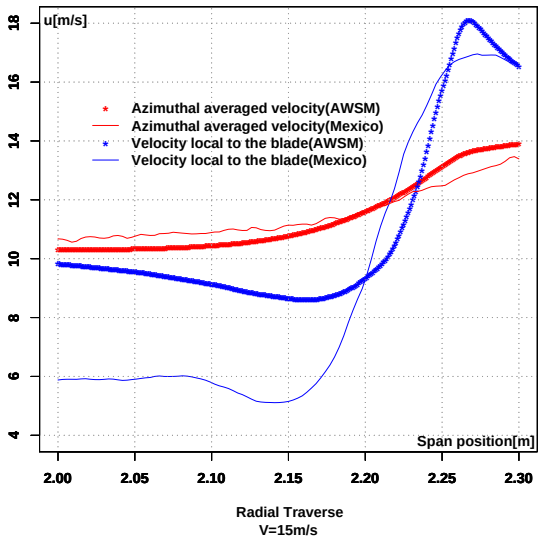

Figure 13.12 *Local and azimuthally averaged velocities in the rotor plane, measured and AWSM calculated, V = 15 m/s*

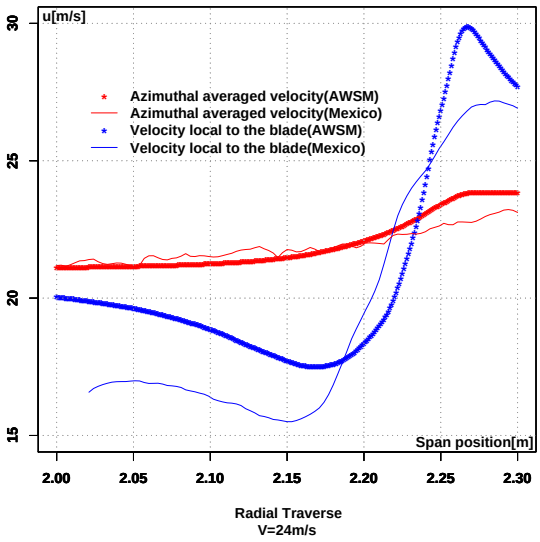

Figure 13.13 *Local and azimuthally averaged velocities in the rotor plane, measured and AWSM calculated, V = 24 m/s*

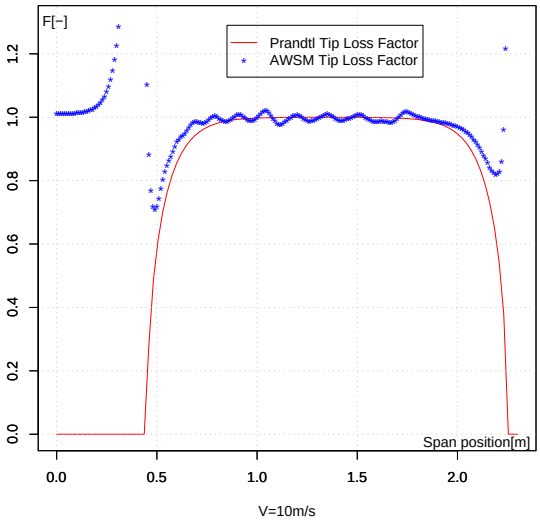

Figure 13.14 *Prandtl tip loss correction compared with AWSM tip loss factor, V = 10 m/s*

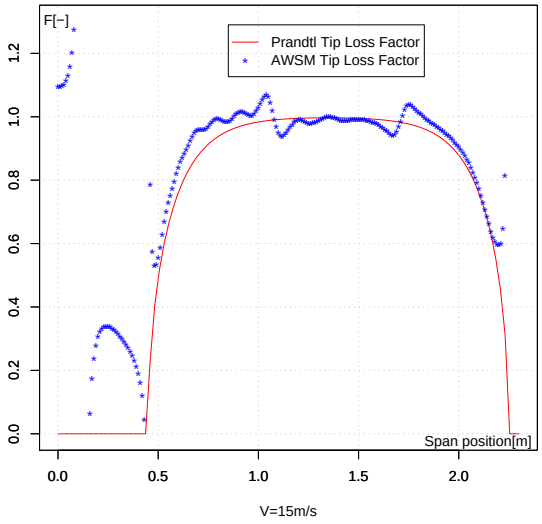

Figure 13.15 *Prandt tip loss factor compared with AWSM tip loss factor, V = 15 m/s*

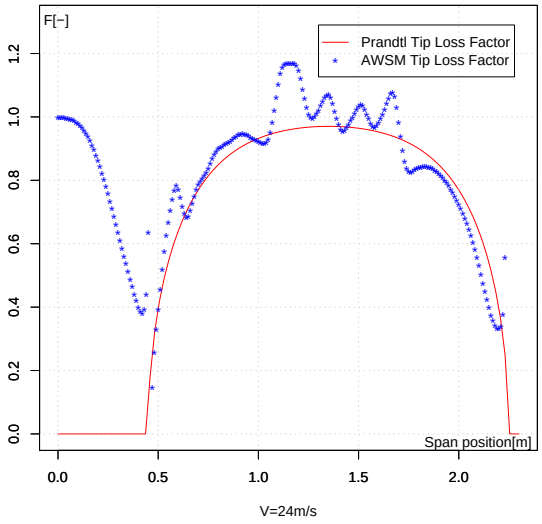

Figure 13.16 *Prandt tip loss factor compared with AWSM tip loss factor, V = 24 m/s*

14 Task 4.6: 3D-Flow Effects

14.1 Introduction on task 4.6

3D flow effects are induced by the rotation of the wind turbine blades and appear close to the surface of the blade. Direct measurements of such effects were not undertaken within the MEXICO experiment. Thus the 3D effects had to be read from the data as one phenomenon causing differences between 2D airfoil model and measurement results and the measured 3D data-set (see section 9).
There are different 3D effects. However, e.g. the effects at the tip have been treated in the section 13 and 3D-effects due to yaw are treated in the next section 15. Here we shall focus on the 3D-flow effects which are related to 3D stall. Such effects have been first described by [60] and have been investigated also for the UAE Phase VI experiment among others by [61] using CFD simulations.

14.2 Effects observed in the measurement

For the UAE Phase VI and the MEXICO experiment Schreck et al. compared the thrust coefficient values of the parked with rotating turbines given by the pressure measurements on the blades in [28]. The authors compared the curves of C_n over the angle of attack α. In the rotating case measurements with inflow velocities from $5.4m/s \leq U_\infty \leq 30m/s$ at $325rpm$ were used. Unfortunately the data for the pressure tabs at 0.25R and 0.35R of the span were not reliable for the parked blade of the MEXICO experiment. However, the results at 0.25R in the rotating case show a maximum of $C_n = 2.081$ (stall C_n) at $\alpha = 20.4°$. This is about twice as much as in the regular 2D measurement. The same was also observed in the UAE Phase VI case. This gives a strong hint for aerodynamic 3D effects in that region. For the 0.6R span position the C_n values show an increase of 8% at $\alpha = 14°$ for the rotating blade. The parked curve shows a different characteristic with a second maximum in C_n around $\alpha = 20°$. Thus Schreck et al. conclude that the rotation amplifies the values for C_n in the investigated part of the blade.
In a research paper on the extraction of airfoil data Yang et al. also found some hints for 3D flow effects in the measurements in [62]. The article describes the application of a method to determine the angle of attack (AOA) by the flow field and pressure data for airfoils. Using this AOA, lift and drag coefficients were extracted from the data for the spanwise positions of 0.6R, 0.82R and 0.92R and compared to pure 2D airfoil measurement data. The results showed lower lift coefficients for pre-stall and a higher one for the post stall region at 0.6R for the rotating 3D measurement. The drag coefficient was in most cases higher for the rotating measurement. Also here the author concluded that a 3D-effect could be the source for the deviations.
In a paper on the comparison and validation of BEM and a free wake panel model [46] also found some indications for 3D effects in the inner part of the blade. Especially strong deviations for the 0.25R and 0.35R positions are related by them to a delayed stall phenomenon.

14.3 3D flow phenomenon from CFD results

Since measurements of the flow close to the blade surface were not done, CFD seemed to be a good tool to analyze 3D flow phenomena. Stall is still a difficult topic in CFD. Therefore the reliability of such simulations should be validated before coming to far reaching conclusions (see e.g. [63]). For the analysis of the 3D flow the simulation of ForWind (here often refered to as Oldenburg_CFD) has been taken. The model description can be found in section C. Out of the given simulations the results agreed best for the case of 424.5 RPM, a pitch angle of $-2.3°$ at an inflow velocity of $U_\infty = 24$ m/s (see e.g. figures 8.3, 8.2 and 8.4 for the pressure curves and

figures 8.26, 8.25 and 8.27 for the radial traverses). This case has been chosen for the evaluation of the 3D flows.
As the simulation was a steady RANS simulation using a rotating reference frame method, the reference blade 1 is in the simulation always pointing in the 0° direction, which is the y-direction in the figures (in this simulation the orientation is: z is the streamwise direction, y- is the vertical and x the horizontal axis). Figure 14.1 shows a slice through the flow field at a position of $x = 0.07$ m from the center line of the blade towards the tail of the blade. A flow near the surface of the blade of the magnitude of ≥ 10 m/s is indicated evolving from the blade root section reaching up to an area of 0.72R of the span. Slices of the flow field showing the flow around the profiles along the blade indicate a similar flow.
This is supported by streamlines as given in the plot 14.2 also showing the pressure contours on the blade. The streamlines indicate a delayed stall region with an origin of the flow near the blade root. This flow is being forced in a vortex like flow along the blade up to 0.72R, which is very close to the position at which the NACA airfoil is implemented. The beginning of the section of the NACA airfoil can clearly be identified by a broader region of very low pressure towards the leading edge of the blade. This suggests, that the choice of the airfoil has an influence on the strength and characteristics of such a 3D stall effect. Further, it seems remarkable, that flow leaving the vortex of the flux in spanwise direction, appears to be concentrated in the transition regions between the different airfoil types.

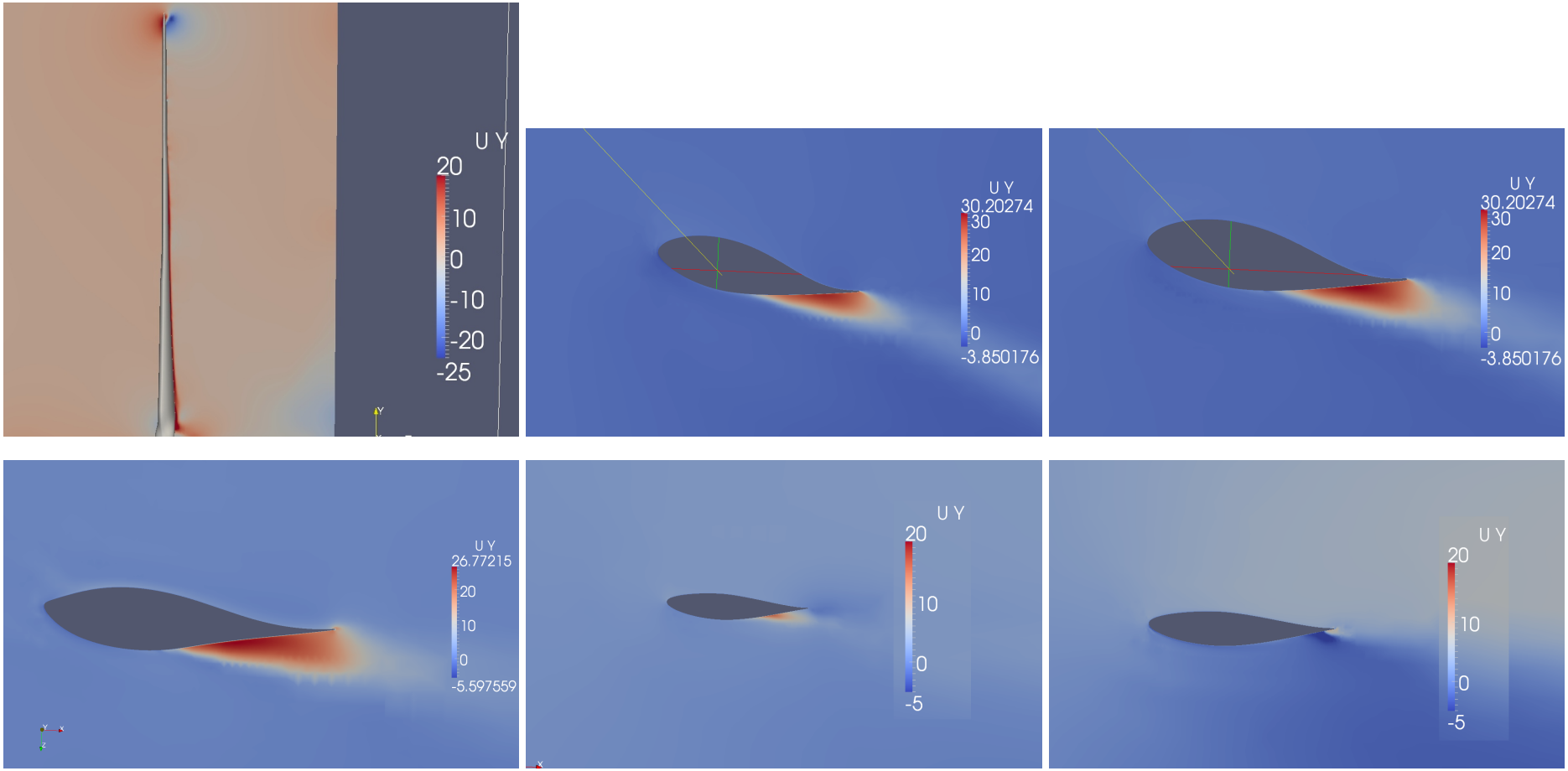

Figure 14.1 *Spanwise velocity at the rotor blade, for the whole rotor blade and at spanwise positions of 0.25R, 0.35R, 0.6R, 0.82R and 0.92R*

Another effect has been observed and discussed in relation to the radial traverses (see figures 8.26, 8.25 and 8.27 for the cases of $U_\infty = 10$ m/s, $U_\infty = 15$ m/s and $U_\infty = 24$ m/s respectively). Especially in the case of $U_\infty = 15$ m/s there is a sharp drop in the velocity behind the rotor in the region of 0.5R of the span. Schepers et al. expected this effect to be caused by the transition region of the airfoil types between 0.4R and 0.5R in [64]. Since the effect can also be observed in the measurement as well as in the CFD simulation of ForWind Oldenburg at $U_\infty = 24$ m/s (see 8.27) some finding about the effect shall be discussed here.
In fig. 14.3 the velocity in streamwise direction at the position of 0.3 m behind the rotor plane is shown. It can be observed that the wake in the rotor plane is not homogeneous. It is rather showing some fluctuations, depicted by the blue and brown stripes in the figure of the wake. This indicates the existence of vortices in the wake of the blade not only at the blade root and the tip section, but also in the blade center region. This is stressed by λ_2-contour plots. The right hand side of fig. 14.3 is showing λ_2-contour plots at the plane 0.3 m behind the rotor plane. The regions of strong fluctuations can here be related to the vortex contours. Fig. 14.4 is showing λ_2-contours around the whole rotor. Three major vortices can be observed originating from the blade: One at the blade root, one at the tip and one in the center of the blade in the region discussed by Schepers et al..

For a further analysis the streamlines around the blade from 0.4R to 0.55R have been plotted in fig. 14.5. The yellow streamlines indicate the flow originating near a point shifted from the stagnation point slightly towards the tip. Between 0.45R and 0.52R an interaction of the flow from the tip with the vortex of the 3D stall can be observed. This leads to a redirection of the flow towards the outer part of the blade. It seems to be the only region where such effect appears as can be seen for a broader region in fig. 14.6. In this transition region of the blade a major change in the tip shape of the airfoil occurs as fig.14.7 indicates. Thus the shape of the tip region of the blade could be the source of the sharp drop in the flow velocity in the mod of the blade.

The effect was only found in this CFD simulation for $U_\infty = 24$ m/s. It seems that the effects is strongly influenced by the separation characteristics of the flow. These don't seem to be grasped correctly in the other CFD simulations at lower inflow velocities of ForWind. Thus the effect was not observed otherwise. As one simulation result is a thin data base, further research is needed to

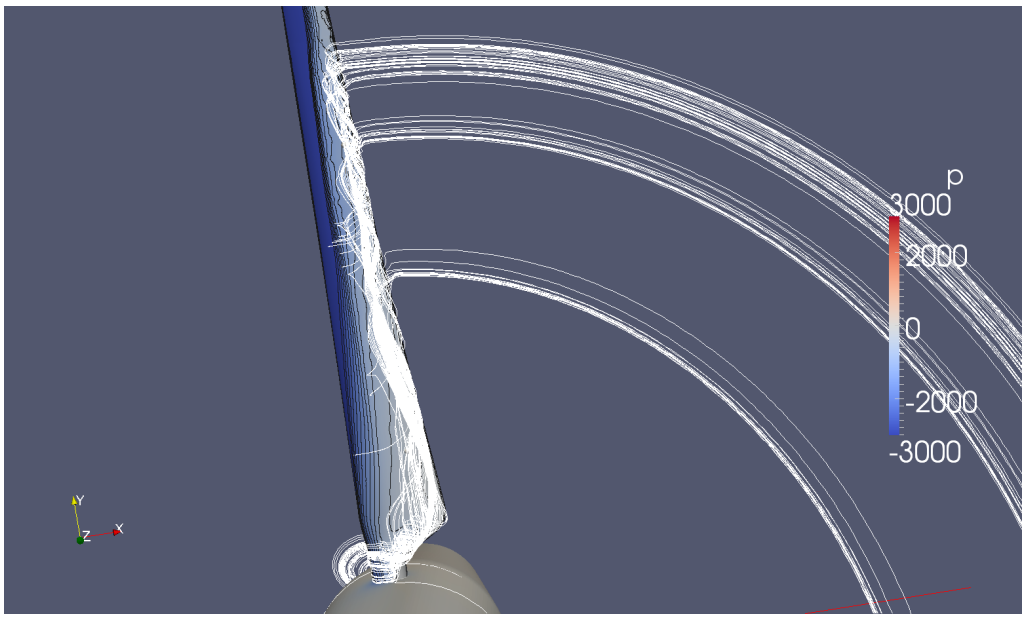

Figure 14.2 *Streamlines and pressure contours around blade 1 from the ForWind CFD simulation. The streamlines are running through a line close to the airfoil between 0.2R and 0.6R of the span.*

substantiate this proposed hypothesis.

14.4 3D-effect models

CFD computations are not very practical for wind turbine load calculations. Therefore models for the 3D-effects are needed for the most used engineering models. Guntur et al. compared the results from different 3D stall models with the results from an inverse BEM method and the measurement results in [44]. The models used were published by [65], [66], [67], [68], [69] and [70]. The results showed that all models had the tendency to overestimate the over all torque and axial forces. On the other hand results for thrust and tangential forces along the span were mostly well grasp by most of the models in the inner blade region for $U_\infty = 10$ m/s and 15 m/s. Normal forces were also well met for the positions 0.25R, 0.35R and 0.6R at $U_\infty = 24$ m/s by the model of Chaviaropoulos and Hansen. In the outer region of the blade all models however overestimate

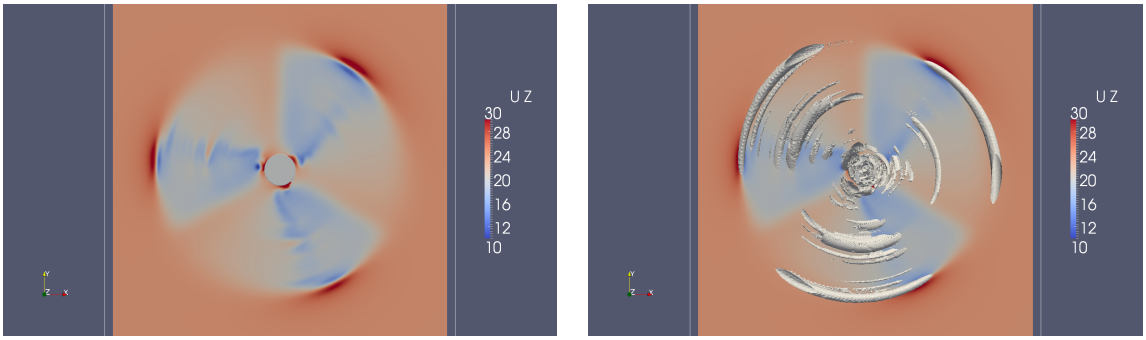

Figure 14.3 *Slice showing the velocity in streamwise direction in the z-plane* 0.3*m behind the rotor. On the right hand side* λ_2*-contours are additionally plotted depicting the existence of a vortex in the mid-blade region.*

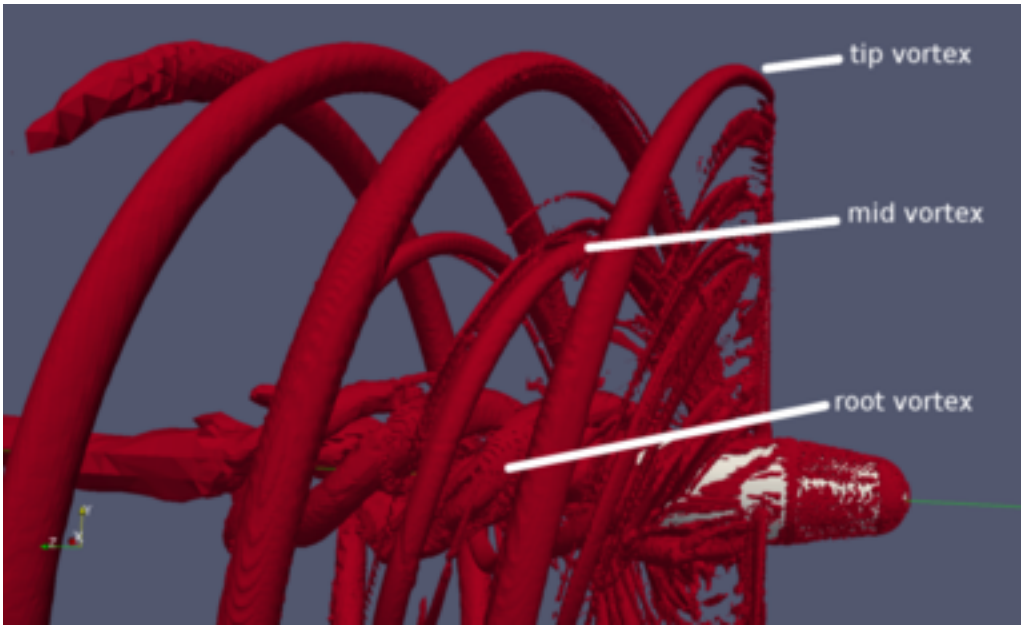

Figure 14.4 λ_2*-contours in the wake of the turbine at* $U_\infty = 24$*m/s showing three major vortices.*

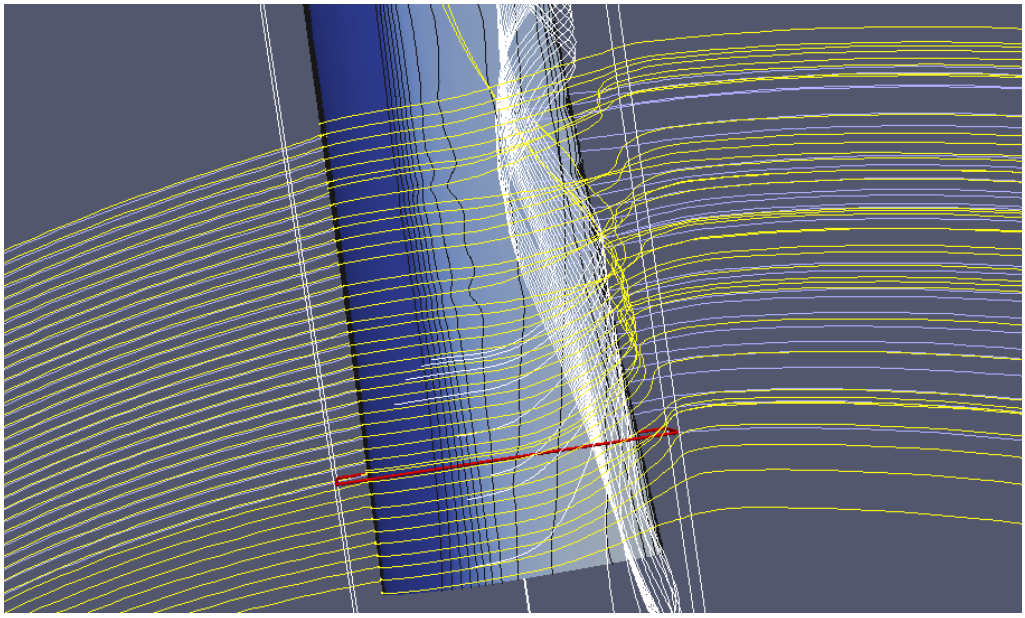

Figure 14.5 *Streamlines at a section of the blade. White are streamlines of the delayed-stall, yellow the streamlines originating near the stagnation point passing the suction side and blue are the lines coming from the vicinity of the stagnation point running on the pressure side of he blade. The figure shows streamlines from 0.4R to 0.55R with a red indication line at 0.44R.*

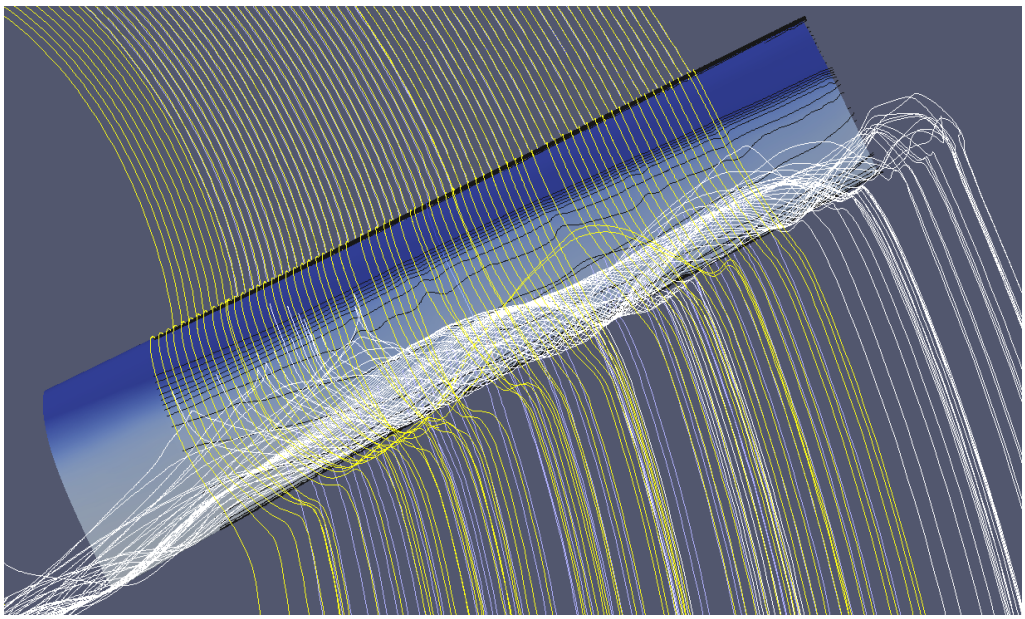

Figure 14.6 *The streamlines like in fig. 14.5 expanded to a region from 0.4R to 0.65R showing that the interaction of the main stream from the tip with the 3D stall vortex is a local phenomenon*

the forces (see fig. 14.8).

Figure 14.7 *Profiles of the blade in the transition region at 0.44R and 0.52R showing a deformation especially of the tip region.*

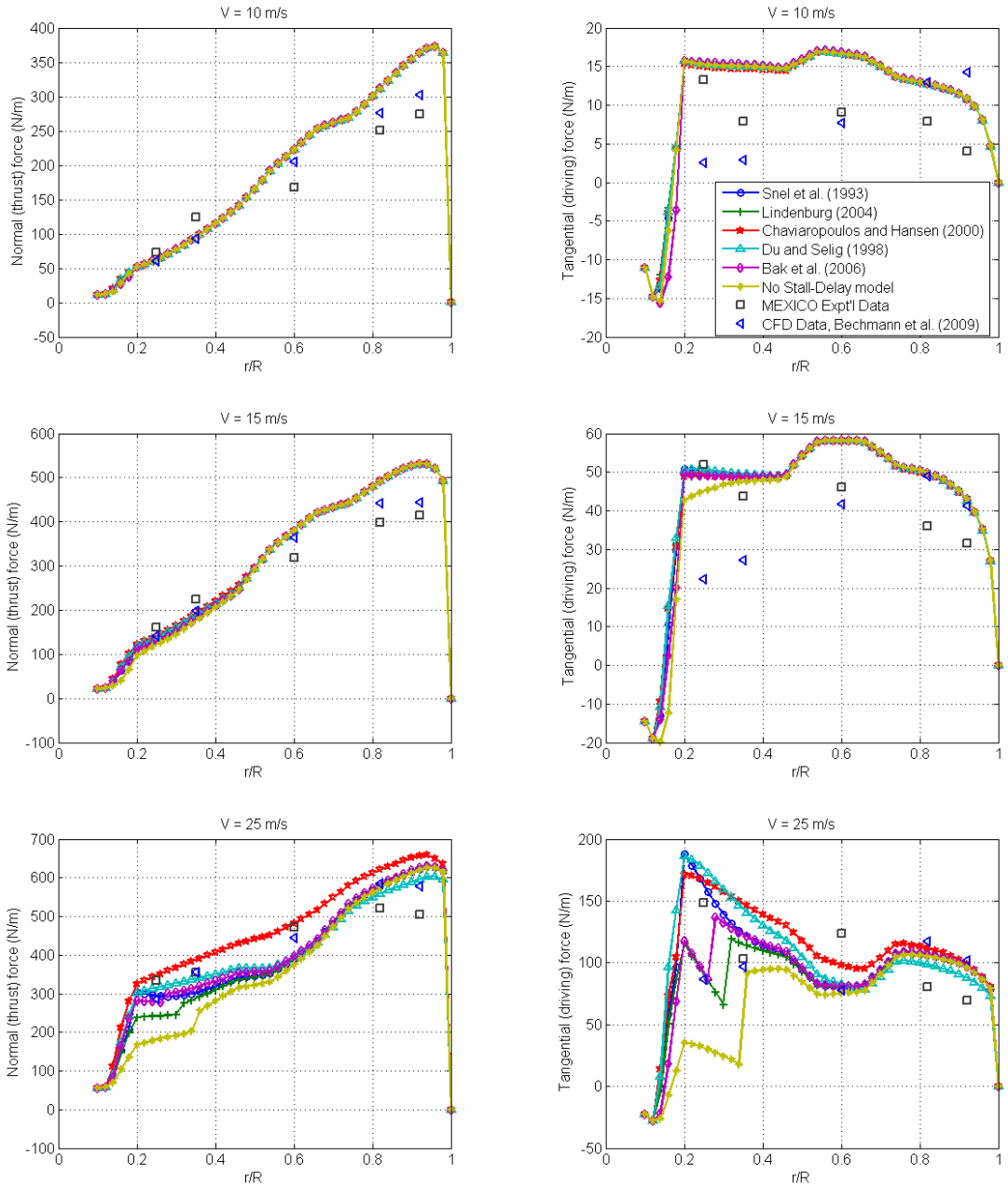

Figure 14.8 *The normal (thrust) and the tangential force distributions along the blade span at different wind speeds from a 2D BEM model with and without 3D stall modeling, CFD data and measurement data (from Guntur [44]).*

14.5 Conclusions on task 4.6: 3D-Flow Effects

At the MEXICO experiment 3D flow effects - especially 3D stall - have been observed and analyzed at different subtasks. CFD calculations suggest a 3D flow effect reaching from the blade root up to the end of the transition zone between the Riso and the NACA airfoil. Additionally an interaction of the main flow over the blade with the 3D flow at the tail of the blade in the transition region between the DU and the Riso profile seems to cause another vortex in the middle of the blade. This suggests the assumption, that the choice of airfoils and the design of the transition zone between the airfoils have a strong impact on the extend of the 3D stall effects. Further research is needed to support the assumption. Also 3D stall effects seem strongly dependent on blade and airfoil shapes. Therefore more research will be needed for an adaption of the 3D stall models to this circumstance.

15 Task 4.7: Instationary Airfoil Aerodynamics

15.1 Introduction on task 4.7

The Mexico experiment applies approximately 150 fast Kulite pressure transducers, distributed over the three MEXICO turbine rotor blades. These pressure transducers were effectively sampled at a high rate of 5514 Hz. Given these high levels of spatial and temporal resolution, the MEXICO data set offered excellent prospects for characterizing instationary effects associated with both yawed and axisymmetric turbine operation. MEXICO time records of c_p were integrated over the sectional chord to obtain time records of C_n. Time records of c_p and C_n were processed to obtain means and standard deviations for c_p and C_n.

Yawed operation produced strong instationary effects in the form of dynamic stall, which are documented in the first section of this chapter entitled "Validation of the Beddoes-Leishman Dynamic Stall Model in the HAWT Environment, Using the MEXICO Data". Axisymmetric operation also generated pronounced instationary interactions in connection with rotationally augmented flow fields. These are described in the second section of this chapter, "Rotational Augmentation Disparities in the MEXICO and UAE Phase VI Experiments".

Together, these two investigations show that the MEXICO data set is well resolved spatially and temporally, and contains a large volume of high quality data that can be exploited to better understand and predict rotor instationary effects. Thus, promising prospects exist for future investigations concerning instationary effects using the MEXICO data set.

15.2 Validation of the Beddoes-Leishman Dynamic Stall Model in the HAWT Environment, Using the MEXICO Data

R. Pereira
Delft University of Technology
The Netherlands
santospereira@tudelft.nl

Summary

It was the aim of this study to assess the load predicting capability of the Beddoes-Leishman dynamic stall (DS) model in a horizontal axis wind turbine (HAWT) environment, in the presence of yaw-misalignment. The DS model was tailored to the HAWT environment, and validated against unsteady thick airfoil data. Posteriorly the DS model was implemented in a blade element-momentum (BEM) code for yawed flow, and the results were compared with data from the MEXICO database. Generally speaking reasonable to good agreement was found. When large yaw-misalignments are imposed, poor agreement was found in the downstroke of the movement between the model and the experiment. Still, over a revolution the maximum normal force coefficient predicted was always within 8% of experimental data at the inboard stations, which is encouraging especially if blade fatigue calculations are being considered.

Introduction on the dynamic stall modelling with the Beddoes Leishman model

For the same angle of attack range **dynamic stall** (DS) is known to impose a large load amplitude on the airfoil section, when compared to the static loading characteristic. This phenomenon is expected to occur in HAWT operation, especially when yaw misalignment is present, and consequentially it becomes crucial to predict the load magnitudes DS will impose on the blades. Several DS models have been proposed, with different degrees of complexity. It was chosen to use the Beddoes-Leishman approach since it is of a semi-empirical nature, i.e. it tries to model the physical phenomena occurring during DS, even though it is relatively simple to implement and requires few empirical constants.

Methodology

Adapting the Beddoes-Leishman DS model

The Beddoes-Leishman DS model was originally developed for helicopter applications, and consequentially it includes the effects of the air's compressibility. In a HAWT environment the expected Mach numbers of operation are $M < 0.3$, and accordingly the DS model was simplified by assuming **incompressible flow**.

Another major difference between helicopter and HAWTs are the airfoil sections used. Usually the profiles for HAWT applications are thick, with relative thicknesses larger than 15%, while helicopter blades are normally equipped with thin airfoil sections.

According to [71], the most critical aspect of DS modelling is to predict the occurrence of leading edge(LE) separation. In the Beddoes-Leishman DS model LE separation is assumed to take place when a certain critical normal force coefficient, $C_{n,I}$, is attained. This value can be obtained from the airfoil's static characteristic by taking the normal force coefficient at which a break in the pitching moment curve is visible.

However, when thick airfoils are considered usually significant trailing edge(TE) separation takes place before LE separation occurs. Accordingly the normal force coefficient may decrease with

increasing angle of attack before the break in the pitching moment curve occurs. This means that using the criterion from [71] the critical normal force coefficient obtained may actually correspond to a value lower than the maximum C_n , which is unrealistic. Consequentially it is clear that a different criteria to compute the critical normal force coefficient is needed for HAWT airfoil sections.

In this study **two different LE separation criteria** were implemented in the DS model. The **first approach** was based on the work of Timmer et al [72], where the LE separation angle of attack is related with the LE thickness. In his work Timmer et al obtained a linear empirical relation based on wind tunnel testing for several thick airfoils:

$$\alpha_{LE_{sep}} = 1170.8(y/c) - 1.33$$

In the expression above the nose thickness is represented by the ordinate, y/c obtained at a relative chordwise position of 1.25%. The critical normal coefficient is the calculated assuming

$$C_{n,I} = 2\pi\alpha_{LE_{sep}} + C_{L,0}\cos\alpha_{LE_{sep}}$$

The **second approach** used to compute the critical normal force coefficient simply takes the maximum value of the normal force coefficient, i.e.

$$C_{n,I} = C_{n,\max}$$

The Ohio State University database of unsteady measurements was used to compare the implemented criteria. Thick airfoils were selected for comparison, and the reduced frequencies of excitation were chosen to be representative of what one may expect to find in a yaw-misaligned HAWT. Some results are shown below:

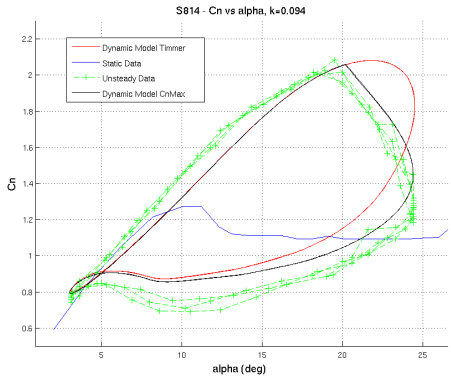

Figure 15.1 *DS model results obtained at high reduced frequency*

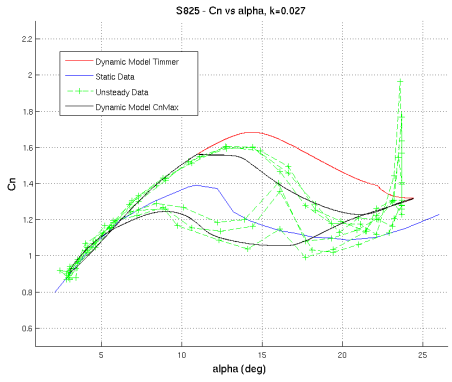

Figure 15.2 *DS model results obtained at low reduced frequency*

In the figures above it is clear that the $C_{n,\max}$ criterion (represented in black) yielded a better agreement with experimental data (represented in green) than the Timmer criterion (represented in red). Experimental data obtained with other airfoils and at other reduced frequencies also compared better with the $C_{n,\max}$ criterion, and consequentially it was used in subsequent calculations.

Implementation in the BEM code

Considering rotary wings, BEM theory states that the variation of the momentum of the air particles in the cylinder containing the rotor disk is equal to the aerodynamic forces on the blades.

In HAWTs the blades will act to slow down the incoming wind, and it is common to express this velocity change by means of induced velocities or induction factors. Usually in BEM codes these induction factors are calculated iteratively.

If yaw-misalignment is present, the induced velocities will change with radial and azimuthal position, and there is no simple theory which accurately describes this velocity distribution. The BEM code used in the present study used an **empirical model** for the induced axial velocities from Schepers et al[73]. Even though there are also induced tangential velocities, the present BEM model does not take them into account, based on the fact that these should be of a much smaller magnitude than the axially induced velocities.

This 'empirical' BEM code was used since previous work [74] showed it performed better than a 'classical' BEM code, i.e. than the approach suggested in classical HAWT aerodynamic literature such as [75].

Rotational augmentation of the aerodynamic coefficients was also included, based on the recommendations given in [76]. For the lift coefficient the correction of Snel was implemented:

$$C_{l,3D} = C_{l,2D} 3 \left(\frac{c}{r}\right)^2 \Delta C_l$$

where $\frac{c}{r}$ is the ratio between the local chord and the local radius, and ΔC_l represents the difference between the static airfoil characteristic and the potential lift coefficient. For the drag coefficient, the correction of Chaviaropoulos and Hansen was used:

$$C_{d,3D} = C_{d,2D} + 2.2 \left(\frac{c}{r}\right) \cos^4(\theta_{tw}) \Delta C_d$$

where θ_{tw} is the local blade twist angle, and ΔC_d is the difference between the 2D drag coefficient and the drag coefficient obtained when the angle of attack is zero.

The DS model and the rotational corrections were implemented in the BEM code , and the "complete" model was obtained. The model was run considering an azimuthal increment of 10 degrees, and 15 elements in the spanwise direction.

Experimental Data Used for Comparison

Dynamic stall phenomena are expected to occur mostly at **inboard sections**, since at these spanwise stations usually larger angles of attack are found, and yaw-misalignments will cause large angle of attack variations over a revolution. Consequentially emphasis is given at the 25 and 35% spanwise stations of the MEXICO data.

The advance/retreating blade effect present in the MEXICO yawed configuration imposes a minimum angle of attack at the vertically downward azimuthal position, which in the current study corresponds to $\Psi = 180$ deg $\rightarrow \alpha_{\min}$, and maximum incidence at the vertically upward angular coordinate, $\Psi = 0$ deg $\rightarrow \alpha_{\max}$. Since this effect will be dominant at the inboard stations when large wind speeds are considered, the **upstroke** of the cycle, i.e. the period when the angle of attack is increasing, corresponds to **azimuthal positions from 180 to 360 deg**. By analogy, the **downstroke** of the cycle, i.e. the period when the angle of attack is decreasing, corresponds to **azimuthal positions from 0 to 180 deg**.

Results and Discussion

The azimuthal variation of the normal force coefficients obtained experimentally (in red) and with the computational model (in blue) is now presented. To assess the influence of the DS model, the results obtained without the DS model(in yellow) are also shown.

Results are shown imposing a moderate and large yaw angles, $\beta = [30; 45]$ deg

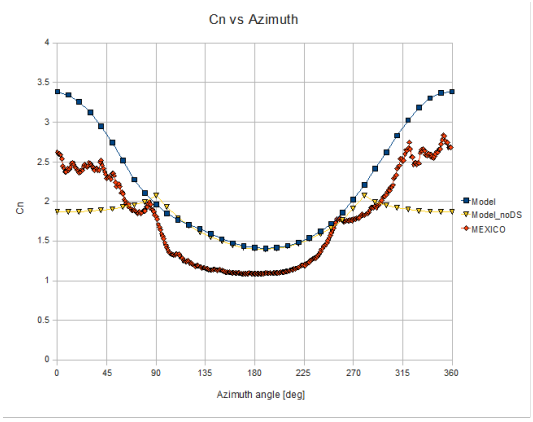

Figure 15.3 *25% Spanwise Station, Beta=30 deg*

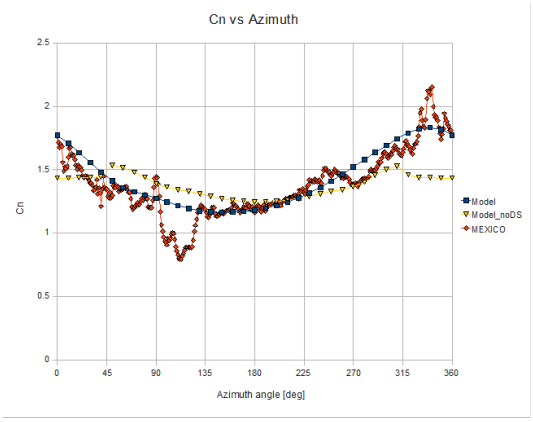

Figure 15.4 *35% Spanwise station, Beta=30 deg*

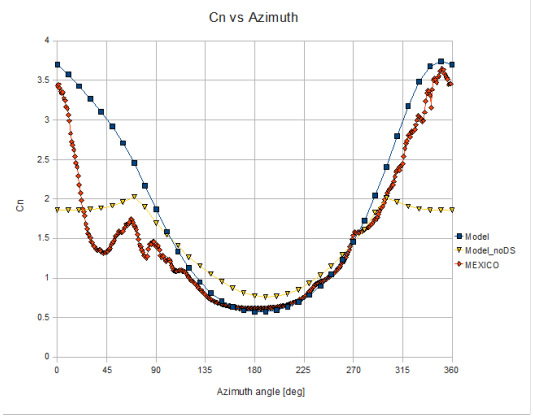

Figure 15.5 *25% Spanwise Station, Beta=45 deg*

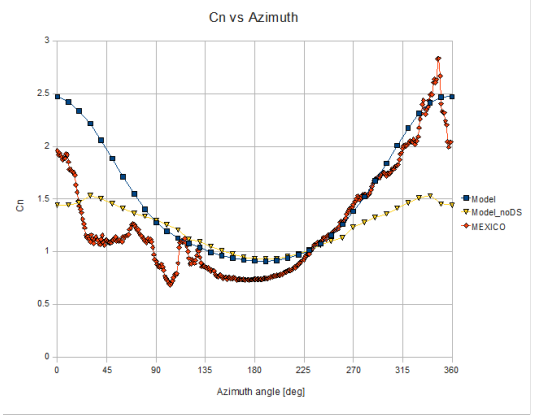

Figure 15.6 *35% Spanwise station, Beta=45 deg*

Generally speaking reasonable to good agreement was found between the predicted loading and the MEXICO data. Including the DS model in the BEM code improves the load prediction capability when compared to the static BEM, especially when large angles of attack are imposed.

When considering large yaw-misalignments the agreement found in the not so good; in the downstroke motion measurements seem to indicate that significant separation occurs, while the implemented model does not predict it. However, quite good agreement was found in the upstroke motion, and consequentially the amplitude of the loading over a revolution is well predicted.

The performance of the implemented calculation method is assessed by computing the **average relative error in the normal force coefficient** obtained with BEM code including the DS model. The magnitude of the error was calculated by averaging the relative error of model results over a revolution and assuming the MEXICO data to be the exact solution:

$$\epsilon_{C_n,\text{Avg}} = \frac{1}{360}\sum_{\Psi=1}^{360}\frac{|C_{n,\text{Model}}(\Psi) - C_{n,\text{MEXICO}}(\Psi)|}{C_{n,\text{MEXICO}}(\Psi)}$$

The results are shown in the table below for several MEXICO trials. The wind tunnel speed is given as U and relative error was calculated for several spanwise positions, with results in percent:

The figures included before show good agreement between the predicted and experimental loading during the upstroke of the movement, even when large yaw misalignments are imposed. Since the extreme loads occurring over a revolution are important in assessing the blade's robustness

Trial	U (m/s)	β (deg)	25% span	35% span	60% span	82% span
152	18	30	12.1	8.1	12.3	10.3
153	24	30	25.4	7.6	6.5	17.9
160	24	15	12.3	11.1	9.9	14.0
167	24	45	25.1	24.0	14.5	6.4
Average	-	-	**18.7**	**12.7**	**11.6**	**12.2**

Table 15.1 *Average Relative Error in Cn over a Revolution*

Trial	U (m/s)	β (deg)	25% span	35% span	60% span	82% span
152	18	30	2.0	0.2	9.9	5.9
153	24	30	19.1	15.0	0.1	2.2
160	24	15	5.0	2.4	14.9	1.1
167	24	45	2.5	12.8	13.5	4.2
Average	-	-	**7.2**	**7.6**	**9.6**	**3.4**

Table 15.2 *Relative Error in the Maximum Cn over a Revolution*

and fatigue resistance, the **relative error** in the **maximum normal force coefficient** over a revolution was computed, according to:

$$\epsilon_{C_n,\text{Max}} = \frac{|C_{n,\text{MEXICO,MAX}} - C_{n,\text{Model,MAX}}|}{C_{n,\text{MEXICO,MAX}}}$$

The results are shown in the table below for several MEXICO trials, with the error in percent:

The average error in the predicted loads over a revolution is approximately 12%, except for the 25% spanwise station. However, the predicted maximum normal force coefficient occurring over a revolution was within 10% of the measured values. Specifically considering the inboard stations, where the DS influence is larger, the accuracy obtained in predicting the maximum C_n was below 8%.

It should be noted that rotational augmentation and DS are complex phenomena which are intrinsically related, but their effects have been superimposed in the current model. Still, the results indicate that, even though the experimental trends were not always captured, the **magnitude of**

the loading amplitude occurring over a revolution in a yawed configuration at high wind speeds was reasonably well predicted. This is important especially for blade fatigue calculations and is an encouraging result.

In yawed operation, the reduced frequency an airfoil section is working at is usually estimated using the 1P as excitation source. However one can argue that the local degree of unsteadiness is related with the time derivative of the angle of attack, which is related also with the yaw angle and wind speed magnitude. In future research DS models could thus be validated experimentally for very high reduced frequencies, which might occur when large yaw misalignments are present.

Conclusions on the validation of the Beddoes Leishman dynamic stall model with Mexico data

The present section developed a BEM code for a yaw-misaligned turbine, which was validated using MEXICO data obtained at moderately high wind tunnel speeds. Posteriorly the Beddoes-Leishman DS model was adapted to the wind turbine framework and validated against 2D wind tunnel aerodynamic data from the OSU. Finally the DS model was implemented in the BEM code and the results of the complete model were compared with the MEXICO data obtained at large wind tunnel speeds. The MEXICO data had to be pre-processed in order to be used for validation.

The most important conclusions are:

The **Beddoes-Leishman DS model** was successfully implemented in a BEM code and results were compared against unsteady 2D data experimental data; generally a good agreement was found.

The DS model was adapted to consider thick airfoil sections by implementing different LE stall criteria. From the methods tested, the $C_{n,\mathrm{MAX}}$ criterion clearly yields better agreement with measurements and consequentially it was selected for subsequent computations.

2D wind tunnel experimental data indicated that even when very thick airfoils are considered LE stall may occur. Consequentially it seems unrealistic to disregard LE separation in HAWT application profiles simply because the airfoils are thick.

Regarding **rotational augmentation**, empirical corrections for the lift and drag 3D coefficients have been compared with results from the MEXICO using an inverse local BEM approach, and reasonable to good agreement was found. These corrections have thus been implemented in the BEM model, up to a relative radius of 0.5.

Results indicate that the angle of attack at which the leading edge separation occurs seems to be unaffected by rotational augmentation; accordingly it was assumed that this critical angle of attack remains constant for all rotationally augmented spanwise sections.

The **DS model was implemented in the BEM code**, and the predicted loads have been compared with the MEXICO data obtained at high wind tunnel speeds in yawed configuration. Generally speaking, reasonable to good agreement was found, and it was also clear that including the DS model improved the load predicting capability when compared to the BEM code using static aerodynamic airfoil coefficients.

Particularly at large yaw angles, the model did not capture the experimental trend in the down-stroke motion in a satisfactory way. This is thought to be related with the increased unsteadiness brought upon by large yaw misalignments which defers separation in the implemented model, even though it seems to occur in the MEXICO.

Still, the loading during the upstroke of the motion was quite well predicted by the model. At the inboard stations, and even when large yaw error were considered, the maximum value of C_n over a revolution obtained with the model was within 7% of experimental results.

As a **final remark** it should be noted that rotational augmentation and DS are complex phenom-

ena which are intrinsically related, but their effects have been superimposed in the current model. Still, the results indicate that, even though the experimental trends were not always captured, the **magnitude of the loading amplitude** occurring over a revolution in a yawed configuration at high wind speeds was reasonably well predicted. This is important especially for blade fatigue calculations and is an encouraging result.

15.3 Rotational Augmentation Disparities in the MEXICO and UAE Phase VI Experiments

S. Schreck	T. Sant	D. Micallef
Nat'l Renewable Energy Lab	University of Malta	University of Malta
United States	Malta	Malta
scott.schreck@nrel.gov	tonio.sant@um.edu.mt	d.micallef@tudelft.nl

Summary

Wind turbine structures and components suffer excessive loads and premature failures when key aerodynamic phenomena are not well characterized, fail to be understood, or are inaccurately predicted. Turbine blade rotational augmentation remains incompletely characterized and understood, thus limiting robust prediction for design. Pertinent rotational augmentation research including experimental, theoretical, and computational work has been pursued for some time, but large scale wind tunnel testing is a relatively recent development for investigating wind turbine blade aerodynamics. Because of their large scale and complementary nature, the MEXICO and UAE Phase VI wind tunnel experiments offer unprecedented synergies to better characterize and understand rotational augmentation of blade aerodynamics. C_n means, C_n standard deviations, and two-dimensional c_p distributions from these two experiments were analyzed and compared. Rotating blade data were evaluated against analogous stationary blade data. Rotational augmentation effects were found to be pervasive, being present over the blade radius and throughout blade operating envelopes at all radial locations investigated. Rotational effects manifested themselves in both mean and time varying statistics.

Introduction on aerodynamic wind tunnel testing of wind turbines

Wind turbine service life is shortened and operability curtailed when unanticipated aerodynamic loads impose excessive stresses on wind turbine structural and mechanical components. Failure to accurately predict turbine aerodynamic loads is due largely to the complex nature of wind turbine blade aerodynamics and incomplete comprehension of the underlying fluid dynamics. At present, key wind turbine aerodynamic phenomena are incompletely characterized and understood.

Historically, experimentation and testing have occupied a central role in discovering, characterizing, and understanding fluid dynamic phenomena that govern wind turbine power production and structural loading. Early field experiments were carried out concurrently at the Netherlands Energy Research Foundation, Delft University of Technology, National Renewable Energy Laboratory,]ø Wind Turbine Test Station, and Imperial College. Notably, these efforts successfully carried out research grade measurements of turbine aerodynamics and structural dynamics in the challenging field environment. These efforts were documented through IEA Wind Annex XIV [77] and Annex XVIII [78].

Unfortunately, the accurate, detailed measurements acquired in these field experiments accentuated a long standing dilemma. Large scale turbine geometries could be densely instrumented and successfully tested, but the uncontrollable and sparsely characterized atmospheric inflows introduced overriding uncertainties. Alternatively, wind tunnel testing offered controlled and uniform inflows, but test section dimensions constrained turbine size, leading to severe mismatches in Reynolds number and other similarity parameters. These uncontrolled inflows and similarity parameter disparities were broadly recognized as significant impediments to deeper comprehension and more accurate prediction of turbine aerodynamics.

This dilemma was first addressed by a series of joint projects between the Aeronautical Research Institute of Sweden (FFA) and the China Aerodynamics Research and Development Cen-

ter (CARDC). This series of projects culminated in 1990, when testing was completed in the CARDC 12 m x 16 m wind tunnel on a two bladed rotor having a diameter of 5.35 m. In addition to nacelle and blade root moments, surface pressures were measured at 232 taps distributed over eight radial stations.[79, 80] Success in these experiments stimulated interest internationally, and laid the foundations for more ambitious plans with larger turbines and wind tunnels, and more elaborate tests.

Resource constraints and facility schedules postponed further wind tunnel testing of larger scale wind turbines until the following decade. In 2000, NREL completed testing of the 10.1 m diameter Unsteady Aerodynamics Experiment (UAE) Phase VI turbine in the NASA Ames 24.4 m x 36.6 m wind tunnel.[81] In 2006, the EU Model Rotor Experiment in Controlled Conditions (MEXICO) Project with a 4.5 m diameter rotor was tested in the DNW 9.5 m x 9.5 m LLF.[82, 83] Notably, these efforts were sufficiently similar to enable corroborative comparisons, while specific differences showed effects not observed previously.

Wind tunnel testing of large scale turbines represents a crucial, though relatively recent development for understanding and predicting wind turbine aerodynamics. For rotational augmentation, prior research extends back some decades, encompassing experimental, theoretical, and computational work. A review of these efforts will not be undertaken herein, but can be found in prior works, e.g. [84]. The current work will concentrate on characterizing and understanding rotational augmentation of blade aerodynamic response, using the aerodynamics measurements acquired in the MEXICO and UAE Phase VI wind tunnel tests.

Experimental Methods

In this section the main characteristics of the Mexico experiment and turbine are recalled from section 4 and compared with the UAE Phase VI wind tunnel test.

MEXICO Turbine

MEXICO testing was carried out in the DNW LLF 9.5 m x 9.5 m open jet, and has been documented by Snel, et al.[82, 83] The MEXICO turbine had a three bladed upwind rotor that was 4.5 m in diameter with zero cone angle. The rotor was pitch controlled and turned counterclockwise (viewed from downwind) at constant speed. Though the experiment encompassed multiple rotor speeds, data analyzed in the current work were acquired at a rotor speed of 325 RPM. A cylindrical tower 0.508 m in diameter with a spiral strake held the nacelle at a hub height of 5.12 m with 2.13 m overhang. This situated the rotor axis at the jet centerline and placed the rotor well upwind of the tower. The MEXICO turbine appears in the left panel of Figure 15.7, in the DNW LLF 9.5 m x 9.5 m.

Full pressure tap rows were located on all three blades, with the tap rows at 0.25R and 0.35R on blade 1, the 0.60R tap row on blade 2, and the 0.82R and 0.92R tap rows on blade 3. A full pressure tap row consisted of 25 to 28 taps, distributed over the blade pressure and suction surfaces. The upper part of Figure 15.8 shows the MEXICO pressure tap distribution on the blade suction surface, with all five full tap rows depicted on one blade. Pressure taps were more densely distributed near the blade leading edge to better resolve the pronounced gradients typically present there. To validate azimuthal uniformity, partial pressure tap rows were distributed over multiple blades at each radius.

The MEXICO experiment blades were both twisted and tapered. The blade taper distribution is evident in Figure 15.8, with maximum blade chord being 0.240 m at 0.20R, and tapering to 0.011 m at the tip. Figure 15.9 documents blade twist, which decreases from 16.4^o at 0.20R to 0.0^o at the tip. Between 0.20R and the tip, blade cross section transitioned from the DU91-W2-250 airfoil ($0.20 \leq$ r/R ≤ 0.46), to the Risoe A1-21 ($0.54 \leq$ r/R ≤ 0.66), and finally to the NACA

Figure 15.7 *MEXICO turbine in the DNW LLF 9.5 m x 9.5 m open jet (left), and the UAE Phase VI turbine in NASA Ames 24.4 m x 36.6 m wind tunnel (right).*

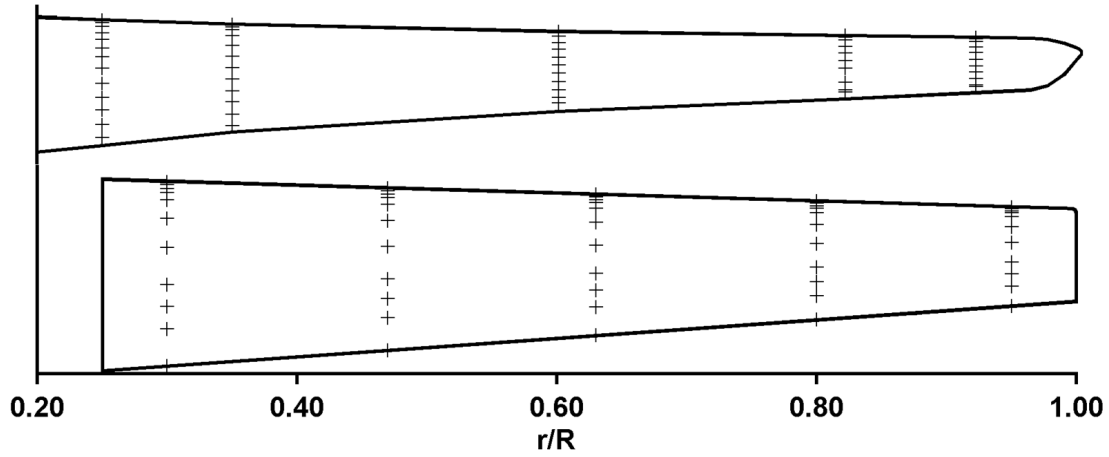

Figure 15.8 *MEXICO and UAE Phase VI blade planform drawings with suction surface tap locations. Leading edge is at the top of each planform.*

64-418 ($0.74 \leq$ r/R ≤ 1.00). The blade pitched about an axis located 0.25c aft of the leading edge, and centered between the blade upper and lower surfaces at that chord location.

Pressure taps were flush with the blade surface and 0.4 mm in diameter. Close coupled beneath each tap was a Kulite XCQ-95 series piezoresistive pressure transducer having sealed gage reference. Close coupling with the pressure taps minimized reduction of the transducers 150 kHz bandwidth, yielding flat frequency response across a broad spectrum. Each of the transducer pressure inputs was scanned at 5514 Hz. Test section speed and air properties were measured using the DNW LLF wind tunnel air data system.

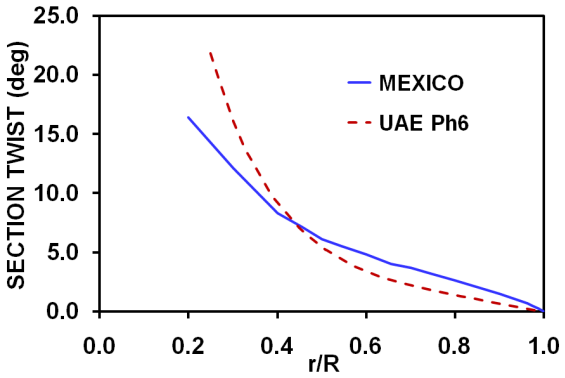

Figure 15.9 *Sectional blade twist for aerodynamically active parts of MEXICO and UAE Phase VI blades.*

Data were collected with the turbine rotor stationary (parked) and with the rotor rotating at a constant speed of 325 RPM. To achieve stationary blade conditions, the instrumented turbine blade was fixed at the 12 o'clock azimuth position and test section velocity (U_∞) was set to 30 m/s. Then, turbine blade pitch was set at 26 selected pitch angles, from 2.3^o to 90^o . At each pitch angle, a 5 s data set was acquired.

For rotating conditions, turbine blade plane of rotation was maintained orthogonal to the test section centerline, yielding a yaw angle of 0^o . Blade pitch was held constant at -2.3^o . Test section speed (U_∞) was varied between 5.4 m/s and 30.0 m/s, at graduated intervals, yielding tip speed ratios (λ) of 14.1 to 2.5. At each (U_∞), a 5 s data set was acquired. For both stationary and rotating conditions, time records of c_p were integrated over the blade sectional chord to get time records of Cn. These time records were processed to obtain mean and standard deviation statistics for both c_p and C_n.

UAE Phase VI Turbine

Several Phase VI UAE configurations were tested in the NFAC 24.4 m x 36.6 m wind tunnel, and are described by Hand, et al.[81] Data analyzed herein were acquired from a two bladed upwind rotor, 10.1 m in diameter, with zero cone angle. The rotor turned clockwise (viewed from downwind) at a constant 71.6 RPM, was stall regulated, and had a maximum rated power of 19.8 kW. A cylindrical tower 0.4 m in diameter supported the turbine at a hub height of 12.2 m (test section centerline), with 1.32 m rotor overhang. This UAE configuration, mounted in the NASA Ames 24.4 m x 36.6 m wind tunnel, is in the right panel of Figure 15.7.

The black blade on the left side of the UAE rotor in Figure 15.7 was equipped with five full pressure tap rows to acquire detailed surface pressure data. A full pressure tap distribution consisted of 22 taps distributed over the pressure and suction surfaces of the blade. Pressure taps were more densely distributed near the blade leading edge to better resolve the pronounced gradients typically present there. The lower portion of Figure 15.8 shows that UAE full pressure tap distributions that were located at r/R = 0.30, 0.47, 0.63, 0.80, and 0.95.

The blades used throughout the NASA Ames wind tunnel test were both twisted and tapered. The blade taper distribution is apparent in Figure 15.8 , with maximum blade chord being 0.737 m at 0.25R, and tapering to 0.356 m at the tip. Figure 15.9 documents blade twist, which decreases from 21.8^o at 0.25R to 0.0^o at the tip. Between 0.25R and the tip, blade cross section was uniform, corresponding to the S809 airfoil. The blade pitched about an axis located 0.30c aft of the leading edge, and centered between the blade upper and lower surfaces at that chord location. Design procedures, constraints, and measures of merit for this blade have been documented in detail.[85]

Surface pressure taps were flush mounted at the blade surface, and had inside diameters of 0.69 mm. From the taps, stainless steel hypodermic tubes with inside diameters of 0.69 mm transmitted surface pressures to the pressure transducers. Hypodermic tubing lengths were minimized to mitigate pressure delay and dispersion effects. Pressures were measured by five Pressure Systems Incorporated ESP-32 electronically scanned pressure transducers located inside the blade near the five full pressure tap distributions. Each of the transducer pressure inputs was scanned at 520.8 Hz. In conjunction with the tubing frequency response, this provided antialiased digitization and minimal gain variation out to 55 Hz.[86] Test section flow speed and air properties were measured using the 24.4 m x 36.6 m wind tunnel air data system.[87]

Data were collected with the turbine rotor stationary (parked) and with the rotor rotating at a constant speed of 71.6 RPM. To achieve stationary blade conditions, the instrumented turbine blade was fixed at the 12 o'clock azimuth position and test section velocity (U_∞) was set to 30 m/s. Then, turbine blade pitch was incremented in 5^o steps, from -15^o to 90^o . After each pitch increment, the flow was allowed to stabilize, and then an 8 s data record was taken.

For rotating conditions, turbine blade plane of rotation was maintained orthogonal to the test section centerline, yielding a yaw angle of 0^o . Blade pitch angle was held constant at 3.0^o . Test section velocity (U_∞) was varied between 5 m/s and 25 m/s, in nominal increments of 1 m/s, corresponding to tip speed ratios (λ) of 7.5 to 1.5. At each U_∞, a 30 s data record containing 36 blade rotation cycles was acquired.

For both stationary and rotating conditions, time records of c_p were integrated over the sectional chord to obtain time records of C_n. Time records of c_p and C_n were processed to obtain means and standard deviations for c_p and C_n.

Results and Discussion

The results below compare MEXICO and UAE Phase VI sectional aerodynamic forces and surface pressure distributions, for radial locations near the blade root and farther out toward the blade tip. These analyses include both mean and time varying statistics. To provide some integration of sectional flow field characteristics, mean surface pressure topologies for select operating conditions also are included.

Local Inflow References

In both the MEXICO and UAE Phase VI experiments, local dynamic pressure was computed as the difference between test section static pressure (p_∞) and local total pressure (p_0). Local total pressure was determined at each full pressure tap distribution as the highest pressure sensed in the tap distribution.

In the current work, C_n was analyzed instead of C_l for two reasons. First, C_n was considered a more physically pertinent parameter of interest because it decouples flow field activity from inflow direction. Second, adoption of C_n permits comparisons of results herein with a broad range of analyses previously accomplished for other experimental data.

To obtain angle of attack (α) in a consistent fashion for the MEXICO and UAE data, an inverse free wake lifting line model was used as described below. This model computed angles of attack corresponding to the MEXICO and UAE Phase VI experimental data at zero yaw, and has been thoroughly validated for both the UAE Phase VI [88] and MEXICO [89] databases. Thus, it furnished angle of attack data that were both accurate and consistent between the two experiments. It should be noted that the lifting line formulation limits the fidelity with which three-dimensional flow field features are resolved at high angles of attack.

The inverse free wake algorithm is diagrammed in Figure 15.10. The algorithm begins with

pressure data from the MEXICO and UAE experiments, which provide the normal and tangential blade loads for every blade spanwise location and rotor azimuth angle at which the data were sampled. In the algorithm, force data can be interpolated for a desired number of spanwise and azimuthal discretization elements. An initial angle of attack at each of these elements is assumed, and then normal and tangential forces are used to find lift and drag.

Using lift data and local inflow velocity with the Kutta-Joukowski theorem, a bound circulation distribution is obtained for every time step. From this, the trailed and shed circulation can be obtained. This enables the velocity field due to the turbine wake to be determined, and the wake is allowed to develop freely under the influence of such a velocity field. A new angle of attack can thus be obtained that will enable a new circulation distribution to be obtained.

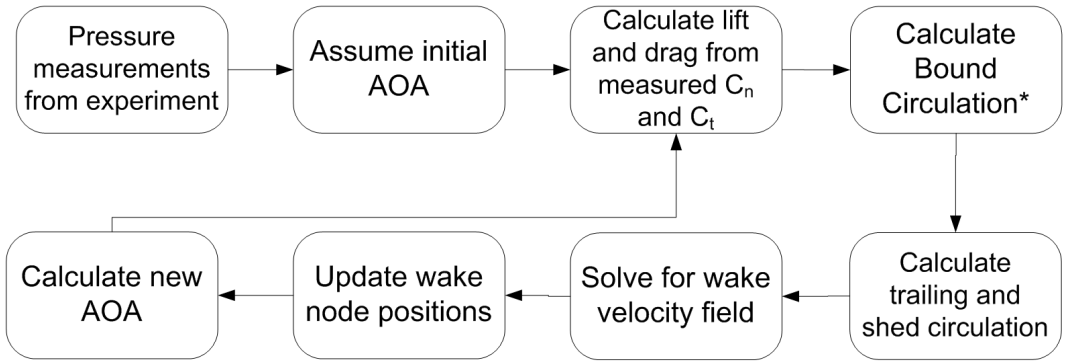

Figure 15.10 *Schematic of inverse free wake model algorithm used to compute angles of attack for MEXICO and UAE Phase VI data.*

The process is repeated until a convergence in angle of attack is achieved. This is usually achieved in two or three iterations. The process is called an inverse free wake method because rather than obtaining the blade loads from two-dimensional airfoil information, it uses experimental measurements in order to solve for the velocity field and hence angles of attack on the rotor blades. Angles of attack (α) for both the UAE and MEXICO experiments were computed using the same inverse free wake model, and so were consistent.

Reynolds numbers (Re) for the stationary (parked) MEXICO blade across the span 0.25 $\leq$ r/R $\leq$ 0.92 at U_∞ = 30 m/s were $0.19 \times 10^6 \leq$ Re $\leq 0.43 \times 10^6$. For the rotating blade (325 RPM) across the same radial span at 5.4 m/s $\leq U_\infty \leq$ 30 m/s, Reynolds numbers were $0.29 \times 10^6 \leq$ Re $\leq 0.51 \times 10^6$. For the stationary (parked) UAE blade across the span 0.30 $\leq$ r/R $\leq$ 0.95 at U_∞ = 30 m/s, Reynolds numbers were $0.78 \times 10^6 \leq$ Re $\leq 1.46 \times 10^6$. For the rotating blade (71.6 RPM) across the same radial span at 5 m/s $\leq U_\infty \leq$ 25 m/s, Reynolds numbers were $0.63 \times 10^6 \leq$ Re $\leq 1.36 \times 10^6$. Prior research [90] has shown that Reynolds number dependencies exercised no significant effect on rotational augmentation for the UAE.

Mean C_n

Figure 15.11 shows mean C_n data corresponding to the farthest inboard radial locations on the MEXICO and UAE Phase VI blades. In the upper panel of Figure 15.11, UAE Phase VI mean C_n data acquired at 0.30R for stationary blade conditions are plotted as a function of α. Here, mean C_n initially increased linearly with at a rate of 0.04 per degree. This slope was substantially lower than the 0.11 per degree rate for two-dimensional airfoils, indicating that three-dimensional influences were significant for this radial location under stationary blade conditions. Upon reaching $\alpha = 8.9^o$, the slope of the curve decreased visibly, but C_n continued to increase until $\alpha = 23.9^o$

deg. At this point, C_n attained a maximum of 0.911 and stall occurred. Thereafter, C_n decreased slightly to a local minimum of 0.861 at 34.0^o, and finally rose to C_n = 0.948 at 43.0^o. MEXICO stationary blade data were not available for the 0.25R radial location.

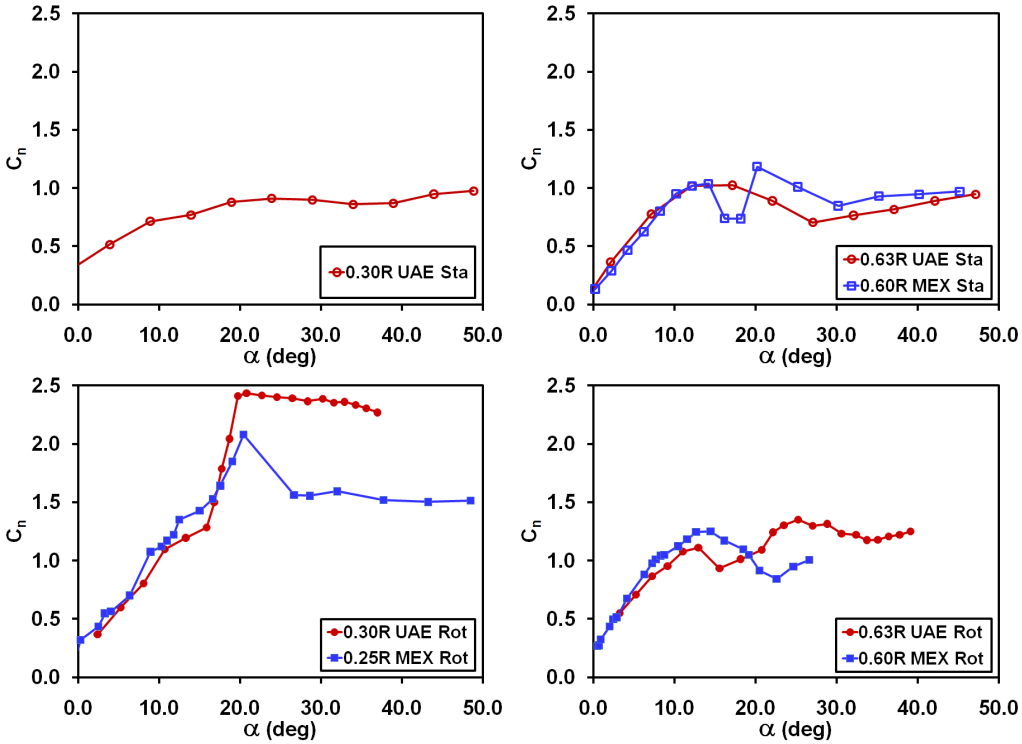

Figure 15.11 *MEXICO and UAE Phase VI mean C_n at inboard radius, for parked (upper panel) and rotating (lower panel) blades.*

Figure 15.12 *MEXICO and UAE Phase VI mean C_n at mid-span radius, for parked (upper panel) and rotating (lower panel) blades.*

The lower panel of Figure 15.11 shows mean C_n data acquired under rotating blade conditions on the MEXICO blade at 0.25R and on the UAE blade at 0.30R. For both data sets, C_n increased with α in pseudo-linear fashion through the approximate range $0^o \leq \alpha \leq 10^o$, at a rate of 0.09 per degree. That this slope was more than twice the slope for the parked blade indicates that rotational influences began to modify the blade flow field at low angle of attack. At $\alpha = 8.9^o$ for the MEXICO data and $\alpha = 10.7^o$ for the UAE, $C_n - \alpha$ curve slope decreased to less than half of its previous magnitude, but steepened again at $\alpha \approx 15^o$, to 0.15 per degree for the MEXICO curve and to 0.30 per degree for the UAE. These C_n kinematics implied that exceeding the two-dimensional static stall angle of attack prompted significant rotational alterations to the flow field on the blade.

These exceptionally steep $C_n - \alpha$ curve subintervals culminated in C_n maxima (stall C_n), which occurred at $\alpha = 20.4^o$ and C_n = 2.081 for MEXICO, and at $\alpha = 20.8^o$ and C_n = 2.436 for the UAE. For both data sets, stall C_n was twice that generally observed for two-dimensional airfoils, and for the UAE was nearly three times that for the stationary blade. Rotating blade stall α was about 5^o higher than that generally measured for two-dimensional airfoils. For the UAE rotating blade stall α approximated stall α for the stationary blade. After reaching maximum (stall) C_n, MEXICO and UAE data displayed dramatically different kinematics. MEXICO C_n dropped precipitously from 2.081 to 1.564 over the α interval from 20.4^o to 26.7^o, and then remained approximately constant. In sharp contrast, UAE C_n declined gradually from 2.436 to 2.270 as α increased from 20.8^o to 37.0^o. Notably, neither inboard C_n-α curve exhibited a maximum, either absolute or local, in the α range commonly associated with two-dimensional airfoil stall. Rather, the only maxima, corresponding to stall, occurred at α levels usually associated with airfoil post

stall.

Figure 15.12 shows data for mid-radius stations on the MEXICO and UAE Phase VI blades. The upper panel of Figure 15.12, contains mean C_n-α data for the stationary MEXICO blade at 0.60R and for the stationary UAE blade at 0.63R. Through the range $0^o \leq \alpha \leq 14^o$, both curves followed highly similar trajectories. Both rose at the same slope of 0.08 per degree until reaching $\alpha = 8^o$. Thereafter, the slopes of both curves decreased progressively with increasing α , and both leveled off at C_n = 1.04 upon reaching $\alpha = 14^o$. At this point, the two curves diverged. The MEXICO curve decreased briefly to 0.737, and then rose sharply to a global maximum of C_n = 1.185 at $\alpha = 20.2^o$. Subsequently, MEXICO C_n decreased gradually to 0.848 at $\alpha = 30.2^o$, and then increased gradually to culminate at 0.971 at $\alpha = 45.2^o$. After diverging from the MEXICO curve, the UAE Phase VI curve decreased gradually to C_n = 0.706 at $\alpha = 27.1^o$, and finally increased in equally gradual fashion to end at 0.946, at $\alpha = 47.1^o$.

The lower panel of Figure 15.12 contains mean C_n data for rotating blade conditions on the MEXICO blade at 0.60R and on the UAE blade at 0.63R. For both data sets, C_n increased linearly with α until reaching $\alpha = 7.2^o$. In this low α range, the MEXICO and UAE C_n-α curve slopes were 0.11 and 0.08 per degree, respectively. As α increased beyond 7.2^o, C_n-α curve slopes decreased visibly for both MEXICO and UAE data. Subsequently, MEXICO C_n reached a maximum of 1.251 at $\alpha = 14.4^o$, and UAE C_n reached a maximum of 1.111 at $\alpha = 12.9^o$. These stall C_n values were higher by 8 percent and 6 percent, respectively, than those for the stationary blade C_n stall. MEXICO stall took place at marginally higher α and reached slightly higher C_n than that for the UAE. Nonetheless, stalling kinematics were highly similar for the two data sets, with C_n decreasing gradually after cresting at maximum (stall) levels. Notably, mid-radius MEXICO and UAE stall parameters (α and C_n) for the rotating blade did not differ radically from their stationary blade counterparts.

Though mid-radius stall kinematics differed little between the stationary and rotating blades, post-stall responses differed significantly. Following stall, UAE C_n declined to a local minimum of 0.935 at $\alpha = 15.5^o$. MEXICO C_n decreased to a slightly lower local minimum of 0.843, at a somewhat higher α of 22.6^o. After this, UAE C_n increased to an absolute maximum (post-stall) of 1.35 at $\alpha = 25.3^o$, and then declined slowly and nonmonotonically to culminate at C_n = 1.249 at $\alpha = 39.1^o$. MEXICO C_n increased from the local minimum for a brief interval, but halted prematurely at $\alpha = 26.6^o$, where C_n = 1.006.

Time Varying C_n

Figure 15.13 contains C_n standard deviation (σ_{C_n}) data for the farthest inboard radial locations on the MEXICO and UAE Phase VI blades. In the upper panel of Figure 15.13, UAE Phase VI σ_{C_n} data for 0.30R under stationary blade conditions are plotted as a function of α. Through the range $0^o \leq \alpha \leq 8.9^o$, σ_{C_n} remained constant at 0.017, and subsequently increased in linear fashion to a maximum of 0.059 at $\alpha = 18.9^o$. After attaining this maximum, σ_{C_n} decreased in intermittent steps over the next 30.0^o interval, and finally reached 0.020 at $\alpha = 48.9^o$. MEXICO stationary blade data were not available for the 0.25R radial location.

The lower panel of Figure 15.13 shows σ_{C_n} data acquired under rotating blade conditions on the MEXICO blade at 0.25R and the UAE blade at 0.30R. In the low α range, σ_{C_n} remained low and approximately level for both the MEXICO and UAE data. Upon reaching α = 15.0 deg, the MEXICO σ_{C_n} began to rise at a modest rate until $\alpha = 20.4^o$. Over approximately the same α interval, UAE σ_{C_n} increased sharply after $\alpha = 13.3^o$, reaching a local maximum of 0.178 at $\alpha = 17.8^o$.

Beyond $\alpha = 20.4^o$, higher α prompted relatively small though visible variations in MEXICO σ_{C_n}, with the lowest σ_{C_n} in this α range being 0.072 at $\alpha = 37.7^o$, and the highest being 0.091 at $\alpha = 48.5^o$. Over a comparable range of $19.7^o \leq \alpha \leq 30.2^o$, UAE σ_{C_n} climbed to a maximum

of σ_{C_n} = 0.214 at $\alpha = 30.2^o$, though the σ_{C_n} rate of increase through $19.7^o \leq \alpha \leq 30.2^o$ was significantly lower than that over $13.3^o \leq \alpha \leq 17.8^o$. Though the σ_{C_n} magnitudes observed for the UAE σ_{C_n} were appreciably higher than those for MEXICO, the two curves were well correlated with respect to slope variations and the occurrence of minima and maxima.

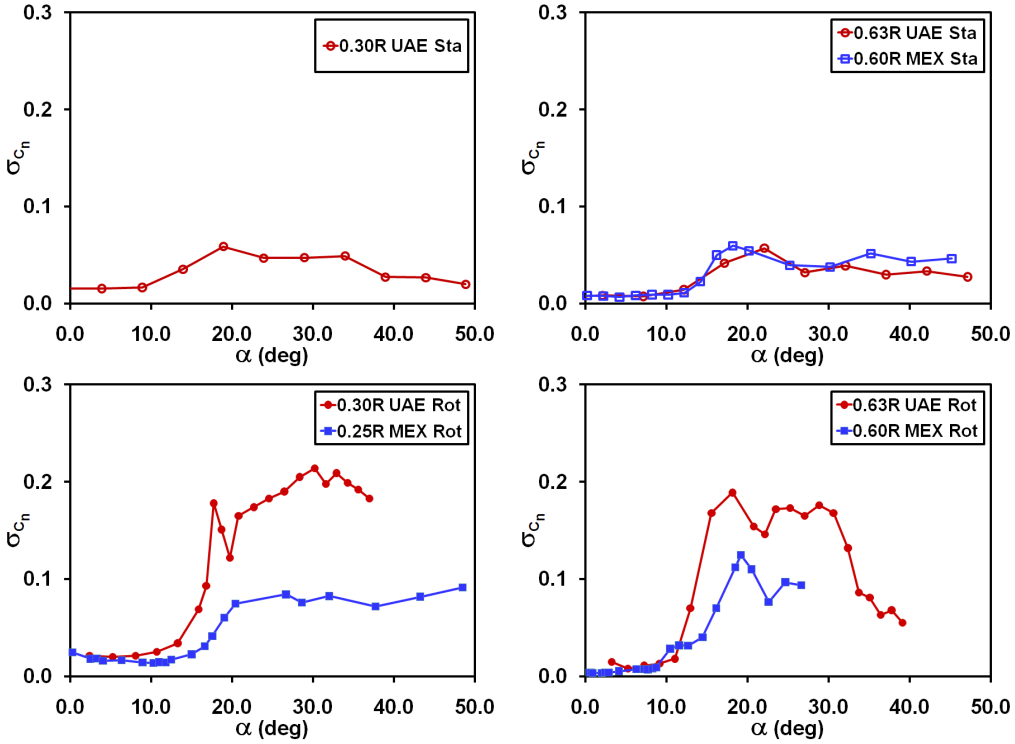

Figure 15.13 *MEXICO and UAE Phase VI σ_{C_n} at inboard radius, for parked (upper panel) and rotating (lower panel) blades.*

Figure 15.14 *MEXICO and UAE Phase VI σ_{C_n} near mid-span radius, for parked (upper panel) and rotating (lower panel) blades.*

Figure 15.14 contains C_n standard deviation (σ_{C_n}) data for the mid-radius locations on the MEXICO and UAE Phase VI blades. In Figure 15.14, the upper panel contains σ_{C_n} data for the stationary MEXICO blade at 0.60R and for the stationary UAE blade at 0.63R. Clearly, the two σ_{C_n}-α curves show striking similarities with respect to maximal magnitudes and slope correlations. Through the range $0.0^o \leq \alpha \leq 12.2^o$, neither curve deviated significantly from the other, with both remaining constant at σ_{C_n} = 0.01. After $\alpha = 12.2^o$, both curves began to rise at moderate and similar rates, with the MEXICO curve peaking at σ_{C_n} = 0.060 at $\alpha = 18.2^o$, and the UAE curve peaking at σ_{C_n} = 0.057 and $\alpha = 22.1^o$. During the subsequent decrease in σ_{C_n}, the two curves continued to resemble each other, with the MEXICO curve reaching a minimum of σ_{C_n} = 0.038 at $\alpha = 30.2^o$, and the UAE curve doing the same at σ_{C_n} = 0.032 and $\alpha = 27.1^o$. At higher values of α, the correlation between the two curves was less evident, though still perceptible.

The lower panel of Figure 15.14 shows σ_{C_n} data acquired during blade rotation from the MEXICO blade at 0.60R and the UAE blade at 0.63R. Like the stationary blade data in the upper panel of Figure 15.14, the data for the MEXICO and UAE rotating blades show remarkable similarities. Below $\alpha = 10^o$, σ_{C_n} remains below 0.01 for 15 of 16 data points in this range. The sole exception is the UAE data point at $\alpha = 3.2^o$, which assumes a value of 0.015. At approximately $\alpha = 10^o$, both the MEXICO and UAE curves begin to rise rapidly. Thereafter, at $\alpha = 19.2^o$, the MEXICO curve peaks at σ_{C_n} = 0.125, and at $\alpha = 18.2^o$, the UAE curve peaks at σ_{C_n} = 0.189.

From this peak, the MEXICO curve decreases to σ_{C_n} = 0.076 at $\alpha = 22.6^o$, and then rises to culminate at σ_{C_n} = 0.094 at $\alpha = 26.6^o$. Similarly, from the UAE peak, the curve descends to

σ_{C_n} = 0.146 at $\alpha = 22.1^o$, and then rises again, reaching σ_{C_n} = 0.165 at $\alpha = 27.0^o$. Though the MEXICO data end at $\alpha = 26.6^o$ and the UAE data continue through $\alpha = 39.1^o$, the correlation between the two data sets through the range $0^o \leq \alpha \leq 27^o$ is dramatic. This implies correspondingly prominent similarities in the unsteady flow physics of the MEXICO and UAE blades near mid-radius.

Sectional c_p Distributions

Blade c_p data were analyzed to better understand the fluid dynamics responsible for the MEXICO and UAE C_n kinematics. Specifically, MEXICO and UAE Phase VI mean sectional c_p distributions, for rotating blade stall conditions, were compared at the inboard and mid-radius locations.

The MEXICO rotating blade c_p data shown in Figure 15.15 were acquired at 0.25R for $\alpha = 20.4^o$. The MEXICO suction surface c_p distribution had a suction peak at 0.002c where c_p = 7.496. Aft of this peak, c_p magnitude decreased sharply over the leading 0.11c, then more gradually from 0.11c to 0.30c, and finally became virtually constant on the aft 0.70c of the suction surface. Over the aft 0.70c, c_p varied between 0.935 and 1.461. On the MEXICO blade pressure surface, stagnation was seen at the 0.16c tap.

Also shown in Figure 15.15 are UAE rotating blade c_p data, which were measured at 0.30R for $\alpha = 20.8^o$. UAE suction surface c_p exhibited no leading edge suction peak, and instead assumed a virtually constant level of approximately 2.5 over the chord range $0.0c \leq x/c \leq 0.56c$. Aft of 0.56c, c_p level varied in pseudo-linear fashion, reaching c_p = 0.394 at the trailing edge. On the UAE blade pressure surface, stagnation was detected at the 0.06c tap location.

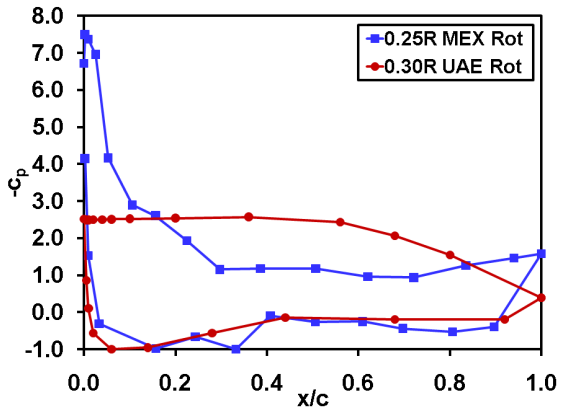

Figure 15.15 *MEXICO and UAE Phase VI stall c_p distributions at inboard radius, for rotating blades. MEXICO = $\alpha = 20.4^o$ and UAE $\alpha = 20.8^o$.*

Notably, the Figure 9 MEXICO and UAE rotating blade stall c_p distributions differed dramatically from each other, even though they were measured at nearly identical α and yielded stall C_n levels that were comparably elevated (Figure 15.11). Thus, it was evident that different c_p distribution features were responsible for observed C_n amplifications. Though the MEXICO and UAE pressure surface c_p distributions were slightly unconventional, none of the attributes present there could account for the C_n amplifications, thus focusing attention on the suction surface.

The MEXICO suction surface c_p distribution displayed two attributes that differed appreciably from stationary airfoils. First, while suction peak height was not significantly greater than that observed on stationary airfoils, suction peak chordwise extent was substantially broader. Second, c_p values of 0.935 to 1.461 in the $0.30c \leq x/c \leq 1.0c$ chord region were two to three times greater than those produced by stationary airfoils. In contrast, the entire UAE suction surface was nonstandard in conformation, was augmented in c_p magnitude, and was responsible for amplifying C_n.

As shown in previous research, these contrasting c_p distributions imply conspicuously different flow field topologies.[91, 92] In refs. [91] and [92], c_p distributions like that in Figure 15.15 for the UAE have been conclusively linked to leading edge separation and downstream shear layer impingement. In future work, analyses like those used in refs. [91] and [92] will be applied to MEXICO c_p distributions to reveal flow field topology development on the MEXICO blade. At present, it can be stated that the Figure 15.15 MEXICO c_p distribution is consistent with a flow field containing a trailing edge separation.

Figure 15.16 shows rotating blade c_p data for the MEXICO blade at 0.60R, and for the UAE blade at 0.63R. The MEXICO data correspond to $\alpha = 14.4^o$ and the UAE data to $\alpha = 12.9^o$, both of which represent stall conditions consistent with the rotating blade data in Figure 15.12. Both c_p distributions are highly conventional, and strongly resemble those for stationary airfoils. Specifically, both the MEXICO and UAE pressure distributions have very narrow suction peaks, with minimum c_p values of 5.816 and 3.874. From 0.02c to midchord, c_p magnitudes for both blades decrease gradually until reaching the midchord. Between midchord and trailing edge, c_p for both blades remains virtually constant at 0.3 to 0.4, again similar to stationary airfoils. The c_p distributions in Figure 15.16 both are consistent with trailing edge separation [91, 92], and significant augmentation relative to stationary airfoil c_p distributions is not evident.

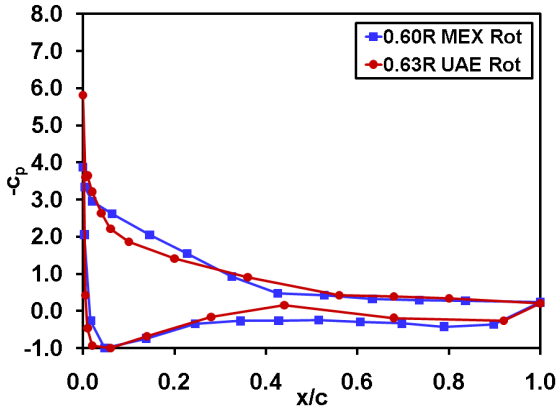

Figure 15.16 *MEXICO and UAE Phase VI stall c_p distributions near mid-span radius, for rotating blades. MEXICO $\alpha = 14.4^o$ and UAE $\alpha = 12.9^o$.*

Conclusions on the comparison between the Mexico and UAE Phase VI experiment

The MEXICO and UAE Phase VI and experiments were complementary in many crucial respects, and thus offer unprecedented synergies to better understand and predict rotational augmentation of blade aerodynamics. Comparisons of the two surface pressure data sets included both C_n mean and C_n standard deviation statistics, and encompassed stationary blade baseline data as well as rotating blade data. Angles of attack were computed for both data sets using the same validated inverse free wake model, which provided an accurate and consistent inflow reference. Analyses of inboard and mid-radius blade locations support the following conclusions.

- Rotational effects on mean C_n are active across the entire blade performance envelope. At low and moderate where inviscid influences dominate, blade rotation steepens C_n-α curves. At elevated α where viscous effects play a major role, blade rotation delays stall to higher α and produces higher stall C_n.
- At each radial location, MEXICO and UAE C_n-α curve steepening, stall α delay, and C_n amplification are closely comparable. However, as indicated by C_n-α curve conformation

in the stall and post-stall α range, MEXICO and UAE stall dynamics differ appreciably for inboard locations and to a lesser extent at mid-radius, consistent with differences in respective airfoil shapes.

- Consistent with disparate inboard C_n-α curves, inboard c_p distributions also are dissimilar. The MEXICO c_p distribution is consistent with a trailing edge separation, while the UAE distribution implies a leading edge separation followed by shear layer impingement.
- Blade rotation amplifies C_n standard deviation levels above those for stationary blades. UAE C_n standard deviation levels consistently exceed those for MEXICO. However, strong correlations exist between MEXICO and UAE C_n standard deviation level variations with respect to α.
- The MEXICO and UAE blade planforms differ substantially. Nonetheless, three-dimensional surface pressure topologies corresponding to peak stall operation share common features, testifying to the robustness of the rotationally modified flow field.

The current work has comparatively analyzed MEXICO and UAE data to validate and generalize knowledge regarding rotationally augmented blade flow fields. Some results presented herein provide confirmation of prior research, while other results provide insights not previously grasped in analyses of either data set alone. Future inquiry using the MEXICO and UAE Phase VI data will foster more complete understanding of rotationally augmented blade flows, and thus facilitate more accurate prediction and improved turbine design.

16 Task 4.9: Dynamic inflow

16.1 Introduction on Task 4.9

As part of the Mexnext activities, Task 4.9 is devoted to study dynamic inflow. Measurements have been taken at fast pitching steps and steep ramps in rotor speed. In such cases the wake behind the rotor and subsequently the induction responds with a certain time delay (dynamic inflow) because it will take some time before the wake constituted by the shed and trailed vortex system is in equilibrium with the new rotor loading . These dynamic inflow effects lead to an overshoot in the load response in the case where the thrust is increased e.g. due to a pitch step. The objective with task 4.9 is to analyze the load transients and derive the associated time constants, ideally determined for different radial positions.

16.2 Participants

Four participants planned the following work within this task.

1 ECN: ECN will compare the measured time constants with the time constants as used in their BEM code. Furthermore a free vortex wake method will be used to simulate these measurements.

2 RISØ-DTU: RISØ-DTU will use several aerodynamic models for computing dynamic inflow conditions such as pitch step and rpm step changes.

3 CENER: CENER will use the FAST code to assess the dynamic inflow effects.

4 Technion: Technion will apply a new blade-element model, coupled with an actuator disk model which is capable of modelling both the aerodynamic loads and the flow field in the rotor plane.

16.3 Initial data analysis by ECN

A first analysis of the data as presented by ECN indicated that the pitch change probably had been much slower than what was the target of 0.05 s from -2.3 ° to 5 ° specified in the test plan. The axial force measured by the balance for the case at 15 m/s shown in Figure 16.1 indicates a pitching that takes a few seconds. Unfortunately the pitch position was not monitored continuously during the measurement campaigns so it has not been possible to reconstruct the actual test conditions in details.

16.4 Analysis of blade bending moments - pitch step

As a follow up on the initial analysis by Pascal [13] the calibrated flapwise and edgewise blade bending moments at radius 0.26 m have been derived in the present work and are shown in Figure 16.2. These results clearly confirm the above results from the balance and again indicate that the pitching has taken a few seconds. At the highest wind speed of 24 m/s the considerable variations in the flapwise moment indicate stalled conditions on the blade.

16.5 Analysis of blade bending moments - steep ramp in rotor speed

Next the dynamic inflow cases using fast changes in rotor speed are analysed. As above four cases were conducted at wind speeds of 10 m/s, 15 m/s, 18 m/s and 24 m/s and a fixed pitch of

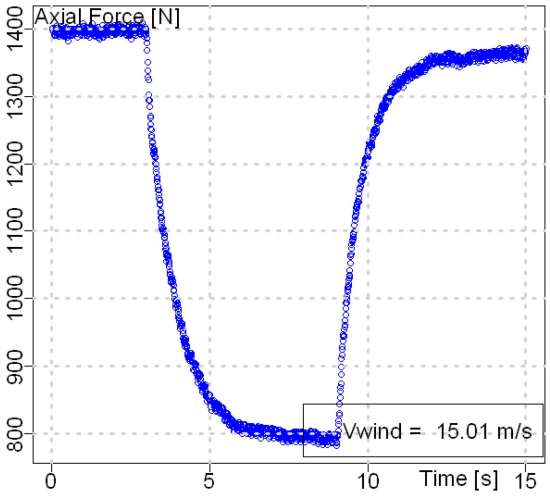

Figure 16.1 *The measured axial force during a pitch step from -2.3 ° to 5.0 °. Figure from [13].*

-2.3 °. The ramp for the decreasing rotational speed from 425 rpm to 325 rpm seems to be slightly less steep than the ramp for the increasing rotational speed and it is seen that it takes about 1 s to decelerate the rotor. The changes in the flapwise moment are fundamentally different for the 10 m/s case than for the other three cases. The increase in loading for decreasing the rotational speed for the 10 m/s case indicates that the thrust coefficient at 425 rpm is high and probably above the ideal loading of the rotor. For the other three test cases the basic tendency of changes in loading for the variation of rotational speed are the same. In particular for there seems to be some dynamic effects at the increase in rotational speed. It should also be noted that the rotational speed changes cause considerable structural dynamic loads in the blades which could be a part of the overshoot in the in the flapwise moment.

16.6 Comparison with simulations

A few of the test cases with the change in rotational speed were simulated with the aeroelastic code HAWC2 from RISØ-DTU using the standard airfoil data for the three airfoils. The measured time trace of the rotational speed was read into the code and the simulations were thus performed for the exact conditions of the measurements. Results for the 15 m/s case and the 18 m/s case are shown in Figure 16.4 and Figure 16.5, respectively.

The first major difference is that the level of the simulated flapwise moment is about a factor 2 bigger than the measured value. The tendency with higher loads in the simulations is in line with the deviations radial distribution of normal and tangential forces seen previously in the present report. Another cause of the deviations could be due to the flapwise deflection of the blades which in combination with the rotation of the blade will decrease the flapwise moment, not modelled in the present simulations. However, even when the HAWC2 moments were scaled to a level comparable with the measurements, the step in loads is still quite different from the measurements. Finally, the simulations do not show dynamic inflow effects for the applied rate of rotational speed changes.

16.7 Conclusions

Based on the presented analysis of the dynamic inflow test cases it was decided not to conduct the planned research activities by the different participants because it is not expected that accurate dynamic inflow time constants can be derived from the experimental data.

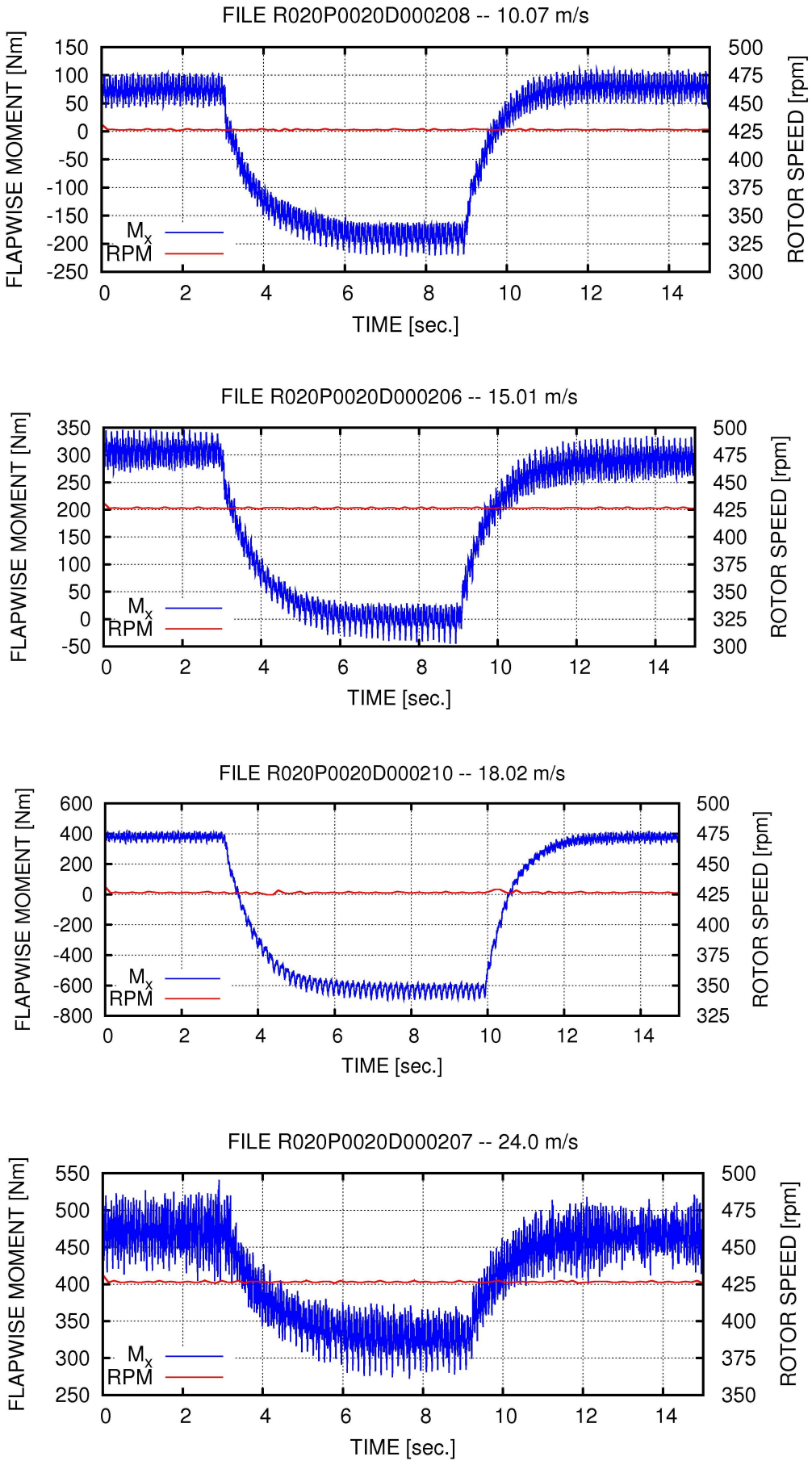

Figure 16.2 *The flapwise bending moments for a pitch step from -2.3° to 5° and a rotor speed of 425 rpm.*

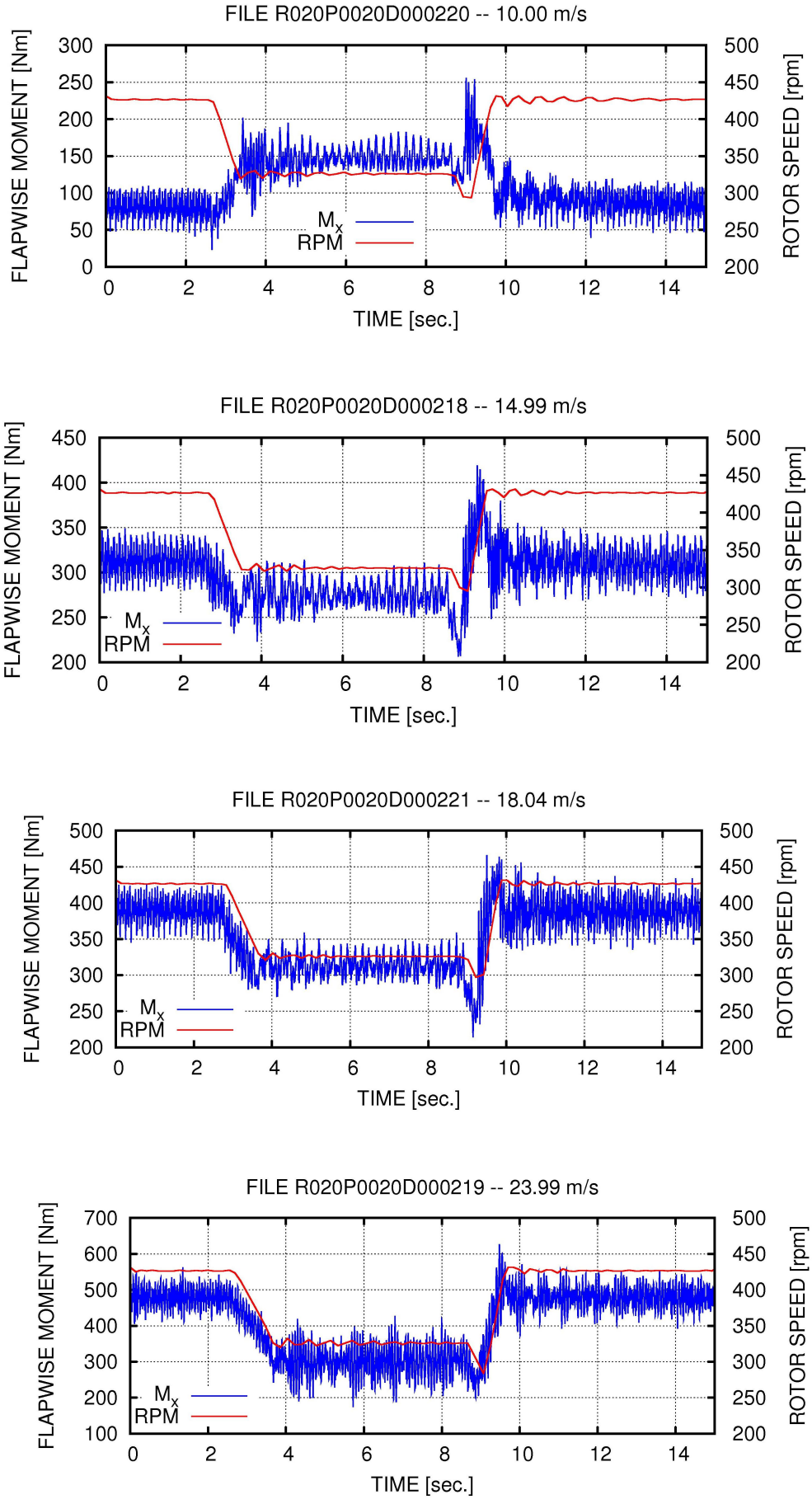

Figure 16.3 *The flapwise bending moments for a change in rotational speed from 425 rpm to 325 rpm and back again to 425rpm.*

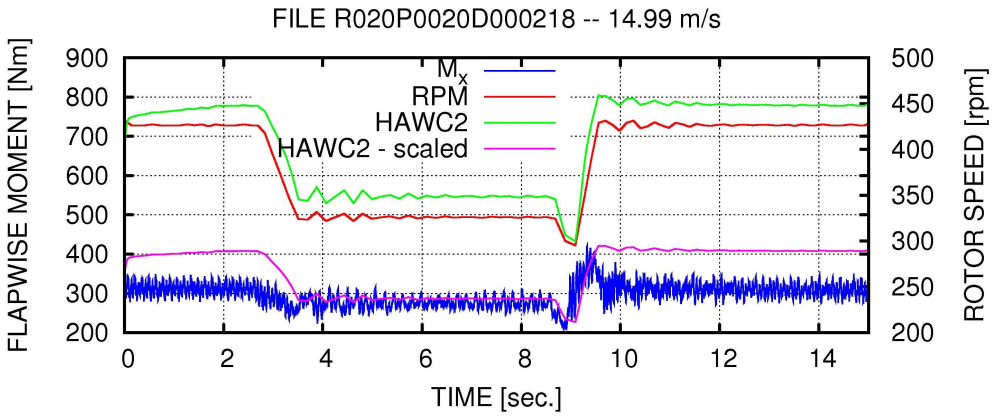

Figure 16.4 *Simulation of the test case of variation in rotor speed at 15 m/s with the aeroelastic HAWC2 code, however, in this case simulating only the aerodynamic loads.*

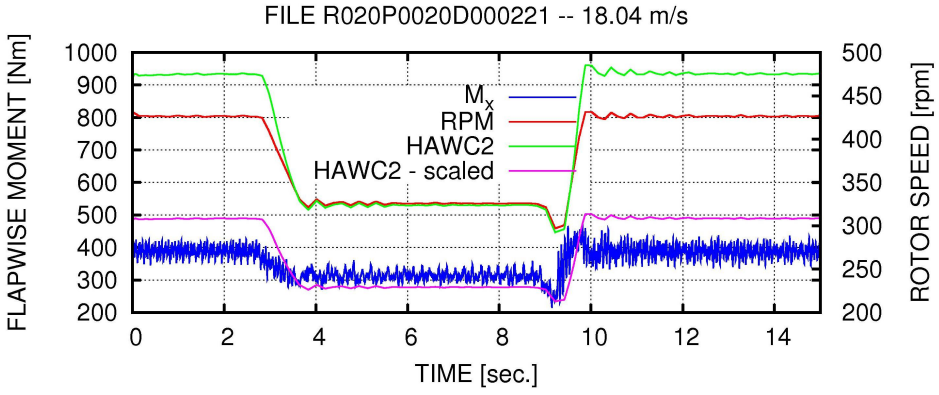

Figure 16.5 *Simulation of the test case of variation in rotor speed at 18 m/s with the aeroelastic HAWC2 code, however, in this case simulating only the aerodynamic loads.*

17 Conclusions and recommendations

The overall objective of IEA Task 29 Mexnext was to establish a collaboration on the analysis of the measurements taken within the Mexico project.

This objective has been met. Over a period of 3 years, 20 leading institutes on the field of wind turbine aerodynamics cooperated closely in Mexnext. Thereto a large number of data have been analyzed and reproduced with various codes. In order to facilitate the interpretation of differences between calculations and measurements the participants supplied model descriptions of their codes. Furthermore an (unusual) critical scrutinization of measurement quality was carried out. This led to suspects on some data but in general terms a good quality was found. Even the geometry of the blade data has been measured which showed relativerly small deviations compared to the design blade geometry. Together with the fact that tunnel effects were found to be limited this led to the belief that most data can be used with confidence.

Then the main results and conclusions from Mexnext are as follows:

- Aerodynamics is very important for the successful employment of wind energy
- It is the combination of measurements of detailed aerodynamic loads and detailed flow field which makes the Mexico experiment unique. Moreover the Mexico experiment was repeated on two smaller scales which led to insights in scaling effects
- Generally speaking the understanding of the 3D flow field around a wind turbine and the near wake has increased enormously.
- An assessment could be made of several codes on basis of loads and velocity measurements.
- At first sight the agreement between calculated and measured loads is less than expected from other projects (e.g. the blind comparison from IEA Task 20, [2]). Further analysis shows that the calculational results from IEA Task 20 were generally more randomly distributed in a wide spread around the measured results. In Mexnext the level of disagreement is of the same magnitude but it is striking to see that all loads along the blade are consistently over predicted. The availability of velocity measurements made it possible to find a 'direction' for the explanation: The relation between loads and velocities does not seem to obey the momentum relation and a vortex shedding is found at the inner part of the blade, possibly due to a change in airfoils. Although some codes do predict some vortex shedding they donot predict the impact on the velocity field in agreement with the measurements.
- Despite the fact that some results are not understood it is extremely important to note that many flow details around a wind turbine are predicted extremely well, even in yawed conditions.
- All engineering codes underpredict the loads at stalled conditions. The same was found in the comparisons made with measurements from IEA Task 14/18 and NREL Phase VI(NASA-Ames). It was found that CFD predicts these loads better. CFD also predicts the loads under yawed conditions better than most engineering models.
- Directions have been given for engineering model improvement: stall delay effects should be enhanced and the tip speed ratio dependency in the Prandtl tip loss factor should be adjusted. Furthermore, in case of asymmetric flow, the velocities at a particular blade should include the velocities induced by the bound vortex of the other blades.
- The Mexico data analyzed in Mexnext are stored in a reported database, which, after signing an NDA is made accessible to outside parties;
- Results have been published and presented in at least 26 papers and articles

The main recommendations are:

- Aerodynamic validation material is far too limited: Much more detailed aerodynamic measurements are needed, both in the field (full scale) as well as in the wind tunnel. Details should be measured of

  - Pressure distributions and loads
  - Flow field
  - Boundary layer
  - Noise sources

  With regard to the latter it should be realized that the acoustics of a wind turbine is 'driven' by the aerodynamics. As such a good understanding of the acoustics requires detailed acoustic measurements in combination with detailed aerodynamic data.

- 'New Mexico' measurements are needed including flow field measurements of the inner part in order to solve the problem of the not predicted vortex shedding.

Bibliography

[1] J.G. Schepers et. al. “Verification of European Wind Turbine Design Codes”. ECN-C-01-055, ECN, April 2002.

[2] D.A. Simms S. Schreck M.M. Hand L.J. Fingersh. “NREL Unsteady Aerodynamics Experiment in the NASA-Ames Wind Tunnel: A Comparison of Predictions to Measurements”. NREL/TP-500-29494, The National Renewable Energy Laboratory, NREL, June 2001.

[3] J.G. Schepers et al. “Final report of IEA Annex XVIII’ Enhanced Field Rotor Aerodynamics Database”’. ECN-C-02-016, Energy Research Centre of the Netherlands, ECN, February 2002.

[4] M.M. Hand et al. “ Unsteady Aerodynamics Experiment Phase VI Wind Tunnel Test Configurations and Available Data Campaigns”. NREL/TP-500-29955, National Renewable Energy Laboratory, NREL, December 2001.

[5] S. Schreck. “IEA Wind Annex XX: HAWT Aerodynamics and Models from Wind Tunnel Measurements”. NREL/TP-500-43508, The National Renewable Energy Laboratory, NREL, December 2008.

[6] J.G. Schepers and H. Snel. “Mexico, Model experiments in controlled conditions”. ECN-E-07-042, Energy Research Center of the Netherlands, 2007.

[7] G. van Kuik. “Upwind final report, "Design limits and solutions for very large wind turbines", Work Package 1B3”. Upwind report, March 2011.

[8] S. Oerlemans and B. Mendez . “Location and quantification of noise sources on a wind turbine”. *Journal of Sound and Vibration*, (299):869–883, 2007.

[9] K. Boorsma and J.G. Schepers. “Description of experimental set-up. Mexico measurements”. ECN-X-11-120, Energy Research Center of the Netherlands, ECN, March 2009.

[10] A. Rosen, A. Wolf, D. Ben-Shmuel and G. Omri. “The Mexico project, Wind Turbine Model Part 1”. TAE report 985 NN, Faculty of Aerospace Engineering Technion-Israel Institute of Technology, July 2011.

[11] A. Rosen, A. Wolf, D. Ben-Shmuel and G. Omri. “The Mexico project, Wind Turbine Model Part 2”. TAE report 986 NN, Faculty of Aerospace Engineering Technion-Israel Institute of Technology, July 2011.

[12] R. Santos Pereira, J.G. Schepers and M. Pavel. “Validation of the Beddoes Leishman Dynamic Stall model for Horizontal Axis Wind Turbines using Mexico data”. In *49th AIAA Aerospace Sciences meeting*, January 2011.

[13] L. Pascal. “Analysis of Mexico measurements”. ECN-Memo-09-010, Energy Research Center of the Netherlands, ECN, January 2009.

[14] D. Micallef. “MEXICO Data Analysis, Stage I - MEXICO Data Validation and Reliability Testst”. TUDelft report, Technical University of Delft, February 2009.

[15] R. Moffat. Describing the unerctainties in experimental results. *Experimental Thermal and Fluid Science*, 1:3–17, 1988.

[16] J.G. Schepers, L. Pascal and H. Snel. "First results from Mexnext: Analysis of detailed aerodynamic measurements on a 4.5 m diameter rotor placed in the large German Dutch Wind Tunnel DNW". In *Proceedings of European Wind Energy Conference, EWEC*, April 2010.

[17] Réthoré, P.-E., Sørensen, N.N., Zahle, F., Bechmann, A., Madsen, H.A . CFD model of the MEXICO wind tunnel. In *EWEA Annual Event held at Brussels*, March 2011.

[18] Réthoré, P.-E., Sørensen, N.N., Zahle, F., Bechmann, A., Madsen, H.A . MEXICO Wind Tunnel and Wind Turbine modelled in CFD. In *AIAA Conference*, June 2011.

[19] J.G. Schepers, Boorsma K, Bon A, Kim, C, Cho T. "Results from Mexnext: Analysis of detailed aerodynamic measurements on a 4.5 m diameter rotor placed in the large German Dutch Wind Tunnel DNW". In *Proceedings of European Wind Energy Conference, EWEC, held at Brussels*, March 2011.

[20] S.F. Hoerner. *Fluid-Dynamic Drag*. Hoerner Fluid Dynamics, second edition edition, 1965.

[21] J.G. Schepers, L. Feigl, R. van Rooij and A. Bruining. "Analysis of detailed aerodynamic measurements, using results from an aero-elastic code ". In *Wind Energy Journal 7:*, pages 357–371, August 2004.

[22] J.B. Barlow, W.H. jr. Rae, and Pope A. *Low-speed wind tunnel testing*. John Wiley & Sons Inc., third edition edition, 1999.

[23] B.F.R. Ewald. Wind tunnel wall correction. AGARDograph 336, October 1998.

[24] H. Snel. Two-dimensional analysis of flow around turbine including collector effects. Discussion document for Mexico project group, Energy Research Center of the Netherlands, ECN, September 2002.

[25] S. Voutsinas et al. "Mexico WP2: Navier Stokes and Euler Simulations to determine the maximum rotor size. MEXICO-DOC- WP2-01-01, National Technical University of Athens, November 2003.

[26] Wen Zhong Shen et al. . Validation of the Actuator Line / Navier Stokes technique using Mexico measurements. In *Proceedings of EAWE conference 'The Science of Making Torque from the Wind' held at Crete*, June 2010.

[27] Rozendal, D. "Flow field measurements on a small scale wind turbine model in the DNW PLST wind tunnel ". NLR-CR-2003-484, National Aerospace Laboratory NLR, 2003.

[28] S. Schreck et al. . Rotational Augmentation Disparities in the UAE Phase VI and MEXICO Experiments Attack. In *Proceedings of EAWE conference 'The Science of Making Torque from the Wind' held at Crete*, June 2010.

[29] S. Schreck. Presentation. IEA Annex 29 Mexnextannual meeting, Montreal, Canada, October 2009.

[30] S. Gomez-Iradi and X. Munduate. Presentation. IEA Annex 29 Mexnextannual meeting, Jeju, South Korea, June 2011.

[31] R. Steijl, G.N. Barakos, and K. Badcock. A framework for CFD analysis of helicopter rotors in hover and forward flight. *International Journal for Numerical Methods in Fluids*, 51(8), 2006.

[32] A. Jameson. Computational algorithms for aerodynamic analysis and design, applied numerical mathematics. *Applied Numerical Mathematics*, 13(5), 1993.

[33] S. Gomez-Iradi, R. Steijl, and G.N. Barakos. Development and validation of a CFD technique for the aerodynamic analysis of HAWT. *Journal of Solar Energy, Engineering-Transactions of the ASM*, 131(3), 2009.

[34] S. Gomez-Iradi and G.N. Barakos. Computational fluid dynamics investigation of some wind turbine rotor design parameters. *Proceedings of the Institution of Mechanical Engineers, Part A: Journal of Power and Energy*, 222(5):445–470, 2008.

[35] K. Boorsma. https://mexnext.ecn.nl. In *Password protected environment for exchange of Mexnex(t) data*, Petten, the Netherlands, 2008. ECN.

[36] F.R. Menter. Zonal two equation kappa-omega turbulence models for aerodynamic flows. In 23^{rd} *Fluid Dynamics, Plasmadynamics, and Lasers Conference*, July 1993.

[37] H. Snel, R. Houwink and J. Bosschers. "Sectional prediction of lift coefficients on rotating wind turbine blades in stall". ECN-C –93-052, Energy Research Centre of the Netherlands, ECN, May 1993.

[38] Z. Du and M.S. Selig . "A 3D stall delay model for horizontal axis wind turbine performance prediction". In *ASME Wind Energy Symposium, Reno USA*, January 1999.

[39] A. Verhoef. "Personal Communication". , Suzlon Blade Technology, SBT, 2011.

[40] C.R. Calle. Mexnext 1:4 Model Wind tunel experimental data. In *Proc. IEAwind Task 29 Meeting*, June 2011.

[41] A. Jeromin and A.P. Schaffarczyk. "Description of calculational models used in MexNext by UAS Kiel". internal Report NN, University of Applied Sciences Kiel, July 2010.

[42] W.Z Shen, M.O.L. Hansen and J.N. Sørensen. "Determination of the angle of attack on rotor blades". *Wind Energy*, 12:91–98, 2009.

[43] M.O.L. Hansen and J. Johansen . Tip studies using CFD and computation with tip loss models. *Wind Energy*, (7):343–356, 2004.

[44] S.K. Guntur, C. Bak and N.N. S ørensen. Analysis of 3D stall models for wind turbine blades using data from the Mexico experiment. In *13th International conference on Wind Engineering, ICWE, held at Amsterdam*, July 2011.

[45] T. Sant, G. van Kuik and G.J.W. van Bussel . Estimating the angle of attack from blade pressure measurements on the NREL phase VI rotor using a free wake vortex model: axial conditions. *Wind Energy*, (9):549–577, 2006.

[46] D. Micallef et al. Validating BEM, direct and inverse free wake models with the Mexico experiment. In *Proceedings of 48th AIAA Aerospace Sciences meeting*, January 2010.

[47] W.Z. Shen, M.O.L. Hansen and J.N. Sørensen . Determination of the Angle of Attack on Rotor Blades. *Wind Energy*, (12):91–98, 2009.

[48] Yang Hua et al. . Determination of Aerofoil Data and Angle of Attack on the Mexico Rotor using Experimental Data. In *Proceedings of EAWE conference 'The Science of Making Torque from the Wind' held at Crete*, June 2010.

[49] D. Micallef. "MEXICO Data Analysis, Stage V - Investigation of the Limitations of Inverse Free Wake Vortex Codes on the Basis of the MEXICO Experiment". TUDelft report, Technical University of Delft, February 2009.

[50] H. Yang, W.Z. Shen, J.N. Sørensen and W.J. Zhu . Extraction of airfoil data using PIV and pressure measurements. *Wind Energy*, (14):539–556, 2011.

[51] W. Z Sheng. Actuator Line / Navier Stokes Computations for Flows past the Yawed MEXICO Rotor. In *Wake Conference, held at Gotland University*, June 2011.

[52] S. Breton, C. Sibuet, and C Masson. Using the Actuator Surface Method to Model the Three-Bladed MEXICO Wind Turbine. In *In Proceedings 48th AIAA Aerospace Sciences meeting*, January 2010.

[53] T. Lutz and K. Meister and E. Krämer. Near Wake Studies of the Mexico Rotor. In *EWEA Annual Event held at Brussels*, March 2011.

[54] H. Vollmers. Detection of vortices and quantitative evaluation of their main parameters from experimental velocity data. *Measurement Science and Technology*, 2001.

[55] Jameson A., Schmidt W., and Turkel E. Numerical Simulation of the Euler Equations by finite Volume Methods using Runge-Kutta Time Stepping Schemes. *AIAA Journal No. 1259*, 1981.

[56] K. Meister. Grid dependency studies on tip vortex preservation in wind turbine CFD simulations. In *Wake Conference, held at Gotland University*, June 2011.

[57] Chi-Wang Shu. Essentially Non-Oscillatory and Weighted Essentially Non-Oscillatory Schemes for Hyperbolic Conservation Laws. Technical report, Institute for Computer Applications in Science and Engineering, NASA Langley Research Center, November 1997.

[58] H. Snel, J.G. Schepers and A. Siccama. "Mexico, the database and results of data processing and analysis ". In *47th AIAA Aerospace Sciences meeting*, January 2009.

[59] H. Snel J.G. Schepers, A. van GArrel, S. Barth. "The Mexico experiment analysis of yaw measurements and comparison with existing models ". In *Proceedings of European Wind Energy Conference, EWEC, held at Brussels*, 2008.

[60] Hermann Himmelskamp. *Profiluntersuchungen an einem umlaufenden Propeller*. PhD thesis, University of Göttingen, 1945.

[61] R. van Rooij and E.A. Arens. Analysis of the experimental and computational flow characteristics with respect to the augmented lift phenomenon caused by blade rotation. In *Journal of Physics*, volume 75 of *Conference Series 75*. IOP Publishing, 2007.

[62] Hua Yang, Wen Zhong Shen, Jens Sørensen, and Wei Jun Zhu. Extraction of airfoil data using piv and pressure measurements. *Wind Energy*, 14:539–556, 2011.

[63] D. Bushnell. Scaling: Wind tunnel to flight. *Anual Rev. of. Fluid Mech.*, 38:111–128, 2006.

[64] J.G. Schepers, H. Snel and K. Boorsma. "IEA Task 29 Mexnext: Analysis of wind tunnel measurements from the EU project Mexico". In *Proceedings of EAWE conference 'The Science of Making Torque from the Wind' held at Crete*, June 2010.

[65] H. Snel, R. Houwink, G.J.W. van Bussel, and A. Bruining. Sectional prediction of 3d effects for stalled flow on rotat- ing blades and comparison with measurements. In *Proc. European Community Wind Energy Conference*, 1993.

[66] A. Björk. Dynamic stall and three-dimensional effects. ec dxgii joule ii project no. jou2-ct93-0345 report . Technical report, The Aeronautical Research Institute of Sweden, 1995.

[67] Z. Du and M.S. Selig. A 3-d stall-delay model for horizontal axis wind turbine performance prediction. In *36th AIAA Aerospace Sciences Meeting and Exhibition*, volume AIAA-98-0021 of *ASME Wind Energy Symposium*, 1998.

[68] K.P. Chaviaropoulos and M.O.L. Hansen. Investigating three-dimensional and rotational effects on wind turbine blades by means of a quasi-3d navier-stokes solver. *J. Fluid Engineering*, 122:330–336, 2000.

[69] C. Lindenburg. Modeling of rotational augmentation based on engineering considerations and measurements. In *European Wind Energy Conference*, 2004.

[70] C. Bak, J. Johansen, and P.B. Andersen. Three-dimensional corrections of airfoil characteristics based on pressure dis- tributions. In *European Wind Energy Conference*, 2006.

[71] J. Leishman and T. Beddoes. A semi-empirical model for dynamic stall. *Journal of the American Helicopter Society*, 45, 1989.

[72] W. Timmer and R van Rooij. Some aspects of high angle-of-attack flow on airfoils for wind turbine application. In *European Wind Energy Conference and Exhibition*, July 2001.

[73] J Schepers and L Vermeer. Een engineering model voor scheefstand op basis van windtunnelmetingen. Technical report, ECN-CX–98-070.

[74] R Pereira. Assessing the load predicting capabilities of the beddoes-leishman dynamic stall model in a hawt environment. Master's thesis, TU Delft, 2010.

[75] T. Burton, D. Sharpe, N. Jenkins, and E. Bossanyi. *'Wind Energy Handbook'*. Wiley, 2001.

[76] S. Breton, F. Coton, and G Moe. A study on rotational effects and different stall delay models using a prescribed wake vortex scheme and nrel phase vi experiment data. *Wind Energy*, 11:459–482, 2008.

[77] J. G. Schepers, A. Brand, A Bruining, J. Graham, M. Hand, D. Infield, H. Madsen, J. Paynter, and D. Simms. Final report of iea annex xiv: Field rotor aerodynamics. Technical report, ECN-C–97-027, 1997.

[78] J. G. Schepers, A. Brand, A Bruining, M. Hand, D. Infield, H. Madsen, T. Maeda, J. Paynter, R. van Rooij, Y. Shimizu, D. Simms, and N. Stefanatos. Final report of iea annex xviii: Enhanced field rotor aerodynamics database. Technical report, ECN-C–02-016, 2002.

[79] H. Dexin and S.E. Thor. The execution of wind energy projects 1986-1992. Technical report, FFA TN 1993-19, Aeronautical Research Institute of Sweden, Bromma, 1993.

[80] G. Ronsten. Geometry and installation of wind tunnels of a stork 5.0 wpx wind turbine blade equipped with pressure taps. Technical report, FAP-A 1006, Aeronautical Research Institute of Sweden, Bromma, 1994.

[81] M. Hand, D. Simms, L. Fingersh, D. Jager, J. Cotrell, S. Schreck, and S. Larwood. Unsteady aerodynamics experiment phase vi: Wind tunnel test configurations and available data campaigns. Technical report, NREL/TP-500-29955, National Renewable Energy Laboratory, 2001.

[82] H. Snel, J. Schepers, and B. Montgomerie. The mexico project (model experiments in controlled conditions): The database and first results of data processing and interpretation. In *The Science of Making Torque from Wind Conference, Journal of Physics: Conference Series 75*, 2007.

[83] H. Snel, G. Schepers, and N Siccama. Mexico project: The database and results of data processing and interpretation. In *AIAA-2009-1217*, 2009.

[84] S. Schreck. Low frequency shedding prompted by three-dimensionality under rotational augmentation. In *AIAA-2010-0640*, 2010.

[85] P. Giguere and M. Selig. Design of a tapered and twisted blade for the nrel combined experiment rotor. Technical report, NREL/SR 500-26173, National Renewable Energy Laboratory, 1999.

[86] C. Butterfield, W. Musial, and D. Simms. Combined experiment phase i final report. Technical report, NREL/TP-257-4655 National Renewable Energy Laboratory, 1992.

[87] P. Zell. Performance and test section flow characteristics of the national full-scale aerodynamics complex 80- by 120-foot wind tunnel. Technical report, NASA TM 103920, 1993.

[88] Sant T., van Kuik G., and van Bussel G. J. W. Estimating the angle of attack from blade pressure measurements on the nrel phase vi rotor using a free wake vortex model: axial conditions. *Wind Energy*, 9(6):549–577, 2006.

[89] D. Micallef, M. Kloosterman, C. Ferreira, T. Sant, and van Bussel G.J.W. Validating bem, direct and inverse free wake models with the mexico experiment. In *AIAA-2010-0462*, 2010.

[90] S. Schreck and M Robinson. Rotational augmentation of horizontal axis wind turbine blade aerodynamic response. *Wind*, 5(2/3):133–150, 2002.

[91] Scott Schreck and M Robinson. Boundary layer state and flow field structure underlying rotational augmentation of blade aerodynamic response. *J. of Solar Energy Eng.*, 125:448–456, 2003.

[92] S. Schreck, N. Soerensen, and M. Robinson. Aerodynamic structures and processes in rotationally augmented flow fields. *Wind E*, 10(2):159–178, 2007.

A Description of data format and test cases

This section describes the data format and test cases for the purpose of the comparison between calculations and measurements (section 8).

A.1 First round: Axial flow

Mexnext: Definition of first round of calculations

J.G. Schepers and K. Boorsma
January 19th, 2010

1. Description of the tunnel and the wind turbine model:

See the tunnel definition document and related data files on the EPOS site. To make sure that everybody uses the same input, the following airfoil coefficient data sets are prescribed from "MexNextExperimentDescription.xls" or the tunnel definition document:

- DU91-W2-250 : $Re_c = 0.5 \times 10^6$ dataset
- RISØ A1-21 : $Re_c = 1.6 \times 10^6$ dataset
- NACA64-418 : $Re_c = 0.7 \times 10^6$ dataset

2. Description of cases.

- Pitch angle: -2.3 degrees
- Rotor speed: 424.5 rpm
- Tunnel speeds, air density, pressure and temperature (note that these numbers are supplied by DNW but apparently they donot precisely fulfill the ideal gas law):
    - Case 1.1: V_{tunnel} = 14.93 m/s, ρ = 1.246 kg/m^3 (T_{inf} = 284.03 ^{o}K, p_{inf} = 101922 N/m^2)
    - Case 1.2: V_{tunnel} =10.01 m/s, ρ = 1.245 kg/m^3 (T_{inf} = 283.98 ^{o}K, p_{inf} = 101807 N/m^2)
    - Case 1.3: V_{tunnel} =23.96 m/s, ρ = 1.236 kg/m^3 (T_{inf} = 285.89 ^{o}K, p_{inf} = 101765 N/m^2)
- Yaw angle: 0 degrees

3. Results to be supplied:

3.1 Lifting line codes:

The comparison of results from lifting line codes (eg BEM codes) mainly focusses on the local aerodynamic forces and the angle of attack at several radial stations. In addition the axial force on the rotor is calculated. The axial force on the rotor and the local aerodynamic forces can be compared with the measured values.

3.1.1 Loads

- Requested data and units:
    - F_{ax} : Axial force on the rotor [N]
    - Torque: Aerodynamic torque of the rotor [Nm]

- For a minimum of 10 (preferably more) radial locations:
    - F_{normal} (i.e. the force normal to the local chord) [N/m]
    - $F_{tangential}$ (i.e. the force parallel to the local chord) [N/m]. If possible, please supply the 'pressure' tangential force without skin friction.

- Files to be supplied:
    - Please supply the data in one ASCII file which should contain the data for all three wind speeds.
    - Format: Each row contains 7 columns with data. Separate the columns by tabs or blanks. The first row gives the identification of data. The second row gives the axial force for the three wind speeds (10, 15 and 24 m/s). Please duplicate the values for F_{ax} since 2 columns are available for each wind speed. The next rows give the data at the three wind speeds for the chosen radial locations (a total of n), increasing from root to tip. Hence, the format is as follows

r	F_{n10}	F_{t10}	F_{n15}	F_{t15}	F_{n24}	F_{t24}
F_{ax}	--	--	--	--	--	--
Torque	--	--	--	--	--	--
r_1	--	--	--	--	--	--
|	|	|	|	|	|	|
|	|	|	|	|	|	|
r_n	--	--	--	--	--	--

Note that this makes the total number of rows to be n + 3
(1 (header) + 1 (axial force) + 1 (torque) + n radial locations)

3.1.2 Lifting line variables

- Requested data and units

    - For a minimum of 10 (preferably more) radial locations:
        - V_{eff} (i.e. the resultant incoming velocity at the blade section) [m/s]
        - α Angle of attack [deg]
        - u_i, the annulus averaged axial induced velocity [m/s]
          The sign is positive in pointing in upwind direction.
        - u_{tan}, the annulus averaged velocity induced in tangential (rotational) direction [m/s]
          The sign is positive pointing opposite of the rotational direction.
        - c_n normal force coefficient = $F_{normal}/(0.5\ \rho\ V_{eff}^2\ c)$ [-]
        - c_t tangential force coefficient = $F_{tangential}/(0.5\ \rho\ V_{eff}^2\ c)$ [-]

- Files to be supplied:
    - Please supply the data in one plain ASCII file which should contain the data for all three wind speeds.

- Format: Each row contains 19 columns, separated by tabs or blanks. The first row gives the identification of data. The next rows give the data at the three wind speeds for the chosen radial locations (a total of n), increasing from root to tip. Hence, the format is as follows:

r	V_{eff10}	α_{10}	u_{i10}	u_{tan10}	c_{n10}	c_{t10}	V_{eff15}	α_{15}	u_{i15}	u_{tan15}	c_{n15}	c_{t15}	V_{eff24}	α_{24}	u_{i24}	u_{tan24}	c_{n24}	c_{t24}
r_1	--	--	--	--	--	--	--	--	--	--	--	--	--	--	--	--	--	--
|	|	|	|	|	|	|	|	|	|	|	|	|	|	|	|	|	|	|
|	|	|	|	|	|	|	|	|	|	|	|	|	|	|	|	|	|	|
r_n	--	--	--	--	--	--	--	--	--	--	--	--	--	--	--	--	--	--

Note that this makes the total number of rows to be n + 1
(1 (header) + n radial locations)

3.2 CFD codes

It is anticipated that many CFD (and free vortex wake) codes calculate the flow field around the rotor and in the wake. Hence results from these codes can be compared with PIV flow field measurements. Some of these codes will also model the pressures (and resulting loads) around the blades which can be compared with the measured data as well.

It is proposed to calculate 3D velocities in the form of radial traverses, just upstream of the rotor and just downstream of the rotor at 6 different blade positions (for codes modeling individual blades) and in the form of axial traverses at two radial positions and 1 blade position.
Note that the blade position refers to the position of blade 1 where blade position = 0 degrees indicates blade 1 pointing vertically upward. The velocities need to be calculated in the horizontal plane at the 9 o clock position (i.e. 270 degrees azimuth). For actuator disc codes the velocities the dependency on blade position is lost and a (more or less averaged) velocity can be supplied only. This obviously makes a comparison with measured values useless near the rotor plane but we still propose to supply the calculated values for a mutual comparison with other calculational results. If possible dimensional pressures and resulting loads should be calculated at the instrumented sections as well.

3.2.1 Loads

See the format specification of the file in section 3.1.1.

3.2.2 Pressure data

- Requested data and units.
  - For all instrumented sections: Azimuthally averaged pressure data in dimensional form [Pa] relative to the ambient pressure as function of x (along the chord) and y (perpendicular to the chord). Note that

(x=0,y=0) is at the nose of the airfoil. Positive y at the suction side. Units of x and y are [m]. Note that x and y donot necessarily need to coincide with the position of the sensors.

- Files to be supplied
  - For every instrumented section and every wind speed a separate (ASCII) file needs to be supplied. Hence a total of 5 (radial positions) * 3 (wind speeds) = 15 files need to be supplied.
  - Format: Three columns with pressures as function of x (along the chord) and y (perpendicular to the chord) starting at the trailing edge, then going along the suction side to the leading edge and then back to the trailing edge along the pressure side. Separate the columns by tabs or blanks. The format is as follows:

x[m]	y[m]	Pressure [Pa]
chord (t.e.)	0	--
--	positive	usually negative
0(l.e.)	0	--
--	negative	usually positive
Chord(t.e.)	0	--

3.2.3. Radial traverses

Radial traverses need to be calculated in the horizontal plane at the 9 o clock position at:

- x = -0.304838 m (upstream of the rotor) and x=+0.306514 (downstream of the rotor). Note that x=0 m is in the rotor plane with positive x directed towards the collector.
- Blade (1) positions: 0, 20, 40, 60, 80 and 100 degrees. Blade position = 0 degrees indicates that blade 1 is pointing vertically upward.
- The radial coordinate should anyhow cover the measurement range from r = 1.15 m to r = 2.75 m (i.e. part of the wake expansion is included).

- Requested data and units
  - All three wind components (u, v and w) as function of r. Note that r=0 m is in the rotor centre. The r-positions donot necessarily need to coincide with the measurement locations. However the measurements are done with a spatial resolution of 4 mm and we recommend a resolution which is more or less comparable to that.
  - Unit of r = [m].
  - u is the axial component (positive from nozzle to collector), v is the radial component (positive from root to tip) and w is the vertical component (tangential, positive upward).
  - Unit of u, v and w = [m/s].

- Files to be supplied:
  - Please supply the data in ASCII files. Separate files should be supplied for the upstream position and the downstream position and for every blade position (for actuator disc models: only 1 (averaged) blade

position). Each file contains the data for all three wind speeds (10, 15 and 24 m/s). Hence the total number of files should be 6 (blade positions) * 2 (x-positions) =12.

- Format: Each row contains 10 columns. Please separate the columns with blanks or tabs. The first row is for identification of the signals. Then the 3D (u, v and w) velocity components are given as function of the radial position for all three wind speeds

r	u_{10}	v_{10}	w_{10}	u_{15}	v_{15}	w_{15}	u_{24}	v_{24}	w_{24}
r_1	--	--	--	--	--	--	--	--	--
|	|	|	|	|	|	|	|	|	|
|	|	|	|	|	|	|	|	|	|
r_n	--	--	--	--	--	--	--	--	--

3.2.4 Axial traverses

Axial traverses need to be calculated in the horizontal plane at the 9 o clock position at:

- r = 1.37697 m and r=1.84797 m. Note that r = 0 m is in the rotor centre.
- Blade (1) position: 0 degrees (i.e. blade 1 pointing vertically upward).
- The axial coordinate should anyhow cover the measurement range from x = -4.5 m (upstream) to x = 5.9 m (downstream)

- Requested data and units
  - All three wind components (u, v and w) as function of x. Note that x=0 m is in the rotor plane with positive x directed towards the collector. The x-positions donot necessarily need to coincide with the measurement locations but measurements are done with a spatial resolution of 4 mm and we recommend a resolution which is more or less comparable to that.
  - Unit of x = [m].
  - u is the axial component (positive from nozzle to collector), v is the radial component (positive from root to tip) and w is the vertical component (tangential, positive upward).
  - Unit of u, v and w = [m/s].

- Files to be supplied:
  - Please supply the data in 2 ASCII files, one file for every radial position where every file contains the data for all three wind speeds (10, 15 and 24 m/s).
  - Format: Each row contains 10 columns. Please separate the columns with blanks or tabs. The first row is for identification of the signals. Then the 3D (u, v and w) velocity components are given for all three wind speeds as function of x.

x	u_{10}	v_{10}	w_{10}	u_{15}	v_{15}	w_{15}	u_{24}	v_{24}	w_{24}
x_1	--	--	--	--	--	--	--	--	--

x_n	--	--	--	--	--	--	--	--	--

A.2 Second round: Yawed flow

Mexnext: Definition of second round of calculations

K. Boorsma and J.G. Schepers
November 2, 2010

1. Description of the tunnel and the wind turbine model:

See the tunnel definition document and related data files on the EPOS site. To make sure that everybody uses the same input, the following airfoil coefficient data sets are prescribed from "MexNextExperimentDescription.xls" or the tunnel definition document:

- DU91-W2-250 : $Re_c = 0.5 \times 10^6$ dataset
- RISØ A1-21 : $Re_c = 1.6 \times 10^6$ dataset
- NACA64-418 : $Re_c = 0.7 \times 10^6$ dataset

2. Description of cases.

- Pitch angle: -2.3 degrees
- Rotor speed: 424.5 rpm
- Tunnel speeds, air density, pressure and temperature (note that these numbers are supplied by DNW but apparently they don't precisely fulfill the ideal gas law):
    - Case 2.1: Yaw angle=30 deg, V_{tunnel} = 14.99 m/s, ρ = 1.237 kg/m^3 (T_{inf} = 285.96 ^{o}K, p_{inf} = 101847 N/m^2)
    - Case 2.2: Yaw angle=15 deg, V_{tunnel} =23.97 m/s, ρ = 1.242 kg/m^3 (T_{inf} = 283.50 ^{o}K, p_{inf} = 101328 N/m^2)

3. Results to be supplied:

3.1 Lifting line codes:

The comparison of results from lifting line codes (e.g. BEM codes) mainly focuses on the local aerodynamic forces and the angle of attack at the 5 instrumented sections. In addition the axial force on the rotor is calculated. The axial force on the rotor and the local aerodynamic forces can be compared with the measured values.

3.1.1 Loads

- Requested data and units as a function of bin averaged rotor azimuth angle [deg] between 0 and 360 deg. Preferably in steps smaller than 5 deg azimuth.

    - F_{ax} : Axial force on the rotor [N]
    - Torq: Aerodynamic torque of the rotor [Nm]
    - For the 5 instrumented radial locations:
        - F_n (i.e. the force normal to the local chord) [N/m].

        - F_t (i.e. the force parallel to the local chord) [N/m]. If possible, please supply the 'pressure' tangential force without skin friction.
- Files to be supplied:
    - Please supply the data in two ASCII files which should contain the data for both cases (case 2.1 and case 2.2).
    - Format: Each row contains 13 columns with data containing axial force, torque and normal and tangential forces at 5 sections. Separate the columns by tabs or blanks. The first row gives the identification of data. The next rows give the data at the specified azimuth positions (a total of n) between 0 and 360 deg. Hence, the format is as follows

Azi	F_{ax}	Torq	F_{n25}	F_{t25}	F_{n35}	F_{t35}	F_{n60}	F_{t60}	F_{n82}	F_{t82}	F_{n92}	F_{t92}
Azi_1	-	-	-	-	-	-	-	-	-	-	-	-
|	|	|	|	|	|	|	|	|	|	|	|	|
|	|	|	|	|	|	|	|	|	|	|	|	|
Azi_n	-	-	-	-	-	-	-	-	-	-	-	-

Note that this makes the total number of rows to be n + 1
(1 (header) + n azimuth positions)

3.1.2 Lifting line variables

- Requested data and units as a function of bin averaged rotor azimuth angle [deg] between 0 and 360 deg. Preferably in steps smaller than 5 deg azimuth.

    - For the 5 instrumented radial locations:
        - V_{eff} (i.e. the resultant incoming velocity at the blade section) [m/s]
        - α Angle of attack [deg]
        - u_i, the annulus averaged axial induced velocity [m/s]
          The sign is positive in pointing in upwind direction.
        - u_{tan}, the annulus averaged velocity induced in tangential (rotational) direction [m/s]
          The sign is positive pointing opposite of the rotational direction.
        - c_n normal force coefficient =
          $F_{normal}/(0.5\ \rho\ V_{eff}^2\ c)$ [-]
        - c_t tangential force coefficient =
          $F_{tangential}/(0.5\ \rho\ V_{eff}^2\ c)$ [-]
- Files to be supplied:
    - Please supply the data in two plain ASCII files which should contain the data for both cases (case 2.1 and case 2.2)
    - Format: Each row contains 31 columns, containing the 6 variables at 5 radial stations. Separate the columns by tabs or blanks. The first row gives the identification of data. The next rows give the data at the specified

azimuth positions (a total of n) between 0 and 360 deg. Hence, the format is as follows:

Azi	V_{eff25}	α_{eff25}	u_{i25}	u_{tan25}	c_{n25}	c_{t25}	V_{eff35}	α_{eff35}	----	u_{tan92}	c_{n92}	c_{t92}
Azi_1	-	-	-	-	-	-	-	-	----	-	-	-
|	|	|	|	|	|	|	|	|	---	|	|	|
|	|	|	|	|	|	|	|	---	|	|	|
Azi_n	-	-	-	-	-	-	-	-	---	-	-	-

Note that this makes the total number of rows to be n + 1
(1 (header) + n azimuth positions)

3.2 CFD codes

It is anticipated that many CFD (and free vortex wake) codes calculate the flow field around the rotor and in the wake. Hence results from these codes can be compared with PIV flow field measurements. PIV data is only available for case 2.1, but since case 2.2 needs to be calculated for the loads anyway this data can be used to compare between CFD codes.
It is proposed to calculate 3D velocities in the form of radial traverses, just upstream of the rotor and just downstream of the rotor at 6 different blade positions (for codes modeling individual blades) and in the form of axial traverses at four radial positions and 1 blade position.
Note that the blade position refers to the position of blade 1 where blade position = 0 degrees indicates blade 1 pointing vertically upward. The velocities need to be calculated in the horizontal plane intersecting the rotor center. For actuator disc codes the dependency on blade position is lost and a (more or less averaged) velocity can be supplied only. This obviously makes a comparison with measured values useless near the rotor plane but we still propose to supply the calculated values for a mutual comparison with other calculated results.
If possible dimensional pressures and resulting loads should be calculated at the instrumented sections as well.

3.2.1 Loads

See the format specification of the file in section 3.1.1.

3.2.3. Radial traverses

Radial traverses need to be calculated in the horizontal plane (rotor center height) at:

- x = -0.15 m (upstream of the rotor) and x=+0.15 (downstream of the rotor). Note that **x** is expressed in the **model coordinate system** as defined in Figure 1 included below.
- Blade (1) positions: 0, 20, 40, 60, 80 and 100 degrees. Blade position = 0 degrees indicates that blade 1 is pointing vertically upward.
- The radial coordinate should anyhow cover the measurement range from y = -3.0 m to y = 3.0 m (roughly going from one tip to the other).

Note that **y** is expressed in the **model coordinate system** as defined in Figure 1.

- Requested data and units
  - All three wind components (u, v and w) as function of y. Note that y=0 m is in the rotor centre. The y-positions don't necessarily need to coincide with the measurement locations. However the measurements are done with a spatial resolution of 4 mm and we recommend a resolution which is more or less comparable to that.
  - Unit of y = [m].
  - Please note that **u, v and w** are defined respectively in the x, y and z directions of the **tunnel coordinate system** (see Figure 1).
  - Unit of u, v and w = [m/s].

- Files to be supplied:
  - Please supply the data in ASCII files. Separate files should be supplied for the upstream position and the downstream position and for every blade position (for actuator disc models: only 1 (averaged) blade position). Each file contains the data for case 2.1 and case 2.2. Hence the total number of files should be 6 (blade positions) * 2 (x-positions) =12.
  - Format: Each row contains 7 columns. Please separate the columns with blanks or tabs. The first row is for identification of the signals. Then the 3D (u, v and w) velocity components are given as function of the y-position for both cases:

y	$u_{2.1}$	$v_{2.1}$	$w_{2.1}$	$u_{2.2}$	$v_{2.2}$	$w_{2.2}$
y_1	--	--	--	--	--	--
|	|	|	|	|	|	|
|	|	|	|	|	|	|
y_n	--	--	--	--	--	--

3.2.4 Axial traverses

Axial traverses need to be calculated in the horizontal plane (rotor center height) at:

- y = -1.84797 m, y = -1.37697 m, y = 1.37697 m and y = 1.84797 m. Please note that **y** is expressed in the **tunnel coordinate system** (see Figure 1).
- Blade (1) position for y = 1.37697 m and y = 1.84797 m: **0** degrees
  Blade (1) position for y = -1.37697 m and y = -1.84797 m: **60** degrees
- The axial coordinate should anyhow cover the measurement range from x = -4.5 m (upstream) to x = 5.9 m (downstream). Note that **x** is expressed in the **tunnel coordinate system** (see Figure 1).

- Requested data and units
  - All three wind components (u, v and w) as function of x.
  - The x-positions don't necessarily need to coincide with the measurement locations but measurements are done with a spatial

resolution of 4 mm and we recommend a resolution which is more or less comparable to that.
    - Unit of x = [m].
    - Please note that **u, v and w** are defined respectively in the x, y and z directions of the **tunnel coordinate system** (see Figure 1).
    - Unit of u, v and w = [m/s].

- Files to be supplied:
    - Please supply the data in 4 ASCII files, one file for every radial position where every file contains the data for case 2.1 and 2.2.
    - Format: Each row contains 7 columns. Please separate the columns with blanks or tabs. The first row is for identification of the signals. Then the 3D (u, v and w) velocity components are given as function of x for both cases:

x	$u_{2.1}$	$v_{2.1}$	$w_{2.1}$	$u_{2.2}$	$v_{2.2}$	$w_{2.2}$
x_1	--	--	--	--	--	--
|	|	|	|	|	|	|
|	|	|	|	|	|	|
x_n	--	--	--	--	--	--

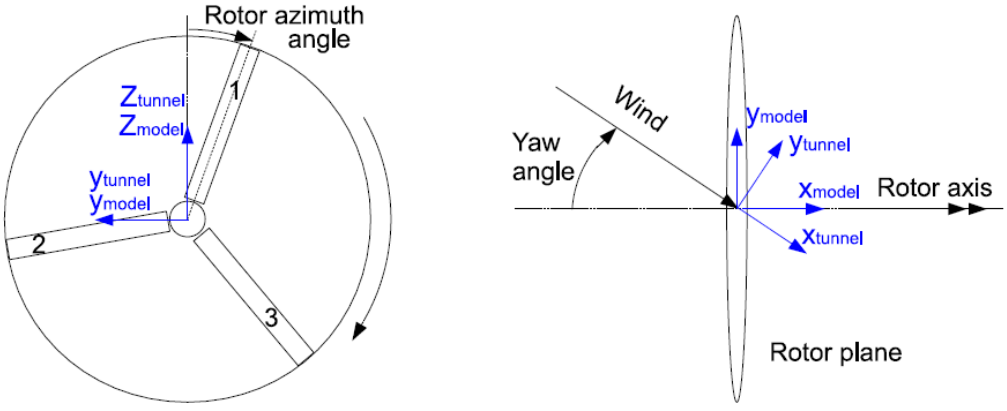

(a) Front view (b) Top view

Figure 1: Definitions and conventions of the MEXICO experiment

B Description of experimental data reduction

This section describes the data reduction of the measurements for the purpose of the comparison between calculations and measurements (section 8).

The MEXICO datapoints used for data reduction have been summarized in Table B.1. The corresponding tunnel velocity, air density and atmospheric conditions for each case have been obtained by averaging over the relevant datapoints. The datapoints for each case are mostly taken within a day and the differences between the datapoint conditions for each case are very small.

Table B.1 *Overview of MEXICO datapoints used for data reduction*

Case[‡]	U_∞ [m/s]	Yaw angle [°]	Variable type	Datapoints
1.1	14.93	0	pressures and loads	273-330
1.1	14.93	0	velocity traverses	273-330, 581-610
1.2	10.01	0	pressures and loads	340-355, 357-371, 373-379, 381-388 390, 392-394
1.2	10.01	0	velocity traverses	339-394, 614-641
1.3	23.96	0	pressures and loads	398-405, 407-415, 417-431, 433-435 437-453
1.3	23.96	0	velocity traverses	398-453, 651-679
2.1	14.99	30[†]	pressures and loads	457-488, 490-512, 516-535, 537-568 570-571, 692-696, 699-720, 724-749
2.1	14.99	30[†]	velocity traverses	457-512, 516-572, 692-696 699-720, 724-749
2.2	23.97	15	pressures and loads	160
2.2	23.97	15	velocity traverses	NA

[‡] Pitch angle amounts to -2.3 ° and rotational speed to 424.5 rpm for all cases.
[†] Datapoints of positive and negative yaw angle have been combined using rotor and blade symmetry.

B.1 Pressure distributions

An overview of the pressure sensors used for data reduction is given in Table B.2. The precalibrated pressure data are used that assume a linear variation of atmospheric reference pressure between the zero measurements taken before and after the datapoint. This calibration is described in [9].

If multiple datapoints are available within one case, the standard deviation between the average values gives an indication of the repeatability. The standard deviation is indicated in the graphs by a grey band around the mean value.

B.2 Loads

All loads are derived from the pressure distributions. The underlying procedures are highlighted below.

Table B.2 *Overview of pressure sensors used for data reduction*

Signal nr‡	Spanwise location∓ [%]	Blade nr	x/c† [%]	y/c† [%]	Signal nr‡	Spanwise location∓ [%]	Blade nr	x/c† [%]	y/c† [%]	Signal nr‡	Spanwise location∓ [%]	Blade nr	x/c† [%]	y/c† [%]
64	25	1	93.99	1.9432	23	35	1	0.95	-2.7069	100	82	3	3.47	3.8012
62	25	1	83.49	4.5741	21	35	1	3.33	-5.1311	98	82	3	1.29	2.2807
60	25	1	72.11	7.2925	43	35	1	8.05	-7.91	105	82	3	0.32	1.1639
58	25	1	62.04	9.4903	41	35	1	15.73	-10.5765	104	82	3	0	0
63	25	1	50.66	11.5255	40	35	1	24.35	-12.0136	103	82	3	0.2	-0.886
61	25	1	38.58	12.7895	38	35	1	33.18	-12.1809	102	82	3	1.1	-1.98
59	25	1	29.67	12.675	36	35	1	40.74	-11.4229	101	82	3	3.24	-3.129
57	25	1	22.49	11.7278	34	35	1	50.59	-9.3113	148	82	3	7.13	-4.364
56	25	1	15.64	10.1019	39	35	1	60.9	-6.0488	146	82	3	12.12	-5.402
54	25	1	10.57	8.3558	37	35	1	69.73	-2.957	151	82	3	18.99	-6.346
52	25	1	5.3	5.7978	35	35	1	80.54	0.0171	149	82	3	29.1	-7.069
50	25	1	2.54	3.9001	27	35	1	89.65	0.8813	147	82	3	39.24	-7.076
55	25	1	0.94	2.3223	93	60	2	83.61	3.23507	145	82	3	49.44	-6.173
32	25	1	0.2	1.1643	91	60	2	73.55	5.08606	144	82	3	60.01	-4.652
30	25	1	0	0	89	60	2	63.29	7.096638	142	82	3	69.23	-3.123
28	25	1	0.19	-1.2165	88	60	2	52.8	9.44662	140	82	3	80.11	-1.34
26	25	1	0.95	-2.7069	86	60	2	42.59	11.63575	138	82	3	89.53	-0.142
31	25	1	3.33	-5.1311	84	60	2	32.54	12.50335	128	92	3	86.34	2.9492
51	25	1	15.73	-10.5765	69	60	2	22.74	11.8986	126	92	3	73.98	5.8315
49	25	1	24.35	-12.0136	82	60	2	14.57	10.21403	124	92	3	62.86	8.1338
48	25	1	33.18	-12.1809	87	60	2	6.34	6.634	122	92	3	51.9	9.8885
46	25	1	40.74	-11.4229	85	60	2	2.04	3.29246	127	92	3	39.9	10.8542
44	25	1	50.59	-9.3113	83	60	2	0.44	1.3147	125	92	3	27.97	10.2798
42	25	1	60.9	-6.0488	81	60	2	0	0	123	92	3	17.47	8.6082
47	25	1	69.73	-2.957	80	60	2	0.32	-0.8528	121	92	3	7.66	5.7624
45	25	1	80.54	0.0171	78	60	2	1.67	-1.76264	120	92	3	3.47	3.8012
29	25	1	89.65	0.8813	76	60	2	4.79	-3.04436	119	92	3	1.29	2.2807
19	35	1	93.99	1.9432	79	60	2	13.79	-6.1763	118	92	3	0.32	1.1639
17	35	1	83.49	4.5741	77	60	2	24.55	-8.22603	116	92	3	0	0
16	35	1	72.11	7.2925	75	60	2	34.44	-8.40668	117	92	3	0.2	-0.886
14	35	1	62.04	9.4903	73	60	2	42.81	-7.55403	114	92	3	1.1	-1.98
12	35	1	50.66	11.5255	72	60	2	51.56	-5.92517	115	92	3	3.24	-3.129
10	35	1	40.09	12.703	68	60	2	60.62	-3.72142	160	92	3	7.13	-4.364
15	35	1	29.67	12.675	70	60	2	69.73	-1.54434	158	92	3	12.12	-5.402
13	35	1	19.69	11.154	71	60	2	89.79	0.602116	156	92	3	18.99	-6.346
11	35	1	10.57	8.3538	113	82	3	86.34	2.9492	154	92	3	29.1	-7.069
9	35	1	5.3	5.7978	112	82	3	73.98	5.8315	159	92	3	39.24	-7.076
25	35	1	2.54	3.9001	108	82	3	51.9	9.8885	157	92	3	49.44	-6.173
24	35	1	0.94	2.3223	106	82	3	39.9	10.8542	155	92	3	60.01	-4.652
22	35	1	0.2	1.1643	111	82	3	27.97	10.2798	153	92	3	69.23	-3.123
20	35	1	0	0	109	82	3	17.47	8.6082	152	92	3	80.11	-1.34
18	35	1	0.19	-1.2165	107	82	3	7.66	5.7625	150	92	3	89.53	-0.142

‡ The signal number is correlated to the column number in the resulting measurement file.
∓ Spanwise location is measured from the rotor center and normalized with the rotor radius.
† Coordinates are normalized using the airfoil chord c. x/c is in chordwise direction, positive from leading edge to trailing edge. y/c is perpendicular to the chord, positive pointing towards the suction side of the airfoil.

B.2.1 Sectional forces

Sectional forces (normal and tangential force) are obtained by integrating the pressure distributions assuming a linear line between the sensor values for each sample (around 27000) in a datapoint. The trailing edge pressure at x/c=1 is assumed to be the average of the pressures measured by the two sensors closest by located on the pressure and suction side.

Contrary to the normal force, the contribution of friction to the tangential force is significant in addition to the pressures. This contribution is however not taken into account in the experimental value, which consist solely of the pressure forces. In addition to that, the resulting tangential pressure force is highly dependent on location and number of pressure sensors. These two effects are more dominant for high angles of attack.

For the first round, the average over all these samples is calculated for each datapoint. For the second round, the sectional forces are presented as a function of the rotor azimuth angle. The azimuth angle is determined by means of the 1P trigger, taking into account the shift of 169.7 ° as documented in [9]. A spline is drawn through the discrete pulses of the sensor, which allows determination of azimuth angle at a given time instance.

A bin analysis with a width of 2 ° azimuth is performed to average the sectional forces between 0 ° and 360 ° for each datapoint. These bin averaged sectional forces are then averaged over the datapoints to obtain the experimental data plotted in the graphs. Like the pressure distributions for axial flow, a grey standard deviation band in the plots gives an indication of the repeatability between the datapoints.

B.2.2 Axial force and torque

Axial force and torque are calculated by integrating the distributed forces linearly between instrumented sections assuming zero loads at the blade root and tip. For axial flow the average loading is assumed to be equal for all three blades. For the yawed flow case, these variables are a function of rotor azimuth angle and the contribution of each blade varies with the blade azimuth angle. The variation of blade loading with **blade** azimuth angle is assumed equal between the blades to determine the rotor azimuth dependent axial force and torque.

B.3 Velocity traverses

For each PIV datapoint the average over either 100 (axial traverse) or 30 samples (radial traverse) is taken. The velocities of the sheets are concatenated to obtain a radial or axial traverse. The exact location taken for the traverses is described in section A.1 and A.2. The overlap between the sheets gives a satisfactory image on the accuracy of the PIV data. The data close to the rotor plane for the axial traverse is complimented with the radial traverse sheets.

It must be noted that the PIV measurements were performed phase locked and hence the data is for a fixed azimuth angle. Hence close to the rotor plane the phase locked measurements can differ significantly from the azimuth averaged velocities.

C Description of codes

This section describes the computational models that are used in the comparison between calculations and measurements (section 8).

Most codes used can be characterized as lifting line codes, which indicates that they need input of the aerodynamic coefficients of the airfoils used in the blade. Many of these lifting line codes use Blade Element Momentum (BEM) theory. Another class can be categorized as Computational Fluid Dynamics (CFD) codes, for which the actual geometry of the blade surface is taken into account instead of using the above mentioned aerodynamic coefficients. The descriptions as provided by the participants are included below.

C.1 Lifting line codes

C.1.1 CENER Fast code

FAST Code (BEM) Employed at CENER

Ainara Irisarri

October 1, 2011

General description of the code

FAST is an aeroelastic simulation code that can model the dynamic response of 2 or 3 bladed horizontal axis wind turbines. It is coupled to the aerodynamic code AeroDyn [1], which calculates the lift, drag and pitching moment coefficients on each section of the blade as well as the forces on each of the elements along the span. Those forces are lately used by the aeroelastic simulation program FAST to calculate the distributed forces on the turbine blades.

The wind input files for calculations can consist on steady mean winds, steady winds with gusts and/or direction changes, or three-dimensional turbulent winds. For generation of the steady winds the routine IECwind is used, while for the turbulent winds TurbSim is employed.

For MexNext project, all winds are steady mean winds: constant and uniform wind fields.

For calculating the induced velocities on the blades, AeroDyn has two models implemented: BEM and a Generalized Dynamic Wake model. For the current work on the MexNext project, the BEM model has been used in all calculations. This model does not include the drag in the calculation of induction, and includes the next corrections:

Tip and hub corrections:

Aerodyn uses a theory originally developed by Prandtl to account for the tip effect. The theory is summarised by a correction factor that is applied to the momentum part of the blade element momentum equations.

There also exists the option of using an empirical relationship based on the Navier-Stokes solutions of Xu and Sankar, that is a correction to the Prandtl model.

To account for the hub effects, a hub loss model is used, that has an identical implementation as the Prandtl tip loss model.

The user can choose whether to apply the tip and hub corrections or not.

Correction for turbulent wake:

To correct the local thrust coefficient of the individual blade elements when the basic BEM theory becomes invalid (induction factor is greater than 0.5), the Glauert correction is implemented in AeroDyn.

Skewed wake correction:

When the wind turbine operates at yaw angles relative to the incoming wind direction, AeroDyn uses a correction to account for the skewed wake effect. Such correction is based on a method developed by Pit and Petters, based on a correction originally developed by Glauert.

Dynamic inflow:

The dynamic inflow model of AeroDyn is based on the Generalized Dynamic Wake theory, that is an expanded version of the Pitt and Peters model. It uses a series

solution to describe the induced velocity field in the rotor plane, which includes Legendre functions in the radial direction and trigonometric functions in the tangential direction. The current GDW model in AeroDyn employs 0P, 1P, 2P and 3P terms. The AeroDyn GDW model is based on the work of Suzuki.

The user can choose whether to use the dynamic inflow correction or not. We did not use it for MexNext.

The aerodynamic calculations in AeroDyn mentioned above are based on pseudo two-dimensional properties of the local airfoil aerodynamics. For calculating the airfoil aerodynamics, the code has two options:

- Static airfoil tables: represented by tables of lift, drag and pitching moment coefficients as function of angle of attack and Reynolds number. To determine the aerodynamic coefficients at a particular angle of attack, the linear interpolation is used.

- Dynamic stall model: the model included in AeroDyn is based on the work of Beddoes and Leishman, with a modification to allow reproducing aerodynamic coefficients at high angles of attack. In addition, CENER has developed the code DYSTOOL, which has been implemented in AeroDyn. DYSTOOL is also based on the Beddoes-Leishman model with several modifications to improve the results. The main advantage is the possibility to include an optimized set of parameters for each aerofoil or unsteady condition, in order to improve the calculations for the corresponding case. The value of the parameters can be adjusted using an independent tool, based on optimization through a methodology of genetic algorithms, and using experimental or reliable computed data as a baseline.

  The user can choose between doing a steady computation, using the original dynamic stall model of FAST or using DYSTOOL, depending on the case to be computed.

The influence of the tower on the blade aerodynamics is also modelled in AeroDyn.

For upwind turbines, the model is based on the work of Bak. The model is dependent upon the drag coefficient of the tower, and provides the influence of the tower on the local velocity field at all points around the tower.

For downwind turbines, the model is based on the work of Powles, were the influence of the tower is augmented by a tower wake velocity deficit.

For MexNext project, as the rotor is far from the tower, the tower model has been disabled in all calculations.

Application of the code for rotating cases

At this task three cases were run, all of them with a steady mean wind and no yaw. At this situation, no dynamic inflow model was applied, and the dynamic stall model was also disabled. Both axial and tangential inductions were computed.

The blade was divided in 26 elements, and two sets of computations were done: one with 2D airfoil data, and the other one using airfoil data corrected for 3D effects.

For the 2D computation, DU91-W2-250 ($Re=0.5*10^6$) and NACA64-418 ($Re=0.7*10^6$) data was used as provided in the ECN report “Description of experimental setup” by Boorsma and Schepers. RISO airfoil data provided at the same report was modified to give more continuity on lift and drag with the other two airfoils.

For the 3D computation, Cl data of airfoils was modified following a method based on experimental results to account for 3D effects (Cd and Cm were left as in 2D).

As 3D effects were tried to be reproduced based on experimental results, the tip and hub effects were also considered to be included in the modified 3D airfoil data itself, so, the corresponding tip and hub corrections were disabled.

Application of the code for rotating cases with yaw

At this task two yaw cases were run:

- Case 1: Yaw angle=30 deg, V_{tunnel} = 14.99 m/s
- Case 2: Yaw angle=15 deg, V_{tunnel} =23.97 m/s

At this situation, no dynamic inflow model was applied to focus on the dynamic stall influence, and DYSTOOL was enabled to account for unsteady dynamic effects. Both axial and tangential inductions were computed.

The blade was divided in 26 elements, and the following airfoils were used: DU91-W2-250 (Re=0.5*10^6), RISOE A1-21 (Re=1.6*10^6) and NACA64-418 (Re=0.7*10^6) data as provided in the ECN report "Description of experimental setup" by Boorsma and Schepers.

To analyze the 2D behaviour in the blade elements, 3D effects are avoided. The tip and hub effects were not considered.

Application of the code for parked cases

15 cases were run, all of them with a constant wind with no shear, differing from one case to another only the pitch angle.

In all cases no dynamic inflow model was applied, and the dynamic stall model was disabled. The calculation for axial and tangential inductions was also disabled, as FAST does only compute the induction due to rotation, and so for parked simulations the calculated values of *a* and *a'* are almost zero.

However, as the influence of the induction due to geometric effects is considerable, as seen by means of experimental results, at CENER a Lifting Line code was used to account for this effect. Then FAST-AeroDyn was fed with those results from the lifting line.

The blade was divided in 26 elements, being the applied airfoil data detached below:

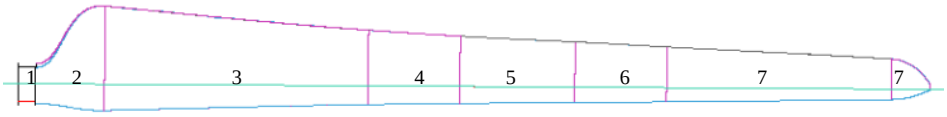

1. Cylinder: Cd = 1.
2. Transition Cylinder – DU91-W250 (Re=0.5*10^6).
3. DU91-W250 (Re=0.5*10^6) as provided in the report from ECN.
4. Transition DU91-W2-250 (Re=0.5*10^6) – RISO-A1-21.
5. RISO-A1-21:
    - Cd and Cm: Re=1,600,000 as provided in the report from ECN.
    - Cl:
        - [-180,-3.0]: as for Cd and Cm.
        - [-3.0, 22.2]: CFD data (WMB code), at Re = 700,000
        - [22.2, 180]: as for Cd and Cm.
6. Transition RISO-A1-21 – NACA64-418 (Re=0.3*10^6).
7. NACA64-418 (Re=0.3*10^6) as provided in the report from ECN, softened to eliminate discontinuities in the whole range [-180, 180].

FAST-AeroDyn skips the calculation of tip and hub corrections when there is no rotation, so those corrections were disabled.

Bibliography

[1] P.J. Moriarty and A.C. Hansen, 2005. "AeroDyn Theory Manual." National Renewable Energy Laboratory, NREL Technical Report, TP-500-36881.

C.1.2 DTU BEM and AL code

BEM

The Blade Element Momentum model combines the axial and tangential loads for each blade element. As shown in Fig.1, the blade has a radius of R=2.25m and rotates at 44.4 rad/s. Fig. 2 shows the velocity components at each blade element where the pitch angle θ, the flow angle ϕ and the angle of attack α are depicted.

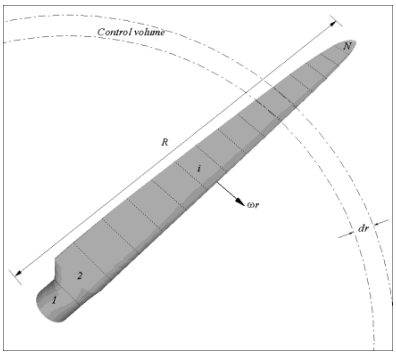

Figure 1: Blade elements on a rotating blade.

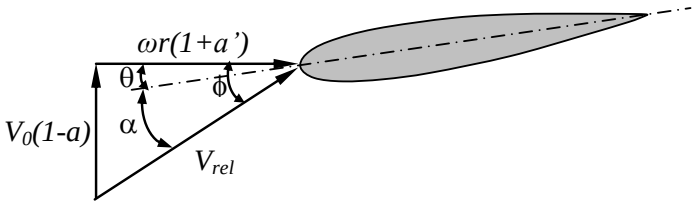

Figure 2: Velocity components at each blade element.

Momentum theory is applied on each element such that the thrust and the torque are calculated as following

$$dT = d\dot{m}(V_0 - V_1) = 2\pi r \rho V (V_0 - V_1) dr = 4\pi r \rho V_0^2 aF(1-aF)dr \quad (1)$$

$$dM = \dot{m} r V_\theta = 2\pi r^2 \rho V \cdot V_\theta dr = 4\pi r^3 \rho V_0 (1-aF) \cdot \omega a' F dr \quad (2)$$

where *a* and *a'* are the induced velocity interference factors in the axial and tangential directions, respectively, and F is the Prandtl tip loss function introduced to model the tip loss effects. Using blade element theory, the axial load and the torque are written as

$$dT = \frac{\rho B c V_0^2 (1-a)^2 dr}{2\sin^2\phi} C_n^r \quad (3)$$

$$dM = \frac{\rho B c V_0 (1-a) \Omega r^2 (1+a') dr}{2\sin\phi\cos\phi} C_t^r \quad (4)$$

The 2D force coefficients are corrected for 3D effects such that

$$C_n^r = F_1 \cdot C_n \quad (5)$$

$$C_t^r = F_1 \cdot C_t \quad (6)$$

where the tip loss function F1 is given as

$$F_1 = \frac{2}{\pi}\arccos\left[\exp\left(-g\frac{B}{2}\cdot\frac{R-r}{r\sin\phi}\right)\right]$$

and

$$g = \exp\left[-0.125(B\lambda - 21)\right] + 0.1$$

The axial and tangential induction factors are calculated with tip loss correction as

$$a = \frac{2 + Y_1 - \sqrt{4Y_1(1-F) + Y_1^2}}{2(1+FY_1)} \tag{7}$$

$$a' = \frac{1}{(1-aF)Y_2/(1-a) - 1} \tag{8}$$

where $Y_1 = 4F\sin^2\phi/(\sigma C_n F_1)$, $Y_2 = 4F\sin\phi\cos\phi/(\sigma C_t F_1)$.

In the present calculation, the drag is included in the calculation of inductions and each blade is divided into 15 elements.

There are two sets of airfoil data employed in the calculations. One set is the original 2D airfoil data obtained from 2D measurements (see Fig. 3 (left)). Another set of airfoil data is based on the original airfoil data and (1) the 2D lift is corrected to have a slightly smaller slope according to the observation on the lift slope of airfoil sections on a rotating blade; (2) the 2D Cl curve of the RISOE-A1-21 is translated to have the same zero lift angle as the other two airfoils, see Fig. 3 (right).

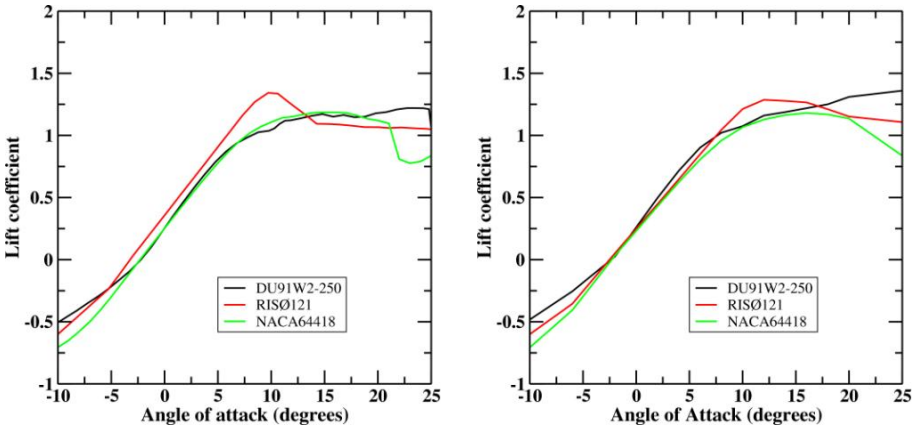

Figure 3: Original 2D airfoil data (left) and modified airfoil data (right).

The Beddoes-Leishman type dynamic stall model is implemented in the BEM code. The tip loss correction described above is included in the computations whereas no root correction model is introduced.

No correction for turbulent wake is introduced.

The tower shadow model is based on the inviscid flow over a circular cylinder. The velocity components around a tower cross section given in polar frame as

$$V_r = V_0\left(1-\left(\frac{a}{r}\right)^2\right)\cos\theta \tag{9}$$

$$V_\theta = -V_0\left(1+\left(\frac{a}{r}\right)^2\right)\sin\theta \tag{10}$$

The velocity in polar coordinates is transformed into Cartesian coordinates at each blade element as

$$V_z = V_r\cos\theta - V_\theta\sin\theta \tag{11}$$

$$V_y = -V_r\sin\theta - V_\theta\cos\theta \tag{12}$$

According to the MEXICO turbine, the tower has a radius of 0.2 m on top and 0.3 m at bottom. The radius in Eq. (9) and (10) are linear interpolated at each tower cross-section to model the correct flow field.

The wind shear model is introduced as a function of height:

$$V_o = V_o(H)\left(\frac{x}{H}\right)^\nu \tag{13}$$

where H is the tower height. The shear model was almost deactivated in the present calculation with ν equal to 0.001. No turbulence and dynamic inflow model are used.

The yaw model has not been implemented and it will be implemented later in the project.

CFD

The EllipSys3D code is used in the CFD computations with and without tunnel. The EllipSys code was developed at the Department of Mechanical Engineering, Technical University of Denmark (DTU) and the Department of Wind Energy, Risø National Laboratory. The code is based on a multi block/cell-centered finite volume discretization of the steady/unsteady incompressible Navier-Stokes equations in primitive variables (pressure-velocity). The predictor-corrector method is used. In the predictor step, the momentum equations are discretized using a second-order backward differentiation scheme in time and second-order central differences in space, except for the convective terms that are discretized by the QUICK upwind scheme. In the corrector step, the improved Rhie-Chow interpolation is used in order to avoid numerical oscillations from pressure decoupling. Since there is no optimal value for the SIMPLE algorithm for unsteady flow computations, the solution is slightly dependent on the relaxation parameters and the time-step. In order to make it more consistent, the improved SIMPLEC scheme for collocated grids is used. Using the scheme the solution is independent of the relaxation parameter and the time-step. The obtained Poisson pressure equation is solved by a five-level multi-grid technique. Since the EllipSys3D code is programmed using a multi-block topology, it can be parallelized relatively easily using Message Passing Interface (MPI).

The turbulence model used for Large Eddy Simulation is the mixed scale turbulence model developed at LIMSI

$$\nu_t = C\left|\bar{\vec{\omega}}\right|^{\alpha} k^{(1-\alpha)/2}\Delta^{(1+\alpha)}$$

where $\Delta = \left(\Delta_x\Delta_y\Delta_z\right)^{1/3}$ is an average grid size, and $\alpha = 0.5$. Assuming similarity between two grid levels, the turbulent kinetic energy can be estimated by using the following filter

$$k = \frac{1}{2}\sum_{j=1}^{3}\left(U_j - \bar{U}_j\right)^2 \approx \frac{1}{2}\sum_{j=1}^{3}\left(\bar{U}_j - \tilde{\bar{U}}_j\right)^2$$

where $\tilde{\bar{U}}_j$ is the filtered velocity of the resolved velocity, $\bar{U}_j$, by the second filter, i.e. the double filtered velocity.

The blades are represented as a line-distributed body force in the Navier-Stokes equations, obtained from the Actuator Line technique. The tower nacelle is not included in the computations. The open tunnel is included to study the tunnel effects.

A Cartesian mesh of 11.8 M mesh points is used in a domain of [-16R, 16R]×[-16R, 16R]×[-16R, 16R] where120x120x240 cells are uniformly distributed in a domain near the rotor [-2R, 2R]x[-2R, 2R]x[-2R, 4R] with the finest mesh of R/30 where R is the rotor radius is used.

The inflow and lateral boundary conditions are specified with the uniform velocity whereas at the outlet convective boundary condition is used.

The blade is divided intro 30 elements in the actuator line model.

The Beddoes--Leishman type dynamic stall model will be implemented later in the project. No inflow or tower shadow models are included.

C.1.3 ECN AWSM code

The AWSM code, see [1], is based on a non-linear lifting line vortex wake model. The code is of a free wake character but for distances larger than 4 rotor diameters downstream of the rotor, the wake is assumed to be 'frozen'.

The blades are modelled as lifting lines. This implies that, similar to BEM codes, aerodynamic profile data should be prescribed as function of the angle of attack. Dynamic stall corrections are not taken into account (although instationary effects which result from the shed vorticity are modelled). A 3D stall correction has been added to the airfoil characteristics.

The AWSM calculations were made under the following assumptions:
- The construction is assumed to be rigid and mass induced loads are neglected;
- The wind speed is constant in time and homogenous. The aerodynamic tower shadow effect has been neglected;
- The rotor speed and pitch angle are constant;

References

[1] A. van Garrel. "Development of a wind turbine aerodynamics simulation module". ECN-C–03-079, Energy Research Centre of the Netherlands, ECN, August 2003.

C.1.4 IFE FLEX5 code

BEM

1. We assume that your model basically combines the axial and tangential momentum equation with the axial and tangential force from the blade element theory.

   Correct.

2. Is drag included in the calculation of induction?

   Yes.

3. In how many elements have you divided the blade?

   21

4. Describe which airfoil data along the blade have been applied. Also describe the origin of these data and possible manipulations (eg 3D corrections).

   The 2D airfoil data provided in the "Description of experimental setup" were used without 3D corrections. Specifically, the data for NACA 64-418 at Re = $7x10^5$, Risø A1-21 at Re = $1.6x10^6$, and DU91-W2-250 at Re = $5x10^5$ were used.

5. Describe dynamic stall model

   Stig Øye's dynamic stall model is used.

6. Describe tip and root correction.

   Prandtl's tip correction is used.

7. Describe correction for turbulent wake

   Stig Øye's dynamic wake model is used.

8. Describe tower shadow modeling.

   The FLEX5's tower shadow model, which is based on potential theory, was not used for these studies.

9. Describe wind modeling (e.g. no turbulence, uniform flow etc).

   Uniform flow was used for all cases.

(The next questions are not applicable for the present calculations yet)

10. Describe yaw model (not applicable yet)

Glauert's yaw model is used.

11. Describe dynamic inflow model (not applicable yet).

Stig Øye's dynamic wake model is used.

12. Miscellaneous remarks

C.1.5 MIE VPM code

Model Description of MIE VPM

1. General description of model

Vortex lattice method based on panel method was used. In the model, the rotor blade surface is divided into quadrilateral panel elements. The lattice panels, which have four vortex filaments, represent the effects of the blade.

2. In how many elements have you divided the blade

In this calculation, the blade is divided in 160 vortex panels. (8 in chordwise direction and 10 in spanwise direction on both the pressure and suction surfaces.)

3. Describe which airfoil data along the blade have been applied. Also describe the origin of these data and possible manipulations (eg 3D corrections)

The airfoil coefficient data sets for DU91-W2-250 ($Re=0.5x10^6$), RISØ A1-21 ($Re=1.6x10^6$) and NACA64-418 ($Re=0.7x10^6$) from "MexNextExperimentDescription.xls" were used without any manipulations.

4. Describe dynamic stall model

In this calculation, the dynamic stall effect was not considered.

5. Describe tower shadow modeling

In this calculation, the tower shadow effects were not considered.

6. Describe wind modeling (eg no turbulence, uniform flow)

Steady uniform flow was used.

7. Miscellaneous remarks

In the discretization of blade, full-cosine spacing method was used in order to obtain denser panels at near the root and tip. Therefore, the resolution of panels at middle was low and it may not enough to describe the change of airfoil along spanwise direction.

C.1.6 RISØ HAWC2 code

Description of the HAWC2 code and the Actuator disc code (AD) used in the 1st comparison round of IEA Annex 29, October 2009

Helge Aagaard Madsen
Risoe DTU
March 8 2010

HAWC2 code

The HAWC2[1] code is a time simulation code for wind turbine response. It has been developed in the years 2003-2006 at the aeroelastic design research programme AED at Risoe DTU in Denmark.
The structural part of the code is based on a multibody formulation where each body is an assembly of timoshenko beam elements. The formulation is general which means that quite complex structures can be handled and arbitrary large rotations of the bodies can be handled. The turbine is modeled by an assembly of bodies connected with constraint equations, where a constraint could be a rigid coupling, a bearing, a prescribed fixed bearing angle etc.
The aerodynamic part of the code is based on the blade element momentum (BEM) theory but extended from the classic approach[2] to handle dynamic inflow, dynamic stall, skew inflow, shear effects on the induction and effects from large deflections. Several turbulence formats can be used. Control of the turbine is performed through one or more DLL's (Dynamic Link Library). The format for these DLL's is also very general, which means that any possible output sensor normally used for data file output can also be used as a sensor to the DLL. This allows the same DLL format to be used whether a control of a bearing angle, an external force or moment is placed on the structure.

The actuator disc (AD) code

The AD code is based on the general purpose CFD code FIDAP[3]. In the past the code has been used for several studies using the actuator disc model. The previous studies comprise: comparison with the BEM model and influence of turbulent mixing and high loading[4], aerodynamics of coned rotors[5], yawed flow aerodynamics[6, 7] and dynamic induction[8] . Based on experience from the previous studies the set-up for the present simulations was chosen. Axisymmetric, swirling flow has been assumed and a

[1] Larsen, T.J.; Hansen, A.M., How 2 HAWC2, the user's manual. Risø-R-1597(ver. 3-1)(EN) (2007) 70 p.
[2] Madsen, H.Aa, Bak, C., Døssing, M., Mikkelsen, R.F., Øye, S. "Validation and modification of the Blade Element Momentum theory based on comparisons with actuator disc simulations": Wind Energy (ISSN: 1095-4244) (DOI: 10.1002/we.359) , Article in Press, 2009.
[3] FIDAP 8 Theory Manual, Fluent Inc., 1998.
[4] Madsen HAa. "A CFD Analysis of the Actuator Disc Flow compared with Momentum Theory Results" In proceedings of IEA Joint Action of 10th Symposium on Aerodynamics of Wind Turbines, Edinburg, December 16-17, 1996 edited by B.M. Pedersen, pp. 109-124.
[5] Madsen, HAa, Rasmussen F. "The influence on energy conversion and induction from large blade deflections". In: Wind energy for the next millennium. Proceedings. 1999 European wind energy conference (EWEC '99), Nice (FR), 1-5 Mar 1999. Petersen, E.L.; Hjuler Jensen, P.; Rave, K.; Helm, P.; Ehmann, H. (eds.), (James and James Science Publishers, London, 1999) p. 138-141
[6] Madsen, HAa. "Yaw simulation using a 3D actuator disc model coupled to the aeroelastic code HawC". In: IEA Joint Action. Aerodynamics of wind turbines. 13. Symposium, Stockholm (SE), 29-30 Nov 1999. Maribo Pedersen, B. (ed.), (2000) p. 133-145
[7] Madsen, HAa, Sørensen, N.N.; Schreck, S. "Yaw aerodynamics analyzed with three codes in comparison with experiment". In: AIAA Paper 2003-519. 41. Aerospace sciences meeting and exhibit, Reno (US), 6-9 Jan 2003. (American Institute of Aeronautics and Astronautics, Inc., Reston, VA, 2003)
[8] Sørensen, NN, Madsen HAa. "Modelling of transient wind turbine loads during pitch motion" (paper and poster). In: Proceedings (online). 2006 European Wind Energy Conference and Exhibition, Athens (GR), 27 Feb - 2 Mar 2006. (European Wind Energy Association, Brussels, 2006) 10 p

mesh stretching 10R in upstream and radial direction and 20R in downstream direction has been used. The disc itself is modeled with two layers of elements in the stream-wise direction and has a extension of 0.05R. Further the simulations were run assuming turbulent flow and a Reynolds number of 10000 based on rotor radius. Finally it is important to note that the input loading from the HAWC2 BEM solution was used and no subsequent iteration was performed in order to match completely the load and flow field.
The AD model has within the MEXICO project been used for studying tunnel effects. However, the present simulations were run without the influence of the tunnel.

C.1.7 TECHNION BEM code

Description of the Technion BEM model

Technion BEM model is based on a combination between the well known blade element theory (for more details see Gur and Rosen 2008), and a new actuator disk theory that has been developed recently in the Technion [see Rosen and Gur 2208 for an axial flow, Kominer and Rosen 2011 for a yawed flow).

The cross sectional lift and drag forces are calculated based on the experimental data for DU91-W2-250 ($Re=0.5x10^6$), RISØ A1-21 ($Re=1.6x10^6$) and NACA64-418 ($Re=0.7x10^6$). The original data is corrected to include rotation effects on the stall behavior (Snel 1991) and influences of dynamic stall (Leishman and Beddoes 1986). A tip correction is also applied during the calculations of the aerodynamic loads along the blades.

The actuator disk model is based on a distribution of sources (that become sinks in the case of a negative sign) over the disk plan, which describes the influence of the disk (blades) on the upstream flow (before crossing the disk plan). The disk plan is divided into polar cells where the unknowns are the source intensities at all the cells. The pressure at each cell is obtained from the blade element aerodynamic loads. The actuator disk model calculates the induced velocities at the disk plan. These velocities are used as input to the blade element calculations. Usually the iterative procedure converges very fast.

Steady uniform incoming wind flow is assumed. An isolated rotor is considered without taking into account any influences of the nacelle or tower.

Gur, O. and Rosen, A., 2008, "Comparison between Blade-Element Models of Propellers", Aeronautical Journal Vol. 112, No. 1138, pp. 687-704.

Kominer, S. and Rosen, A., 2011, "A New Actuator Disk Model for Yawed Flow" in preparation

Leishman J.G. and Beddoes T.S., 1986, “A Generalized model for Airfoil Unsteady Aerodynamic Behavior and Dynamic Stall Using the Indicial Method”, 42nd Annual Forum of the American Helicopter Society pp. 243-265.

Rosen, A. and Gur, O., 2008, "A Novel Approach to Actuator Disk Modeling", AIAA Journal Vol. 46, No. 11, pp. 2914-2925.

Snel, H.R., 1991, “Scaling Laws for the Boundary Layer on Rotating Wind Turbine Blades”, Proceedings of the Fourth IEA Symposium on the Aerodynamics of Wind Turbines.

C.1.8 UVIC BEM and accelerated potential flow based code

1) a BEM-based code with corrections based on apriori potential flow models
for coning and yaw/dynamic inflow
2) an accelerated potential-flow based code
using a Wessigner lifting line representation of the blades, fixed and free wake models composed of vortex particles, filaments and sheets with corrections for diffuse cores and dissipation. Both codes can be run with prescribed blade circulation values integrated from experimental pressure measurements to separate wake effects from sectional aerodynamic effects.

C.2 CFD

C.2.1 CENER CFD

CENER & Liverpool University's WMB code description

Sugoi Gomez-Iradi
October 1, 2011

1. Code description

WMB (Wind Multi-Block) is the CFD method developed together between the University of Liverpool and CENER and validated for HAWT [1, 2]. It is capable of solving the compressible Unsteady Reynolds Averaged Navier-Stokes (URANS) flow equations on multi-block structured grids using a cell-centred finite-volume method for spatial discretization. The present solver was designed to account for the motion of the blades, their structural deformation, as well as, turbulent flow conditions, although for this project the blades were considered rigid. A second-order implicit method [3] was employed, and the resulting linear system of equations was solved using a pre-conditioned Generalised Conjugate Gradient (GCG) method.

For the unsteady simulations carried out in the MexNext project, implicit dual-time stepping was employed based on Jameson's [4] pseudo-time integration approach. From the beginning, the solver was designed with parallel execution in mind and for this reason a divide-and-conquer approach was used to allow for multi-block grids to be computed on distributed-memory machines and especially low-cost Beowulf clusters of personal computers. Details about the parallel performance can be found in [5].

2. Components included in the computations

The meshed geometry was obtained from MexNext EPOS site [6] and was named as *BladeCore-B_ Airfoil_ 11.step*.

For standstill case a single blade and for rotating cases an isolated rotor configuration with three blades were modelled. However, there is the aim of modelling the full configuration: rotor, spinner, nacelle, tower and tunnel walls.

3. Grids and Boundary conditions

CFD results were computed in coarse and fine grids in order to verify the grid convergence together to perform the first computations. The main grid characteristics are defined in Table 1. The structured hexa cell multi-block grids were created with ICEMCFD 12.0 and the mesh

around the blades had a H-type topology. The post-processing was done with Tecplot 360 2010.

The boundaries of the parked case were located as described in Table 1, the inflow at 3 radii (R) away from the rotational plane and the outflow at 6R distance. The far-field was set to 4R from the edge of rotation. At blade surfaces solid or non-slip condition was applied.

For the rotational cases, the inflow, outflow and far-field were located at 6 R distance from the centre of rotation of the turbine, where the pitch axis of the three blades coincide.

Mesh name	Total Size (cells)	chord-wise (cells)	span-wise (cells)	Boundaries (Chord units)	Boundaries (R units)
First Rotating	9,325,800	210	124	I=28.125, O=56.25	I=3, O=6
Refined Rotating	25,244,112	234	164	& FF= 37.5	& FF= 4
First Parked	5,670,912	230	140	I=56.25, O=56.25	I=6, O=6
Refined Parked	11,435,620	282	191	& FF= 56.25	& FF= 6

Table 1: Employed mesh characteristics (I=Inflow, O=Outflow & FF=Far-Field).

4. Computations

The URANS computations were carried out with the k-ω SST turbulence model of Menter [7] from the various one- and two-equations models that are implemented in the code. Computations were done as fully turbulent, so it was not included any transition model.

The parked or standstill computations were done as quasy-steady, which means that the grids were rotated from 90° of pitch to 1° with a rotating speed of 0.02°/second and obtaining solutions at every time step. The idea behind this procedure is to obtain steady results allowing the solver to converge better and faster in each time step.

The rotating cases were unsteady computations that reached the maximum of 16, 13 and 8 full revolutions for the 10, 15 and 24m/s cases without yawed flow. The mesh had a rotation of 1° per time step and 120 pseudo-iterations were performed at each of them. As a reference, a single revolution in 108 nodes took less than three days (66h).

For this work, a Beowulf cluster available at CENER together with the CESGA supercomputer centre, thanks to the MICINN (ICTS- 2009-40) program, have been used. At CENER Intel Xeon Processor X5650 nodes were employed and at CESGA the Itanium Montvale cores. Calculations in up to 512 nodes were performed.

Bibliography

[1] S. Gomez-Iradi, R. Steijl and G.N. Barakos, Development and Validation of a CFD Technique for the Aerodynamic Analysis of HAWT, Journal of Solar Energy Engineering-Transactions of the ASME, 131(3):031009, 2009. DOI:10.1115/1.3139144.

[2] S. Gomez-Iradi and G.N. Barakos, Computational Fluid Dynamics Investigation of Some Wind Turbine Rotor Design Parameters, Proceedings of the Institution of Mechanical Engineers, Part A: Journal of Power and Energy, 222(5):455-470, 2008. DOI:10.1243/09576509JPE526.

[3] R. Steijl, G. Barakos and K. Badcock, A Framework for CFD Analysis of Helicopter Rotors in Hover and Forward Flight, International Journal for Numerical Methods in Fluids, volume 51(8), 2006, DOI:10.1002/fld.1086

[4] A. Jameson, Computational Algorithms for Aerodynamic Analysis and Design, Applied Numerical Mathematics, volume 13(5), 1993

[5] R. Steijl, P. Nayyar, M. Woodgate, K. Badcock and G. Barakos, Application of an Implicit Dual-Time Stepping Multi-Block Solver to 3D Unsteady Flows, International Conference on Parallel CFD, College Park Campus, Maryland, USA, 24-27 May 2005

[6] https://www.mexnext.ecn.nl (login/password needed)

[7] F.R. Menter, Zonal Two Equation Kappa-Omega Turbulence Models for Aerodynamic Flows, 23^{rd} Fluid Dynamics, Plasmadynamics, and Lasers Conference, Orlando, USA, 6-9 July 1993

C.2.2 ETS CFD

CFD

1. General description of model (RANS (turbulence model), LES, incompressible, compressible etc)

Navier Stokes equations; rotating reference frame; steady formulation allowing the study of zero yaw angle; incompressible, laminar flow (i.e. no turbulence is modelled)

2. Which components have been modeled (eg blades, tower nacelle, tunnel etc)

The blades have been modelled using actuator surfaces. These surfaces represent the blades with singular surfaces of velocity and pressure discontinuities. Velocity discontinuities are set so that they reproduce (1) velocity circulation around blade sections and (2) vorticity flux conservation; the intensity of the circulation is calculated using blade element analysis.

3. Origin of geometrical description

The center of the rotor is used as the origin

4. Describe meshing:

The solution domain is a box. A cartesian, structured mesh is used. 141*141 grid points are used in the rotor plane, and 145 points are used in the axial direction (parallel to the incoming wind). Each actuator surface modelling each blade is represented using 9*34 points in the chorwise and spanwise directions respectively.

5. Describe boundary conditions

Boundary conditions at the outlet plane are of greater importance. At this boundary, the pressure is set to a uniform value of zero, while the axial velocity gradient is set to zero. Velocity is set to the constant incoming inflow velocity at all other domain boundaries. The upstream and downstream boundaries are set at respectively 10.8R and 9.8R, while the boundaries around the rotor are located at 8.2R from the center of the rotor, with R the radius of the blades.

6. Describe numerical solution algorithm

To solve the set of partial differential equations describing the flow evolution (the Navier-Stokes equations in their incompressible, steady-state form), the 3D Control-Volume Finite-Element Method (CVFEM) of Saabas & Baliga [1] is used. This consists of a co-located method where the variables solved (i.e. the pressure and three velocity components) are stored at the nodes. Appropriate modifications are made to embed in this method the actuator surfaces consisting of 2D surfaces located normally to the upstream flow, namely in the rotational plane, and whose associated velocity jumps are stored on the AS nodes.

7. Miscellaneous remarks

We are currently investigating convergence problems that we still experience when modelling the flow far downstream from the turbine rotor.

[1] Saabas, H., Control Volume Finite Element Method for Three-Dimensional, Incompressible, Viscous Fluid Flow, Ph.D. thesis, Mc Gill University, 1991.

C.2.3 Forwind CFD

Description of CFD model and RANS solver used by ForWind-Oldenburg for the MexNEXT-Project

Bernhard Stoevesandt, Ivan Herraez, Henry Plischka

General description of the model

At ForWind we used the open source code OpenFOAM – version 1.7.1 for the CFD simulation. The solver used was the MRFSimpleFoam solver, which is based on the Reynolds Averaged Navier Stokes Equations which were solved in a rotating frame of reference. A k-ω SST model proposed by Menter in 2001 [1] has been used for the turbulence modeling. The calculations were steady. The rotor was modeled completely, however the nacelle has been shortened, so that it end about 0.5m behind the rotor plane. The complete domain was regarded in the rotating frame of reference. Calculation have been done for a pitch of -2.3° at 0° yaw for an inflow velocity of 10, 15 and 24 m/s.

Which components have been modelled?

So far blades and the front of the nacelle have been modeled. However for the blades only blade 1 has been used and copied twice to the other position, so that all geometries of the blades are equal.

Origin of geometrical description

The geometry of the blades have been extracted from the blade_iges1.igs-file provided from Technion. The geometry has been simplified by cleaning and closing the surfaces using CATIA V5. The nacelle has been modeled by using the description given in the Mexico-technical report by ECN, ECN-X-09-0XX.

Describe meshing

For the MexNext calculations a cartesian mesh with so called snapped cells to the geometry as it was done with the OpenFOAM meshing tool SnappyHexMesh. The mesh consists of 32 million hexahedral and split hexahedral cells. A refinement level has been reached of cell sized of 0.48 mm cells on the leading and trailing edge and 0.98 mm on the rest of the suction and pressure side of blade 1. Only blade 1 has been refined completely as the geometry of the blades were equal. There are about 900000 surface cells on blade 1 with a hexahedral prism layer consisting of three cells with a $y+<2$ for the innermost cells. The refinement level of the near wake area (up to 1/2 D) was 15 mm. There was no prism layer refinement for the nacelle. The domain was cylindrical with a diameter of about 6D in the cross-flow direction. The length was set to 5D in front and 10D behind the rotor plane.

Describe boundary conditions

As boundary condition on the blades and the nacelle the k-ω SST wall function is used as provided in OpenFOAM. Fot the inflow a Dirichlet condition was used and for the outflow a von Neuman condition. The turbulence at the inflow was set to be at a turbulence intensity of 0.8% as specified for the tunnel.

Describe numerical solution algorithm

For the analyses the MRFSimpleFoam solver as part of OpenFOAM-Verions 1.7.1 has been used for the simulations. OpenFOAM is an open source field operation and manipulation package, which is mostly used for finite volume CFD calculation. It consists of different solvers for many application. The MRFSimpleFoam is a so called SIMPLE (implicit steady) solver for RANS calculations for multiple rotating reference frames. For the calculations the Gauss linear scheme has been used, which is of second order.
The turbulence has been calculated using the k-ω SST model by Menter in a version proposed in 2001.

Future simulations

As the actual simulations have been done as steady ones, the future simulations will be done as unsteady ones. The mesh might be further refined in certain regions.

[1] F. Menter, T. Esch: Elements of Industrial Heat Transfer Predictions
, in Proc. of 16th Brazilian Congress of Mechanical Engineering (COBEM), Nov. 2001, Uberlandia, Brazil

C.2.4 RISØ CFD

Risø-DTU EllipSys3D code description

Niels N. Sørensen

January 21, 2011

1 Code description

The in-house flow solver EllipSys3D is used for both axial and yaw computations. The code is developed in co-operation between the Department of Mechanical Engineering at the Technical University of Denmark and The Department of Wind Energy at Risø National Laboratory, see [1, 2] and [3]. The EllipSys3D code is a multiblock finite volume discretization of the incompressible Reynolds Averaged Navier-Stokes (RANS) equations in general curvilinear coordinates. The code uses a collocated variable arrangement, and Rhie/Chow interpolation [4] is used to avoid odd/even pressure decoupling. As the code solves the incompressible flow equations, no equation of state exists for the pressure, and in the present work the Semi-Implicit Method for Pressure-Linked Equations (SIMPLE) algorithm of Patankar and Spalding [5, 6] or the Pressure Implicit with Splitting of Operators (PISO) algorithm of Issa [7, 8] is used to enforce the pressure/velocity coupling, for steady state and transient computations respectively. The EllipSys3D code is Parallellized with the Message-Passing Interface (MPI) for executions on distributed memory machines, using a non-overlapping domain decomposition technique.

Both steady state and unsteady computations can be performed. For the unsteady computations the solution is advanced in time using a 2nd order iterative time-stepping (or dual time-stepping) method. In each global time-step the equations are solved in an iterative manner, using under relaxation. First, the momentum equations are used as a predictor to advance the solution in time. At this point in the computation the flowfield will not fulfil the continuity equation. The rewritten continuity equation (the so-called pressure correction equation) is used as a corrector making the predicted flowfield satisfy the continuity constraint. This two step procedure corresponds to a single sub-iteration, and the process is repeated until a convergent solution is obtained for the time step. When a convergent solution is obtained, the variables are updated, and we continue with the next time step. Thus, when the sub-iteration process is finished all terms are evaluated at the new time level.

For steady state computations, the global time-step is set to infinity and dual time stepping is not used, this corresponds to the use of local time stepping. In order to accelerate the overall algorithm, a multi-level grid sequence is used in the steady state computations. The convective terms are discretized using a third order Quadratic Upstream Interpolation for Convective Kinematics (QUICK) upwind scheme, implemented using the deferred correction approach first suggested by Khosla and Rubin [9]. Central differences are used for the viscous terms, in each sub-iteration only the normal terms are

treated fully implicit, while the terms from non-orthogonality and the variable viscosity terms are treated explicitly.

The code can solve both moving frame and moving mesh, in the present simulations the moving mesh option is used even for the steady state case were the special 'Steady state moving mesh algorithm' is used, see Sørensen [10]. In the present work the turbulence in the boundary layer is modeled by the k-ω Shear Stress Transport (SST) eddy viscosity model [11] using both fully turbulent and transitional settings. The transitional computations are based on the $\gamma - \widetilde{\mathrm{Re}}_\theta$ correlation based transition model of Menter [12]. The backbone of the model is two transport equations one for intermittency γ and one for the local transition onset momentum thickness Reynolds number $\widetilde{\mathrm{Re}}_{\theta t}$. The two non-public correlation functions relating $\mathrm{Re}_{\theta c}$ and F_{length} to $\widetilde{\mathrm{Re}}_{\theta t}$ is used according to the the ones determined by Sørensen [13].

The equations for the turbulence model and the transition model are solved after the momentum and pressure correction equations in every sub-iteration/pseudo time step, and in agreement with the recommendations of Menter et al. [12], a second order upwind Total Variation Diminishing (TVD) scheme based on the MinMod limiter is used for the transport equations for turbulence and transition.

The three momentum equations, the $k-\omega$ equations and the two transition model equations are solved decoupled using a red/black Gauss-Seidel point solver. The solution of the Poisson system arising from the pressure correction equation is accelerated using a multigrid method.

2 Components included in the computations

Only the rotor blades are included in the computations, see 1. Eventually, the nacelle may be included in future simulations.

The geometry is based on the original files by Technion delivered during the design of the rotor in the Mexico project.

3 Computational grid

The full three bladed rotor is modeled in order to use the same mesh for both axial and yawed conditions.

The mesh is a O-O-topology where the individual blades are meshed with 256 cells around the blade chord, 128 cells in the spanwise direction and a 64×64 block at the blade tip, see 2. In normal direction, 256 cells are used with high concentration of cells within the first 1-2 diameters away from the rotor, see 3. The height of the cells at the wall is 5×10^{-6} meter in order to resolved the boundary layers and keep y^+ around 1, the outer boundary of the domain is located $\tilde{4}0$ meters from the rotor center or approximately 10 rotor diameters away. The grid generation is performed with 3D enhanced hyperbolic grid generation program HypGrid3D which is an 3D version of the 2D hyperbolic grid generator described in [14].The total number of cells used is 28.3 million cells, see 4. In the present version the mesh consist of 864 blocks.

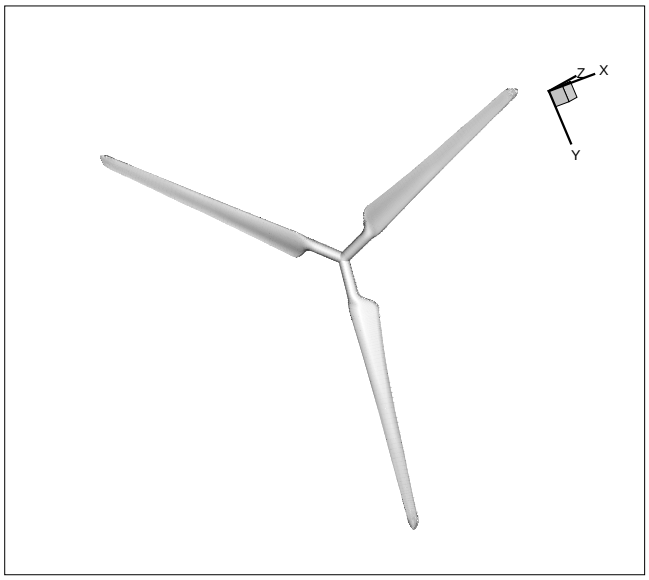

Figure 1: The rotor of the simplified turbine used in the computations

4 Boundary Conditions

Inlet conditions corresponding to the described cases are specified at the upstream part of the outer boundary, see 4, while outlet conditions corresponding to fully develop assumption are used at the downstream part of the outer domain boundary. No-slip conditions are applied at the rotor surface.

5 Miscellaneous remarks

The computations were performed on the Risø-DTU Thyra PC-cluster where the compute nodes are Dual CPU Dual-Core AMD Opteron Processor 2218 with a clock frequency of 2.6 MHz and with Infini-band interconnect. Running on one node corresponds to 4 cores or $\sim$ 4 Cpu's.

For the present mesh with 28.3 million cells, a steady state computations running on 27 nodes (108 cores) takes approximately 5.7 sec iteration. For the 15 m/s case it takes around 5000 iteration to obtain a converged solution or 8 hours. Running on 54 nodes (216 cores) the approximate iteration time is around 2.7 sec, or around 4 hours. Typically, the computations are performed for more than 5000 iteration on the fines level in order to assure that the solution is stable at the obtained level.

For the unsteady yaw simulations using 6 sub-iterations, each time step takes around 31 seconds on 24 nodes (96 cores). Using a time step of 1×10^{-4} or $\sim$ 1400 timestep per revolution, one revolution can be obtained in 12 hours. It is observed that the one timestep with 6 sub-iterations, corresponding approximately to 6 steady state iteration also takes approximately six times as long. Using eg. 48 nodes (192 cores), the time would lower to approximately 6 hours. Typically, the yaw simulations would need a few revolutions to enter a 'periodic state'. Exploiting the full parallel potential of the 864 block mesh,

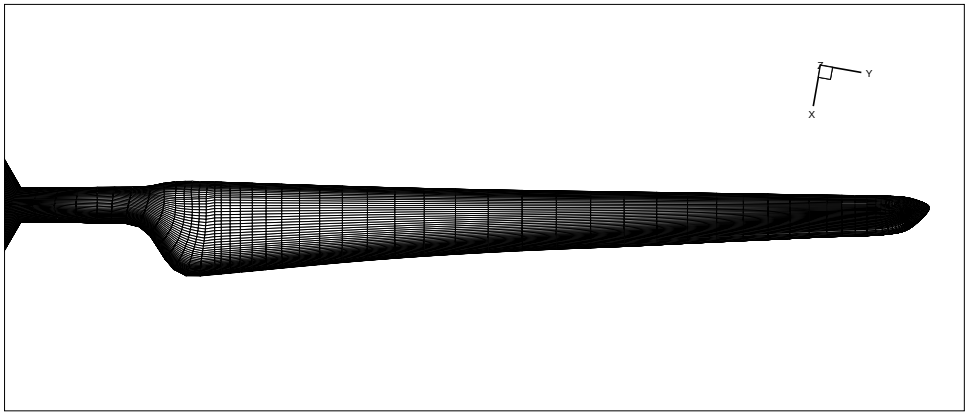

Figure 2: Surface mesh used for resolving the blade of the MEXICO rotor

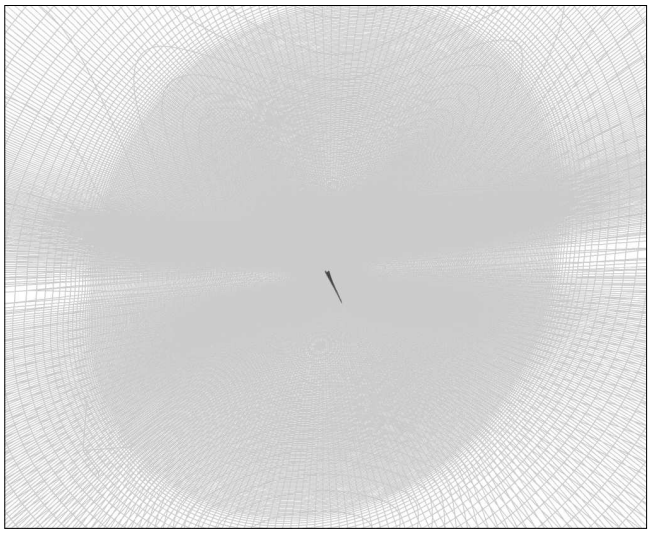

Figure 3: Details of the volume mesh close to the rotor geometry

the time would be expected to reduced to $1/9$ of the 12 hours or approximately 1.5 hour per revolution.

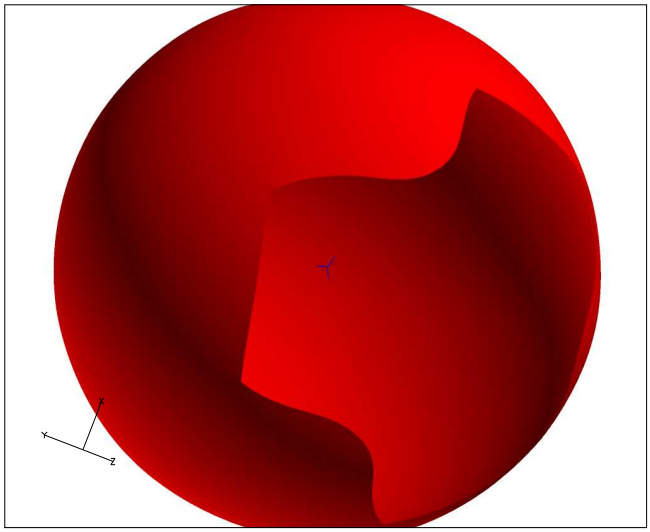

Figure 4: The outer boundary of the computational domain, showing the inlet and outlet areas

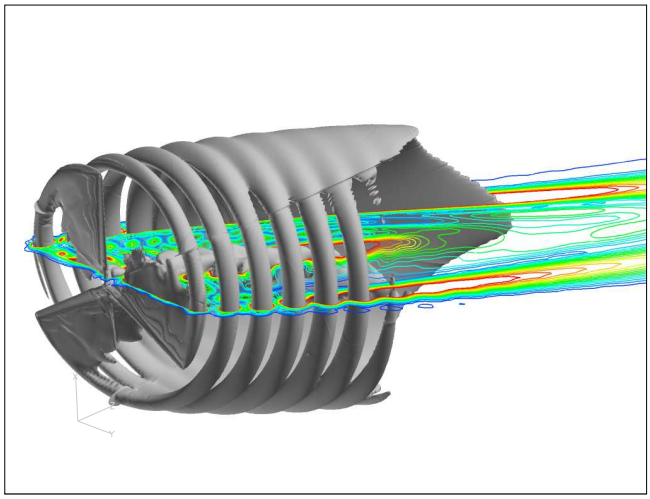

Figure 5: The vortex system behind the rotor for the 30 degrees yaw case

References

[1] J. A. Michelsen. Basis3D - a Platform for Development of Multiblock PDE Solvers. Technical Report AFM 92-05, Technical University of Denmark, 1992.

[2] J. A. Michelsen. Block structured Multigrid solution of 2D and 3D elliptic PDE's. Technical Report AFM 94-06, Technical University of Denmark, 1994.

[3] N. N. Sørensen. General Purpose Flow Solver Applied to Flow over Hills. Risø-R-827-(EN), Risø National Laboratory, Roskilde, Denmark, June 1995.

[4] C. M. Rhie. *A numerical study of the flow past an isolated airfoil with separation*. PhD thesis, Univ. of Illinois, Urbana-Champaign, 1981.

[5] S. V. Patankar and D. B. Spalding. A Calculation Prodedure for Heat, Mass and Momentum Transfer in Three-Dimensional Parabolic Flows. *Int. J. Heat Mass Transfer*, 15:1787, 1972.

[6] S. V. Patankar. *Numerical Heat Transfer and Fluid Flow*. Hemisphere Publishing Corporation, 1980. ISBN: 0891165223.

[7] R. I. Issa. Solution of the Implicitly Discretised Fluid Flow Equations by Operator-Splitting. *J. Computational Phys.*, 62:40–65, 1985.

[8] R. I. Issa, A. D. Gosman, and A. P. Watkins. The Computation of Compressible and Incompressible Recirculating Flows by a Non-iterative Implicit Scheme. *J. Computational Phys.*, 62:66–82, 1986.

[9] P. K. Khosla and S. G. Rubin. A diagonally dominant second-order accurate implicit scheme. *Computers Fluids*, 2:207–209, 1974.

[10] N. N. Sørensen. Rotor computations using a 'Steady State' moving mesh. IEA Joint Action Committee on aerodynamics, Annex XI and 20, Annex XI and 20. Aero experts meeting, Pamplona, Spaine, May 2005.

[11] F. R. Menter. Zonal Two Equation k-ω Turbulence Models for Aerodynamic Flows. AIAA-paper-932906, 1993.

[12] F. R. Menter, R. B. Langtry, S. R. Likki, Y. B. Suzen, P. G. Huang, and S. Völker. A Correlation-Based Transition Model Using Local Variables, Part I - Model Formulation. In *Proceedings of ASME Turbo Expo 2004, Power for Land, Sea, and Air*, Vienna, Austria, June 14-17 2004. ASME. GT2004-53452.

[13] N. N. Sørensen. CFD modeling of laminar-turbulent transition for airfoils and rotors using the gamma - Retheta model. In *2008 European Wind Energy Conference and Exhibition*, , pages 106–112, Brussels (BE), 31 Mar - 3 Apr 2008 2008. EWEC.

[14] N. N. Sørensen. HypGrid2D a 2-D Mesh Generator. Risø-R- 1035-(EN), Risø National Laboratory, Roskilde, Denmark, Feb 1998.

C.2.5 Technion CFD

Description of the CFD calculations of the Mexnext test cases.
Rachel Gordon and Aviv Rosen. Technion – Israel Institute of Technology.

General description of the model:
The calculations were carried out using STAR-CD Ver. 3.26 code. The code is based on the finite volume approach and it uses multi-block meshes which enable the prediction of flows over complex geometries.
In the present work the transient, turbulent, incompressible RANS equations were solved.

Turbulence model:
The k-ε/High Reynolds Number turbulence model (with a wall function) was used for the three cases: V=10m/s, yaw=0º; V=14.93m/s, yaw=0º.; V=14.99m/s, yaw=30º.
The **K-ω/SST**/High Reynolds Number model was used for the two higher incoming velocity flow cases: V=23.96m/s, yaw=0º; and V=23.97m/s, yaw=15º.

We switched to the **K-ω/SST**/High Reynolds Number turbulence model due to insufficient agreement with the experimental data obtained with the k-ε model for these two higher incoming velocity flow cases. The k-ε model is incapable of accurate modeling of the flow separation over the blades, which occurs at higher incoming wind speeds.

Components modeling:
The modeling includes the blades, hub, nacelle and tower.

Origin of geometrical description:
For the two flow cases: V=10m/s, yaw=0º; and V=14.93m/s, yaw=0º, the geometrical description of the blades is based on the IGES file: 'blade_iges[1].igs' which is an earlier version of the current iges file dated Nov. 09.
For the three other flow cases: V=23.96m/s, yaw=0º; V=14.99m/s, yaw=30º; and V=23.97m/s, yaw=15º, the geometrical description of the blades is based on the iges file dated Nov. 09.
The tower and nacelle geometrical description is based on the model description in the ECN-X-09-0XX technical report.

Mesh description:
The mesh was built using GRIDGEN code. The mesh is comprised of two domains: the inner domain which rotates with the blades, and the outer domain which is fixed in space. At each time step the two domains are attached to each other. The meshes of the inner and outer domains are built of several blocks: The inner domain mesh is built of 27 blocks and the outer domain mesh is built of 14 blocks, i.e. the mesh is built of 41 blocks, altogether.

For the two flow cases: V=10m/s, yaw=0º; and V=14.93m/s, yaw=0º, the mesh is built of structured blocks having:

4,104,084 cells; 4,273,115 vertices

For the three other flow cases: V=23.96m/s, yaw=0º; V=14.99m/s, yaw=30º; and V=23.97m/s, yaw=15º, a finer mesh was used. The inner domain mesh is built of 27 blocks, 6 of which (that are close to the nacelle) are unstructured blocks. The outer domain mesh is built of 14 structured blocks. The entire mesh is built of:

6,7750,68 cells; 6,615,248 vertices

The outer mesh is a hollow cylinder defined by:

$-10.2683\text{m} \leq x \leq 19.42\text{ m}; \quad 0 \leq r \leq 10.9\text{m}$

where x=0. is the rotor plane

Following are figures of the wind turbine model, the inner and the outer meshes.

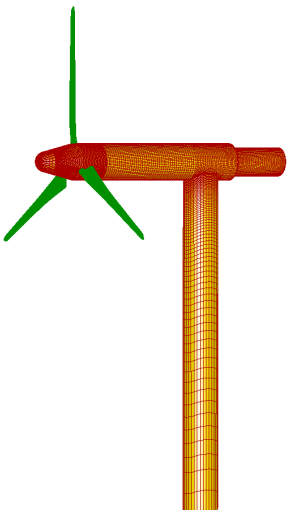

The wind turbine model

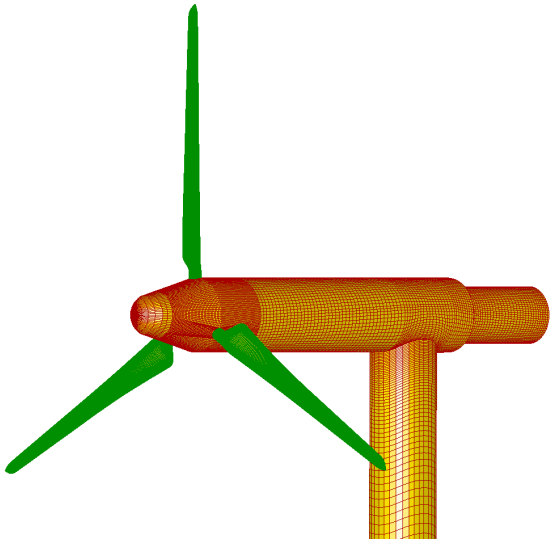

Zoom of the wind turbine model

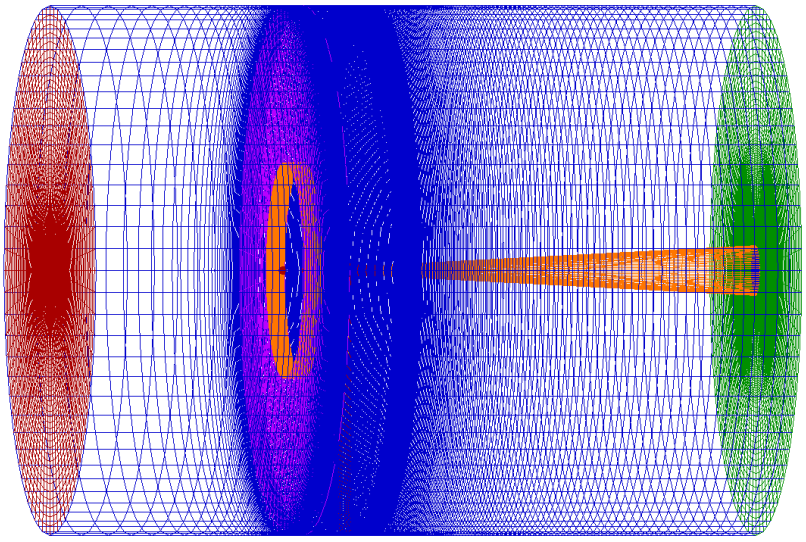

3D view of the inner + outer domains mesh

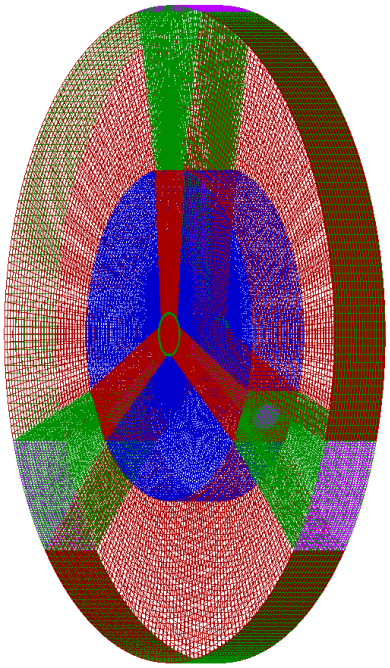

3D view of the inner domain mesh

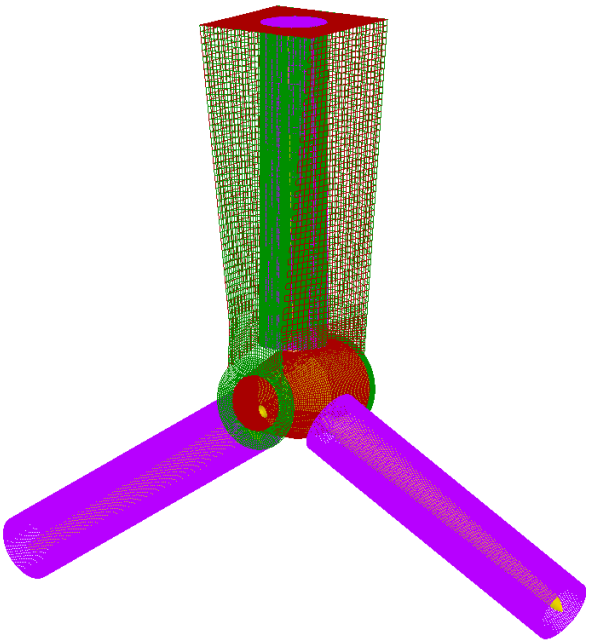

3D view of the two half cylinder blocks around the blades and the wrapping block surrounding the top blade with its two half cylinder blocks.

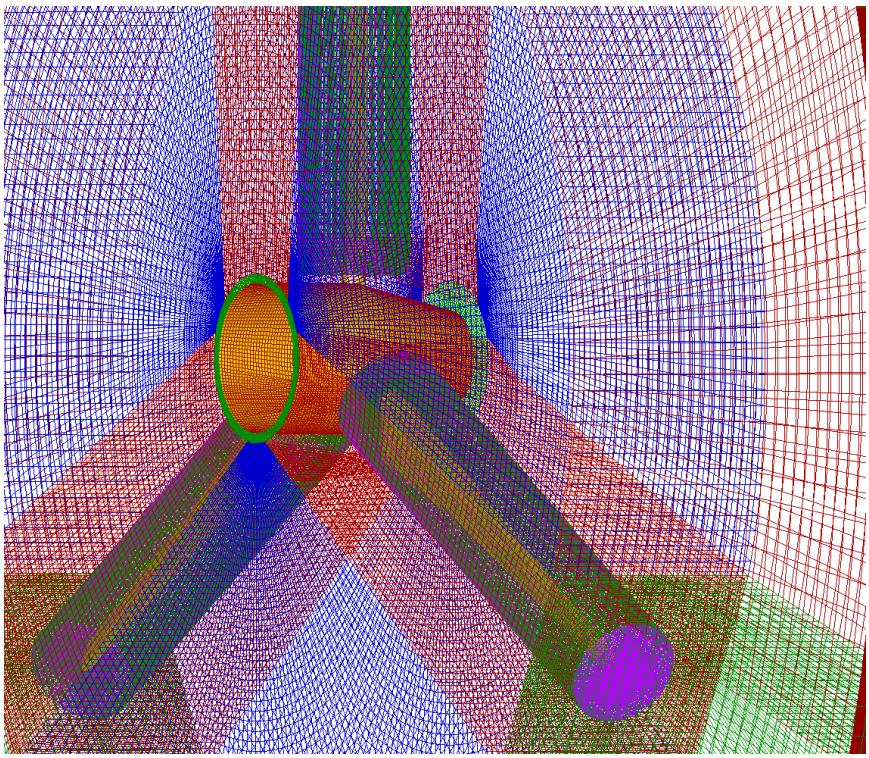

Zoom of the 3D view of the inner domain mesh

For both the coarse and fine meshes that were used in the present calculations, each of the two half cylinder blocks that surround the blades has 121 grid points along the chord, with high concentration at the leading and trailing edge, and 62 grid points along the span.

Boundary conditions:

Inlet boundary condition on the front boundary of the computational domain,
Pressure boundary condition on all other boundaries (i.e. constant static pressure).

Numerical solution algorithm:

The PISO (Pressure Implicit with Splitting of Operators- see Ref. [1]) numerical algorithm is used for solving the transient problem.

The first order Up-Wind scheme is used for the spatial discretization and the first order fully implicit scheme is used for the temporal discretization.

References

[1] J. H. Ferziger and M. Peri´c. Computational Methods for Fluid Dynamics. Springer, Berlin, 3rd. edition, 2002.

C.2.6 TUDelft Panel code

CFD (Potential Flow Panel Model)

1. General description of model (RANS (turbulence model), LES, incompressible, compressible etc)

The model used in this analysis was a potential flow free-wake panel code developed in house at TUDelft. The body and the wake are represented by a source and doublet distribution which are solved for at each and every timestep. One of the major limitations of the model is that it lacks a stall model. For this reason it should be used only in attached flow conditions. Moreover, the model is a dynamic model and is hence suited for yawed flow calculations (again for attached conditions only so no dynamic stall can be modelled).

2. Which components have been modeled (eg blades, tower nacelle, tunnel etc)

Only the blades have been modelled

3. Origin of geometrical description

The origin is positioned at the rotor center in the rotor plane.

4. Describe meshing:

44 spanwise and 32 chordwise elements have been used for 10 rotor revolutions with an azimuthal step of 5 degrees.

5. Describe boundary conditions

Apart from the wind velocities and yaw angles required in cases 2.1 and 2.2, the following inputs were used:

- A Ramasamy-Leishman vortex core and vortex growth model was used
- The initial vortex core size was set to 0.5 the maximum chord.

6. Describe numerical solution algorithm

The following is a simplification of the numerical algorithm used:

- Source and doublet distributions are calculated by the use of a Dirichlet boundary condition at the first time step in which the wake contribution is 0.
- A set of nodes are released behind the blade/body making up the wake.
- The source and doublet distributions are this time calculated on both the body and the wake.
- The velocity field is calculated on each and every wake node.
- The wake node positions are updated from these velocities.
- The process is repeated for every time step.

- The resulting velocities, pressures may hence be calculated for every time step.
- The loads may then be evaluated from these pressures.

7. Miscellaneous remarks

It is to be expected that case 2.2 simulation will results in over predicted loads. This is due to the fact that for this case the blade operates almost entirely in a stalled condition. This model does not take into account dynamic stall.

C.2.7 UAS Kiel CFD

Description of calculation models used in MexNext by UAS Kiel

Authors: A. Jeromin (andreas.jeromin@fh-kiel.de)
A. P. Schaffarczyk (alois.schaffarczyk@fh-kiel.de)

Date: 05 July 2010

Table of contents

List of figures

List of tables

General description of model

The DLR TAU-Code

The DLR TAU-Code is a software system for the prediction of compressible, three-dimensional, viscous or inviscid flows. The flow regime goes from subsonic to hypersonic. A high number of different turbulence models are supplied by TAU. Using hybrid unstructured meshes the prediction of flows about complex geometry is possible. TAU is composed of different modules for pre-processing, solving, mesh adaptation and deformation, transition and more. For mesh generation and post-processing external tools are needed. The use of TAU on parallel computers is based on the message passing interface (MPI).
Originally, TAU was developed for numerical simulations of aircraft-type configurations but can be applied to a wide range of problems.
For more information on DLR TAU-Code and contacting the TAU development team see website: http://tau.dlr.de

Solver setup for computations

Table 1: Setup of TAU solver

Setting	Value
Solver	Compressible RANS
Turbulence model	Original Spalart-Allmaras one equation turbulence model without transition
Reference velocity, Reference density, Reference pressure	According to Case 1.1, 1.2 or 1.3 as defined in document "Definition_first_cases_v19_01_10.doc"
Mesh movement	Rotating mesh, rigid body movement, rotation around x-axis, rotation frequency = -2547.0 1/s
Low Ma Preconditioning	PrimOld with MAPS+ for upwind flux
Simplifications	Nose cone and nacelle rotating with the blade

Components modeled (geometry)

Geometry setup

Table 2: Geometry setup / Components modeled

Component	Description
Volume	120 °-section, 1/3rd of rotor = 1 blade
Blade	1 full blade with suction side, pressure side, tip, root Blade axis: Y
Nacelle	Simplified as cylinder, 1/3rd geometry Length: 2500 mm Radius: 275 mm
Nose Cone	Simplified as frustum and half sphere, 1/3rd geometry Frustum length: 400 mm Half sphere radius: 150 mm

Component	Description
Far field	Axial dimension: [-10 m : 20 m] Radial dimension: [0 m : 12 m]
Periodic boundaries	Periodic for 120 ° to left and right hand sides Rotation axis: X

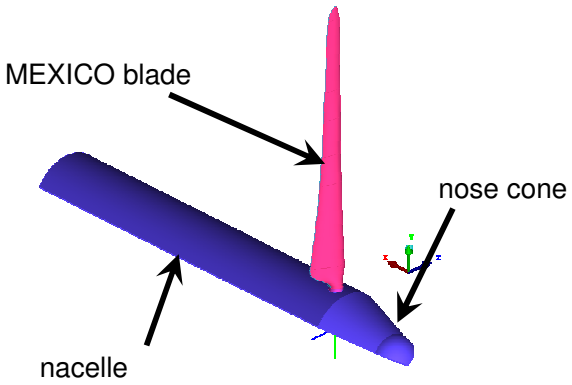

Figure 1: Geometry of blade, nacelle and nose cone

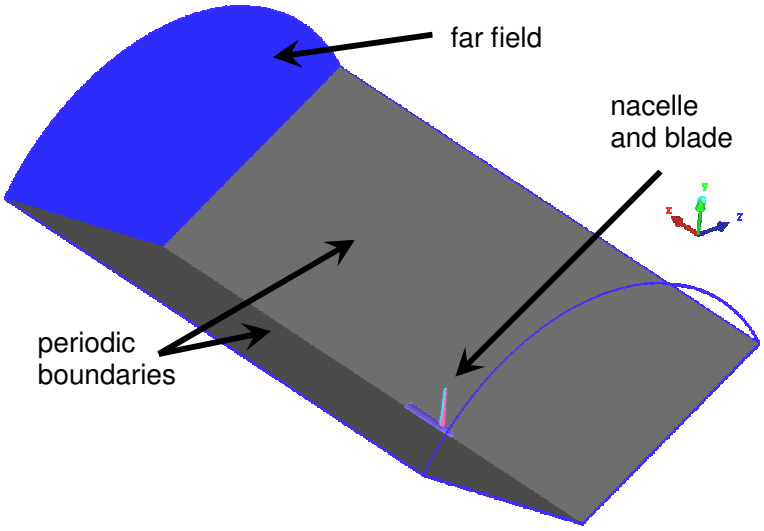

Figure 2: Geometry of far field and periodic boundaries

Origin of geometry

Table 3: Origin of geometry

Component	Description
Blade	CAD file provided on internal MexNext project website
Nacelle and nose cone	Report: NRG-21810/09.97106, page 12, A.K. Kuczaj, 2009
Far field and periodic boundaries	Arbitrary

Description of mesh

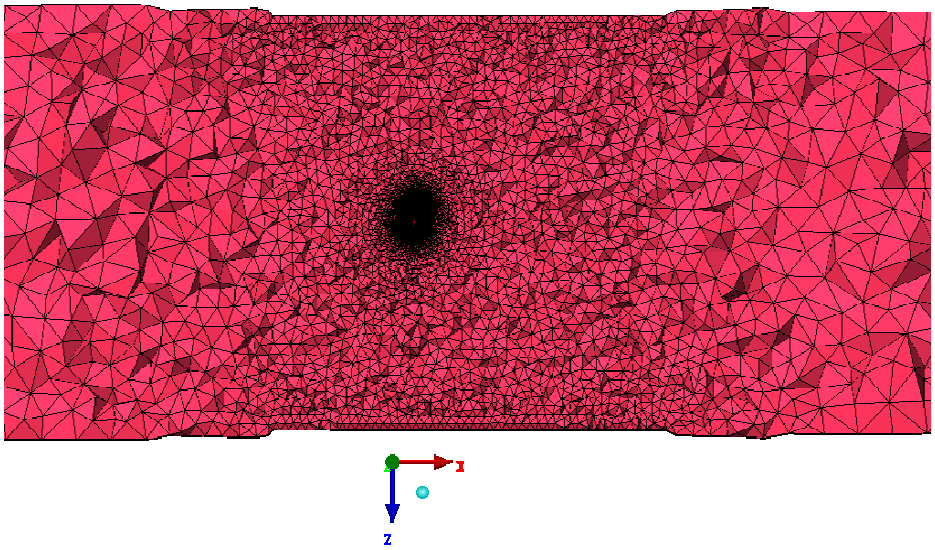

Figure 3: Cut through mesh at r=1.25 m near blade section

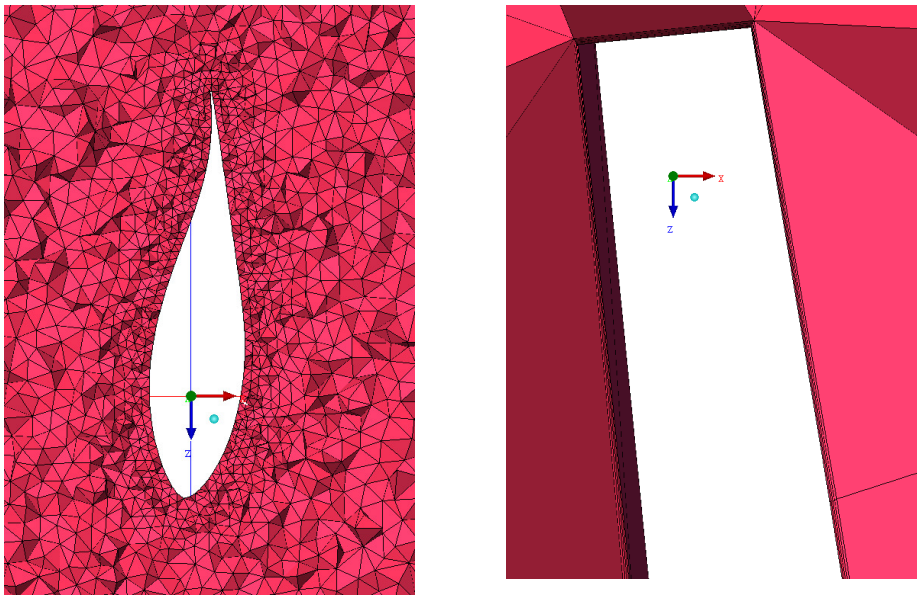

Figure 4: Cut through mesh at r=1.25 m, close up of blade and prism cells at trailing edge

Table 4: Mesh size

Component	No of elements	Element types
Volume	6,121,519	Tetrahedra, Pyramids, Prisms
Blade pressure side	70,984	Triangles
Blade suction side	72,415	Triangles
Nacelle and nose cone	3,782	Triangles, Quadrilaterals
Far field	6,230	Triangles
Periodic boundaries	2 x 9,457	Triangles
Total	**6,293,844**	

Total number of nodes: 1,257,956

Description of boundary conditions

Far field

Far field was modeled with reference settings according to Case 1.1, 1.2 or 1.3, respectively.

Blade, nacelle, nose cone

Blade, nacelle and nose cone were modeled as viscid walls. The boundary layers were assumed to be fully turbulent, no transition was used. All surfaces were rotating with the rotation frequency of the blade

Description of numerical solution algorithm

Table 5: Setup of solution algorithm

Setting	Value
Relaxation solver	Runge-Kutta (explicit)
Runge-Kutta stages	3
Runge-Kutta coefficients	0.15; 0.5; 1
Preconditioning	PrimOld
Upwind flux	MAPS+
Multigrid cycle	4w

For further details on the solution algorithm in TAU please refer to [1] and [3].

Appendix

List of abbreviations

DLR Deutsches Zentrum für Luft- und Raumfahrt e. V. (German Aerospace Center)
MPI Message passing interface
SAO Original Spalart-Allmaras turbulence model

References

[1] TAU-Code User Guide, Manual for Release 2009.1.0, Deutsches Zentrum für Luft- und Raumfahrt e. V., 2009
[2] Transition module (V8.76) User guide (V1.0 beta), Manual, Deutsches Zentrum für Luft- und Raumfahrt e. V., 2009
[3] Technical Documentation of the DLR TAU-Code; Technical report, Institute of Aerodynamics and Flow Technology, DLR

C.2.8 UStutt IAG CFD

Description of CFD model and RANS solver used by the Institute of Aerodynamics and Gas Dynamics (IAG), University of Stuttgart (U STUTT) through the MexNext project

Konrad Meister, Thorsten Lutz, Ewald Krämer

General description of the model

The model used at the IAG to simulate the aerodynamics of the Mexico rotor is based on the solution of the Reynolds Averaged Navier-Stokes equations (RANS). For the present calculations the k-ω turbulence model of Wilcox is being used. The simulations which have been done are steady ones and use the symmetry of the rotor to reduce calculation time. The rotation of the rotor is simulated by rotating the whole domains. These calculations have been done for 10, 15 and 24 m/s upstream velocity with 0° of yaw with a pitch of -2.3°. Unsteady calculations of this scenario have been tested successfully, and will be done soon.

Which components have been modelled?

Until now the blades and nacelle have been modelled. The tower is not modeled yet so that symmetry conditions can be applied for the simulation and the calculation can be done as a steady one. In the upcoming unsteady simulations the tower will be considered. So far wind tunnel effects have not been considered.

Origin of geometrical description

As basis for the blades 43 profile cuts have been extracted from the blade iges file (File from the MexNext website from 26th November 2009). These cuts are used as the basis for the generation of the 3d blade mesh. To receive good consistence between the original geometry and the meshed blade 24 of 44 profile cuts have been extracted in the shaft region and 6 directly in the tip region.

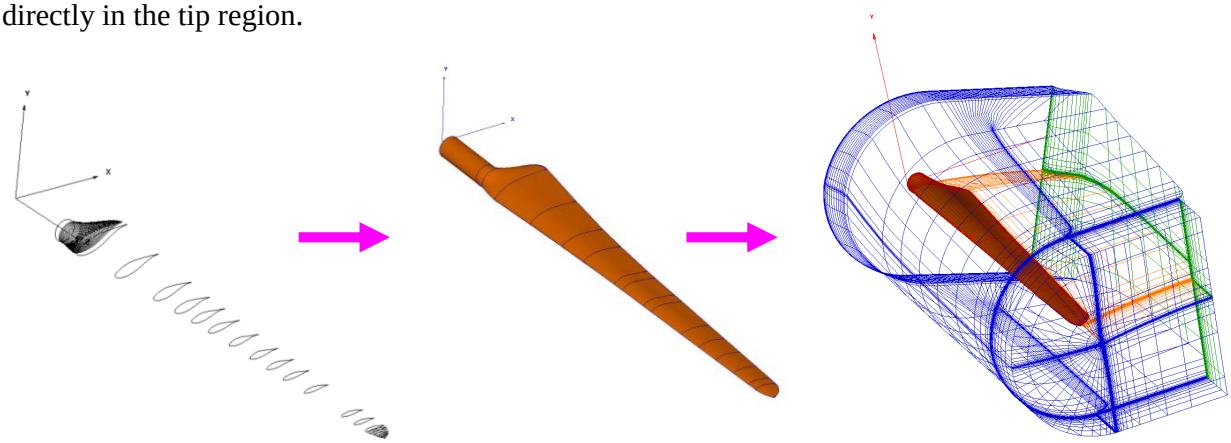

Fig. 1: Script based blade mesh generation

The surface geometry of the nacelle has been created in CATIA. Therefore the dimensions which have been described in the “DRAFT-ExperimentDescription (version 8)” document have been used.

Describe meshing

For the MexNext calculations block structured RANS meshes are being used at the IAG. There are three different types of meshes, namely the blade mesh, the nacelle mesh and the background mesh. Each mesh is created independent from the others, in order to achieve optimized grid quality for each geometry part. The blade and nacelle meshes are rotating in the background mesh. To couple these grids together the Chimera technique is used.

Blade

The blade mesh consists of 3.1 million cells for each blade, has C-block structure (fig. 1) and shows several mesh refinements at the leading and trailing edge and in the tip region. The wake of the blade mesh is refined in total and the mesh is twisted locally to the twist of the blade. Moreover, the boundary layer of the blade is fully resolved by a y^+ value of ≈ 1 and consists of about 30 to 40 cells across the boundary-layer height.

Nacelle

The nacelle mesh is about 2 million cells and has O-block structure. Since the calculations done until now are just steady ones the wall of the nacelle is defined as Euler wall. With the planned unsteady calculations Navier-Stokes walls will be applied at the nacelle with a resolution as described for the blade meshes.

Background

The background mesh consists of 7.2 million cells. The structure is a one third cylinder. For steady calculations the symmetry boundary conditions are used. As the background mesh with the use of symmetry boundary conditions does not need so many cells the size of the background mesh has been expanded so that the distance from the outer boundary to the rotor is 8 rotor diameters. Furthermore the area where the wind turbine is positioned is refined. In case of unsteady calculations the grid structure will be 3d Cartesian.

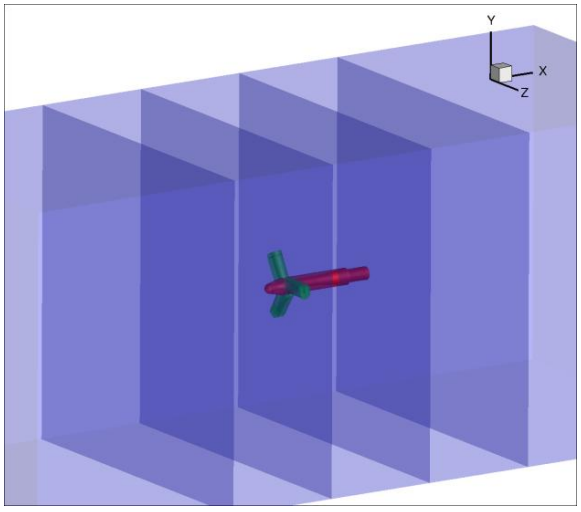

Fig. 2: Grids of the MEXICO rotor (three blades nacelle and background mesh)

Describe boundary conditions

As boundary condition on the blades a Navier-Stokes wall is used. The surface of the nacelle until now is defined as an Euler wall. The boundary conditions of the background mesh are of the type “farfield”. In case that only one third of the turbine is calculated periodic boundary conditions are used at the cuts of the turbine parts and the background mesh.

Describe numerical solution algorithm

For the analyses of the MEXICO rotor the RANS FLOWer is being used at the IAG. This code was developed by the German Aerospace Center (DLR) and solves the three-dimensional compressible Reynolds-averaged Navier-Stokes equations in integral form. The numerical procedure is based on block structured meshes and uses a central cell-cell-vertex or cell-centered or AUSM finite volume formulation for the spatial discretisation.
The types of computations which have been done until now are steady ones. They use central differences and are of second order in space and time. The time integration is done by an explicit hybrid multi stage Runge-Kutta scheme.” The turbulence terms are calculated through the Wilcox k-omega turbulence model. To speed up convergence the solution procedure is embedded into a sophisticated multigrid algorithm. The simulation uses overlapping grids, which is supported by CHIMERA technique.

Future simulations

As the actual simulations have been done as steady ones, the future simulations will be done as unsteady ones. There the tower will be considered and the Euler wall on the nacelle will be switched into a Navier Stokes wall to consider adhesion on the wall. After having done the unsteady calculations wind tunnel effects will be considered in a next calculation round.